

Photonics: Photodiodes and Metamaterials for Thermophotovoltaics and Photodetection Applications

A dissertation

submitted by

Corey M. Shemelya

In partial fulfillment of the requirements
for the degree of

Doctor of Philosophy

in

Electrical Engineering

TUFTS UNIVERSITY

Date

May, 2013

ADVISOR: Thomas Vandervelde

Abstract

Photonics is the study of the propagation and interaction of light and matter. This research aims to utilize the general field of photonics to optimize multiple stages of a thermophotovoltaic energy generator as well as create a dynamic polarization sensitive surface for use in photodetection technologies. To accomplish these sizable goals multiple types of photonic structures and devices have been studied and characterized including high-temperature metamaterial emitters, 2-dimensional photonic crystal filters, dynamic metamaterial polarization-filters, and interfacial miss-fit array photodiodes. The goal of this research is to provide a series of cutting edge building blocks which could be integrated together in a variety of different applications. The results of this work have potential applications ranging from photodetection, to photonic filtering, to renewable energy generation.

Acknowledgements:

Tom: You have been much more than an academic advisor, your guidance and friendship has meant so much to me. Thank you.

Dante: This research would not have been as successful or enjoyable without your constant help and support. Thank you, I could not have done it without you.

John, Chandler, Abbey, Nicole: You were there when I needed someone to bounce ideas off of or provide a distraction from research. Thank you.

Tom and Brian: When research went awry, the ability to come home de-stress with you was one of the things which helped me to carry on the next day.

Mom, Dad, Nana, and Grampy: Thank you for supporting me, even when you have no idea what I am talking about. Love you.

Christina: Thank you for everything my beautiful, not to mention, intelligent wife. I love you.

Table of Contents

Abstract.....	ii
Acknowledgements:	iii
List of Figures	v
Chapter 1.....	2
1.1 Electromagnetic Radiation.....	4
1.2 Applications of TPV	9
1.3 Applications of Metamaterials.....	12
Chapter 2.....	15
2.1 Semiconductors	17
2.2 Metamaterials.....	48
Chapter 3.....	70
3.1 TPV Emitters.....	72
3.2 TPV Filter	79
3.3 TPV Diode.....	86
3.4 Dynamic Metamaterial Filters.....	91
Chapter 4.....	103
4.1 Simulation Methods.....	105
4.2 Processing Techniques	113
4.3 Testing Techniques	133
Chapter 5.....	149
5.1 Metamaterial High Temperature Emitter	151
5.2 Metallic Photonic Crystal Filters	168
5.3 Interfacial Misfit Array (IMF) Photodiodes	179
5.4 Metamaterial Polarization Grid	190
Chapter 6.....	216
6.1 Metamaterial High Temperature Emitter	218
6.2 Metallic Photonic Crystal Filter	233
6.3 IMF Photodiode	241
6.4 Metamaterial Polarization Grid	251
6.5 Summary of Discussion	272
Bibliography	277
Appendix	293

List of Figures

Chapter 1

Figure 1.1.1 Normalized solar spectrum, over 50 percent of incident photons are in the infrared. ^[4]

Figure 1.1.2: Visualization of the propagation of a photon. Blue represents the magnetic field and red represents the electric field. Both the E and B field are at 90 degrees to each other.

Figure 1.1.3: Reflection off of a smooth surface. The majority of TE polarized light is reflected, while the majority of TM polarized light is transmitted. N_1 and N_2 correspond to different indexes of refraction.

Figure 1.2.1: Diagram of a TPV device. Left is the diode stage and filter stage, middle is the emitter stage, and right is a broadband energy source.

Figure 1.2.2: The IR wavelength range with the corresponding black body temperature and typical photodiode materials which operate at that wavelength. ^[5]

Figure 1.2.3: Cost Assumptions for a TPV device used in a cost per watt calculation.

Figure 1.3.1: Metamaterial absorber response as compared to existing technologies. The high absorption and narrow band peak (red) may provide many advantages over the broadband response currently employed (blue).

Chapter 2

Figure 2.1.1.1: The splitting of orbitals into energy bands at low interatomic distances. ^[10]

Figure 2.1.1.2: The allowed and forbidden regions as a function of energy and atomic spacing. ^[10]

Figure 2.1.1.3: The conduction and valence bands of silicon along with the different energy bands. ^[11]

Figure 2.1.1.4: Hole formation. The excited electron leaves the valence shell and can then move more freely within the semiconductor as part of the conduction band. This creates a positively charged hole. The electron and hole can recombine if they meet and the electron loses its excited energy. ^[10]

Figure 2.1.1.5: Direct (a)(b) and indirect transitions (c) . There is a different k value for indirect transitions leading to heat or vibration transfer of energy to the lattice in order to complete the transition. Direct transitions do not interact with the lattice and therefore there is not energy lost to lattice vibrations. ^[15]

Figure 2.1.1.6: The Fermi level with respect to changing temperature: As temperature increases there are more electrons in the conduction band; however, there is never a change in the total number of electrons within the material. ^[26]

Figure 2.1.2.1: all three materials are neutral in charge, however the doping process creates areas where there are local positive (gallium) and negative (arsenic) charges within the lattice. ^[33]

Figure 2.1.3.1: *a)* p-n junction with an ohmic contact *b)* mesa junction *c)* diffused planar junction *d)* ion implanted junction with contact. ^[38]

Figure 2.1.3.2: the charge distribution of a p-n junction. Notice that there are positive charges in the n-type material and negative charges in the p-type material creating a potential across the junction. ^[41]

Figure 2.1.3.3: Band diagram of a diode. The barrier is based on the potential barrier . (1 eV is equal to $q(1 \text{ Volt})$).

Figure 2.1.3.4: Applying a forward or reverse bias voltage changes the magnitude of current flow into the diode by lowering the potential between the conduction and valence bands of the n and p type semiconductors. The lowered potential changes the depletion width as well. ^{[47][49]}

Figure 2.1.3.5: Ideal dark diode equation as a function of applied voltage. The total current shifts when optically generated and thermally generated carriers are introduced. However, these concepts are introduced below with PV and TPV photodiodes.

Figure 2.1.4.1: The ideal diode equation with the addition of optically generated carriers. The open circuit voltage and short circuit current are marked.

Figure 2.1.4.2: Indirect transitions and the two step transition of a conduction electron to the valence band. Notice that this can also be modeled as an electron losing energy to fall into the defect center and then losing more energy and transitioning back into the valence band. ^[54]

Figure 2.1.4.3: Recombination types and corresponding recombination rates as well as the effects on open circuit voltage and short circuit current. These are at both low level and high level carrier injections. ^[19]

Figure 2.1.4.4: The Fill factor is the area formed by multiplying V_{mp} by I_{mp} divided by the area under the total current curve.

Figure 2.1.4.5: Representation of a p-i-n photodiode.

Figure 2.2.1.1: Four quadrants defined using positive and negative permeability and permittivity. Quadrant 1 consists of dielectrics such as optical waveguides, Quadrant 2 consists of metals, Quadrant 3 consists of magnetic materials such as ferrites, and Quadrant 4 is the location of “left handed” materials such as metamaterials.

Figure 2.2.1.3: Depicting the “left handed” and “right handed” transmission (blue) at an interface using Equation 2.2.1.5. ^[9]

Figure 2.2.1.4: The propagation of light derived from the wave equation separated into quadrants based on the sign of the permittivity and permeability. Quadrant 1 and Quadrant 3 allow for the propagation of light. Quadrant 2 and Quadrant 4 create exponentially decaying evanescent waves.

Figure 2.2.1.5: First experimentally verified metamaterial structure. ^[63]

Figure 2.2.2.1: A dynamic MM structure, when electrons are excited within the Si layer, the split gap begins to act as a larger capacitor, altering the MM response. ^[64]

Figure 2.2.2.2: A Schottky diode, notice the exponential increase in current at positive bias and constant current at negative biases.

Figure 2.2.3.1: One dimensional photonic crystal (left), Two dimensional photonic crystal (middle), Three dimensional photonic crystal (right). ^[65]

Figure 2.2.3.2: *Left:* the lattice constants of a photonic crystal, they are defined as a vector based on the x and y plane. *Right:* reciprocal lattice constants in momentum space. ^[89]

Figure 2.2.3.3: The light lines as a function of frequency and the wave vector for three structures: bulk GaAs (left), GaAs and GaAlAs alternating layers (middle), and GaAs and Air alternating layers (right). Notice the increasing photonic band gap with increasing variation in index of refraction. ^[84]

Figure 2.2.3.4: A two dimensional photonic crystal with the periodic a value and rod radius r . ^[66]

Figure 2.2.3.5: Two dimensional photonic crystal of veins for TE polarizations (left) and a two dimensional photonic crystal of rods for TM polarizations(right). ^[67]

Figure 2.2.3.6: *Left:* Image showing the rod areas which support a TM photonic band gap and the vein areas which support a TE photonic band gap. *Right:* The band structure of the two dimensional lattice shown in the inset. The blue shaded region is the irreducible Brillion zone and points Γ , M, and K are the points of high symmetry^[68]

Chapter 3

Figure 3.1.1: Three examples of PhC tungsten emitter technologies. *Left and Right:* log cabin PhC emitter designs.^{[71][72]} *Middle:* square “vein” pattern used to alter the TE optical mode.^[74]

Figure 3.1.2: Spectral response of the PhC on left. Notice the much higher spectral response at 1.7 μ m as compared to that of un patterned tungsten.^[74]

Figure 3.1.3: Simulated results of a Ta PhC emitter with various etch depths and hole radius.^[84]

Figure 3.1.4: *Left:* perfect absorber square lattice features.^[97] *Middle:* perfect absorber circular structures.^[98] *Right:* perfect absorber cross structures.^[99]

Figure 3.1.5: *Left:* measured absorption of an Au cross pattern.^[99] *Middle:* measured absorption of an Au square pattern.^[100] *Right:* measured absorption of an Au circle pattern.^[98]

Figure 3.1.6: Experimental verification of Kirchoff’s law using a MM perfect emitter at different temperatures.^[104]

Figure 3.1.7: Multiple sizes of a Au cross MM pattern tiled in order to combine resonances and produce a broad MM resonance peak.^[104]

Figure 3.1.8: The optical response of the same MM structure before (left) and after (right) deformation due to heating.^[80]

Figure 3.2.1: Left: False color TEM of the Si-SiO 1D PhC. Top-right: Reflectance of Si-SiO 1D PhC. Bottom-right: TPV efficiency incerase with implimentation of the 1D PhC.^{[78][108]}

Figure 3.2.2: Three types of semiconductor PhCs used as ARCs and filters for PV technologies. Left and Right: Semiconductor with air rods. Middle: Semiconductor rods in air structure.^{[112][113][115]}

Figure 3.2.2: Left: measured absorption with the addition of a PhC. Right: The spectral quantum efficiency of a photodiode with and without a 2D PhC.^{[111][114]}

Figure 3.2.3: Two variations of defect modes within a PhC lattice. *Left:* A single hole is removed creating the defect mode. *Right:* this pattern consists of multiple hole radii and missing holes in order to create polarization sensitivity. ^{[119][122]}

Figure 3.2.4: The spectral responses of defect mode PhCs, the largest amplitude corresponds to the defect resonance. *Left:* Spectral response of a single defect mode. *Right:* spectral response of multiple polarizations with multiple defect modes. ^{[120] [122]}

Figure 3.2.5: Three types of metallic PhC patterns. *Left:* Square PhCs. ^[125] *Middle:* Hexagonal PhC pattern. ^[123] *Right:* Square PhC pattern. ^[129]

Figure 3.2.6: Improvement of spectral response, responsivity, and photoresponse due to the addition of a metallic PhC. *Left:* hexagonal PhC pattern. ^[123] *Middle:* square PhCs. ^[125] *Right:* square PhC pattern. ^[129]

Figure 3.2.7: Increase in responsivity and wavelength shift due to the addition of a SiN_x layer deposited via CVD. This response is predicted to be due to an ARC effect. ^[124]

Figure 3.3.1: *Top:* strained layer with no IMF present, the top GaSb layer has a longer lattice constant in the y-direction and shorter in the x-direction leading to dislocations as thickness increases. *Bottom:* IMF layer with every 14th atom missing at the interface. The result is a strain free GaSb layer. ^[135]

Figure 3.3.2: *Left:* The addition of an IMF layer produces a uniform material above the GaSb/GaAs interface. *Right:* Dark lines represent threading dislocations not found when the IMF layer is present. ^[136]

Figure 3.3.3: *Left:* electroluminescence of a VLED photodiode showing a narrow bandgap of the GaSb layer. *Right:* Responsivity of a photodiode using an IMF layer. ^{[137][141]}

Figure 3.3.4: VECSEL performance of a latticed match substrate (blue) and that with an IMF layer (red). ^[136]

Figure 3.3.5: *Left:* IMF material growth showing no threading dislocations. *Middle:* A threading dislocation appearing near the edge of an IMF growth. *Right:* large numbers of dislocations forming when no IMF layer is present. ^[156]

Figure 3.4.1.1: Left: SRR patterns produced at scales under 1μm in length. Right: resonance response of these small SRR devices. ^[172]

Figure 3.4.1.2: Incremental modification of a SRR device into thin nano-bars. These structures provide the bases for the split wire pair MM structure. ^[169]

Figure 3.4.3: A fishnet MM devices consisting of two metallic layers with a dielectric spacer ^[178]

Figure 3.4.1.4: *Left:* simulated transmission and reflection characteristics for a silver MM fishnet structure. ^[178] *Right:* Experimentally obtained reflection and transmission characteristics for a silver and silicon fishnet design. ^[179]

Figure 3.4.1.5: *Top:* Transmission and reflection of a SWP MM. ^[183] *Bottom:* SEM image of a SWP MM along with experimental and simulated transmission results. Notice the notch filter type transmission obtained with the SWP structure. ^[184]

Figure 3.4.1.6: *Left:* cross-sectional image of a typical metallic grating polarization filter. *Right:* transmission of each polarization, notice the large transmission for p-polarized light and large reflection for s-polarized light at all frequencies. ^[191]

Figure 3.4.1.7: *Left:* Each MM structure in the polarizer device. The SRR and SWP utilize the semiconductor and the split-gap and the fishnet is made up of the semiconductor/Schottky barrier/metal stack as opposed to the traditional metal/dielectric/metal stack. *Right:* expected transmission response of the polarization grid. The SWP and SRR act as a notch filter and the fish-net structure acts as a band pass filter.

Figure 3.4.2.1: *Left:* a split ring resonator with highly doped Si located at the split-gap, optical pumping increases the carrier concentration in the Si. The result is a larger capacitance across the split gap and an altered MM response. ^[64] *Right:* A SRR on a highly doped substrate the optically excited charge carriers “short” the split gap, altering the MM response. ^[195]

Figure 3.4.2.2: *Left:* As the Si gains charge carriers, the resonance frequency of the MM structure is shifted. ^[64] *Right:* as the split gap is “shorted” the MM resonance is removed, not simply shifted to another frequency. ^[195]

Figure 3.4.2.3: *Left:* voltage controlled SRR MM structure designed to increase resonance by depleting the split-gap region. ^[200] *Right:* voltage controlled SRR MM designed to alter the capacitance of the split gap (not creating a short) in order to alter the resonance frequency. ^[203]

Figure 3.4.2.4: *Left:* Applied voltage used to increase the MM resonance by creating a charge depleted region in a doped semiconductor. Resulting in increased transmission. ^[200] *Right:* Applied voltage used to shift the MM response using a charge depletion region. ^[203]

Figure 3.4.2.5: *Left:* Thermally tuned dynamic MM, the optical split gap can be “shorted” using thermally generated charge carriers. ^[206] *Right:* MEMS MM

structure, one arm of the cross can be altered physically to change the resonance frequency.^[209]

Chapter 4

Figure 4.1.1.1: Yew Square with the electric field vectors located in the center of the edges in the direction of the blue arrows. The magnetic field vectors are located in the center of the faces and in the direction towards the middle of the cube.

Figure 4.1.1.2: Original vectors and the vectors located one unit step to the right. If the unit cell was one above (in the **k** direction) or behind (in the **j** direction), then the **k** and **j** units would be indexed by one.

Figure 4.1.1.3: The electric and magnetic field vectors in time. The variable **n** represents the current time; therefore **n+1** represents a future time step and **n-1** represents a past time step.

Figure 4.2.1.1: Substrate oxide chemical cleaning list.

Figure 4.2.2.1: *Left:* A Suss MJB4 Mask Aligner. *Right:* The OAI Model 204IR Mask Aligner. Shown are the microscope objectives and monitors for mask alignment. Also, the mercury lamp and sample/mask holder are shown.^{[216][215]}

Figure 4.2.2.2: *Left:* example of a photolithography mask chromium is represented as black. *Right:* Positive photoresist (circle) after exposure and development.

Figure 4.2.2.2: General processing notes for all photoresists use. Note that all development times are using MF-CD 26 developer

Figure 4.2.2.4: A thicker resist allows easier penetration of the developer.

Figure 4.2.2.5: Metallization patterned using photolithography. Light pattern is gold, darker pattern is the GaSb semiconductor substrate after removal of photoresist.

Figure 4.2.3.1: Raith 150 electron beam lithography system. The system includes software controlled pattern generator, field effect scanning electron microscope, and 20 keV electron source.^[217]

Figure 4.2.4.1: Denton E-beam evaporator. The sample chamber, target chamber, and connector are indicated.^[218]

Figure 4.3.4.2: Typical Schottky and ohmic contact characteristics. Schottky contacts typically allow less current to flow due to a conduction band barrier, as an external bias is applied, this barrier shrinks, allowing greater current flow as well as a non-linear response. Ohmic contacts are designed to have very little barrier between the semiconductor and metallization, the result is high current flow and little electrical resistance.

Figure 4.2.4.3: E-Beam thermal evaporator metallization recipes used.

Figure 4.2.4.1: Process parameters summarized for CVD applications.

Figure 4.2.5.1: Reactive ion etching. *Top Left:* Reactive gases are introduced to the chamber and a plasma is created using these gases. The gases then react with the surface of the sample. *Top Right:* The plasma imparts enough energy to the reacted chemicals to allow the reactive chemicals to bond to the substrate and then are released as gas molecules to be removed from the chamber. *Bottom:* the process is continued until the desired etch depth is reached. The resulting trench is very anisotropic due to an applied voltage between the substrate and plasma.

Figure 4.2.5.2: Etch parameters used during device fabrication.

Figure 4.3.1.1: The process from which features are resolved using an SEM backscatter detector. There are many more secondary electrons produced at surface features resulting in more electron flux on the detector. Thus an image is produced. ^[220]

Figure 4.3.1.2: *Left:* inlens detector used to image a GaSb aperture surrounded by Au. *Right:* SE2 detector used to image the same aperture. ^[219]

Figure 4.3.1.3: Diagram of an SEM with both inlens and SE2 detectors, stigmator and focusing controls, lenses, apertures, and controls software. ^[220]

Figure 4.3.2.1: Two types of FTIRs. *Left:* Jasco Microscope reflection FTIR using a cassegrain lens allowing for reflection measurements averaged at angles from 25 degrees to 45 degrees. ^[221] *Right:* Thermoscientific FTIR allowing for normal incident transmission measurements and near normal reflection measurements (10 degrees). ^[222]

Figure 4.3.2.2: The Michelson interferometer of an FTIR. The interference pattern formed due to the light source and moving mirror allows for wavelength resolution through frequency domain measurements.

Figure 4.3.3.1: Solar simulator capable of optical intensities from 1-10 suns calibrated using a reference cell. The I-V measurement is then obtained using the source meter.

Figure 4.3.3.2: The sample stage of the solar simulator where a PV or TPV diode can be connected to the source meter using micro-manipulators.

Figure 4.3.4.1: Photoluminescence setup. Light emitted from the HeNe laser is first chopped. Then the incident intensity can be altered with a neutral density filter and focused onto the sample using a lens. Any photoluminescence from the sample is collected by another lens and focused on the monochromator. The monochromator allows only one wavelength through to the detector at any moment. The signal is then recorded by the detector.

Figure 4.3.5.1: Electroluminescence setup. The sample is excited using a function generator. The resulting electroluminescence is collected by lenses and optically chopped. A monochromator then scans through a set wavelength range with a photodetector collecting the electroluminescent signal.

Figure 4.3.6.1: Depiction of a variable wavelength ellipsometer. White light is filtered with a monochromator to a specific wavelength. The light is then linearly polarized and guided through a quarter wave plate resulting in circularly polarized light. The circularly polarized light is incident on the sample which causes a polarization change dependent on the sample's properties.

Figure 4.3.6.1: The J. A. Woollam Spectroscopic Ellipsometer. Shown is the sample holder, rotation stage, polarizer, quarter wave plate, analyzer, and photodetector.^[223]

Chapter 5

Figure 5.1.1: A list of potential materials for use in a high temperature TPV emitter. The four most promising materials are highlighted in grey.

Figure 5.1.2: MM emitter structure: circular Pt MM features, alumina dielectric spacer, and Pt back grounding plane.

Figure 5.1.3: An Au MM absorber constructed to operate at a wavelength of 1500 nm. Absorption was tested at room temperature using an ellipsometer at 15 degrees from normal incidence. *Inset:* MM design.

Figure 5.1.4: *Top:* Au MM pattern before heating to 360 °C. *Bottom:* MM pattern after heating to 360 °C. The dark shapes represent areas where the gold and silicon combine in an eutectic.

Figure 5.1.5: *Left:* Absorption measured before and after heating. The formation of the eutectic causes a complete loss of MM absorption even though the patterned elements are present. *Right:* Optical image of MM patterned samples with and without heating.

Figure 5.1.6: Simulated results of a Pt MM absorber.

Figure 5.1.7: Surface current at three points in the Pt perfect absorber stack at resonance (8 μm). *Top Left:* the top of the Pt rod. *Top Right:* the Pt rod/ Al_2O_3 interface. *Bottom Middle:* the Al_2O_3 /Pt grounding plane interface.

Figure 5.1.8: The E-field at three points in the Pt perfect absorber stack at resonance (8 μm). *Top Left:* the top of the Pt rod. *Top Right:* the Pt rod/ Al_2O_3 interface. *Bottom Middle:* the Al_2O_3 /Pt grounding plane interface.

Figure 5.1.7: Pt nano-rods deposited on 20 nm of Al_2O_3 with a 100 nm Pt grounding plane.

Figure 5.1.8: Reflection data taken from the Pt perfect absorber MM of figure 5.1.4.

Figure 5.1.9: Absorption measurements for three MM structures with varying radius and spacer thicknesses. Notice the read peak at 800 nm.

Figure 5.1.10: Emissivity testing setup. The sample is heated using a temperature controller; the emission is then collected using collimating lenses and optically chopped. The chopped signal is filtered with a monochromator and then collected with a photodetector.

Figure 5.1.11: Emission at 500 $^\circ\text{C}$. This temperature is not high enough to exhibit strong optical emission in the visible, as such a very noisy signal is observed.

Figure 5.1.12: MM response before and after heating. A temperature of 500 $^\circ\text{C}$ caused an altered absorption pattern with and without a MM pattern as well as strong discoloration in the sample.

Figure 5.1.13: After heating the MM pattern is intact, however there appears to be significant damage to the thin Al_2O_3 layer.

Figure 5.1.14: Absorption results from the Pt/ Al_2O_3 /Pt on sapphire MM structure. *Blue Dash:* Simulated absorption results. *Blue Line:* Absorption at 15 degrees from normal incidence before heating to 650 $^\circ\text{C}$. *Red Line:* Absorption at 15 degrees from normal incidence after heating to 650 $^\circ\text{C}$.

Figure 5.1.15: Pt/ Al_2O_3 /Pt on sapphire MM structure. *Left:* Before heating. *Right:* after repeated heating to 650 $^\circ\text{C}$.

Figure 5.1.16: Emissivity as a function of wavelength as well as absorption obtained using an ellipsometer after repeated heating.

Figure 5.2.1: Spectral content and pulse time of the Lumerical Simulation Source. *Top:* pulse intensity as a function of time. *Middle:* Intensity of E-field as a function of wavelength content (notice black body curve and peak wavelength of 1.3 μm). *Bottom:* Intensity of E-field as a function of frequency content.

Figure 5.2.2: Representative structures tested in this section. Only Si_3N_4 as an ARC, a GaSb PhC, and GaSb/ Si_3N_4 PhC were fabricated and tested.

Figure 5.2.3: Predicted absorption increases using FDTD simulation software. Notice the lack of improvement with the addition of a back reflecting plane.

Figure 5.2.4: Comparison of absorption with the addition of a back reflector. The resulting interference pattern decreases absorption as shown in Figure 5.2.3.

Figure 5.2.5: Fabricated PhC pattern shown under scanning electron microscopy.

Figure 5.2.6: Absorption data of substrates with no ARC determined from ellipsometry at an angle of 23 degrees from the surface normal. The y-axis represents relative absorption as feature sizes were much smaller the measured background spectrum causing errors in absolute magnitude.

Figure 5.2.7: Absorption data of substrates with SiN_x ARC determined from ellipsometry at an angle of 23 degrees from the surface normal. The y-axis represents relative absorption as feature sizes were much smaller the measured background spectrum causing errors in absolute magnitude.

Figure 5.2.7: Diode structure used with a metallic PhC structure.

Figure 5.2.8: SEM image of PhC enhanced diode. *Left:* the edge of the aperture is shown and the PhC acts as a continuation of the ohmic contact. *Right:* PhC pattern over the center of the photodiode.

Figure 5.2.9: I-V curve of a GaSb photodiode with and without a PhC. This data was taken from the same diode in order to maintain consistency with processing and I-V characteristics.

Figure 5.2.10: The resulting performance metrics of the PhC enhanced GaSb TPV diode stage. Of particular note is the I_{sc} , max power, and conversion efficiency, which result from an increased number of photogenerated excitations.

Figure 5.3.1: Two structures grown using molecular beam epitaxy. *Top:* R9-81 is a GaSb junction grown on GaAs with a IMF layer. *Bottom:* R9-86 is an identical junction grown on a GaSb substrate.

Figure 5.3.2: XRD data for the IMF layer. The measured lattice constant for the R9-81 was consistent with a GaSb on GaSb junction.

Figure 5.3.3: photodiode fabrication process. The sample is first etched to the bottom contact and then coated with Si_3N_4 . The Si_3N_4 is then etched leaving behind a layer of sidewall passivation. Finally the contacts are metalized to create a photosensitive structure.

Figure 5.3.4: *Insert:* Image of a TLM pattern on the top contact layers. *Bottom:* Ohmic contact I-V curves for R9-81 top contacts using various circular TLM patterns.

Figure 5.3.5: Standard photodiode mesa patterns.

Figure 5.3.6: *Left:* comparison of the R9-86 photodiode and R9-81 photodiode. *Right:* relative I-V characteristics.

Figure 5.3.6: Apertures ranging from 30 μm to 300 μm fabricated to test relative surface recombination rates.

Figure 5.3.7: Top: Aperture I-V curves obtained for the GaSb on GaSb R9-86 sample. Bottom: I-V curves obtained for the GaSb on GaAs with IMF layer.

Figure 5.3.8: Current densities obtained from the apperture diode set for the R9-86 (*Top*) and R9-81 (*Bottom*) sample set.

Figure 5.3.9: Spectral response from 800 nm to 2000 nm, the high noise is due to low optical transmission in the filtering grating of the monochromator.

Figure 5.3.10: Optimized Structure to further test benefits of using an IMF layer. These designs consist of a three sample group. Sample 1 is shown above. Sample 2 adds a IMF layer between layer 0 and 1. Sample 3 replaces layer 0 with a GaSb substrate.

Figure 5.3.11: Optimized growth is simulated to perform with a higher efficiency as well as provide better crystal quality due to a lower doped n-type contact region.

Figure 5.4.1.1: Metamaterial pattern, substrate, and semiconductor layer used to create a dynamic MM response.

Figure 5.4.1.2: Simulated transmission characteristics of the MM polarization grid. Purple is the S-polarized transmission and green is the Y-polarized transmission. Highlighted in a black square is the resonance frequency of the MM for each polarization.

Figure 5.4.1.3: Magnetic field and surface current at the Au/GaAs interface. For each pair, top images are vector and bottom images are magnitude. *Top Left:* Off resonance (66 THz) X-polarized surface current direction and H-field magnitude. *Top Right:* Off resonance (66 THz) Y-polarized surface current direction and H-field magnitude. *Bottom Left:* X-polarized surface current direction and H-field magnitude at resonance (60 THz). *Bottom Right:* Y-polarized surface current direction and H-field magnitude at resonance (57.5 THz).

Figure 5.4.1.4: Electric Field at the Au/GaAs interface. For each pair, top images are vector and bottom images are magnitude. *Top Left:* Off resonance (66 THz) X-polarized surface current direction and H-field magnitude. *Top Right:* Off resonance (66 THz) Y-polarized surface current direction and H-field magnitude. *Bottom Left:* X-polarized surface current direction and H-field magnitude at resonance (60 THz). *Bottom Right:* Y-polarized surface current direction and H-field magnitude at resonance (57.5 THz).

Figure 5.4.1.6: Experimental transmission for X and Y-polarized light obtained using FTIR data.

Figure 5.4.1.7: Static transmission Characteristics comparing simulation and experimental data at the resonance frequency (61 THz).

Figure 5.4.1.8: *Top Left:* effective permeability and permittivity. *Top Right:* the effective index of refraction of the MM. *Bottom Left:* Real and imaginary permittivity values. *Bottom Right:* Real and imaginary permeability values.

Figure 5.4.1.9: *Top Left:* effective permeability and permittivity. *Top Right:* the effective index of refraction of the MM. *Bottom Left:* Real and imaginary permittivity values. *Bottom Right:* Real and imaginary permeability values.

Figure 5.4.1.10: Experimental demonstration of MM scalability. When the pattern size is in one direction, the corresponding polarization resonance peak is also altered.

Figure 5.4.1.11: The MM response is removed as the thickness of the GaAs layer is increased.

Figure 5.4.1.12: Doping dependence of MM response. There is a blue-shift experienced with increased doping levels, as well as a decrease in transmission consistent with higher conductivity.

Figure 5.4.2.1: Dynamic Simulation results obtained by altering the conductivity of the GaAs layer. *Top:* Y-polarization. *Bottom:* X-polarization.

Figure 5.4.2.2: Simulated and ideal on/off and polarization ratios at 60 THz.

Figure 5.4.2.3: Ohmic contact measurements for four potential substrates with doping levels of $<1 \times 10^{15} \text{ cm}^{-3}$, $5 \times 10^{16} \text{ cm}^{-3}$, $1 \times 10^{18} \text{ cm}^{-3}$, and intrinsic GaAs on sapphire.

Figure 5.4.2.4: Schottky contacts fabricated on three substrates with doping levels of $<1 \times 10^{15} \text{ cm}^{-3}$, $5 \times 10^{16} \text{ cm}^{-3}$, $1 \times 10^{18} \text{ cm}^{-3}$, and intrinsic GaAs on sapphire.

Figure 5.4.2.5: *Left:* linear TLM patterns used to test ohmic contact recipes. *Right:* top square is the Schottky diode and bottom “U” is the ohmic contact pad. This structure was used to test the Schottky response.

Figure 5.4.2.6: MM pattern with Schottky contact and ohmic contact pad. The structure was constructed in such a way as to reduce noise when transmission measurements were performed.

Figure 5.4.2.7: *Left:* image of the arc-welded sample after testing. *Right:* SEM image of the two contact pads and short formed due to the weld.

Figure 5.4.2.8: The addition of Si_3N_4 to the MM pattern. *Left:* SEM image showing the Si_3N_4 , metamaterial, and exposed GaAs. *Right:* fully constructed MM pattern with Si_3N_4 layer, metamaterial, GaAs layer, and contact pads.

Figure 5.4.2.9: Current-Voltage characteristics for three highly doped n-type GaAs thin films grown on a sapphire substrate. At an applied voltage of 20 V the max current obtained is 0.5 mA.

Figure 5.4.2.10: Contact tests for thin film GaAs epitaxially grown on sapphire. At an applied voltage of 20 V, the maximum current generated is 0.8 mA and is generally consistent between all contact recipes attempted.

Figure 5.4.2.11: SEM images of the MM surface after identical processing techniques. *Left:* Bulk GaAs commercially obtained wafer. *Middle:* Undoped GaAs grown using MBE on sapphire. *Right:* Highly doped ($1 \times 10^{18} \text{ cm}^{-3}$ doping) GaAs grown using MBE on sapphire. Both Middle and Right surfaces should be smooth as shown in the Left image.

Figure 5.4.2.12: Metamaterials mounted in the chip holder and wire-bonded to the outside contacts.

Figure 5.3.2.13: *Left:* Fully mounted MM in the FTIR. *Right:* leads are attached to the ohmic and Schottky contact pads and an external bias is applied.

Figure 5.4.2.14: Dynamic results obtained using very high resistance contacts to highly doped GaAs on Sapphire.

Figure 5.4.2.15: Dynamic results obtained using $5 \times 10^{16} \text{ cm}^{-3}$ doped DSP GaAs with a MM pattern. The results demonstrate dynamic transmission characteristics (3% decreases in transmission) for materials not at resonance wavelengths.

Figure 5.4.2.16: Simulated alteration in conductivity needed for the GaAs on sapphire metamaterial to achieve a 3% drop in conductivity at wavelengths demonstrating bulk properties and not MM resonant frequencies. Using this data the expected change in conductivity with an applied bias is 3,000 S/m.

Chapter 6

Figure 6.1.1: Design of the high temperature thermal emitter. Three designs were constructed and tested. *Sample 1:* Pt radius of 91 nm, Al_2O_3 of 20 nm. *Sample 2:* Pt radius of 72 nm, Al_2O_3 of 20 nm. *Sample 3:* Pt radius of 91 nm, Al_2O_3 of 10 nm.

Figure 6.1.2: Simulated Absorption. *Purple:* Absorption of 72 nm radius Pt rods with 20 nm of Al_2O_3 . *Red:* Absorption of 91 nm radius Pt rods with 20 nm of Al_2O_3 . *Blue:* Absorption of 91 nm radius Pt rods with 10 nm of Al_2O_3 .

Figure 6.1.3: *Left:* the incident radiation creates a surface current in the metamaterial structure. This current is isotropic as to effect all incident polarizations. *Right:* the electric field within the structure is also altered in the Z-direction. The effect of both characteristics is an altered permeability and permittivity.

Figure 6.1.4: Fabricated devices. *Left:* 10 nm Al_2O_3 insulation layer. *Middle:* 20 nm Al_2O_3 insulation layer. *Right:* 20 nm Al_2O_3 insulation layer (scale inset).

Figure 6.1.5: *Left:* 45 degree angle of 10nm thick Al_2O_3 sample. *Right:* top view of same sample.

Figure 6.1.6: Experimental Absorption. *Black Check Box:* simulated absorption peaks obtained for all MMs, of note is the relative intensity for each peak. *Black Box:* Experimental absorption for each structure. The relative intensity as well as resonance wavelengths, matches that of the simulated results.

Figure 6.1.7: *Top:* Emission testing results at 500 °C. It is unclear if noisy signal was completely due to low thermal energy density or of if heating damage reduced signal quality. *Bottom:* Absorption response before and after heating of MM to 500 °C.

Figure 6.1.8: Left: SEM image after heat testing to 500 °C. Right: Same structure before heat testing.

Figure 6.1.9: Measured absorption before heat cycling and after 4 cycles to temperatures exceeding 600 °C, the simulated MM response is also shown.

Figure 6.1.10: *Left:* Metamaterial structure before heating. *Right:* Same structure after repeated heating to 650 °C.

Figure 6.1.11: Deformation due to repeated heating, these defects are worth noting, however, they have been shown to have little effect on pattern emission or absorption.

Figure 6.1.13: MM emissivity normalized with respect to the emission of Pt. The emissivity was measured independently at a variety of temperatures. Increasing the temperature was found to decrease the noise present; however, in all cases the resonance peak remained unchanged.

Figure 6.1.14: The expected emission of the MM at temperatures greater than 1400 °C. This data is based on the experimentally obtained emissivity from Figure 6.1.15.

Figure 6.1.15: *Top:* High Temperature MM absorber centered at 1350 nm. *Bottom:* PhC with cut-off frequency of 1650nm based on the emissivity of Ref. [84]. The MM emitter follows the spectral response of a GaSb photodiode much more closely than the PhC emitter. Both structures are based on emissivity data at a temperature of 1700 °C.

Figure 6.2.1: Simulated and experimental absorption. Experimental absorption was taken at an angle of 23 degrees from the surface normal leading to decreased observable absorption at resonance (black circles). *Top:* PhC with no ARC compared to GaSb with no ARC. The characteristic responses of the PhC are shown as black squares. *Bottom:* PhC with an ARC, GaSb with an ARC, and GaSb without an ARC. The characteristic PhC responses are shown within the black squares.

Figure 6.2.2: I-V curve characteristics. *Top:* I-V curves obtained for the samples at a solar concentration of 10 suns. *Bottom:* the defining characteristics obtained from the I-V curves including short circuit current, open circuit voltage, fill factor, max power, and conversion efficiency.

Figure 6.2.3: *Left:* Region of optical enhancement for a PhC is limited to a depth of approximately 1.5 μm . *Right:* the structure of the photodiode used in the measurement. The absorber layer is located at a depth of 300 nm to 1.5 μm . The result is a 20% smaller absorption region compared to simulated results.

Figure 6.2.4: The metrics used to determine the quantitative effects of applying a metallic PhC as a front side filter enhancement to a TPV diode. As a TPV diode without a SiN layer is not feasible, the leftist three metrics use this structure as a

baseline. *Denotes compared to unaltered GaSb. #Denotes compared to GaSb with SiN_x

Figure 6.2.5: Potential Future applications of metallic PhCs. These devices can be used as a combination front contact and antireflective coating replacing traditional contacts (right mesa). This figure shows a MIMs diode geometry which is a diode geometry which can be improved by employing a metallic PhC front side contact.

Figure 6.3.1: Two structures grown using molecular beam epitaxy. Top: R9-81 is a GaSb junction grown on GaAs with a IMF layer. Bottom: R9-86 is an identical junction grown on a GaSb substrate.

Figure 6.3.2: Current-Voltage characteristics as well as diode characterization metrics discussed in Section 2.2.4. The data shows a marked decrease in performance of an IMF p-n junction in comparison to a GaSb on GaSb junction.

Figure 6.3.3: I-V curves obtained for arrays of varying size aperture diodes. The current obtained from each aperture should decrease proportionately to aperture surface area. *Top:* GaSb on GaSb array of apertures. *Bottom:* IMF aperture array.

Figure 6.3.3: Current density obtained from varying aperture diodes. Ideally the current densities should be linear; however, variables such as surface recombination and ideal contact spacing may influence the current density. *Top:* GaSb on GaSb samples. *Bottom:* IMF sample.

Figure 6.3.4: Spectral Response of both the GaSb on GaSb (R9-86) and IMF (R9-81) samples compared to the spectral response of a commercially available GaSb TPV diode. Although the commercial cell shows better efficiency, the sharper cut-off frequency of the R9-86 and R9-81 samples allude to higher general crystal quality.

Figure 6.4.5: I-V characteristics of the GaSb on GaSb (R9-86) and IMF (R9-81) contact materials. Neither top nor bottom demonstrated ideal ohmic behavior; however, the top contacts did show highly resistive ohmic results. Bottom contacts for both the R9-81 and R9-81 were shown to be Schottky contacts until an applied voltage of approximately 3 V. These samples typically operate at voltage of less than 1 V making these common contact materials non-ideal for TPV applications.

Figure 6.4.6: Optimized Structure to further test benefits of using an IMF layer. These designs consist of a three sample group. Sample 1 is shown above. Sample 2 adds a IMF layer between layer 0 and 1. Sample 3 replaces layer 0 with a GaSb substrate.

Figure 6.4.7: The proposed IMF layer produces a lower I_{sc} , however, the device was designed to operate using a bottom contact layer of decreased doping concentration. This is hoped to reduce potential defects related to highly doped material growths allowing IMF analysis based on lattice mismatched strain with reduced effects due to other mechanisms.

Figure 6.4.2.1: *Left:* structure created in order to produce the unique MM response seen on the Right. This structure combines properties of Fishnet, SRR, and SWP type metamaterials. *Right:* the expected response of the MM polarizer grid shown on the Left. This structure uses two polarization sensitive MM resonance peaks.

Figure 6.4.1.2: Surface current and H-field vector. *Top Left:* X-polarized radiation not at resonance. There is a surface current across the splitgap causing the MM to act as a traditional polarization bar. The result is decreased transmission. *Top Right:* Y-polarized radiation not at resonance. There is little surface current interaction between the Y-splitgap. The result is an unaffected transmission. *Bottom Left:* X-polarization at resonance. The interaction across the X-splitgap is removed, the result is a transmission pass-band. *Bottom Right:* Y-Polarization at resonance. Surface current begins to flow across the Y-splitgap resulting in a decreased transmission.

Figure 6.4.1.3: E-field vector and magnitude. *Top Left:* X-polarized light not at resonance. There is a stronger Z- direction E-field within the metallic elements creating the surface current. *Top Right:* Y-polarization in the E-field is directed in the Y-plane therefore orthogonal to the incident radiation. *Bottom Left:* X-polarized light at resonance. The E-field is now directed in the X-plane and therefore orthogonal to the incident radiation. *Bottom Right:* The E-field begins to interact in the Z-plane and not Y-plane resulting in a transmission dip due to loss of orthogonality.

Figure 6.4.1.4: Experimental and simulation data for both optical polarizations. Dashed lines are simulation results and solid curves were obtained experimentally. Blue results are Y-polarized light and Red lines are X-polarized cases.

Figure 6.4.1.5: Independent manipulation of X and Y feature parameters allows for independent shifts in X and Y resonance peaks. *Left:* SEM images of two unoptimized structures. *Right:* Corresponding polarization sensitive transmission for each structure.

Figure 6.4.1.6: *Left:* Effective index for X-polarized light. There is a large dip in magnitude at resonance to the same value as GaAs. *Right:* Effective index for Y-polarized light. There is a slight increase at resonance, however, not a large enough value to explain the decreased transmission.

Figure 6.4.1.7: Effect of doping concentration on total percent transmission as well as resonance wavelength. Higher doping concentrations increase the material permittivity thereby creating a blue shift in resonance. Also, higher doping levels coincide with larger conductivities resulting in a decreasing resonance peak. *Top:* X-Polarization. *Bottom:* Y-Polarization.

Figure 6.4.2.1: Dynamic metamaterial response due to an increase in GaAs conductivity ranging from 0 S/m to 10,000 S/m. This MM is designed to operate at 60THz. *Top:* Y-Polarization. *Bottom:* X-Polarization.

Figure 6.4.2.2: Initial simulated dynamic MM filter characteristics for a conductivity change of 10,000 S/m

Figure 6.4.2.3: *Left:* Experimental dynamic results for a MM patterned on bulk GaAs. An external bias of 5 V and injection current of 410 mA was applied over the MM structure. The bulk GaAs removes the MM resonance response; however the bulk response due to an applied voltage can still be determined. *Right:* Simulated response of a MM structure patterned on a bulk GaAs substrate and the conductivity change (3,000 S/m) needed near the surface to obtain a bulk transmission loss of 3%.

Figure 5.6.2.4: A variety of contact recipes used on a 400 nm thick GaAs on sapphire wafer. All contacts performed relatively consistently whether it was a traditional ohmic contact (annealed Ge/Au/NiAu) or a traditionally Schottky contact (Ti/Au). This leads one to believe that material quality is not sufficient to support high quality electrical contacts.

Figure 5.6.2.5: SEM images of material surface, both images contain identically processed metamaterial structures. *Top:* a MM patterned on a commercially available bulk GaAs wafer. *Bottom:* a MM patterned on 400 nm of GaAs on sapphire grown using molecular beam epitaxy.

Figure 5.6.2.6: Alternate GaAs on sapphire growth process. *Top:* process currently used. *Middle:* Design proposed to improve crystal quality. *Bottom:* High quality process utilizing an SLS buffer layer to reduce crystal defects. ^[6.2.4]

Figure 6.4.2.7: Metamaterial resonance shifts due to increases in doping. The substrate was determined to have low electrical conductivity during contact testing, and as such the increased doping concentration can also be modeled as an increase in carrier concentration independent of corresponding conductivity increases.

Figure 6.4.2.8: *Top:* Simulated dynamic metamaterial response considering both a conductivity change of 3,000 S/m and an injection current of 410 mA. This

simulation takes into consideration carrier induced refractive index changes as well as induced conductivity changes. *Bottom:* The corresponding filter characteristics of the simulated results. These filter characteristics can be even further improved with conductivity increases greater than 3,000 S/m or increased applied voltages and injection currents. As such, these figures should be considered realistic simulated data and not optimum data.

Photonics: Photodiodes and Metamaterials for Thermophotovoltaics and Photodetection Applications

Chapter 1

Introduction

Photonic materials have an unlimited variety of potential applications. However, this section focuses on the use of photonic materials for two specific applications. The first is implementation of photonic structures in energy generating devices. The goal will be to provide new energy generating devices as well as improving efficiencies for current technologies. The second application is the use of photonic materials for dynamic filtering technologies. In particular, photonic materials will be explored for use in creating improved polarization sensitive photodetectors.

List of Abbreviations - Chapter 1

TE - E_s - transverse electric	ν - photon frequency
TM - E_p - transverse magnetic	p - photon momentum
TPV - thermophotovoltaic	c - speed of light
MIMs - monolithically interconnected modules	λ - wavelength
PhC - photonic crystal	\mathbf{E} – electric field
MM - metamaterial	\mathbf{B} – magnetic field
E - photon energy	IR - infrared
h - Plank's constant	

1.1 Electromagnetic Radiation

Einstein's 1905 paper proposed that electromagnetic energy is quantized or made up of a discrete set of values.^[1] Essentially, Einstein's theory allowed light to be modeled as wave packets, known as photons. Photons have properties of both waves and particles, however, they are neither. Photons can have different energies and, because energy and wavelength are related linearly as seen in Equation 1.1.1, photons can have different wavelengths. Furthermore, even though photons do not have a mass, they can have a specific momentum as seen in Equation 1.1.2. Equation 1.1.3 describes the relationship between photon wavelength and photon frequency,

$$E = h\nu \quad \dots \text{1.1.1,}$$

$$p = \frac{h\nu}{c} \quad \dots \text{1.1.2,}$$

$$\nu = c/\lambda \quad \dots \text{1.1.3,}$$

where E is the energy of the photon, h is Planck's constant, ν is the photon frequency, p is the photon's momentum, c is the speed of light, and λ is the wavelength of the photon.^[2]

Photons make up all electromagnetic waves, including, but not limited to visible light. For example, ultraviolet light and infrared light are also composed of photons. Photons are also emitted by warm bodies, which is why very hot substances can appear to glow a particular color. The photons emitted by these bodies have various wavelengths and, therefore, a wide range of energies. All bodies can emit this type of radiation; however at typical environmental

temperatures on Earth, most of these photons are infrared and, therefore, cannot be seen with the human eye.

The Sun provides a large influx of photons to the earth, with over 173,000 Terawatts (units of energy per second) incident on the Earth's surface. ^[3] The energy spectrum of solar photons follows the blackbody curve for a 6000K object, the temperature of the Sun's photosphere. When the photons travel through the Earth's atmosphere some are absorbed resulting in the solar spectrum shown in Figure 1.1.1.

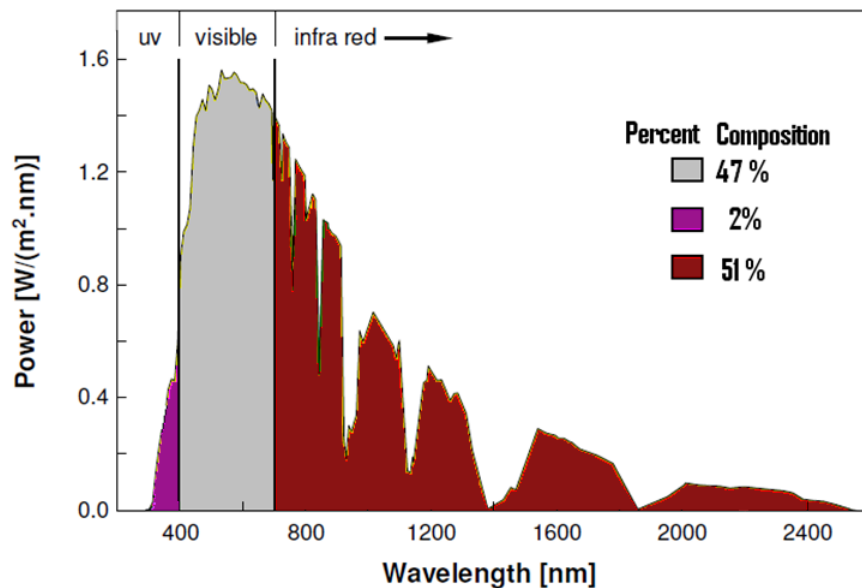


Figure 1.1.1 Normalized solar spectrum, over 50 percent of incident photons are in the infrared. ^[4]

Figure 1.3.1 is normalized to show the relationship of the solar power spectrum to that of the photon wavelength. In other words, Figure 1.1.1 shows that infrared photons have less energy per wavelength than visible and ultraviolet photons (Equation 1.1.1). However, infrared photons make up more of the power incident on the earth. Therefore, by converting infrared radiation into usable and renewable energy, large amounts of useful power can theoretically be produced.

It is also important to note that most light emitted from solar radiation is in the form of unpolarized light. Unpolarized light is formed from individual photons each with an uncorrelated electric field vector (the magnitude and direction of E in Equation 1.1). This makes more physical sense if light is observed as a wave as shown in Figure 1.1.2.

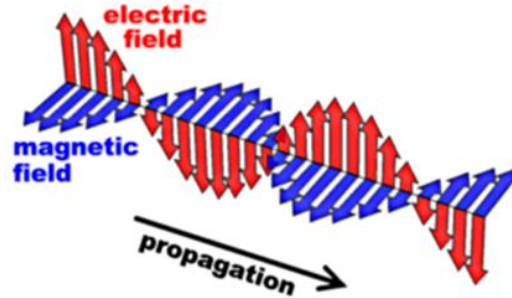


Figure 1.1.2: Visualization of the propagation of a photon. Blue represents the magnetic field and red represents the electric field. Both the E and B field are at 90 degrees to each other.

Also, it is true that the electric field is always perpendicular to the magnetic field and both are perpendicular to the direction of propagation. The electric and magnetic fields can also be related by Equation 1.1.4.

$$\mathbf{E} = c\mathbf{B} \dots 1.1.4$$

Where \mathbf{E} is the electric field, c is the speed of light and \mathbf{B} is the magnetic field or the magnetic flux density. In most cases, optical radiation is described in terms of the E-field, and the B-field is replaced using Equation 1.1.4. For this reason the polarization of a light source is described by the direction of its electric field vector.

It is also important to note that dielectric surfaces tend to polarize reflected light. The electric field vector from photons reflected off of the surface of a

dielectric tends to have the electric fields aligned in the same direction. In order to better explain this phenomenon, a few basic definitions are in order. First, this example uses unpolarized light. Also, general terminology describes this case as: an electric field oscillating perpendicular to the plane of incidence (E_s or TE, transverse electric polarized light) and an electric field oscillating parallel to the plane of incidence (E_p or TM, transverse electric polarized light). It is important to note both TM and TE refers to the direction of electric field in relation to the plane of incidence and is named such simply because the magnetic field component is always perpendicular to the electric field component. Therefore, TM polarized light is perpendicular to TE polarized light.

As mentioned above, smooth dielectric surfaces tend to polarize reflected light. This is due to the boundary conditions of the electric field at an optical interface (derived in Appendix 1.1). However, it follows that a smooth dielectric surface will reflect mostly TE polarized light, as can be seen in Figure 1.1.3.

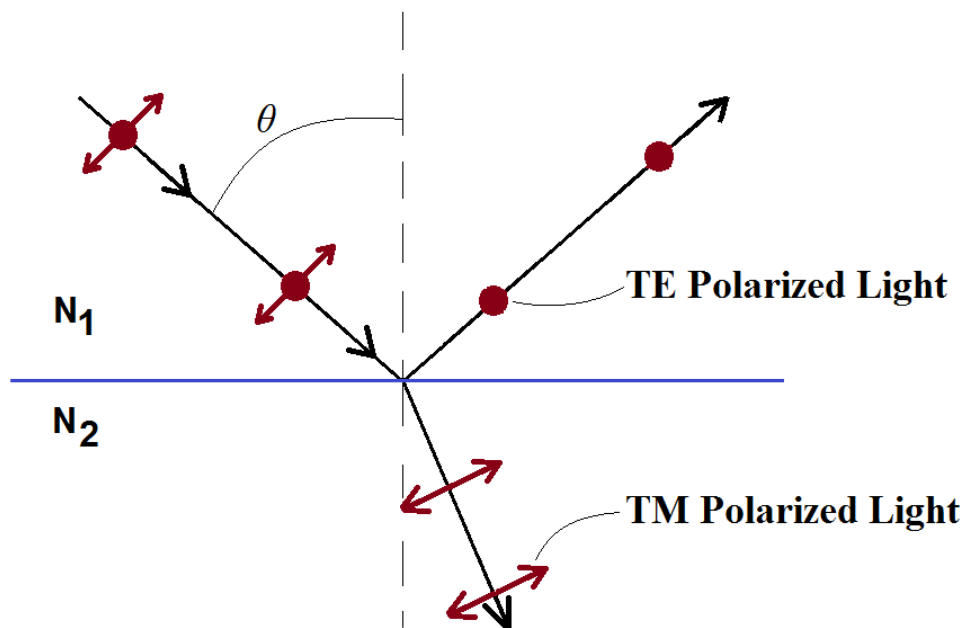


Figure 1.1.3: Reflection off of a smooth surface. The majority of TE polarized light is reflected, while the majority of TM polarized light is transmitted. N_1 and N_2 correspond to different indexes of refraction.

The total percent reflection and percent transmission can be calculated using reflection and transmission coefficients (shown in Appendix 1.1) derived from the Fresnel equations. However, the purpose of this section is to simply explain that unpolarized light can be polarized due to reflections off of a smooth dielectric surface.

Reflection based polarization can provide extremely valuable data when used in conjunction with polarization selective photodetectors. For example, most man-made objects consist of very smooth flat surfaces. In actuality, it becomes difficult to produce any structure without some sort of smooth flat feature. It is for this reason that car windows appear reflective on a sunny day, but a pair of polarized sunglasses can eliminate the glare. In comparison, natural objects tend to not exhibit these properties. As such, polarization detection has

been extremely important in detection of artificial structures and materials, and this is just one example of polarizers potential uses.

1.2 Applications of TPV

Thermophotovoltaic (TPV) devices are a technology which converts both radiated energy and conducted heat into usable electricity. TPV devices are typically four stage devices: an emitter, a filter, a photodiode, and an external energy source (shown in Figure 1.2.1).

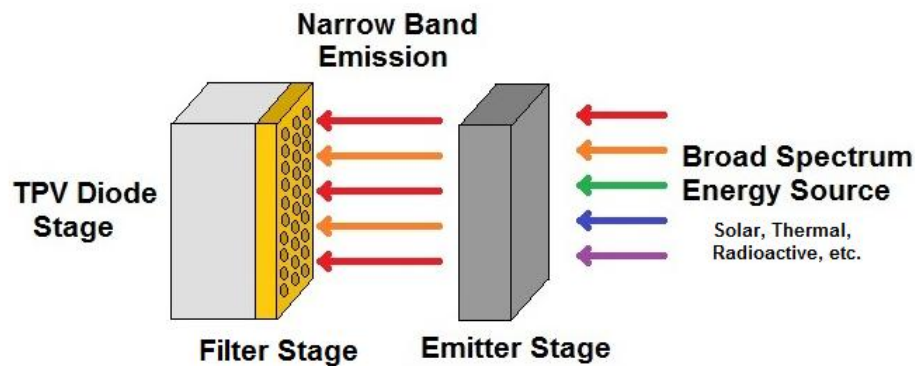


Figure 1.2.1: Diagram of a TPV device. Left is the diode stage and filter stage, middle is the emitter stage, and right is a broadband energy source.

For reference in our discussion on TPV application, the parts of a TPV device will be briefly discussed. The emitter stage is imparted with energy from a broad energy spectrum (i.e. conductive heating, thermal radiation, radioactive source). The emitter stage then radiates a narrow band spectrum. A filter stage further narrows the spectrum to match the properties of the diode stage. The diode stage then converts the narrow band emission into electrical energy.

There are many energy sources, from which TPV can generate electricity. These sources include sunlight, combustion, radioisotopes, and other warm bodies. Typically TPV devices operate in the infrared region of photons, shown in Figure 1.2.2. This figure shows that current applications of TPV range from source temperatures of 2000+K to cutting edge technologies around 350K. The goal of present TPV research in our lab is to maximize efficiencies for this entire wavelength range.

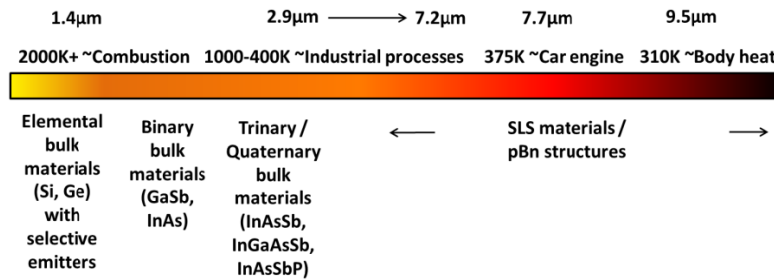


Figure 1.2.2: The IR wavelength range with the corresponding black body temperature and typical photodiode materials which operate at that wavelength. ^[5]

TPV also has the added benefit of allowing integration with present day power generation facilities. For example, waste heat and transmission losses in the USA account for approximately 57% of all the energy generated in 2010.^[5] Recovering just 1% of this wasted energy, 56 quads, could power up to 13 million homes for an entire year.^[6] According to the United States Census Bureau, 13 million homes accounts for approximately 10% of occupied homes.^[7] TPV can clearly benefit the energy forecast through integration with present technologies; not requiring entire new energy generation stations. For example, electricity produced by natural gas utilizes combustion to heat steam in a boiler, which turns

a turbine, this generates electricity electro-mechanically. TPV can be integrated after the turbine to recover the wasted heat generated in this process (a temperature of 533 K). Price per watt calculations can be conducted with a blackbody emitter stage, a conservative system efficiency of estimate of 15%, and pricing constraints shown in Figure 1.2.3.

Item needed	Cost
Substrates (2in x 2in chips)	\$350 each (in bulk)
MBE growth cost	\$2,000 (9 wafer batches)
Processing	\$150 each
Packaging & Installation	\$150 (estimate)
Total for 2inx2in surface:	~\$872

cost for a 1m x 1m surface is projected at = \$338,000

Figure 1.2.3: Cost Assumptions for a TPV device used in a cost per watt calculation.

Using the new Greenland Energy Center natural gas power plant as a base model, it was determined that an additional 10% in start-up cost will increase the initial power plant efficiency by approximately 9% (122kW of energy).^[8] In order to recoup the cost of the TPV system in the first year, the initial cost per kW of the TPV energy generation would be \$1.87, compared to \$1.09 for natural gas. This cost could be lowered in order to alter the return on investment time; however, no additional fuel would be needed to power the TPV devices.^[8] The result would be a lower net cost per watt after the cost of the TPV system was recovered.

TPV devices have applications in a wide variety of energy generation applications and temperatures, from those of a hundred degrees C to those of high

temperature combustion. This research aims to increase the efficiencies of three stages of TPV devices at both low and high temperatures using technologies such as interfacial misfit arrays, monolithically interconnected modules (MIMs), metamaterial emitters, and photonic crystal filters (these technologies will be discussed later). The results of this research are aimed at allowing TPV devices to be integrated into existing technologies in order to improve our energy forecast.

There are also many other areas of research and possible applications that can be benefited by a fully functional TPV diode. For example, infrared photodetectors rely on very expensive and fragile semiconductor materials in order to form an image from the generated photocurrent. The same photodiode used in an efficient TPV converter can be applied to a photodetector. For this reason, if the TPV photodiode is efficient, there are also significant applications in devices such as heat sensors or night vision goggles.

1.3 Applications of Metamaterials

A metamaterial (MM) is any material that has an artificially designed permeability and permittivity. The first true metamaterials were proposed by V.G. Veselago and were used to describe a “left handed” material, or a material with simultaneously negative electric permittivity and negative magnetic permeability.^[10] The first experimentally verified metamaterial was fabricated by Smith et al in 1999.^[9] Since 1999, the field of metamaterials has expanded to include fields such as photonic crystals (PhC) and plasmonics. With the large breadth of research into metamaterials, it becomes necessary to focus on specific

areas of the field; as such metamaterial applications will be limited to metallic metamaterials as those created by Smith et al, and photonic crystal metamaterials.

The first two potential applications are perfect metamaterial emitters/absorbers and metamaterial polarizers. For these applications it is desirable to maximize the metamaterial resonance with a specific photonic “pass-band”. These devices typically use a two layer structure for which it becomes possible to match the material impedance to that of free space, minimizing the reflectance at a specific frequency. The result is a narrow spectrum absorption or transmission as shown in Figure 1.3.1.

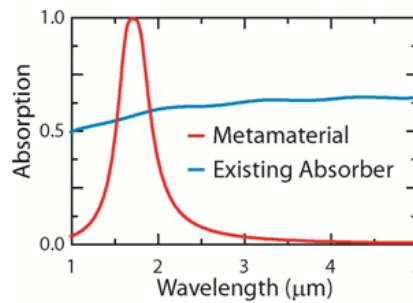


Figure 1.3.1: Metamaterial absorber response as compared to existing technologies. The high absorption and narrow band peak (red) may provide many advantages over the broadband response currently employed (blue).

These devices have been proposed for use in TPV emitter applications, notch filtering applications, polarization filters, and sensing. The proposed benefit of the devices is the ability to achieve near unity absorption/transmission/reflection for a narrow band of frequencies. Other research has been focused on altering the properties of these metallic MMs. This is accomplished by applying an external electrical bias or optical pumping; and operates by altering the effective permeability and permittivity of the MMs.

A PhC is another type of metamaterial, however, which operates under different physical principles than a traditional metallic MM. The PhC utilizes a photonic bandgap, or a region through which photons are quantum mechanically forbidden to propagate. The result is a photonic filter in one, two, or three dimensions. The applications for a PhC have ranged from optical waveguides, to TPV emitter stages, to dielectric optical filters.

With the thousands of possible uses of metamaterials, this research focuses on metallic perfect absorbers/emitters for TPV applications, photonic crystal MMs for TPV filtering applications, and metallic polarization sensitive MMs for photodetector applications. The final goal of this dissertation is to provide photonic building blocks which may be used interchangeably. For example, a TPV diode stage can be used with a MM for photodetection or a MM emitter and MM filter can be used with the same TPV diode for power generation.

Chapter 2

This section hopes to build on the principles of semiconductor physics and optics in order to provide a means to solve the problems discussed in chapter 1. In particular, this chapter will describe semiconductors materials used to create thermophotovoltaics and photodetector photodiodes. Also, optical structures such as metamaterials will be discussed for improving thermophotovoltaic emitters, thermophotovoltaic filters, and photodetector polarization sensitive filters.

List of Abbreviations - Chapter 2

Part 1- Semiconductors

E - energy	m_e - electron mass	w - depletion width	F_{fill} - fill factor
TPV - thermophotovoltaic	E_g - band gap energy	N'_A - excess acceptor concentration	V_{mp} - voltage at max power point
N_a - ionized p-type dopants	N_D - ionized n-type dopants	n_{po} - electrons in p-type material	I_{mp} - current at max power point
\hbar - hbar or 2π divided by planks constant	J_p - hole current density	p_{no} - holes in n-type material	MPP - max power point
\mathbf{k} - crystal momentum vector	J_n - electron current density	V_{oc} - open circuit voltage	η_Q - quantum efficiency
E_f - Fermi energy	J - current density	τ_n - carrier lifetime	P - power
k - Boltzmann constant	μ_p - hole mobility	tL_p - electron recombination length	CE - η_c - conversion efficiency
E_v - valence band energy	μ_n - electron mobility	L_n - hole recombination length	EQE - external quantum efficiency
E_c - conduction band energy	D_n - electron diffusion coefficient	I_{sc} - short circuit current	MPP - max power point
p_0 - # of conduction holes	D_p - hole diffusion coefficient	SRH - Shockley-Read-Hall	V_{mp} - voltage at max power point
n_0 - # of conduction electrons	q - charge of electron	J_{sat} -saturation current	F_{fill} - fill factor
t_p - hole collision time	t_n - electron collision time	α_r - recombination rate	I_{mp} - current at max power point
m_{dse}^* - effective density of state mass of electrons	m_{dsh}^* - effective density of state mass of holes	IQE - internal quantum efficiency	η_Q - quantum efficiency
N_c - effective conduction band density of states	N_v - effective valence band density of states	EQE - external quantum efficiency	CE - η_c - conversion efficiency
n_i - intrinsic carriers per unit volume	N'_D - excess donor concentration	MBE - molecular beam epitaxy	V_{bi} - built in voltage

2.1 Semiconductors

The TPV cell is based on complex theory involving solid state physics, quantum mechanics and electrodynamics. In order to appreciate the design and fabrication of the TPV cell, one must understand the physics of how a TPV diode can generate an electrical current. Most of the basic theory involves the manipulation of semiconductor band structures and the interaction of light with these band structures. The goal of this section is to develop the problems associated with the TPV diode stage. Chapter Three will describe how this research proposes to solve the problems arising in this chapter.

2.1.1 Band structure

Atoms are made up of a nucleus and an electron cloud. The electron cloud is made up of many different electron orbitals with different energy values associated with each orbital. If two or more atoms are forced together, the electron orbitals begin to overlap. ^[10] Electrons are fermions and as such are governed by the Pauli Exclusion Principle, which states that no two electrons can have the same quantum state. Therefore, the overlapping energy states, or orbitals must be split into multiple bands, shown in Figure 2.1.1.1. ^[10]

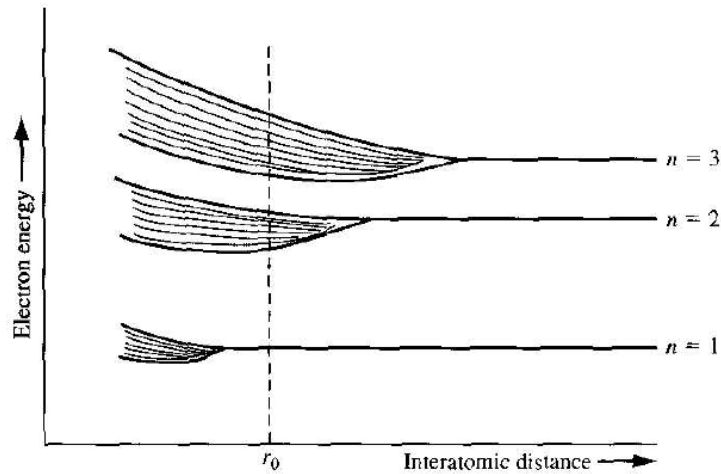


Figure 2.1.1.1: The splitting of orbitals into energy bands at low interatomic distances. ^[10]

As implied by various quantum mechanical models, the area between these energy bands cannot be occupied by the electrons, for they are not consistent with any of the atoms' atomic orbitals. ^[10] These regions, where electrons cannot be present, are known as forbidden regions. An example for the band structure of silicon is shown in Figure 2.1.1.2, where the forbidden regions are shaded. ^[10]

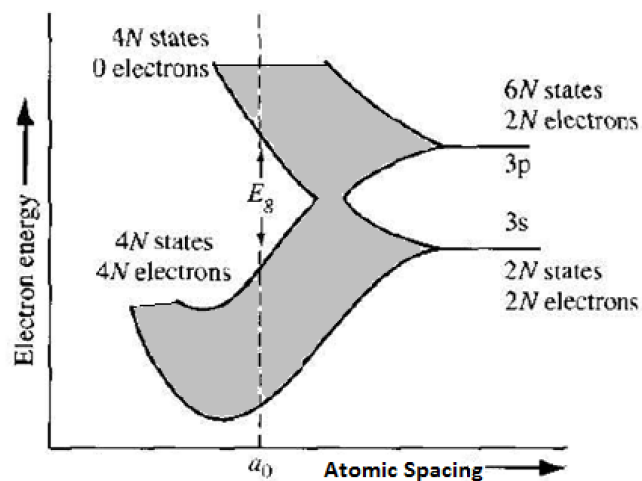


Figure 2.1.1.2: The allowed and forbidden regions as a function of energy and atomic spacing. ^[10]

In a band diagram, the higher energy level bands are known as conduction bands and the lower energy bands are known as the valence bands.^[10] Figure 2.1.1.3 shows the band structure of Si with different bands and energy levels.

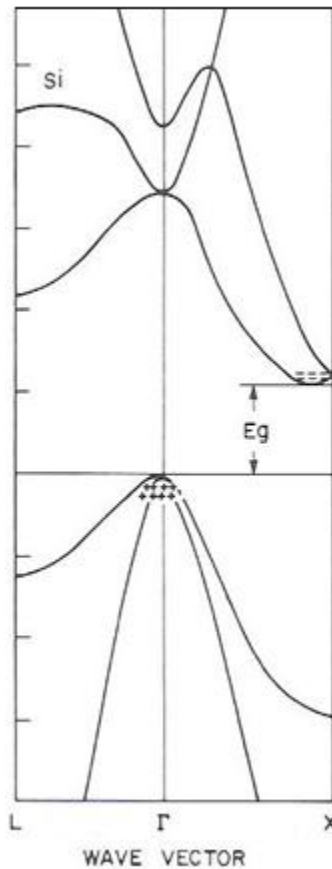


Figure 2.1.1.3: The conduction and valence bands of silicon along with the different energy bands.^[11]

One of the properties of a semiconductor is neutral charge.^[12] When one of the electrons is excited to the conduction band by another form of energy (i.e. heat or photon excitement), the previously occupied place within the valence band becomes empty. The electron is now free to move about the semiconductor in the higher energy conduction band.^[12] In order to maintain charge neutrality within

the material there must be a positive charge to negate the flowing electron. This area of positive charge is known as a hole.^[12]

The electron and the hole move through the lattice with different degrees of ease. This variance can be expressed as an effective mass of the charge carrier and is a multiple of the actual mass of the electron. The two masses are not identical in magnitude as an effective mass is based on the band in which the electron or hole is located. However, because a hole is effectively the lack of an electron, the two particles have opposite charges and together are known as excitons.^[13] Without the presence of a potential difference, i.e. a voltage, the conduction electron will quickly lose excited energy and return to the valence shell replacing the hole. This process is known as recombination and can create a phonon (lattice vibration), a photon, or both.^[12] Both hole creation and recombination is shown in Figure 2.1.1.4.

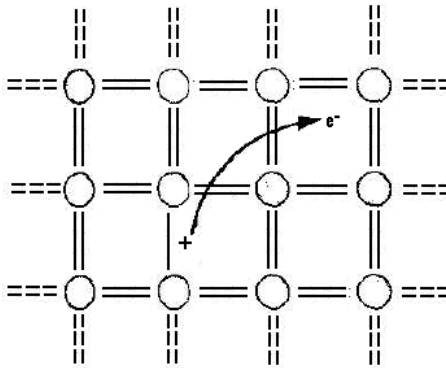


Figure 2.1.1.4: Hole formation. The excited electron leaves the valence shell and can then move more freely within the semiconductor as part of the conduction band. This creates a positively charged hole. The electron and hole can recombine if they meet and the electron loses its excited energy.^[10]

There are multiple ways to excite electrons into the conduction band. Among them are phonon (increasing thermal energy and lattice vibrations) and

photon absorption.^{[12]&[14]} Thermal energy is due to semiconductor heating and is not useful for TPV applications. Thermal excitation is a function of the semiconductor temperature which, in turn, increases the recombination rates. Increasing recombination in turn lowers the ability for a current to be generated. However, energy from photons is extremely useful to photovoltaic devices. When an electron is excited due to a photon, there are two possible paths which allow an electron into the conduction band: direct and indirect transitions.^[15]

For TPV applications, the simpler of the two paths is more desirable: the direct transition. This transition occurs if the bottom (lowest energy state) of the conduction band has the same momentum vector (k) as the top (highest energy state) of the valence band, as shown in Figure 2.1.1.5.^[17] The crystal momentum vector (\mathbf{k}) is described mathematically in Equation 2.1.1.1,

$$E = \frac{k^2 \hbar^2}{2m_e} \dots \text{2.1.1.1,}$$

where E is energy, m_e is the electron effective mass and \hbar is a constant equal to $1.055 \times 10^{-34} \frac{\text{m}^2 \text{kg}}{\text{s}}$.^[16] In a direct transition, there is no change in the k value, corresponding to no change in the crystal momentum.^[17] Therefore, no heat is added to or removed from the system.^[17] Both transitions are shown in Figure 2.1.1.5.

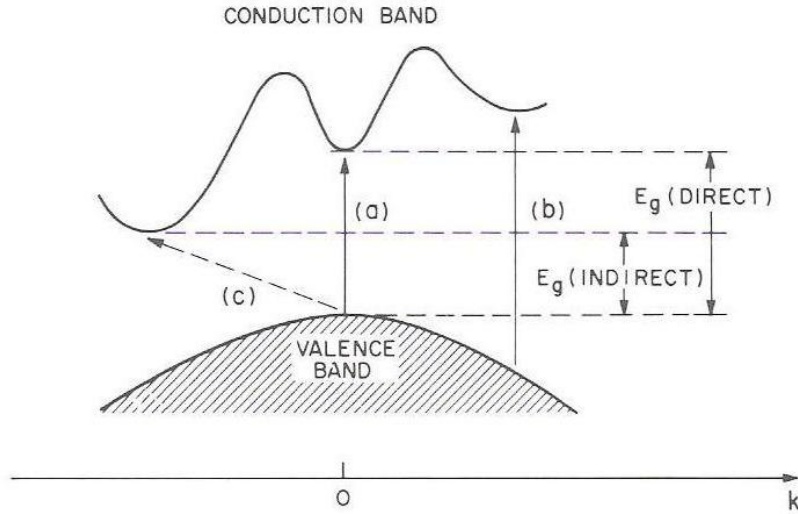


Figure 2.1.1.5: Direct (a)(b) and indirect transitions (c) . There is a different k value for indirect transitions leading to heat or vibration transfer of energy to the lattice in order to complete the transition. Direct transitions do not interact with the lattice and therefore there is not energy lost to lattice vibrations. ^[15]

Indirect transitions are a bit more complicated as can be seen from figure 2.1.1.5. These transitions involve changes in the crystal momentum vector. ^[18] In order for an indirect transition to occur, there must be enough photonic energy to allow an electron to reach the conduction band and also match the momentum of the crystal. The transfer of energy to change the electron/crystal momentum creates heat and vibrations, or phonons, within the crystal. As mentioned earlier, the generation of heat is not desirable for the TPV converter as it will increase the electron/hole pair, or exciton, recombination rate. ^[19]

As mentioned before, the energy imparted to the semiconductor due to indirect transitions produces heat and phonons. ^[15] Phonons are oscillations of the semiconductor lattice and can be visualized as two different types of waves, the higher frequency optical branch and the lower frequency acoustic branch. ^[20] Within the acoustic branch (in one dimension) each atom oscillates in the same

direction with a specific frequency. However, with the optical branch, atoms oscillate in opposite directions.^[21] It is important to remember that phonons are oscillations of the lattice.^[22] Therefore, for indirect band gap transitions, energy is required to both excite the electron into the conduction band and conserve momentum through energy transfer to the lattice (the creation of phonons).^[18]

Electrons within materials have a wide range of energies, most of which fall within the valence band. However, there is an important energy level known as the Fermi energy. This energy is defined by Kittel as the energy of the highest filled energy level when all electrons are at their ground state.^[23] The Fermi level is located half way between the valence band and conduction band in most undoped semiconductors.^[24] As the temperature increases, some electrons are imparted thermal energy and move above the Fermi level.^[25] Eventually, electrons gain enough energy to move into the conduction band and the semiconductor can then begin to conduct electricity. This is the origin of the term semiconductor; there are no conduction electrons at zero Kelvin, but at room temperatures there are carriers present in the conduction band. A graphical representation of the Fermi level as a function of temperature is shown in Figure 2.1.1.6.

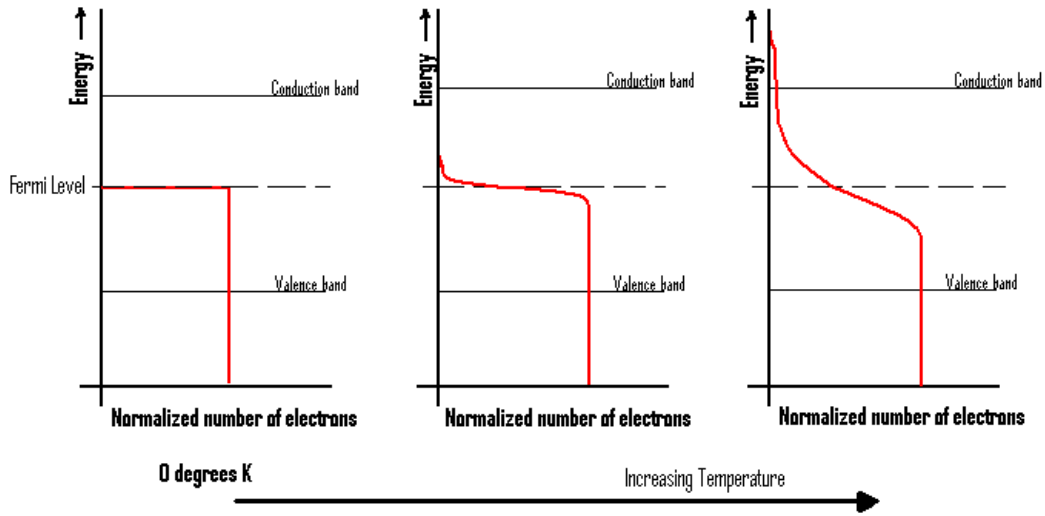


Figure 2.1.1.6: The Fermi level with respect to changing temperature: As temperature increases there are more electrons in the conduction band; however, there is never a change in the total number of electrons within the material.^[26]

Using the Fermi level, it is possible to find the probability that an electron is at a particular energy.^[27] The probability is found by using the Fermi-Dirac probability function (plotted in Figure 2.1.1.4 and described in Equation 2.1.1.1),

$$f(E) = \frac{1}{1 + e^{\frac{(E-E_f)}{kT}}} \quad \dots 2.1.1.1$$

where $f(E)$ is the probability of an electron being at the energy (E), E_f is the Fermi energy, k is now the Boltzmann constant, and T is the temperature.^[27] Knowing the Fermi-dirac probability is quite important when analyzing a semiconductor; for example, the number of conducting electrons and holes can be found by integrating the Fermi-Dirac distribution function and the density of states over the conduction band (electrons) or valence band (holes).^[28] The total number of electrons and holes can be found using Equations 2.1.1.2 and 2.1.1.3 respectively,

$$n_o [1/\text{cm}^3] = \int_{E_c}^{\infty} S_n(E) f_n(E) dE \quad \dots 2.1.1.2$$

$$p_o [1/\text{cm}^3] = \int_{-\infty}^{E_v} S_p(E) f_p(E) dE \dots 2.1.1.3$$

where E_v is the energy of the top of the valence band, E_c is the energy at the top of the conduction band $f_n(E)$ is the Fermi-Dirac distribution for electrons, $f_p(E)$ is the Fermi-Dirac distribution for holes, $S_p(E)$ is the density of states in the valence band, and $S_n(E)$ is the density of states in the conduction band.^[28] The density of states represents the spacing between the discrete energy levels within the semiconductor.^[29] Physically the density of states changes the Fermi-Dirac distribution to a discrete representation of the probability function. In other words, the Fermi-Dirac distribution can find probabilities even for forbidden energy levels; however, with the addition of the density of states a more realistic model can be developed. The density of states is represented near the bottom of the conduction band as Equation 2.1.4 and at the top of the valence band by Equation 2.1.5,

$$S(E) = \frac{1}{2\pi^2} \left(\frac{2m_{dse}^*}{\hbar^2} \right)^{3/2} \sqrt{E - E_c} \dots 2.1.1.4$$

$$S(E) = \frac{1}{2\pi^2} \left(\frac{2m_{dsh}^*}{\hbar^2} \right)^{3/2} \sqrt{E_v - E} \dots 2.1.1.5$$

where $S(E)$ is the density of states, m_{dse}^* and m_{dsh}^* are the effective density of states mass of the holes and electrons (respectively)^[29] After integration (and applying the Boltzmann approximation) the total number of conduction electrons and holes are represented by Equations 2.1.1.6 and 2.1.1.7,

$$n_0 = N_c e^{-\frac{E_c - E_f}{kT}} \dots 2.1.1.6$$

$$p_0 = N_v e^{-\frac{E_f - E_v}{kT}} \dots 2.1.1.7$$

where N_c and N_v are the effective density of states in the conduction and valence bands respectively.^[30] N_c and N_v are shown in Equations 2.1.1.8 and 2.1.1.9 and are functions of temperature and effective mass.

$$N_c [1/\text{cm}^3] = 2 \left(\frac{m_{dse}^* kT}{2\pi\hbar^2} \right)^{3/2} \dots 2.1.1.8$$

$$N_v [1/\text{cm}^3] = 2 \left(\frac{m_{dsh}^* kT}{2\pi\hbar^2} \right)^{3/2} \dots 2.1.1.9$$

N_c and N_v are independent of any type of doping profile. It is therefore useful to represent the total number of carriers per unit volume, $n_i [1/\text{cm}^3]$ (shown in Equation 2.1.1.10) in terms of N_c and N_v such as in Equation 2.1.1.11,

$$n_i^2 = n_0 p_0 \dots 2.1.1.10$$

$$n_i = \sqrt{N_c N_v} e^{-\frac{E_g}{kT}} \dots 2.1.1.11$$

where E_g is the band gap energy ($E_c - E_v$).^[31] For any particular material the intrinsic number of carriers does not change with doping. When a dopant is added to a semiconductor the intrinsic carrier concentration is useful to find the specific electron or hole concentrations.

2.1.2 Doping

The previous section describes intrinsic semiconductors, or semiconductors that are not doped with another material. The process of doping replaces atoms within the semiconductor with atoms of different elements. The doped semiconductor is now known as an extrinsic semiconductor.^[32] The doping atoms (dopants) have more electrons than the original atoms (donor impurity

atoms) or fewer electrons (acceptor impurity atoms). Donor dopants allow for more conduction electrons whereas acceptor dopants produce a material with more holes.^[33]

Silicon has four valence electrons and therefore bonds with its four nearest silicon atoms, and therefore, can be doped with boron, gallium, phosphorous, and arsenic. When the electrons of pure silicon are excited into the conduction band, bonds must be broken to allow the electron to move freely through the material.^[10] If the silicon is doped with arsenic or phosphorus (donor materials), however, there is an excess of electrons within the material and it becomes easier to excite electrons into the conduction band. When a silicon atom is replaced with a gallium or boron atom (acceptor materials), there are not enough valence electrons to bond with the four nearest neighbors. The lack of bonding electrons creates holes.^[33] Figure 2.1.2.1 shows visually the structures of intrinsic silicon, gallium doped, and arsenic doped semiconductors.

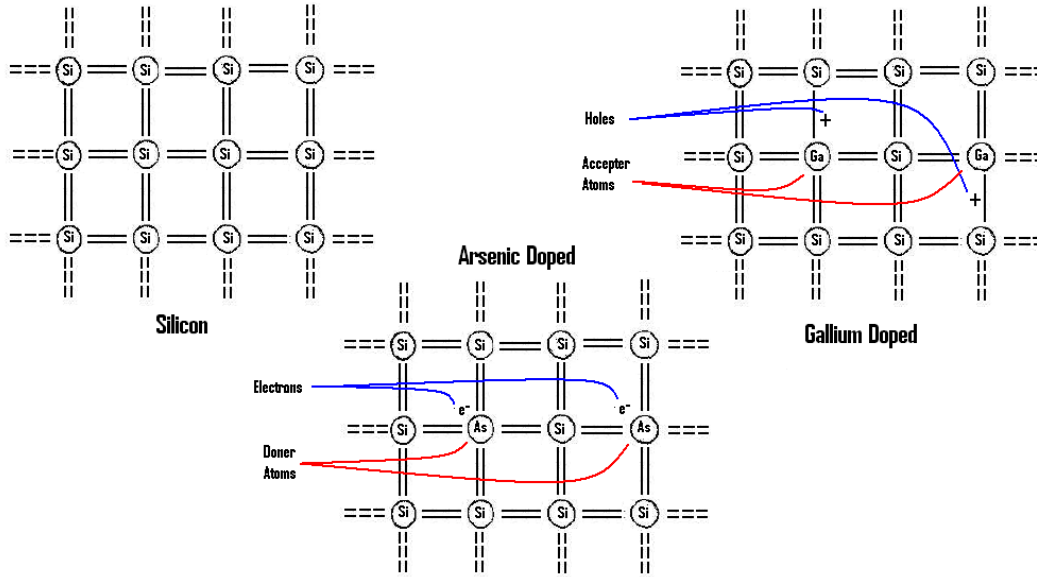


Figure 2.1.2.1: all three materials are neutral in charge, however the doping process creates areas where there are local positive (gallium) and negative (arsenic) charges within the lattice. ^[33]

In general, extrinsic semiconductors donor atoms are known as n-type materials, as there are excess negative charges. ^[33] Similarly, semiconductors that have acceptor atoms are known as p-type materials, as there are excess positive holes. ^[33] The number of dopants alters the conductivity of the material as it may be either easier or harder to create a conduction electron. This can be clearly seen through an altered Fermi-level.

As impurities are added to a semiconductor, the location of the Fermi level shifts. ^[24] The amount of change can be found using Equations 2.1.1.6 and 2.1.1.7 and solving for $E_c - E_f$ or $E_f - E_v$; however, n_0 and p_0 are doping dependant values. When doping is introduced, the equation for n_0 in a n-type semiconductor becomes Equation 2.1.2.1,

$$n_0 = \frac{N_D - N_A}{2} + \left[\left(\frac{N_D - N_A}{2} \right)^2 + n_i^2 \right]^{1/2} \dots 2.2.1$$

where N_a is the ionized p-type dopants and N_D is the ionized n-type dopants.^[34]

The number of conducting holes in a n-type semiconductor are found by solving Equation 2.1.1.10 for p_0 . Similarly, the number of conducting holes in p-type semiconductor is found by Equation 2.1.2.2,

$$p_0 = \frac{N_A - N_D}{2} + \left[\left(\frac{N_A - N_D}{2} \right)^2 + n_i^2 \right]^{1/2} \dots 2.1.2.2$$

and the number of conducting electrons are found once again solving Equation 2.1.1.10 for n_0 .^[34] In a *p*-type semiconductor there are many less electrons than holes; because of this, the electrons are known as minority carriers and the holes as majority carriers. Conversely, in an *n*-type semiconductor, the holes are the minority carries and electrons are the majority carriers. The carrier concentrations and carrier types become very important when *n*-type and *p*-type materials are joined to make a diode, such as in TPV applications, or when dealing with an electrical current flowing through a semiconductor, such as with dynamic MM applications.

The total current within a semiconductor is made up of the diffusion and drift currents for both conduction electrons and conducting holes. The hole current density (J_h), electron current density (J_e), and total current density (J) are shown in Equations 2.1.2.3, 2.1.2.4, and 2.1.2.5,

$$J_p = qp_o\mu_p\mathcal{E} + qD_p \frac{d}{dx}p_o(x) \dots 2.1.2.3$$

$$J_n = qn\mu_n\mathcal{E} + qD_n \frac{d}{dx}n_o(x) \dots 2.1.2.4$$

$$J = qp_o(x)\mu_p\mathcal{E} + qD_p \frac{d}{dx}p_o(x) + qn_o(x)\mu_n\mathcal{E} + qD_n \frac{d}{dx}n_o(x) \dots 2.1.2.5$$

where μ_p and μ_n are the hole mobility and electron mobility respectively, $p_o(x)$ and $n_o(x)$ are the hole and electron concentrations as a function of position within the semiconductor, D_n and D_p are the electron and hole diffusion coefficients respectively, q is the charge of an electron, and \mathcal{E} is the electric field present.^[35] The electron and hole mobilities are a function of the average times between electron or hole collisions with atoms or phonons (t_n or t_p respectively) and the effective mass of the holes and electrons.^[36] The electron and hole mobility equations are given in Equations 2.1.2.6 and 2.2.7,

$$\mu_p = \frac{qt_p}{m_h^*} \dots 2.1.2.6$$

$$\mu_n = \frac{qt_n}{m_e^*} \dots 2.1.2.7$$

The t_n and t_p values are functions of both temperature and doping concentrations; however they are found quantitatively.^[36] The electron and hole diffusion coefficients are found through the Einstein relation (Equation 2.1.2.8),^[37]

$$\frac{D}{\mu} = \frac{kT}{q} \dots 2.2.8$$

It is important to note that if there is no gradient in doping concentration, then Equation 2.1.2.5 becomes Equation 2.1.2.9,

$$J = qp_o(x)\mu_p\mathcal{E} + qn_o(x)\mu_n\mathcal{E}, \dots 2.1.2.9$$

which can be simplified to ohm's law. The above semiconductor physics can then be applied to one of the most important discoveries in the semiconductor industry. This occurred when an n -type material and a p -type material were combined to form a diode.

2.1.3 The Diode

The basic diode consists of an n-type material joined to a p-type material. The two materials are grown together using various methods such as ion implantation and molecular beam epitaxy (MBE). A few possible diode geometries and construction methods are pictured in Figure 2.1.3.1

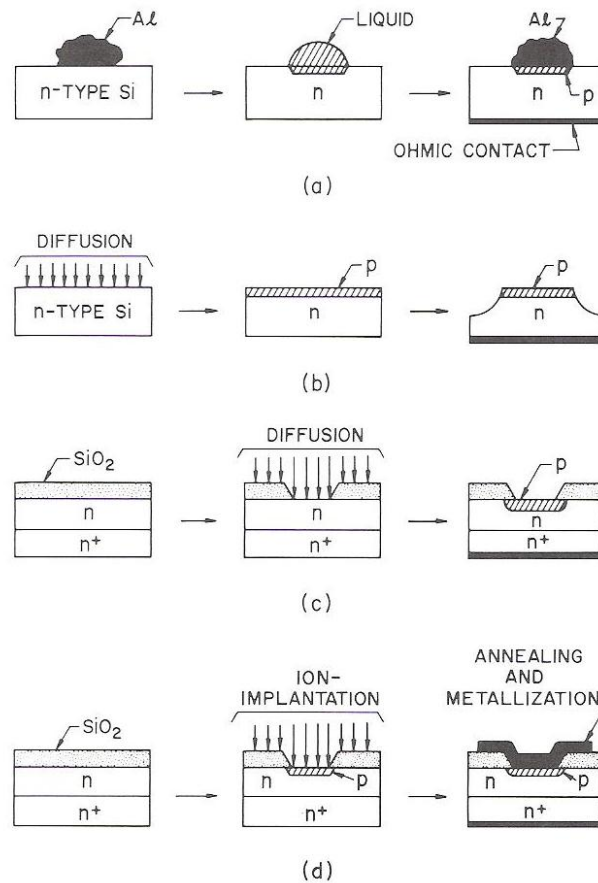


Figure 2.1.3.1: a) p-n junction with an ohmic contact b) mesa junction c) diffused planer junction d) ion implanted junction with contact. ^[38]

Figure 2.1.3.1 depicts the maturity of the *p-n* junction. It is a technology that has been applied to many different applications including TPV, photodetectors, dynamic MMs, and most every semiconductor electronic device.

At the junction of a p -type and n -type material an interesting phenomenon occurs. Even while in thermal equilibrium (no applied voltage) the conducting electrons in the n -type material and the holes in the p -type material interact with each other.^[39] This can be seen mathematically in Equation 2.1.2.5 as there is now a gradient in the electron and hole concentrations. This gradient creates a drift current of electrons and holes across the p - n junction.^[40] In order to maintain charge neutrality the drift current must be directly canceled by a diffusion current. The only way to create a diffusion current is through the presence of an electric field; therefore, an electric field must form across the junction.^[40]

Physically, electrons diffuse across the junction between the two materials and combine with the holes on the other side. Both n -type and p -type materials are electrically neutral before this diffusion occurs. After diffusion, the n -type material has lost electrons and the p -type material has gained an equivalent number of electrons. The rearrangement of charge forms a positive charge on the n -side of the barrier and a negative charge on the p -side. A representation of this situation is shown in Figure 2.1.3.2

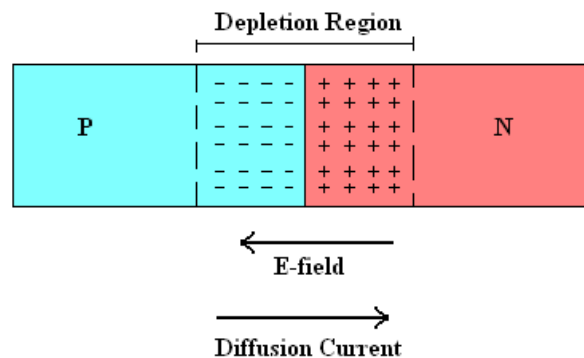


Figure 2.1.3.2: the charge distribution of a p-n junction. Notice that there are positive charges in the n-type material and negative charges in the p-type material creating a potential across the junction.^[41]

The resulting electric field, creates a voltage across the p-n junction.^[42] This potential difference is known as the built in voltage and is represented by Equation 2.1.3.1 for a non-degenerately doped semiconductor,

$$V_{bi} = \frac{kT}{q} \ln \left| \frac{N'_D * N'_A}{n_i^2} \right| \dots 2.1.3.1$$

where N'_D is the excess number of donors on the n-side ($N_D - N_A$), and N'_A is the number of excess acceptors in the p-side ($N_A - N_D$).^[43] The potential formed at the p-n junction bends the valence and conduction bands, forming a band diagram in the shape of figure 2.1.3.3.^[44]

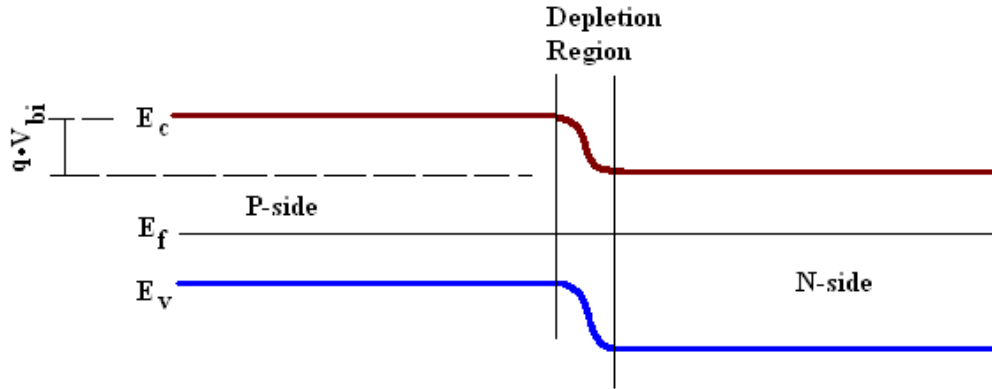


Figure 2.1.3.3: Band diagram of a diode. The barrier is based on the potential barrier.

(1 eV is equal to $q(1 \text{ Volt})$).

These equations are valid in both dynamic and equilibrium conditions. In equilibrium conditions, the electric field becomes strong enough to cancel out the diffusion term.^[42] In this case, the electrons can no longer flow across the boundary and the total current density becomes zero.^[39] The region that forms due to the charge separation is known as the depletion region.^[41]

The depletion region is so named because there are few conducting holes or conduction electrons within this area, as shown in Figure 2.1.3.2.^[45] Unlike the material as a whole, this region is not electrically neutral due to the rearrangement of electrons and holes.^[45] When only the built in voltage is present within the diode, the width of the depletion region can be represented by Equation 2.1.3.2,^[46]

$$w = \sqrt{\frac{2\varepsilon V_{bi}}{q} \left(\frac{1}{N_A} + \frac{1}{N_D} \right)} \dots 2.1.3.2$$

where w is the total width of the depletion region. This equation becomes important to PV and TPV as only electron/hole pairs generated within the depletion region will lend to the photocurrent and open circuit voltage.

The width of the depletion region will increase or decrease with an applied potential.^[45] If electrons are allowed to flow into the n-type material, the current would be expected to continue through the semiconductor. However, this is not the case in a p-n junction. When the flowing electrons reach the edge of the depletion region in the p-type material, they recombine with holes, creating an even stronger electric field and a larger depletion region.^[47] The increased electric field effectively stops the current. When current cannot pass through the diode due to an applied voltage, it is known as a reverse bias. Even at reverse biased, there is some current flow through the diode. This current is known as the saturation current (J_{sat}) and is due to electrons in the p -type material or holes in the n -type material being pulled into the depletion region by the applied voltage, shown below in Figure 2.1.3.4.^[48]

When the flow is reversed and electrons enter through the p-type material, the depletion region shrinks along with the electric field. The electrons are therefore able to reach the other side of the diode.^[49] This type of applied potential is known as a forward bias and is shown in figure 2.1.3.4. These properties make the diode a one way device, meaning current can flow through in one direction but does not flow in the reverse direction. Figure 2.1.3.4 shows visually the growing and shrinking depletion regions along with the direction of current flow.

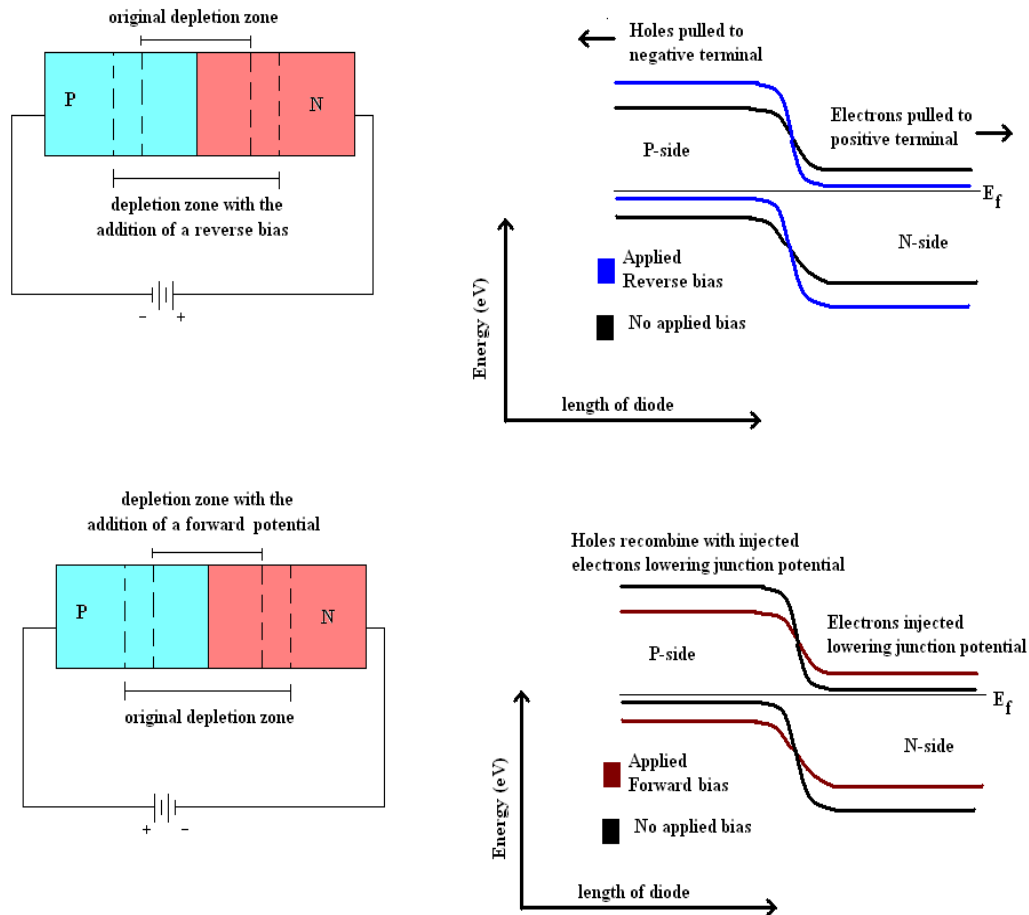


Figure 2.1.3.4: Applying a forward or reverse bias voltage changes the magnitude of current flow into the diode by lowering the potential between the conduction and valence bands of the n and p type semiconductors. The lowered potential changes the depletion with as well.^{[47][49]}

In TPV, the ultimate goal is to extract as much power as possible. If an outside voltage is applied, then the total efficiency of the cell would likely decrease as energy must go into providing the voltage. As such, photodiodes will be described without the dependence on an applied forward or reverse bias.

The total ideal current density of a diode is only a function of applied voltage. For a long diode, the Ideal Diode equation becomes Equation 2.1.3.3, assuming the width of the n -type and p -type material is much greater than the electron and hole recombination lengths, L_n and L_p ,

$$J = q \left(\frac{D_n n_{po}}{L_n} + \frac{D_p p_{no}}{L_p} \right) \left(e^{\frac{qV_{applied}}{kT}} - 1 \right) \dots 2.1.3.3$$

where n_{po} is the number of electrons in the p -type material, p_{no} is the number of holes in the n -type material, D_n is the diffusion coefficient of electrons in the p -type material, D_p is the diffusion coefficient of holes in the n -type material, L_n is the recombination length of electrons in the p -type material, L_p is the recombination length of holes in the n -type material, and $V_{applied}$ is the applied voltage.^[50] For a thin diode, the total current is described by Equation 2.1.3.4,

$$J = q \left(\frac{D_n n_{po}}{X_{n \text{ undepleted}}} + \frac{D_p p_{no}}{X_{p \text{ undepleted}}} \right) \left(e^{\frac{qV_{applied}}{kT}} - 1 \right) \dots 2.1.3.4$$

where $X_{n \text{ undepleted}}$ is the undepleted width of the n -type material, and $X_{p \text{ undepleted}}$ is the undepleted width of the p -type material. Both Equation 2.1.3.3 and Equation 2.1.3.4 are of the form of Equation 2.1.3.5 with the saturation current depending on the thickness of the diode.^[51]

$$J = J_{sat} \left(e^{\frac{qV_{applied}}{kT}} - 1 \right) \dots 2.1.3.5$$

When plotted, Equation 2.1.3.5 takes on the form of Figure 2.1.3.5.

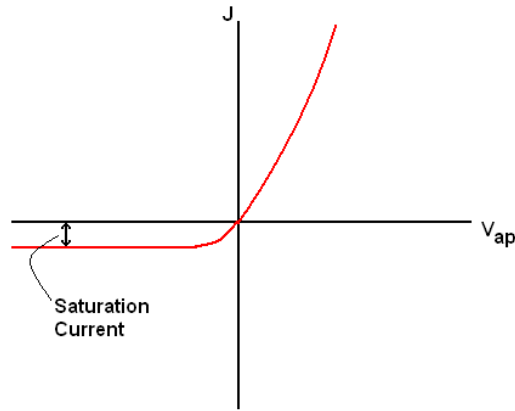


Figure 2.1.3.5: Ideal dark diode equation as a function of applied voltage. The total current shifts when optically generated and thermally generated carriers are introduced. However, these concepts are introduced below with PV and TPV photodiodes.

2.1.4 The TPV Diode Stage

The TPV diode operates on similar principle as the common p - n junction. In actuality a TPV diode is a photodiode consisting of a p - n junction. Just as with a normal diode, a depletion region forms at the interface of the p -type and n -type regions, and an electric field is formed over the depletion region. As stated in Section 2.1.3, there are direct and indirect transitions through which electrons can be excited into the conduction band. When one of these excitations occurs within the depletion region, the built in voltage causes the hole/electron pair to be separated. The charge separation disturbs the equilibrium state and if the diode is

in an open circuit, a potential voltage occurs (V_{oc}). If the circuit is shorted, there will exist a current (I_{sc}) between the p -type and n -type regions. The values of V_{oc} and I_{sc} are different for each photodiode and can simply be measured with an ammeter or voltmeter. Figure 2.1.4.1 shows the ideal diode equation with the addition of photo generated carriers. The intersection of the current equation and the x-axis produces the open circuit voltage (V_{oc}), while the intersection of the y-axis and the current equation produces the short circuit current (I_{sc}).

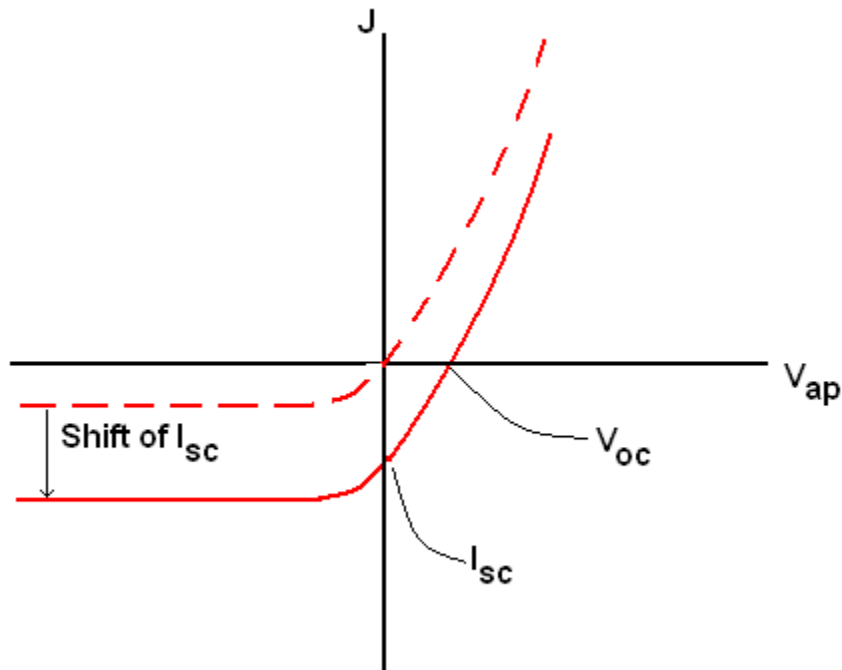


Figure 2.1.4.1: The ideal diode equation with the addition of optically generated carriers. The open circuit voltage and short circuit current are marked.

Not all of the optically generated electron/hole pairs result in a photocurrent. Electrons may recombine with holes and return to the valence band. The carrier recombination rate has a strong material and temperature

dependence. In all cases, recombined carriers no longer contribute to the photocurrent unless they are once again excited to the conduction band.^[52]

There are two types of recombination events, direct and indirect.^[53] Direct recombination events are spontaneous and produce photons. The direct recombination rate is proportional to the number of electrons in the conduction band, the number of holes, and a material dependent constant to represent the recombination probability.^[53] The recombination rate allows one to solve for the carrier lifetime (τ_n), shown in Equation 2.1.4.1,

$$\tau_n = \frac{1}{\alpha_r(n_o + p_o)} \quad \dots 2.1.4.1,$$

where α_r is the recombination rate constant, n_o is the equilibrium value of electrons, and p_o is the equilibrium value of holes.^[53] The carrier lifetime is the amount of time on average, that an electron remains in the excited state without spontaneously recombining into the valence band.^[53]

Indirect transitions are not as easy to describe as direct transitions. One of the most significant types of recombination is known as Shockley-Read-Hall (SRH) recombination. This type of indirect transition occurs in two steps at defect centers.^[54] A defect is known as a trapping center if the particle is more likely to be re-excited back into the conduction band. However, if the conduction band electron is more likely to recombine down to the valence band, then the site is known as a recombination center. To transition back to the valence shell, first an electron or hole is captured. If this recombination center can capture the other half of the electron/hole pair, the two particles recombine. Therefore, SRH transitions require two steps: an electron capture and a hole capture. Figure

2.1.4.2 shows the hole capture, recombination, and the electron capture from the valence band.^[54] It is important to note that hole or electron capture releases energy through phonon excitation.^[54] This in turn will create more thermally generated carriers, which increases the recombination rate of the photodiode. Therefore, eliminating defects and trap states is extremely important in TPV.

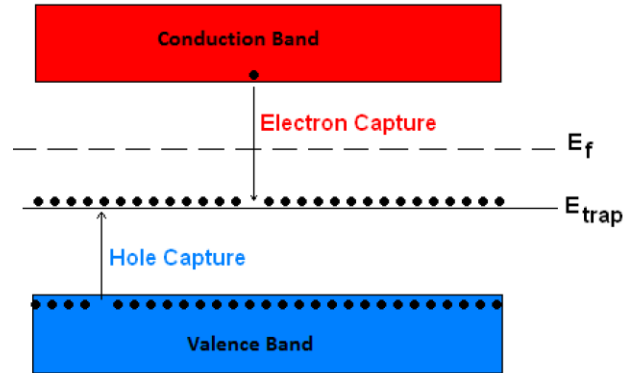


Figure 2.1.4.2: Indirect transitions and the two step transition of a conduction electron to the valence band. Notice that this can also be modeled as an electron losing energy to fall into the defect center and then losing more energy and transitioning back into the valence band.^[54]

An important detail to realize is that in order for the defect center to act as an efficient trap site, its energy level must be below the Fermi energy. Therefore, the defect has both a substantial population of electrons and open lattice sites. These open sites are where recombination occurs.^[54]

There are other forms of indirect recombination including Auger recombination and surface recombination. Both of these recombination phenomena may also involve defects; for example, surface recombination occurs at the surfaces of a photodiode, usually an air/semiconductor barrier.^[19] At these interfaces, the periodicity of the semiconductor is broken creating numerous

energy levels between the valence and conduction bands. These gaps act as recombination sites.

Auger recombination, however, is different than other recombination events in that the energy released from recombination excites another electron (but not into a new band). This newly excited electron loses its energy to phonons which in turn heats the semiconductor.^[19] As the band gap becomes smaller, Auger recombination becomes more prevalent, leading to more recombination in TPV cells. This is one problem we hope to overcome in this research. Figure 2.1.4.3 shows different types of recombination as well as their effect on carrier lifetime, open circuit voltage, and short circuit current.

Recombination rate		Injection level	
		Low-level injection	High-level injection
Auger	$C_n n^2 p + C_p n p^2$	$J_{Auger} = qH(C_n N_D + C_p N_A) \times n_i^2 \exp(qV/kT)$ $V_{OC} = \frac{kT}{q} \ln \left[\frac{J_{sc}}{qH(C_n N_D + C_p N_A) n_i^2} \right]$	$J_{Auger} \cong qH(C_n + C_p) \times n_i^3 \exp(3qV/2kT)$ $V_{OC} = \frac{2}{3} kT \ln \left[\frac{J_{sc}}{qH(C_n + C_p) n_i^3} \right]$
Radiative	Bnp	$J_{rad} = q H B n_i^2 \exp(qV/kT)$ $V_{OC} = \frac{kT}{q} \ln \left[\frac{J_{sc}}{q H B n_i^2} \right]$	$J_{rad} = q H B n_i^2 \exp(qV/kT)$ $V_{OC} = \frac{kT}{q} \ln \left[\frac{J_{sc}}{q H B n_i^2} \right]$
SRH	$\frac{np}{\left\{ \tau_{n0}(p+p_1) \right\} + \tau_{p0}(n+n_1)}$	$J_{SRH} = \frac{qHn_i^2}{N_D \tau_{n0}} \exp(qV/kT)$ $V_{OC} = \frac{2kT}{q} \ln \left[\frac{J_{sc} N_D \tau_{n0}}{q n_i^2 H} \right]$	$J_{SRH} = \frac{qHn_i \exp(qV/2kT)}{(\tau_{n0} + \tau_{p0})}$ $V_{OC} = \frac{2kT}{q} \ln \left(\frac{J_{sc} (\tau_{n0} + \tau_{p0})}{q \cdot n_i \cdot H} \right)$
Surface	$\frac{np}{\left\{ (p+p_1)/S_n \right\} + (n+n_1)/S_p}$	$J_{surface} = q n_i^2 \left(\frac{S_p}{N_D} + \frac{S_n}{N_A} \right)$ $V_{OC} = \frac{kT}{q} \ln \left(\frac{J_{sc}}{q \frac{n_i^2}{N_D} S_p + q \frac{n_i^2}{N_A} S_n} \right)$	$J_{surf} = q n_i (S_n + S_p) \exp(qV/2kT)$ $V_{OC} = \frac{2kT}{q} \ln \left[\frac{J_{sc}}{q n_i (S_n + S_p)} \right]$

Figure 2.1.4.3: Recombination types and corresponding recombination rates as well as the effects on open circuit voltage and short circuit current. These are at both low level and high level carrier injections.^[19]

A photodiode is typically characterized by three efficiencies (internal quantum efficiency, IQE; external quantum efficiency, EQE; and conversion efficiency, CE) as well as the ideal diode fill factor. Both quantum efficiencies are is the efficiency of converting photons into conduction electrons. For example, if every photon incident on a photodiode creates an exciton, the device has one-hundred percent IQE. If only eighty-percent of these electrons reach the diode contacts, then the diode has an eighty-percent EQE. The quantum efficiency can provide useful information on how well a particular p - n junction creates

electron hole pairs. The conversion efficiency is then determined by the total power which is able to be extracted by the diode.

These three metrics provide significantly different information. For example, alone, the IQE may be misleading. If an electron/hole pair is formed outside of the depletion region, an electric field is not present to create charge separation. As such, recombination will occur before a current can be obtained. Even if an electron/hole pair can be separated, there is a chance that the carriers will thermalize (recombine with a thermally generated electron or hole).^[7] Therefore, the IQE alone cannot determine how successful any particular photodiode may be at converting photons into useable energy.

Comparably, conversion efficiency, η_c , shown in Equation 2.1.4.2, is considered to be the ratio of the power output by the photo diode compared to the incident power of the photons

$$\eta_c = \frac{P_{out}}{P_{in}} \dots 2.1.4.2$$

where P_{out} is the power out from the photodiode, and P_{in} is the incident power due to the photon flux of all wavelengths.^[55] Theoretically, one-hundred percent conversion efficiency represents when all power incident is converted into electrical power. Theoretically, maximum conversion efficiencies of 85 percent have been predicted for highly concentrated light sources with no losses and an infinitely large emitter.^[7]

In order to simplify the conversion efficiency analysis, the concept of fill factor can be employed. The fill factor, shown in Figure 2.1.4.4, is the area

between the ideal diode equation and the x-axis and y-axis divided by the max power (V_{mp} multiplied by I_{mp}).^[56]

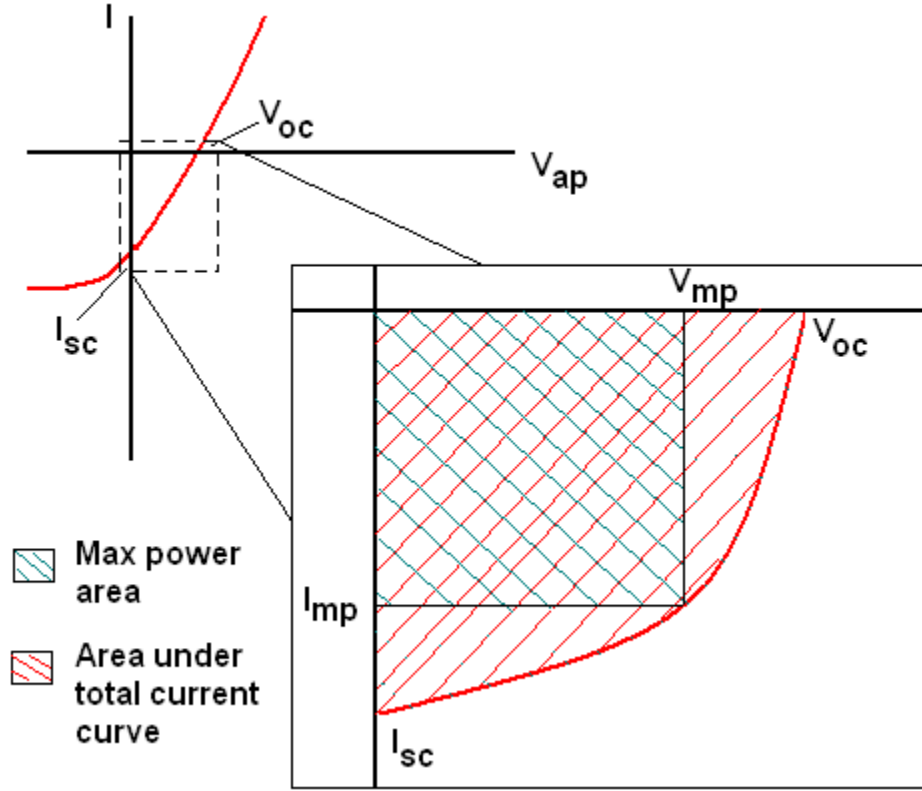


Figure 2.1.4.4: The Fill factor is the area formed by multiplying V_{mp} by I_{mp} divided by the area under the total current curve.

The fill factor (F_{fill}) can be described mathematically by Equation 2.1.4.3,

$$F_{fill} = \frac{I_{mp}V_{mp}}{-\int_0^{V_{oc}} I(V) dV} \dots 2.1.4.3$$

where $I(V)$ is the experimentally found current equation as a function of applied voltage, also known as the I-V curve.^[56] The fill factor can only be found experimentally as it is dependent on the material and growth properties of each specific sample. In terms of fill factor, the conversion efficiency can now be written as Equation 2.1.4.4,^[56]

$$\eta_c = \frac{F_{fill} I_{sc} V_{oc}}{P_{in}} \quad \dots 2.1.4.4$$

In order to help decrease the losses associated with recombination, the most common photodetectors utilize an intrinsic, or *i*-region, between the *n*-type and *p*-type materials. The intrinsic region is not required to be completely intrinsic, but does need to have a high resistivity.^[57] For a *p-i-n* photodiode, the electric field, and hence potential voltage, is formed across the entire intrinsic region. Because the *i*-region is larger than the depletion region of a comparable *p-n* junction, there are more electron/hole pairs successfully separated. As such, a larger photocurrent can be created. This assumption only holds true as long as the carrier lifetime, shown in Equation 2.1.4.1, is larger than the distance of the *i*-region.^[57] The quantum efficiency of a *p-i-n* photodiode is represented by Equation 2.1.4.5 ,

$$\eta_Q = \left(\frac{J_{op}}{q} \right) / \left(\frac{P_{op}}{h\nu} \right) \quad \dots 2.1.4.5 ,$$

where η_Q is the quantum efficiency, J_{op} is the density of the current due to photons (photocurrent), J_{op}/q is carriers per unit area per second, P_{op} is the optical power density, $h\nu$ is the energy of a photon (h is planks constant and ν is the frequency of the photon), and $P_{op}/h\nu$ is the number of photons per unit area per second incident on the detector.^[57] The *p-i-n* photodiode is sensitive to the frequency of light incident. In particular, the energy of the photon must be around the band gap energy of the intrinsic layer.^[57] If, for example, the photons do not have enough energy to excite carriers, then they will not be absorbed. However, if the energy of the photons is too high, the photons will be absorbed before they penetrate into the *i*-region and recombine before they form a photocurrent.^[57]

This makes the *p-i-n* junction very appealing to photodetectors as it will only detect a particular range of frequencies. Also, the *p-i-n* junction can be useful in TPV applications as the junction can be tuned to the incident spectrum from an emitter stage. A representation of a *p-i-n* photodiode is shown in Figure 2.1.4.5.

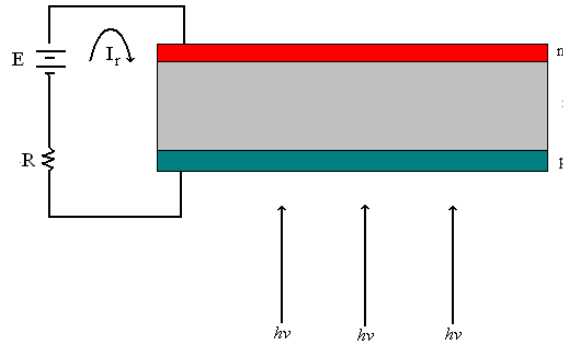


Figure 2.1.4.5: Representation of a p-i-n photodiode.

To summarize, a photodiode of a TPV cell works in a few steps. First, photons are incident on a diode. The diode can either be a simple *p-n* junction or the more tunable *p-i-n* junction. The photons with high enough energy then excite the electrons within the semiconductors to the conduction band. Excitation can either occur through direct transitions or through indirect transitions which involve a heat transfer to the crystal structure. If the electrons are excited near the depletion region, charge separation occurs and the electrons create a current through a closed circuit or create a potential difference across an open circuit.

As mentioned earlier, many of the problems associated with TPV diodes occur due to low quantum efficiency, high SRH recombination, and high Auger recombination (especially at long wavelengths). An in-depth analysis of semiconductor physics was needed to understand where these problems originate

and how to solve them. For example, the two ways to increase the TPV diode's quantum efficiency is to match the incident spectrum to the semiconductor's bandgap or increase the interaction time for photons/electrons. Also, decreasing Auger and SRH recombination can be done by decreasing the depletion region for long wavelength applications and improving crystallinity respectively. It is the goal of this research to optimize these three mechanisms using the metrics such as I-V curve analysis and characterization of crystal quality. Novel device growth structures, fabrication techniques, as well nanostructures will also be implemented with the goal of improving TPV diode efficiencies.

2.2 Metamaterials

This section covers the basic theory behind two types of metamaterials, split ring resonators and photonic crystals. The theoretical framework of this section is focused on understanding how multiple types of metamaterials can manipulate photons. The applications of these photonic structures can be directly integrated into photodetection and TPV. In particular, these metamaterials will be used to create filters, perfect emitters, and polarizers in order to solve problems such as increasing diode and photodetector quantum efficiency as discussed in section 2.1.

List of Abbreviations

Part 2 - Metamaterials

MM - metamaterial	A - absorbance	V - electric potential
μ - permeability	W - work	R - resistance
ϵ - permittivity	J - current density	I - electrical current
n - index of refraction	ω_p - plasma frequency	Z - impedance
\mathbf{B} - average magnetic flux density	ϵ_{eff} - effective permittivity	μ_{eff} - effective permeability
\mathbf{E}_0 - max electric field	\mathbf{E} - electric field	IR - infrared
\mathbf{r} - propagation direction	\mathbf{B}_{ave} - average B-field	PhC - photonic crystal
ω - wave frequency	\mathbf{H}_{eff} - average H-field	\mathbf{k} - Bloch wave vector
t - time	\mathbf{H} - average magnetic field	\mathbf{b} - inverse lattice constant
p - Veselago variable	σ - conductivity	\mathbf{a} - lattice constant
R - reflectivity	C - capacitance	Γ - gamma point
T - transmittance	Q - charge	ω - angular frequency

2.2.1 Development of Metamaterials

Metamaterials have recently gained much attention for their unique optical properties. In particular, there has been interest in frequency ranges from the visible to the microwave, and applications in waveguides, perfect absorbers, and perfect emitters. The first predicted metamaterial was by V.G. Veselago from the P. N. Lebedev Physics Institute in 1964.^[9] Veselago predicted a “left handed” material with negative electric permittivity and magnetic permeability. These materials are different from traditional materials in that standing waves can still propagate, unlike ferromagnetic materials or metals. Also, many traditional properties such as Snell’s law operate in reverse. Further discussion on “left handed” materials will consult with figure 2.2.1.1.

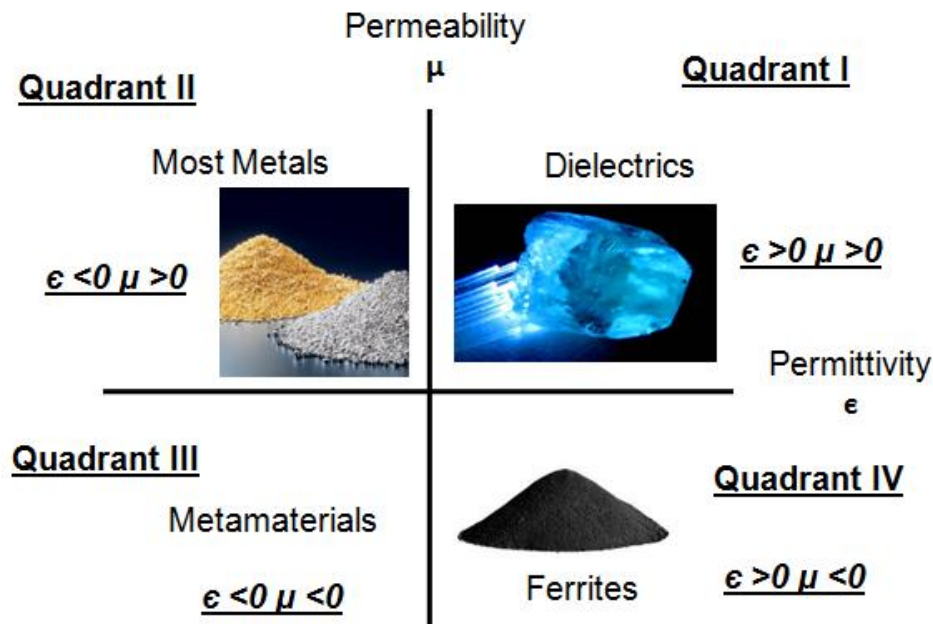


Figure 2.2.1.1: Four quadrants defined using positive and negative permeability and permittivity. Quadrant 1 consists of dielectrics such as optical waveguides, Quadrant 2 consists of metals, Quadrant 3 consists of magnetic materials such as ferrites, and Quadrant 4 is the location of “left handed” materials such as metamaterials.

All materials can be characterized with positive or negative permeability (μ) and permittivity (ϵ). In particular, materials can be classified into four distinct categories: $\epsilon > 0$ and $\mu > 0$, $\epsilon < 0$ and $\mu > 0$, $\epsilon > 0$ and $\mu < 0$, $\epsilon < 0$ and $\mu < 0$. Particular attention should be paid to the $\epsilon < 0$ and $\mu < 0$ category which exhibits “left hand” material properties in monochromatic light.^[9] Furthermore, these four quadrants describe the physical properties of material, be it a ferromagnetic, metal, dielectric, semiconductor, or metamaterial (Figure 2.2.1.1).

In order to facilitate the discussion on “left handed” materials and move to the creation of the field of metamaterials, it is necessary to define some equations and properties, such as refractive index, the wave vector, and the group velocity. First, the index of refraction (n) is defined in Equation 2.2.1.1^[9],

$$n^2 = \epsilon * \mu \quad \dots 2.2.1.1$$

Also, the harmonic wave equation should be defined (Equation 2.2.1.2),

$$\mathbf{E} = E_0 e^{i(\mathbf{k} \cdot \mathbf{r} - \omega t)} \quad \dots 2.2.1.2,$$

where \mathbf{E} is the electric field intensity, E_0 is the max electric field, \mathbf{k} is the wave vector (defined in Equation 2.2.1.3), \mathbf{r} is the propagation direction, ω is the wave frequency, and t is the time.^[58]

$$\mathbf{k} = \pm \sqrt{\left(\frac{\omega}{c}\right)^2 n^2} \quad \dots 2.2.1.3,$$

where c is the speed of light.^[58] Equation 2.2.2.1.2 can then be modified to Equation 2.2.1.4,^[58]

$$E = E_0 e^{i(p \frac{\omega}{c} \sqrt{\epsilon * \mu} - \omega t)} \quad \dots 2.2.1.4.$$

Veselago goes on to derive the variable p from Maxwell's Equations. ^[9] The derivation determines that “right handed” materials have a p value of +1, whereas “left handed” materials have a p value of -1. ^[9] In effect, the p value determines the sign of k ; “left handed” materials have a negative k and “right handed” materials have a positive k .

In Quadrant I of figure 2.2.1.1 ($\epsilon > 0$ and $\mu > 0$), a material has typical “right handed” properties. For example, if both ϵ and μ are positive, then a wave can propagate within the material, as can be seen in Equation 2.2.1.4. Quadrant II and IV prove to be different, if $\epsilon < 0$ or $\mu < 0$, then $\sqrt{\epsilon * \mu}$ becomes imaginary, and Equation 2.2.1.4 simplifies to an exponential decay allowing no propagating waves. This simple outlook does not always capture the entire picture as surface oscillations may form at the interface when certain boundary conditions are met. ^[59] Such conditions include a specific propagation constant and dielectric constant allowing the formation of surface plasmon polaritons; however, this is outside the necessary background for this work. ^[59]

Quadrant III of figure 2.2.1.1 describes “left handed” materials. In this quadrant, Equation 2.2.1.4 once again becomes a wave as both $\epsilon < 0$ and $\mu < 0$. However, the p value derived by Veselago has some interesting implications to potential applications of these “left handed” materials. For example, Snell's law becomes Equation 2.2.1.5,

$$\frac{p_1 \sin \theta_1}{p_2 \sin \theta_2} = \sqrt{\frac{\epsilon_2 \mu_2}{\epsilon_1 \mu_1}} \dots 2.2.1.5.$$

where the subscript 1 represents material 1 and subscript 2 represents material 2, shown in Figure 2.2.1.2. ^[9]

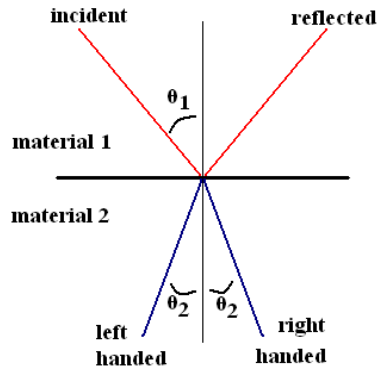


Figure 2.2.1.3: Depicting the “left handed” and “right handed” transmission (blue) at an interface using Equation 2.2.1.5. ^[9]

As can be seen from Figure 2.2.1.3 and Equation 2.2.1.5, the p factor will reverse the sign of the transmission angle through a “left handed” material. The change in transmission angle has allowed for amazing properties which have been utilized in the creation of metamaterial superlensing. Figure 2.2.1.4 summarizes the modified harmonic wave equation and depicts optical transmission in each of the four quadrants.

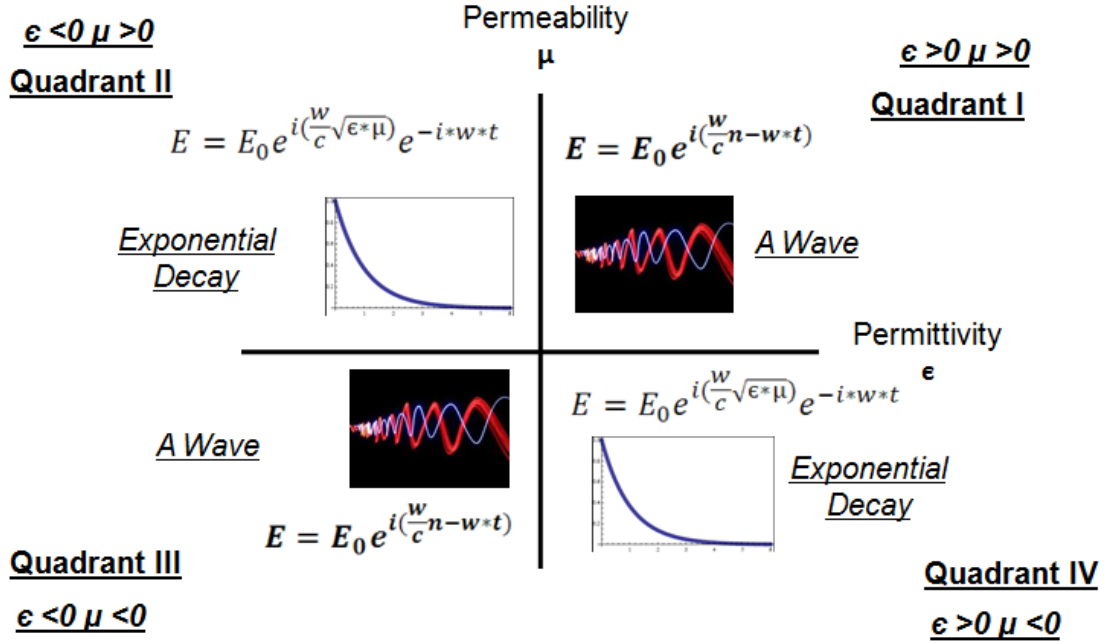


Figure 2.2.1.4: The propagation of light derived from the wave equation separated into quadrants based on the sign of the permittivity and permeability. Quadrant 1 and Quadrant 3 allow for the propagation of light. Quadrant 2 and Quadrant 4 create exponentially decaying evanescent waves.

One of the more important points to note is that a metamaterial does not have to fall into quadrant III. Equation 2.2.1.1 shows that if one can alter the permittivity or permeability, one can match multiple indexes of refraction, and create zero reflection. All metamaterials have been shown to be very useful at creating a designer index of refraction. As such, these devices have been the subject of a significant amount of research. For example, the split ring resonator geometry allows the magnetic response to be tuned independently of the electric response. Through the tuning of each of the resonances it is possible to match the impedance $Z(\omega)$ to free space ($\epsilon \sim \mu, \rightarrow Z = Z_0$) and minimize the reflectance at a specific frequency. This is characterized by Equation 2.2.1.6,

$$R = 1 - T - A \quad \dots \quad 2.2.1.6$$

where R is reflectivity, T is transmittance and A is absorbance. If the material is impedance-matched to the surrounding media, the transmission is governed by the quantity n_2kd , where d is the absorber thickness. Therefore, the transmission through an index matched metamaterial is governed by the absorption within the bulk with no influence from surface reflections.

Up to this point, only the material properties of metamaterials have been discussed. However, the question arises, “What materials have both $\epsilon < 0$ and $\mu < 0$, or how can one tune these properties?” As shown through energy density (W), it becomes physically possible for negative index materials to be created.^[9] In effect, if there is no dispersion or absorption, total energy would be negative for “left handed” materials, as shown in Equation 2.2.1.7.^[9]

$$W = \epsilon E^2 + \mu H^2 \dots 2.2.1.7$$

Negative total energy, however, is not physically possible. However, if both sides of Equation 2.2.1.7 are multiplied by frequency(w) and then the derivative is taken with respect to w the result (Equation 2.2.1.8) does not allow for negative energy.^{[1] [60]} It is known that ϵ and μ are frequency dependent, therefore total energy can be positive even with negative permeability and permittivity.^[9]

$$W = E^2 \frac{d(w\epsilon)}{dw} + H^2 \frac{d(w\mu)}{dw} \dots 2.2.1.8$$

The problem then becomes determining a material that satisfies $\epsilon < 0$ and $\mu < 0$.^[9] V. G. Veselago suggested ferromagnetic materials which have large magnetic susceptibilities may qualify. Within his analysis, it became theoretically possible for these materials to have both $\epsilon < 0$ and $\mu < 0$. Veselago finally suggested several semiconductors that would satisfy these conditions if carrier

mobility could be increased.^[9] However, it was not until 1999 that the first true metamaterials were produced.

There has been considerable effort to construct engineered electromagnetic materials, beginning with original work by Pendry *et al.* to create an artificial material with negative permittivity.^[61] This initial worked theorized that if a metal wire was fabricated on a dielectric material, the permittivity of the interface could be approximated by using the effective electron mass of the metal/dielectric (m_{eff} in Equation 2.2.1.9) and the effective electron density of the metal/dielectric (J_{eff} in Equation 2.2.1.10),

$$m_{eff} = \frac{\mu_o q^2 \pi r^2 N}{2\pi} \ln(a/r) \dots 2.2.1.9$$

$$J_{eff} = N \frac{\pi r^2}{a^2} \dots 2.2.1.10$$

where μ_o is the permeability of free space, q is the charge on an electron, r is the radius of the wire, a is the lattice constant of the pattern, and N is the electron density of the metal. If these values are inserted into Equation 2.2.1.11 to determine the plasma frequency, w_p , of the structure, the effective permittivity can be calculated using Equation 2.2.1.12.

$$w_p^2 = \frac{N_{eff} e^2}{\epsilon_0 m_{eff}} \dots 2.2.1.11$$

$$\epsilon_{eff} = 1 - \frac{w_p^2}{w^2} \dots 2.2.1.12$$

Equation 2.2.1.12 may not completely capture the effective permittivity of present-day metamaterials, but, it was nonetheless revolutionary. Equation 2.2.1.12 allows that by placing a metallic structure on a dielectric, an effective

negative permittivity can be obtained over the entire surface due to an increased effective electron density, as compared to the dielectric. ^[61]

This line of thought was continued to determine an effective permittivity. It should be noted that the effective permeability can be calculated using the average magnetic field (**H**) and average magnetic flux density (**B**). For example if the effective permeability was to be calculated for an array of hollow cylinders, it would be done starting from the definition of an average **B**-field, \mathbf{B}_{ave} in Equation 2.2.1.13, and average **H**-field, \mathbf{H}_{eff} in Equation 2.2.1.14, and ending with approximately Equation 2.2.1.15 (the full derivation can be found in [62]),

$$B_{ave} = \mu_0 \mu_{eff} H_0 \dots 2.2.1.13$$

$$H_{eff} = H_0 - \frac{\pi r^2}{a^2} J \dots 2.2.1.14$$

$$\mu_{eff} \approx 1 + i \frac{\pi r^3 w \mu_0}{2 \sigma a^2} \dots 2.2.1.15$$

where σ is the conductivity of the metal and J is the current density in the cylinder. In this exercise μ_{eff} has an imaginary component, but is never negative in value. However, if a capacitive element, C , is added to the hollow cylinder array, the effective permeability becomes Equation 2.2.1.16.

$$\mu_{eff} = 1 - \frac{\pi r^2}{a^2 \left(1 + \frac{2\sigma}{wr\mu_0} i - \frac{3}{\pi^2 \mu_0 w^2 C r^3}\right)} \dots 2.2.1.16$$

Equation 2.2.1.16 can be negative in value. These two relatively simple examples describe how a structure can be created with an artificially designed permeability and permittivity. The structure must have metallic elements present which alter a dielectric's plasma frequency, and in turn, its permittivity. The amount of metal used directly determines the value of the permittivity, allowing very fine control.

Also, the surface must allow for a flowing current (Equation 2.2.1.14) and have a capacitive element in the circuit (Equation 2.2.1.16).^[62] The amount of current flowing, and the value of the capacitance directly control the value of the effective permeability. The gap within the metallic ring (Figure 2.2.1.5) is known as a *split gap*, and can be modeled as a parallel plate capacitor. Using these tuning mechanisms, it became possible to fabricate the first true metamaterial devices known as split ring resonators, shown in Figure 2.2.1.5.^[63]

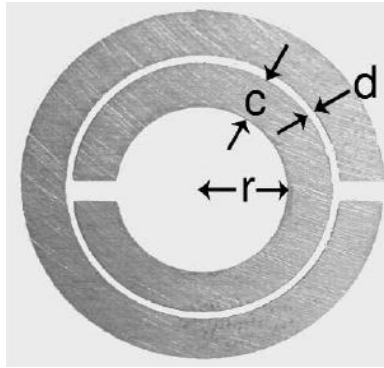


Figure 2.2.1.5: First experimentally verified metamaterial structure.^[63]

There are problems with present permeability/permittivity metamaterials. While these devices are perfectly scalable to new wavelengths, technological limitations have kept these devices from operating in the near-IR and mid-IR. However, the benefits of these metamaterials, including perfect absorption/reflection/transmission, imply that the integration of these MM devices into the IR would benefit both IR photodetection and TPV research. Therefore, it was the goal of this research to create an IR metamaterial perfect emitter for TPV applications which would provide spectral control and improve the quantum efficiency of a TPV diode. Also, a metamaterial polarization grid was created with the hope of improving IR-photodetection technologies.

2.2.2 Dynamic Metamaterials

The field of metamaterials has had exciting breakthroughs since the initial conception of designer permittivity and permeability structures. One of the relatively new and exciting advancements in the field is the development of dynamic, or active, metamaterials. These devices are designed to alter the MM optical response with the addition of external stimuli. This work aims to use dynamic metamaterials to create optical filters for photodetector applications. The purpose of these filters is to provide dynamic on/off ratios to replace large filter wheels or increase available pixel counts in current photodetector technology. This section will build on Section 2.2.1 and present the theory of dynamic metamaterials with the hope of providing more insight into this work's proposed solutions.

In order to explaining how a metamaterial can become dynamic, one must examine Equation 2.2.1.1 and Equation 2.2.1.16. In particular, it should be noted that the index of refraction, and in turn the optical properties, of a metamaterial are directly related to the capacitance element within the metamaterial. It stands to reason, if one can alter the capacitance of the split gap within a metamaterial, the resonance properties will also be altered. In this model of a MM there are two methods to alter this capacitance; however, in both methods, one must first model the split gap as a parallel plate capacitor.

The first method involves the excitation of optical carriers within a semiconductor. As electrons are excited within a semiconductor, the free electrons are increased, and the semiconductor becomes more conductive. As

shown in Figure 2.2.2.1, a semiconductor can be arranged in such a way that the active area of the split gap increases as the conductivity of a semiconductor increases.

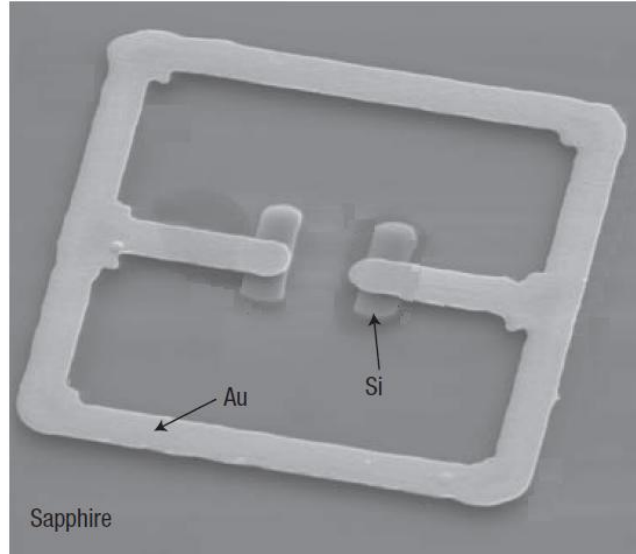


Figure 2.2.2.1: A dynamic MM structure, when electrons are excited within the Si layer, the split gap begins to act as a larger capacitor, altering the MM response. ^[64]

For example, when there is optical excitation of free electrons within the silicon of Figure 2.2.2.1, the semiconductor begins to act as a metallic element, effectively increasing the active area of the parallel plate capacitor. As shown in Equation 2.2.2.1, when the area, A , of a capacitor is increased, the capacitance, C , is altered as long as there is no change in plate separation, l .

$$C = \frac{\epsilon A}{l} \dots 2.2.2.1$$

The second method of altering the capacitance of a MM is based on the application of a voltage to the MM pattern. In order to determine the effect of an applied voltage, one must examine the definition of current, I , in Equation 2.2.2.2,

$$I = Q/t \dots 2.2.2.2$$

where Q is charge, and t is time. Also, the capacitance of a parallel plate capacitor is shown from Equation 2.2.2.3

$$C = Q/V \dots 2.2.2.3$$

where V is the potential over the two plates. Combining these two equations, and applying Ohms law gives Equation 2.2.2.4

$$C = t/R \dots 2.2.2.4$$

If we then apply Pouillet's law for resistance within a parallel plate capacitor, we obtain Equation 2.2.2.5.

$$C = \frac{\sigma A t}{l} \dots 2.2.2.5$$

where σ is the conductivity between the plates, A is the area of the plates, and l is the distance between the plates. It is also important to note that conductivity can be described by Equation 2.2.2.6

$$\sigma = J/\mathbf{E} = \frac{I/A}{V/l} = \frac{Il}{VA} \dots 2.2.2.6$$

where J is current density, and \mathbf{E} is electric field. Also, impedance, Z , will be utilized in Section 4.1.2. The impedance of a surface is described by Equation 2.2.2.7.

$$Z = V/I \dots 2.2.2.7$$

With Equation 2.2.2.8, it also becomes evident that altering the applied voltage to current ratio will change the impedance of a surface. This has a direct effect on permittivity and permeability as can be seen in Equation 2.2.2.8 and 2.2.2.9.

$$\mu = nZ \dots 2.2.2.8$$

$$\varepsilon = n/Z \dots 2.2.2.9$$

Upon examination of Equation 2.2.2.5, 2.2.2.6, and 2.2.2.7 it becomes evident that altering the capacitance, and therefore the resonance of a MM, depends on altering the conductivity. In particular, the capacitance element of the MM is directly related to the impedance across the split gap, and therefore the permittivity and permeability of the surface. The ability to create a dynamic MM is now shown to be dependent on the ability to create a non-linear relationship between current and voltage utilizing the metallic elements of a MM. Therefore we must utilize a non-linear device such as a diode in order to have a rapidly changing I/V ratio.

The typical method used to fabricate an applied voltage dynamic metamaterial is to deposit the MM pattern as a Schottky contact on a medium doped semiconductor. The result is the formation of a Schottky barrier diode. As can be seen from Figure 2.2.2.2, the Schottky barrier has a non-linear I/V curve allowing for large potential changes in conductivity.

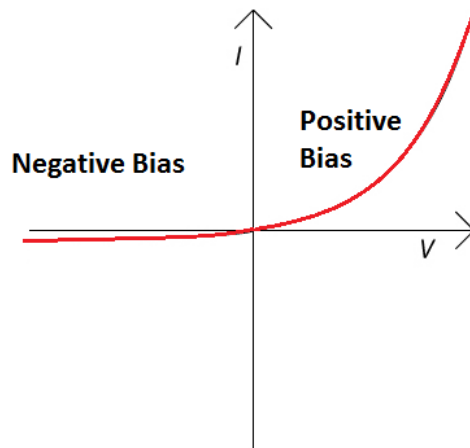


Figure 2.2.2.2: A Schottky diode, notice the exponential increase in current at positive bias and constant current at negative biases.

This type of dynamic MM can be run with a positive or negative bias. These operational modes operate in a similar fashion. With positive bias, current increases greatly with respect to voltage, the result is a larger conductivity. However, with a negative applied bias, voltage is changing much faster than the current. The result in this case is a much lower capacitance and a lower conductivity. Ultimately, in both cases, the result is the same, the MM response is altered with applied bias. This work will utilize the theory for a dynamic metamaterial for applications in photodetection applications. In particular, this work will use a forward biased MM polarizer for application in mid-IR photodetectors.

2.2.3 Photonic Crystals

Photonic crystals (PhC) will be used to create light trapping devices for TPV and photodetectors in the near and mid IR frequency ranges. A PhC has a few benefits over MMs within this frequency range. These include ease of fabrication and simplicity of design. Therefore, to create a full spectrum of photonic tools, PhCs are investigated.

Photonic crystals operate under classical electrodynamic principles as well as quantum mechanical principles. The full derivation of all varieties of PhCs can be found in a very well written text entitled “Photonic Crystals, Molding the Flow of Light” by John D. Joannopoulos.^[65] For the purposes of this work, the fundamental concepts of PhCs will be discussed as well as the various metrics used to analyze these crystals.

A photonic crystal is a repeating array of dielectric materials. There are three different varieties of photonic crystals: one, two, and three dimensional (shown in Figure 2.2.3.1).^[65] The names imply the number dimensions for which a photonic crystal is periodic. For example, a one dimensional photonic crystal is only periodic in one dimension and therefore, has photonic properties in one plane.^[65]

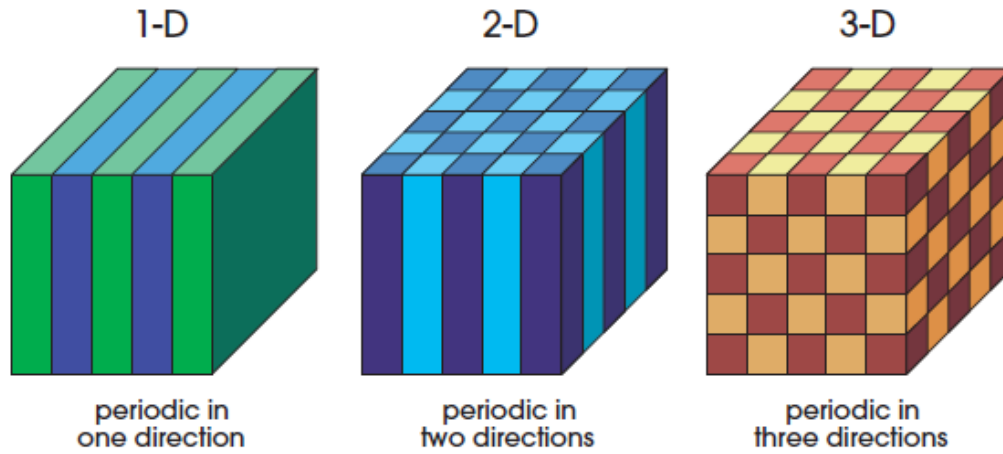


Figure 2.2.3.1: One dimensional photonic crystal (left), Two dimensional photonic crystal (middle), Three dimensional photonic crystal (right).^[65]

In order to successfully describe a photonic crystal, two terms should first be defined. First is the Bloch wave vector (\mathbf{k} [rad/m]).^[87] The wave vector is a conserved quantity in a periodic medium, such as a PhC, and in a homogenous system represents the direction of energy flow. Therefore, if there is a \mathbf{k} value of 0, known as the Γ point, it is implied that there is no energy flow and a standing wave must be present.^[70] Within the wave vector are three structural specific constants known as lattice constants (\mathbf{a}). The lattice constant is the physical distance between two elements in a periodic pattern. The full definition of \mathbf{a} as a

vector can be seen in Figure 2.2.3.2. However, it is typically more convenient to define \mathbf{a} in momentum space, where the reciprocal lattice constants ($2\pi/a$ or \mathbf{b}) are used.^[88]

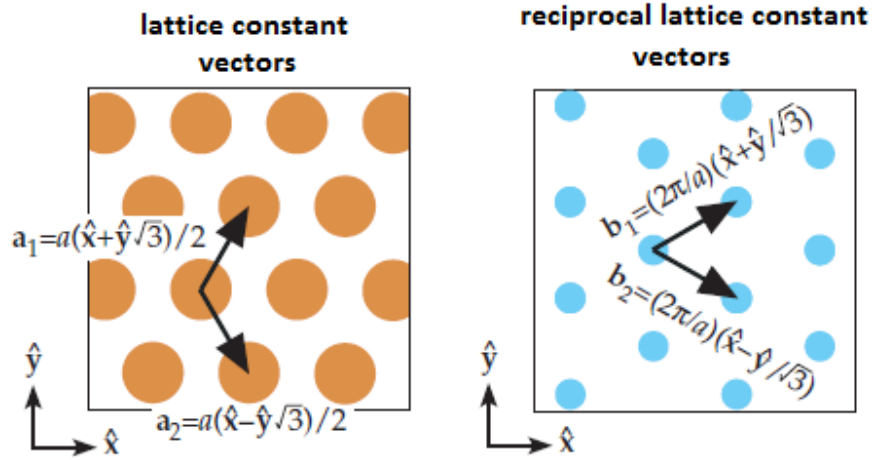


Figure 2.2.3.2: *Left:* the lattice constants of a photonic crystal, they are defined as a vector based on the x and y plane. *Right:* reciprocal lattice constants in momentum space.^[89]

The Bloch wave vector \mathbf{k} , can now be defined by Equation 2.2.3.1,

$$\mathbf{k} = k_1 \mathbf{b}_1 + k_2 \mathbf{b}_2 + k_3 \mathbf{b}_3 \dots \quad 2.2.3.1$$

where the subscripted values of \mathbf{k} and \mathbf{b} are in the direction of the nearest elements within the smallest physically repeatable area (known as the Brillouin zone).^[88] The next definition which needs to be described is angular frequency, $\omega(\mathbf{k})$, as a function of the Bloch wave vector (Equation 2.2.3.2),

$$\omega(\mathbf{k}) = \frac{|\mathbf{k}|c}{\sqrt{\epsilon}} \dots \quad 2.2.3.2$$

where ϵ is the dielectric constant of the material where the light is traveling, this value will change based on the mode of the wave vector.^[84] With Equation 2.2.3.2 it becomes possible to plot the allowed frequencies of light (ω) for any particular

direction of energy flow (\mathbf{k}). This line is known as the *light line* and is shown in Figure 2.2.3.3.^[84]

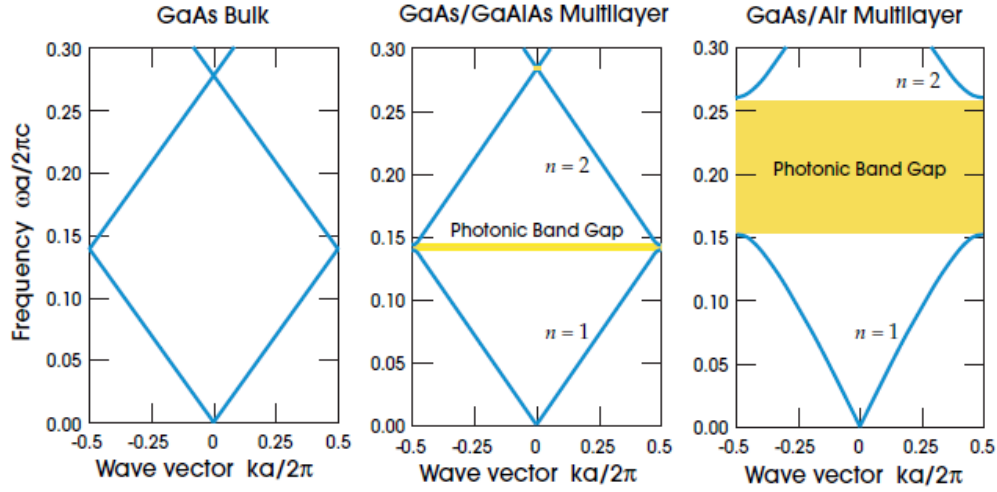


Figure 2.2.3.3: The light lines as a function of frequency and the wave vector for three structures: bulk GaAs (left), GaAs and GaAlAs alternating layers (middle), and GaAs and Air alternating layers (right). Notice the increasing photonic band gap with increasing variation in index of refraction.^[84]

The light line is one of the more important metrics in analyzing a PhC. Using graphs such as those shown in Figure 2.2.3.3 it becomes possible to determine frequency ranges where energy is no longer allowed to propagate through the crystal and frequencies where standing waves form within the crystal. The former of these regions is known as a photonic bandgap.^[84]

The photonic bandgap is formed as the wave vector \mathbf{k} moves out of the Brillouin zone ($\mathbf{k}=\pi/a$), it is then indexed by n , where n is the mode ($\mathbf{k}=n\pi/a$).^[89] For \mathbf{k} values at the location of π/a , the mode has a wavelength of $2a$.^[89] This means the wave can only be centered in either the low dielectric material or high dielectric material, and still maintain the required symmetry of a standing wave.^[83] Quantum mechanically, lower frequency modes concentrate their energy

in regions with a higher dielectric constant, and higher frequency modes have a larger amount of energy in low dielectric materials.^[82-83] Therefore, a larger photonic band gap occurs where there is a larger change in dielectric constant, ϵ , as implied previously in Equation 2.2.3.2.^[81] Note that there is no photonic bandgap if there is no change in dielectric constant.^[84]

Of particular note to this research is the two dimensional photonic crystal shown in Figure 2.2.3.4

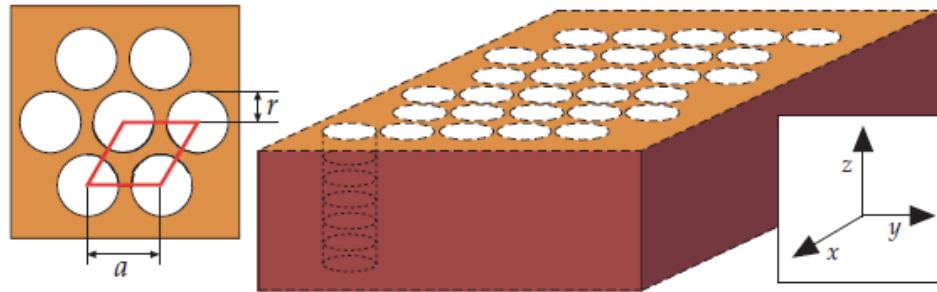


Figure 2.2.3.4: A two dimensional photonic crystal with the periodic a value and rod radius r .^[66]

The geometry of this two dimensional periodic structure may seem overly complex when compared to Figure 2.2.3.1. However, there is a good reason to have low permittivity dielectric holes surrounded by a high permittivity dielectric bulk. For example, if there is square lattice of dielectric holes surrounded by air (shown in right of Figure 2.2.3.5), there would be a photonic band gap for only the transverse magnetic portion of the incident electromagnetic wave.^[66] However, a lattice of only high dielectric veins, as shown in left of Figure 2.2.3.5, would create a band gap for only the transverse electric waves.^[66] In order to excite both polarizations, these two structures must be combined.

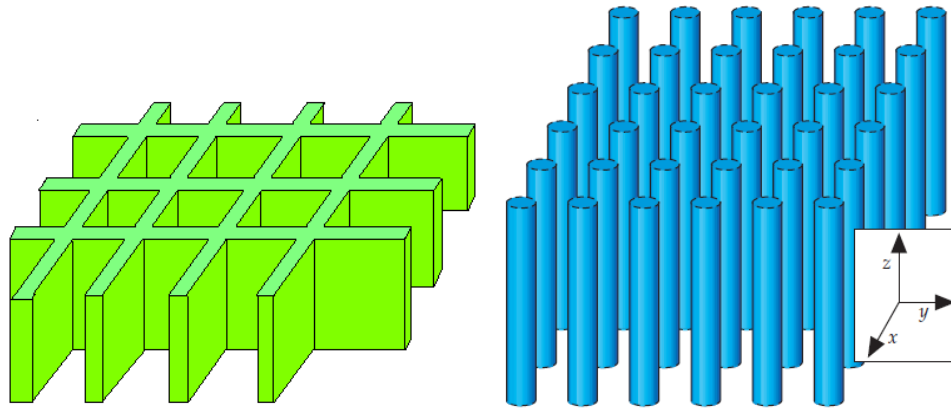


Figure 2.2.3.5: Two dimensional photonic crystal of veins for TE polarizations (left) and a two dimensional photonic crystal of rods for TM polarizations(right).
[67]

The resulting structure must incorporate high indexed material physically connected together, as with the vein pattern of Figure 2.2.3.5. Also, to affect the TE polarization, there must be a separation of the high dielectric material as seen with the rod pattern of Figure 2.2.3.5. The resulting compromise is shown in Figure 2.2.3.6. This photonic crystal pattern has been shown to form an 18.6 percent complete photonic band gap shown in Figure 2.2.3.6. [66]

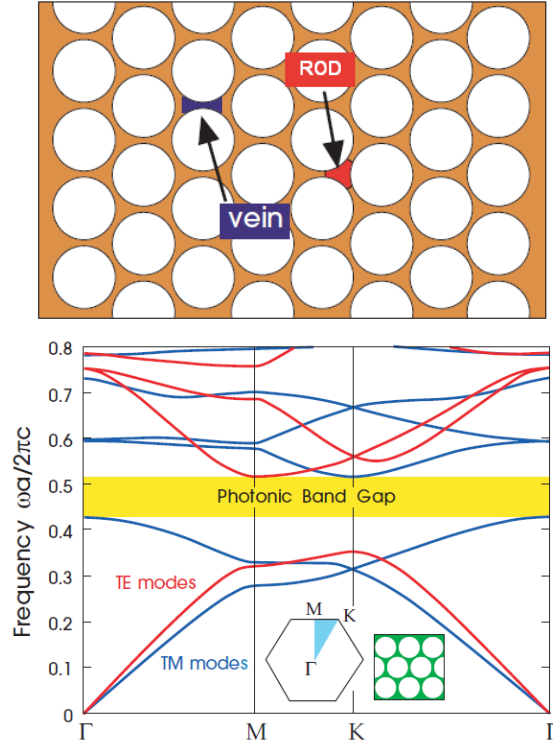


Figure 2.2.3.6: *Left:* Image showing the rod areas which support a TM photonic band gap and the vein areas which support a TE photonic band gap. *Right:* The band structure of the two dimensional lattice shown in the inset. The blue shaded region is the irreducible Brillouin zone and points Γ , M, and K are the points of high symmetry^[68]

2D Photonic crystals can also be utilized to add complete confinement for a specific wavelength. Light can propagate vertically (z-direction) into the photonic crystal; however, due to the photonic band gap, the electromagnetic radiation along the light line cannot escape in the x-y plane.^[69] When this light has a frequency corresponding to the gamma point (Γ of Figure 2.2.3.6), the Bloch wave vector is equal to zero and a standing wave forms within the cavity. The result is light trapping of a specific wavelength in the form of a standing wave. This is the basic theory of long photonic crystal fibers. However, if the PhC is not approximating infinity in z-direction length, energy from the standing

wave is lost through evanescent waves in leaking in the $\pm z$ direction. By tuning the PhC gamma point to a desired wavelength, evanescent waves can be created at that wavelength.^[70]

Light horizontally confined within a 2D PhC leaks slowly into the surrounding vertical media.^[66] The result is an increased interaction time between semiconductors and photons. As an added side effect, the PhC will also act as a filter, confining only a specific frequency range of light and reflecting longer wavelengths or transmitting shorter wavelengths. These two properties allow PhCs to have specific applications with TPV as well as photodetection. The latter has been proven successful in previous photodetector research and the former will be conducted within this body of work.

Chapter 2 discussed the physics of both semiconductors and metamaterials. In particular, the metrics such as fill factor, IQE, EQE, and CE were used to describe semiconductor photodiodes. Also, metamaterial devices such as SRRs, Fishnets, SWPs, and PhCs were examined. Chapter 3 will discuss the implementation of these devices and how they can be used to improve existing technologies.

Chapter 3

Present Field and Project Goals

This chapter is dedicated to detailing the current state of the art technologies in each research area described in this work. It is the goal to introduce the relevant work in each area, and then determine metrics for improvement upon the field. This section will be broken into four parts. First, several types of TPV emitters such will be considered, including current state of the art photonic crystal emitters and metamaterial perfect absorber technologies. Next, TPV filters, such as the one dimensional PhC filter stages currently employed in TPV, will be introduced. Then metallic PhC filters will be discussed and compared to current TPV filter technologies. Similarly, existing IMF devices will be explored. Finally, this section will end with the current state of dynamic metamaterial filter technologies.

List of Abbreviation - Chapter 3

TPV - thermophotovoltaic	CE - conversion efficiency
MM - metamaterial	Isc - short circuit current
TE - transverse electric	MPP - max power point
TM - transverse magnetic	IMF - interfacial misfit arrays
PhC - photonic crystal	MBE - molecular beam epitaxy
IR - infrared	VECSELs - vertical-external-cavity surface emitting lasers
FWHM - full width half max	SLS - strain layer superlattice
PV - photovoltaic	Voc - open circuit voltage
CVD - chemical vapor deposition	FF - fill factor
ARC - antireflective coating	SRR - split ring resonator
QE - quantum efficiency	SWP - split wire pair
MIMs - monolithically interconnected modules	MEMs - microelectromechanical system

3.1 TPV Emitters

As part of a relatively young field, nanostructured TPV emitter technologies have been evolving regularly for over a decade and have undergone many changes. Beginning around the year 2000, emitter research was focused on three dimensional photonic crystal emitters. These emitters utilized alternating layers of tungsten rods in order to tune the TE mode of a photonic crystal structure (Section 2.2.3). There are multiple varieties of these structures, such those shown in Figure 3.1.1. ^[71-76]

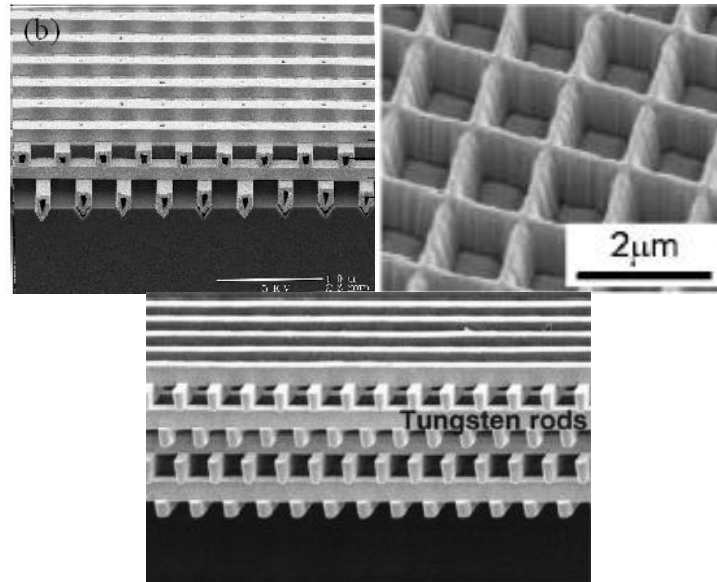


Figure 3.1.1: Three examples of PhC tungsten emitter technologies. *Left and Right:* log cabin PhC emitter designs. ^{[71] [72]} *Middle:* square “vein” pattern used to alter the TE optical mode. ^[74]

These structures were unique in the field of TPV emitters and, as can be seen from Figure 3.1.2, were able to provide a somewhat narrow band emission spectrum.

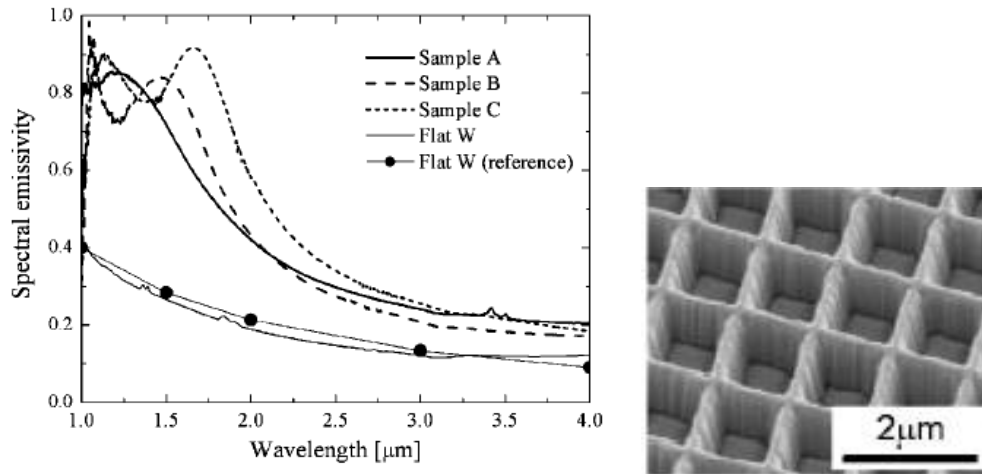


Figure 3.1.2: Spectral response of the PhC on left. Notice the much higher spectral response at 1.7 μm as compared to that of un patterned tungsten. ^[74]

Since then, research has shifted towards 2D photonic crystals. Most of this research has focused on PhC arrays with air rods, shown in Figure 2.2.3.4. Many initial attempts at PhC emitters focused on the use of dielectrics, such as Si, or dielectrics coated with a metal, for example Si and Cr. ^[77-79] There have also been attempts at combining 1D and 2D photonic crystals in order to create a spectral emitter focused at approximately 6.3 μm . ^[80]

These dielectric devices have since lost fashion, instead present emitter research has focused on metallic PhC emitters. In particular, tungsten and tantalum PhCs have been the focus of much research. ^[81-84] The most recent of these publications discusses the importance of chemical stability in a PhC used for TPV emitters. ^[84] In particular, it alludes to the work undertaken to encapsulate tungsten with other elements, such as hafnium and aluminum, in order to increase material durability. ^[85] Tungsten has also been shown to be very hard to micro-manufacture, limiting its potential uses. ^[84] Due to these problems, the

conception of a tantalum PhC was achieved.^[84-86] The emission spectrum for the tantalum (Ta) PhC is shown in Figure 3.2.3.

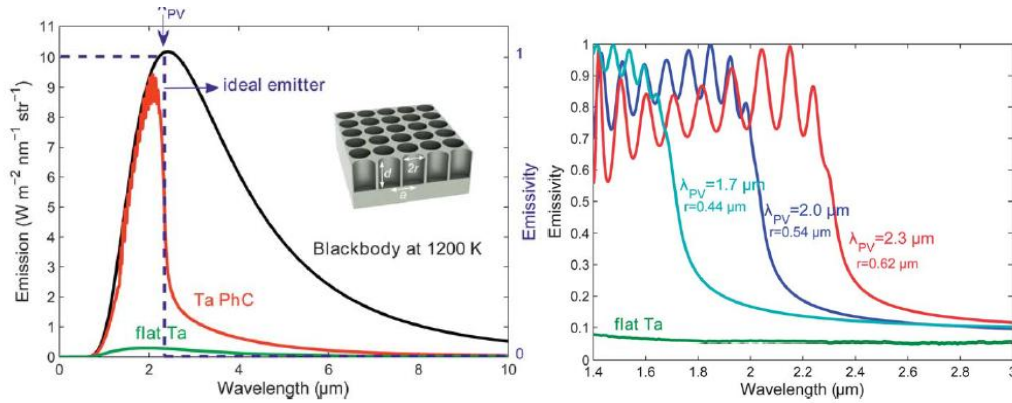


Figure 3.1.3: Simulated results of a Ta PhC emitter with various etch depths and hole radius.^[84]

As can be seen in Figure 3.1.3, state of the art PhC TPV emitter systems have a sharp turn on frequency.^[84] This is ideal in a TPV emitter as it eliminates low energy photons from causing heating within the diode stage. However, the emissivity of the Ta PhC remains very large at higher energies, as seen on the left side of Figure 3.1.3.^[84] Resulting in a large number of very high energy photons incident on the TPV cell. In order to more finely tune the TPV emitter emissivity, this section proposes the use of a device known as a metamaterial perfect absorber.

Metamaterial absorbers are a relatively new technology, given that the first such named device appeared in literature in 2008.^[87-90] Three of these initial absorber devices were designed to operate in the GHz frequency range by utilizing Au metallization with a polyimide dielectric spacer.^[88-90] In contrast to these Au structures, Schaich and Puscasu created an Al structure on a SiO₂

dielectric spacer.^[87] It is important to note this alternative material choice, as all current perfect absorber technologies utilize Au as the metallization material.

Over the next few years, there have been many structures created which act as perfect absorbers at frequencies less than 10 THz (over 30 μm).^[91-94] These structures are very interesting for their high absorption properties. However, for the applications at near-IR frequencies, the structural details of these absorbers are not able to be fabricated due to problems of scale. To this purpose, there has been substantial work in creating a perfect emitter/absorber at visible/IR wavelengths.^[96] Figure 3.1.4 depicts three of the most common of the visible/IR metamaterial absorber structures.

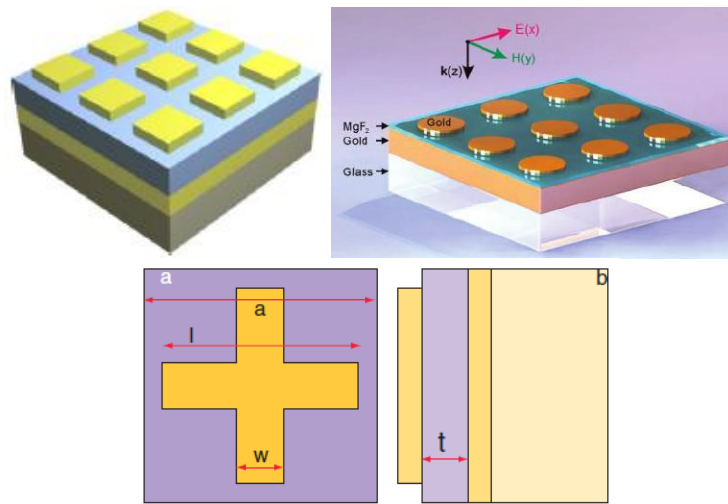


Figure 3.1.4: *Left:* perfect absorber square lattice features.^[97] *Middle:* perfect absorber circular structures.^[98] *Right:* perfect absorber cross structures.^[99]

There has been great success using these nanostructures. Many of the devices have shown narrow band absorption approaching 100%, shown in Figure 3.1.5. Given the success as perfect absorbers, these devices have unique applications as TPV emitters. This is due to Kirchoff's law of thermal radiation

which states that at thermal equilibrium, emissivity is equal to absorptivity. As such, these devices become perfect emitters at a given wavelength. The magnitude of the emission becomes equal to the emissivity multiplied by the blackbody spectrum at the MM's temperature, shown in Figure 3.1.6.

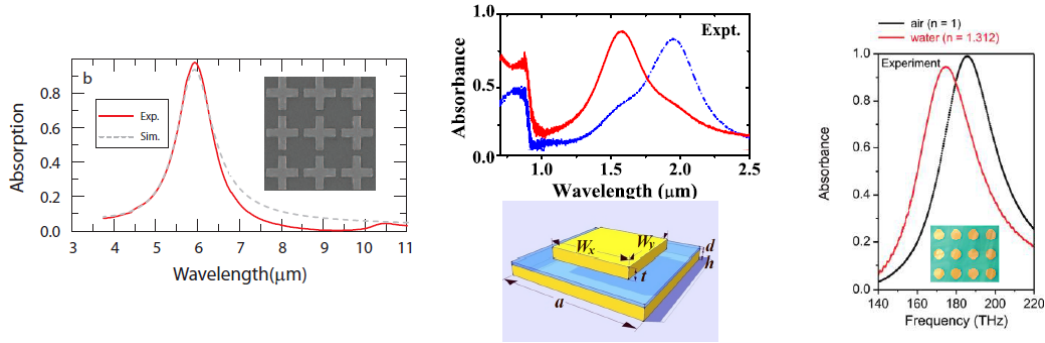


Figure 3.1.5: *Left:* measured absorption of an Au cross pattern.^[99] *Middle:* measured absorption of an Au square pattern.^[100] *Right:* measured absorption of an Au circle pattern.^[98]

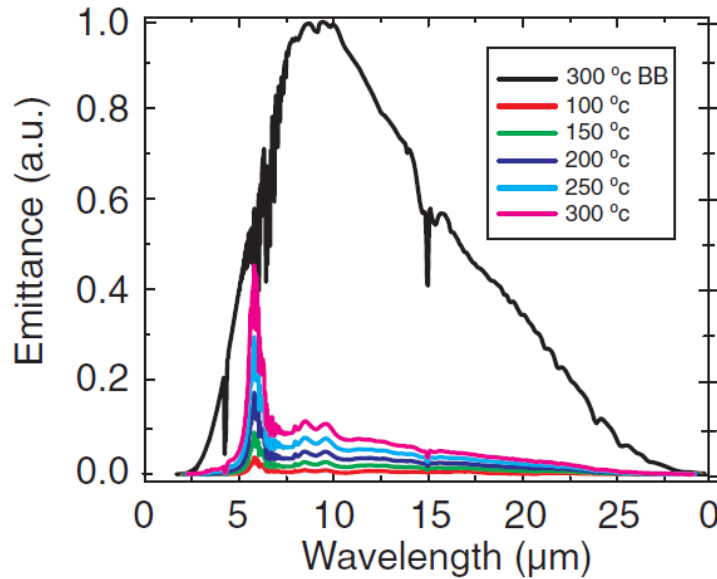


Figure 3.1.6: Experimental verification of Kirchoff's law using a MM perfect emitter at different temperatures.^[104]

Most MM emitters show a very narrow absorption bands corresponding to a full-width-half-max (FWHM) of approximately $1\mu\text{m}$, shown in Figure 3.1.5, when operating at IR to visible wavelengths.^[97-105] However, simulation predicts the possibility of a narrow band perfect emitter with a 500 nm FWHM at optical frequencies.^{[105][106]} This would provide a great advantage over PhC emitters which typically have a much larger emission spectrum.^[71-84] Unlike PhC emitters, MM patterns of different sizes can be tiled with many different sized patterns in order to create a large optical emission spectrum, as shown in Figure 3.1.7.^[104]

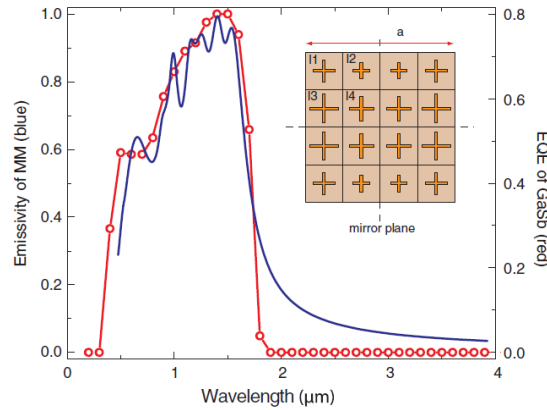


Figure 3.1.7: Multiple sizes of a Au cross MM pattern tiled in order to combine resonances and produce a broad MM resonance peak.^[104]

There is, however, a major hurdle to overcome in the fabrication of a MM TPV emitter. All of the MM devices described within this field are fabricated from Al, Au, or in GHz applications Cu. In order to be successfully utilized for TPV applications, these devices must operate at high temperatures. For example, the bandgap of GaSb corresponds to a blackbody temperature centered at 1600 °C; however, gold will melt long before this temperature is reached (1064 °C). The impact of overheating a MM perfect absorber can be seen in work done by Wang *et al.*^[80] This work confirms that the reshaping of a MM absorber has

drastic effects on wavelength of operation as well as wavelength selectivity, Figure 3.1.8.^[80]

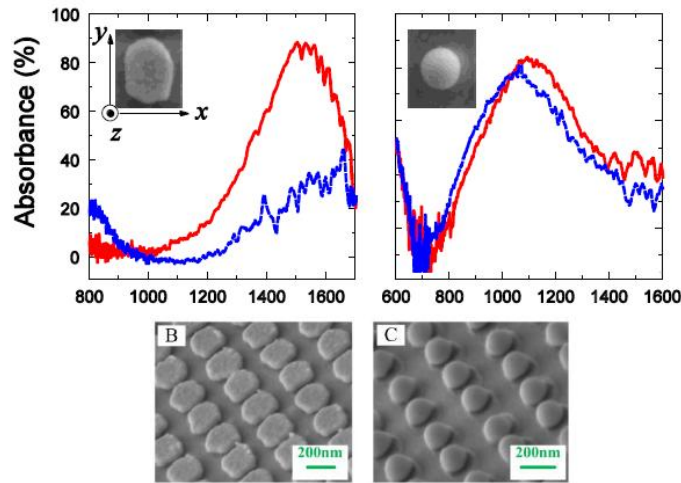


Figure 3.1.8: The optical response of the same MM structure before (left) and after (right) deformation due to heating.^[80]

In order to combat this problem, this research proposes a novel solution. A platinum MM perfect absorber which utilizes a structure based on previous research. This material choice provides unique challenges as the free electron mobility and collision frequency of Pt lower than traditional MM metallizations. The lower parameters imply that MM resonance conditions will be more difficult to meet. However, based on previous research in the field, various metrics can be examined in order to determine success. For example, Hao *et al* has created one of the only operational MM under $1.5 \mu\text{m}$.^[100] This author utilizes a Au metamaterial, has a peak absorption approaching 70%, and a FWHM of $1.2 \mu\text{m}$.^[100] Using these parameters, the proposed Pt MM can be properly assessed in relation to the current research.

3.2 TPV Filter

The purpose of a TPV filter stage is to reflect light with energy below, or above the bandgap of the diode stage, in order to provide the most efficiently converted spectrum possible for the TPV diode. To date, there has been little work in improving spectral filter technologies. For example, spectral control research has been limited to optimization of the TPV emitter stage, as discussed in Section 3.1. This section, however, will explore the present field of TPV filters, which consists most notably of 1D PhC layers. Semiconductor 2D photonic crystals used for PV filtering will also be considered, as well as metallic PhC structures used for photodetector technologies. This discussion will then describe a 2D metallic PhC designed for use as a front side spectral filter in a TPV photodiode, which was first proposed by us in [107].

As described in Section 2.2.3, a 1D PhC is a repeating structure of very thin dielectric layers. The generally accepted 1D PhC TPV filter is based on a Si-SiO alternating layer stack.^{[78][108][109]} The structure, reflectance spectrum, and TPV efficiency of this PhC is shown in Figure 3.2.1. The structure of Figure 3.2.1 have demonstrated very good reflection characteristics for photons with energy below the bandgap of a TPV diode, thereby reducing diode heating.

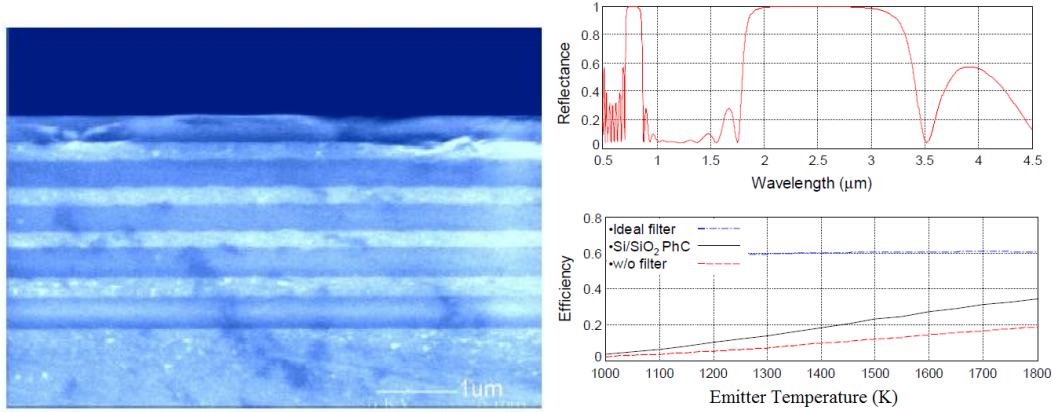


Figure 3.2.1: *Left:* False color TEM of the Si-SiO₂ 1D PhC. *Top-right:* Reflectance of Si-SiO₂ 1D PhC. *Bottom-right:* TPV efficiency increase with implementation of the 1D PhC. ^{[78] [108]}

These 1D PhC stacks have also been implemented in conjunction with a 2D PhC emitter stage with limited success.^[78] As an example, Ref. [78] claims decreased efficiency when a combination PhC filter and spectral emitter was used. However, improved TPV efficiencies were reported when utilizing only a spectral specific emitter stage.^[78] As such, with one exception, research in 1D PhC filters has since diminished due to the more promising possibilities in spectral emitter technologies. Recently, work was published using a Ag-SiO₂ 1D PhC filter for TPV applications.^[110] This work shows effective bandgap transmission around 78% for a GaSb TPV cell; however, an decreased transmission of high energy photons reduces overall TPV efficiencies.^[110] There have been many other studies within the field of 1D PhC for waveguide applications, but with the limited successes shown in TPV applications, this section will describe other possible spectral filter solutions.

Recently, interest in the field of photovoltaics has led to a surge in schemes to maximize the efficiencies of present cell technologies. One such

optimization method is the use of semiconductor PhCs layers as optical confinement and enhancement layers. Most of these PhC patterns are constructed of Si-H/air or Si-H/SiN_x and are optimized for Si PV technologies. [111-115] PV research allows for the comparison of important metrics such as diode efficiency, which are important for TPV diodes, but not relevant to other fields such as photodetection. Some of these semiconductor PhC patterns are shown in Figure 3.2.2.

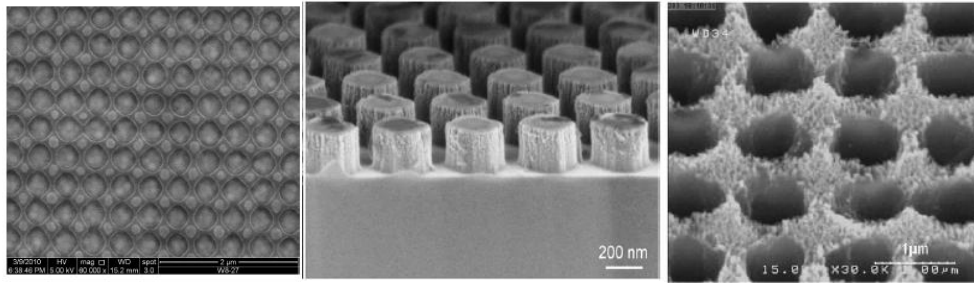


Figure 3.2.2: Three types of semiconductor PhCs used as ARCs and filters for PV technologies. *Left and Right:* Semiconductor with air rods. *Middle:* Semiconductor rods in air structure. [112][113][115]

As with the PhC emitters described in Section 3.1, these semiconductor PhCs produce a very steep band edge and a broad transmission peak. However, the most important metrics for success when describing PV enhancement is with absorbance and increased PV efficiency.

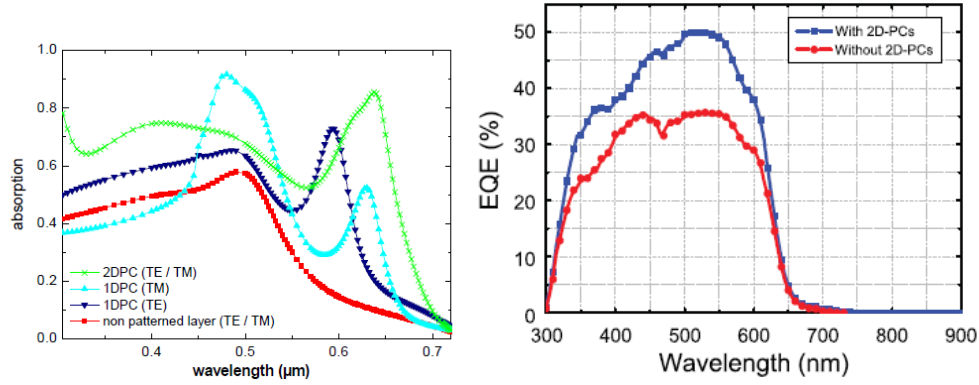


Figure 3.2.2: Left: measured absorption with the addition of a PhC. Right: The spectral quantum efficiency of a photodiode with and without a 2D PhC. ^{[111][114]}

As can be seen in Figure 3.2.2, there is a potential for a large increase in the efficiency of a PV cell simply with the addition of a PhC. Given this success there has been other work into PhC enhancements for a PV cell such as dual cavity design with backside PhC reflectors. ^[116-118] However, more complicated structures have shown limited success. As will be described in Section 5.1, these attempts may actually decrease device performance.

These previous studies in the field of photonics provide evidence that the addition of a front-side photonic crystal can increase the performance of a PV diode. However, this work hopes to take the research a step further and combine photodetector technologies with those of the semiconductor PhC technologies in PV research. In particular, it is the goal to translate metallic PhC seen in IR photodetectors into TPV diode stage surface enhancement and spectral filter.

Two varieties of metallic PhC patterns have been used to increase the responsivity of photodetector technologies. Initial PhC photodetectors were created with complex designs such as a repeating pattern of defects within a traditional PhC lattice, shown in Figure 3.2.3. ^[119-122] The irregular shaped holes,

or lack of holes, creates defects within the lattice, allowing narrow band transmission through the PhCs photonic bandgap. The result is increased narrow-band photodetector responsivity, shown in Figure 3.2.4. ^[119-122]

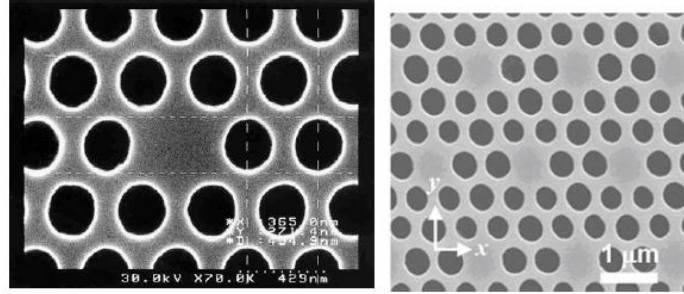


Figure 3.2.3: Two variations of defect modes within a PhC lattice. *Left:* A single hole is removed creating the defect mode. *Right:* this pattern consists of multiple hole radii and missing holes in order to create polarization sensitivity. ^{[119][122]}

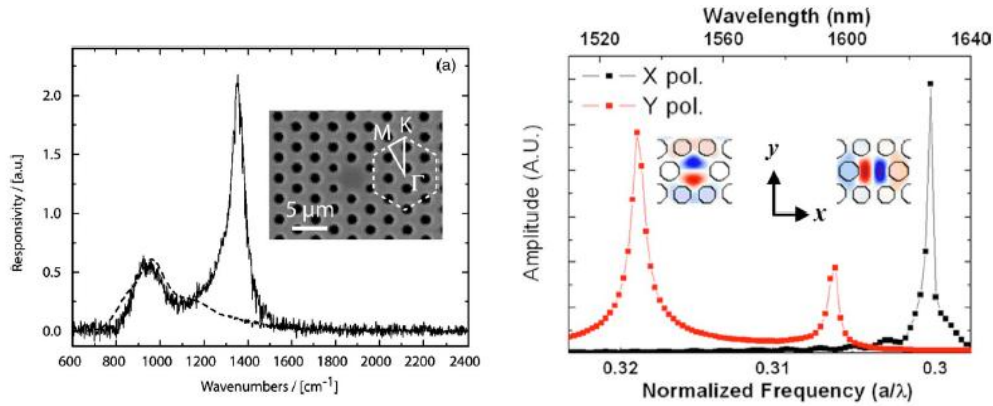


Figure 3.2.4: The spectral responses of defect mode PhCs, the largest amplitude corresponds to the defect resonance. *Left:* Spectral response of a single defect mode. *Right:* spectral response of multiple polarizations with multiple defect modes. ^{[120][122]}

These leaky mode photodetector filters allowed for very narrow band responsivity. However, for TPV applications a larger pass band is required in order to maximize output. To this end, the discussion on metallic PhC photodetectors will continue to non-defect mode metallic PhCs.

There has been much research over the past few years in non-defect mode metallic PhC for photodetector applications. The discussion in this work will focus on square and hexagonal PhC patterns, as well as round and square rods (shown in Figure 3.2.5).^[123-131]

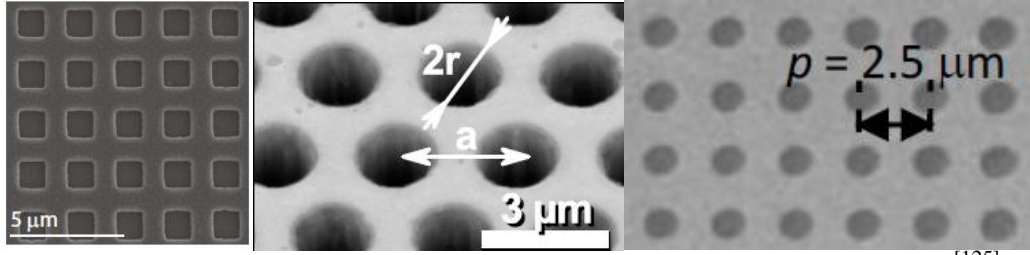


Figure 3.2.5: Three types of metallic PhC patterns. *Left:* Square PhCs.^[125] *Middle:* Hexagonal PhC pattern.^[123] *Right:* Square PhC pattern.^[129]

These photonic crystals were designed to operate at the bandgap of InAs. Therefore, The resonance wavelength for these structures is much farther into the infrared (greater than 4 μm) than required for our TPV applications (less than 2 μm).^[123-131] However, the performance of these PhCs are perfectly scalable to shorter wavelengths. When the metallic PhCs were implemented, the spectral response and photocurrent generated shows a marked improvement, as seen in Figure 3.2.6.

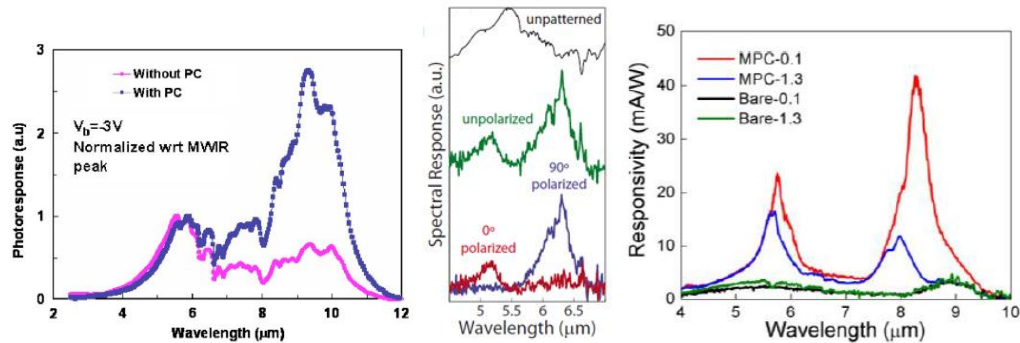


Figure 3.2.6: Improvement of spectral response, responsivity, and photoresponse due to the addition of a metallic PhC. *Left:* hexagonal PhC pattern.^[123] *Middle:* square PhCs.^[125] *Right:* square PhC pattern.^[129]

Other work has been done to show the post-processing tunability of these PhC patterns using a SiN_x layer grown via chemical vapor deposition (CVD) processes.^[124] Results in this study show a stronger responsivity value (although shifted) as the thickness of the SiN_x is increased, as shown in Figure 3.2.7. The author of the paper, as well as previous work by us in Ref [107], conclude that this is due to the SiN_x acting as an antireflective coating (ARC).^[124]

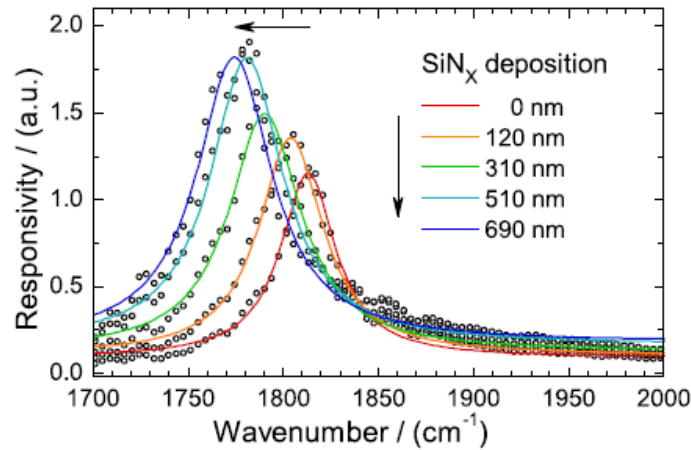


Figure 3.2.7: Increase in responsivity and wavelength shift due to the addition of a SiN_x layer deposited via CVD. This response is predicted to be due to an ARC effect.^[124]

Currently, TPV research utilizes a 1D PhC filter stage which acts as only a transmission/reflection filter.^{[78][108-110]} These 1D PhC TPV filter technologies can be enhanced using the discussed PhC structures. For example, previous work has shown that photovoltaic efficiencies can be enhanced using semiconductor PhC structures.^[111-115] Also, as described in Chapter 2.2.3 and Ref. [107], a 2D photonic crystal adds benefits including light trapping and potential QE increases due to leaky-mode interactions. Also, these metallic photonic crystals have shown

to increase both spectral responsivity and photocurrent within photodiodes.^[119-132]

It is for these reasons that this work proposes a 2D metallic PhC for a front-side TPV filter stage. As an added benefit, this proposed device can be treated with a SiN_x layer in order to increase efficiency utilizing an ARC response.^[124] The metrics of success for this work are an increase in photogenerated charge carriers as compared to standard diode processing techniques, ie. an ARC. The methods used to determine this increase will be I_{sc} , MPP, and CE. In order to verify that the response is due to the addition of a PhC, the structures will also be examined with ellipsometry in order to determine single wavelength optical absorption.

3.3 TPV Diode

The diode stage of a TPV device typically consists of a single heterojunction with a bandgap matched to the TPV emitter stage. This section hopes to increase the tools available to the TPV diode stage by introducing an interfacial misfit array (IMF) layer in order to allow a GaSb TPV diode to be grown epitaxial on a GaAs substrate. With the success of an IMF layer, many new options in TPV diode design are opened. Future possibilities include lattice mismatched TPV diode stages and IMF integrated two junction monolithic interconnected modules (MIMs). IMF layers can allow new material growth combinations and the possibility of avoiding growth constraints such as lattice matching.

Misfit dislocations can be generated at the interface when two materials with differing lattice constants are grown monolithically, through MBE or

CVD.^{[133][134]} Lattice mismatched systems are often used in thin film applications; however, as film thickness increases misfit dislocations have led to reduced device performance.^[134] Figure 3.3.1 depicts the strain at a GaAs/GaSb interface with and without an IMF layer.

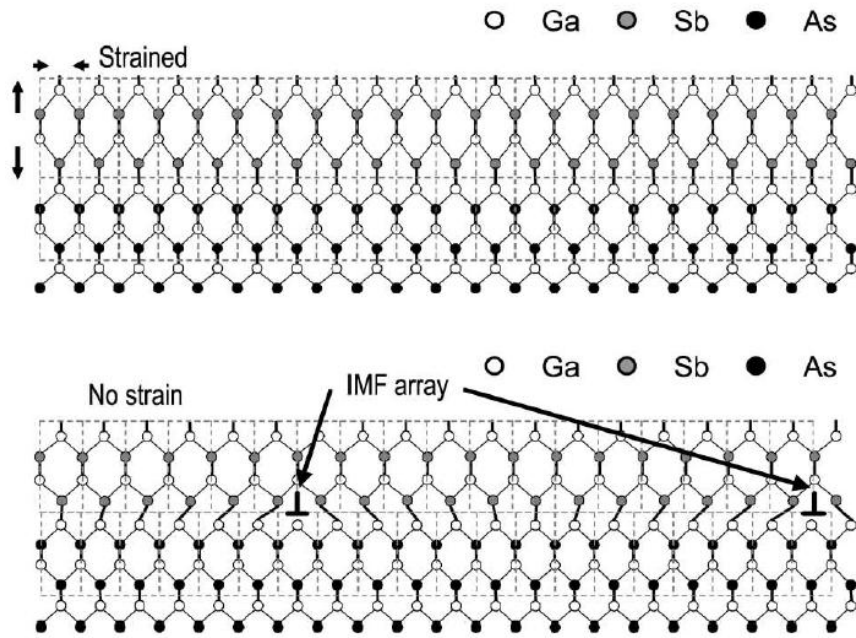


Figure 3.3.1: *Top:* strained layer with no IMF present, the top GaSb layer has a longer lattice constant in the y-direction and shorter in the x-direction leading to dislocations as thickness increases. *Bottom:* IMF layer with every 14th atom missing at the interface. The result is a strain free GaSb layer.^[135]

As can be interpreted from Figure 3.3.1, an IMF layer is an intentional arrangement of 90 degree edge dislocation at the interface of two materials. In the case of a GaAs/GaSb interface, the IMF layer utilizes a 13:14 Sb:Ga ratio in order to create these horizontal dislocations. Due to the introduction of an IMF layer, interfacial strain is reduced, which results in a dislocation free material, shown in Figure 3.3.2.

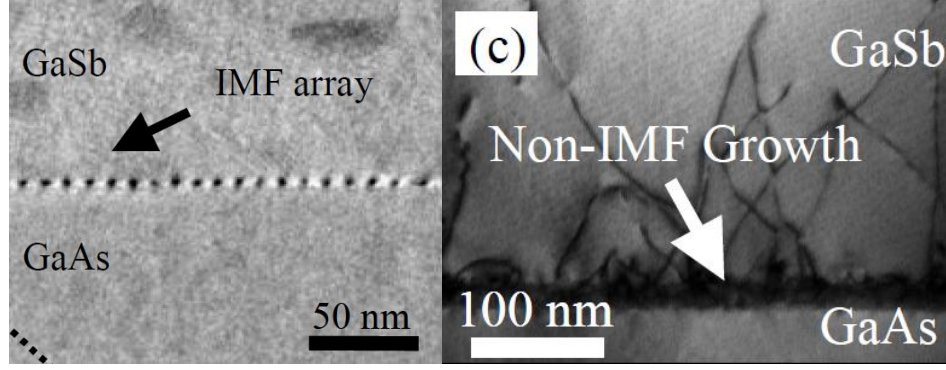


Figure 3.3.2: *Left:* The addition of an IMF layer produces a uniform material above the GaSb/GaAs interface. *Right:* Dark lines represent threading dislocations not found when the IMF layer is present.^[136]

The utility of an IMF layer has been shown with the creation of light emitting diodes, quantum well lasers, photodiodes, and vertical-external-cavity surface emitting lasers (VECSELs).^[136-144] Unfortunately, few of these papers do direct device performance comparisons of results with and without the IMF layer. However, the emission spectrum of the lasers and responsivity of the IMF photodiodes, shown in Figure 3.3.3, are promising for a high quality material growth.

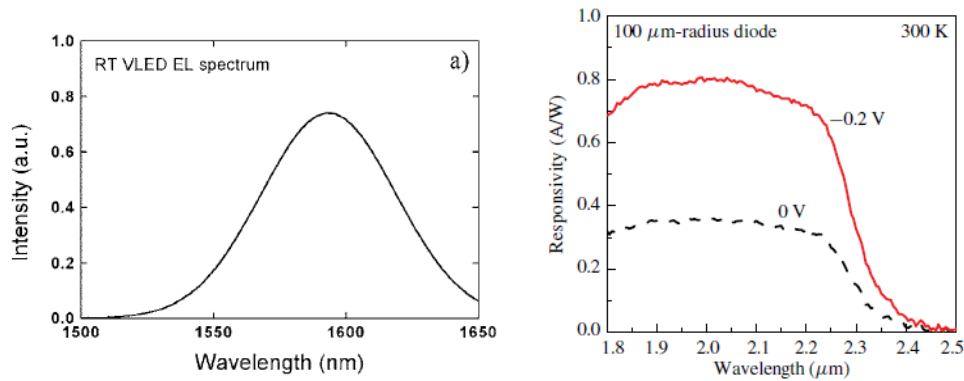


Figure 3.3.3: *Left:* electroluminescence of a VLED photodiode showing a narrow bandgap of the GaSb layer. *Right:* Responsivity of a photodiode using an IMF layer.^{[137][141]}

As further evidence for proper strain relief when utilizing IMF layers, Balakrishnan *et al* demonstrated an operational VECEL using an IMF layer. This VECEL produced a very similar photoluminescence both with an IMF layer and with a lattice matched substrate.^[136] The structure as well as photoluminescence images can be seen in Figure 3.3.4.

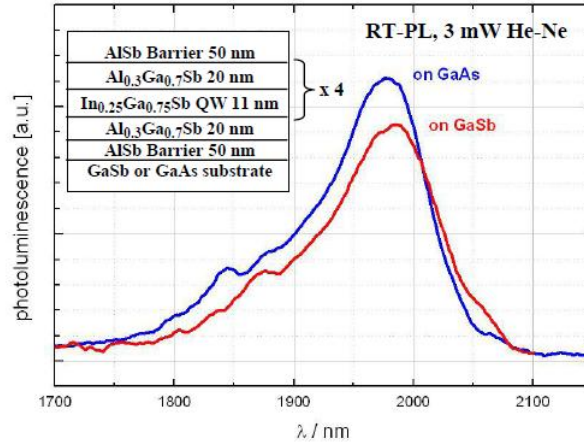


Figure 3.3.4: VECEL performance of a latticed match substrate (blue) and that with an IMF layer (red).^[136]

Since the issuing of a patent for construction techniques of IMF layers via molecular beam epitaxy, there has been limited research for potential device applications.^[145] However, there has been work classifying the material quality of IMF layer devices grown using alternative growth mechanisms.^{[134][135][146-157]} Throughout these studies, the consensus becomes that the addition of an IMF layer allows for the growth of lattice mismatched materials with increased lattice relaxation, as well as few, if any, threading dislocations. Some of these images are shown in Figure 3.3.5.

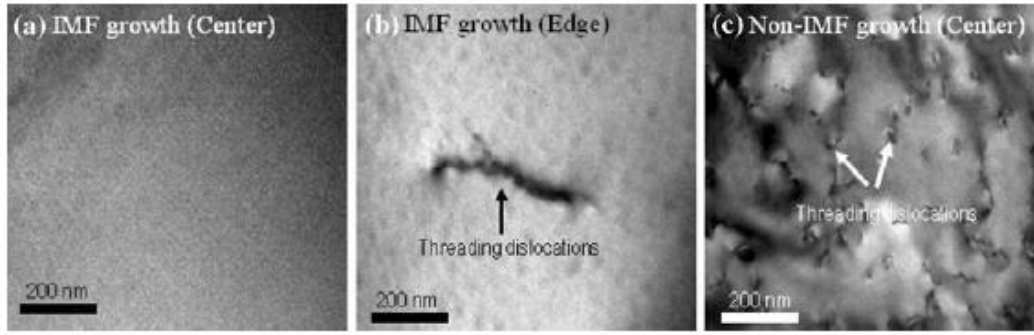


Figure 3.3.5: *Left:* IMF material growth showing no threading dislocations. *Middle:* A threading dislocation appearing near the edge of an IMF growth. *Right:* large numbers of dislocations forming when no IMF layer is present. ^[156]

The unique properties of the IMF layer are of particular interest to TPV diode. TPV devices are constantly expected to operate at both lower band gaps and with higher efficiencies (for this motivation refer to Chapter 1). However, the incident spectrum of a TPV device is constantly tuned to the bandgap of the TPV diode. As such there has been little research done into multijunction TPV cells.^[158-160] The work which has been done, concludes that multijunction TPV cells may offer greater power density with a lower TPV emitter temperature.^[160] If IMF layers are shown to exhibit similar TPV diode efficiencies to lattice matched layers, it becomes possible to test complex structures such as strained layer superlattices (SLS) grown in two junction forms. These SLS structures are typically constructed from GaAs- and GaSb-based materials. Also, SLS diodes have already been characterized with IMF growth.^[148] SLS is particularly interesting as it allows for designer bandgap semiconductor materials, and are also extremely useful at long wavelengths. Further information on long wavelength SLS materials can be found in Ref [161-168]. With these potential applications,

the implementation of IMF on a TPV diode may open a range of new structures for both single junction and multijunction TPV devices.

As such, the quality of IMF TPV cells will be measured based on the metrics defined for standard TPV cells (i.e. FF, MPP, I_{sc} , V_{oc} , etc.). In order to also achieve the best measure of cell quality, photoluminescence and electroluminescence measurements will be taken and compared to both control samples as well as with the above literature. To improve the understanding of IMF devices within literature, this work will also compare TPV diodes with and without an IMF layer on a lattice mismatched substrate.

3.4 Dynamic Metamaterial Filters

3.4.1 Metamaterial Filters

This section deals with the work in the field of dynamic metamaterials and metamaterial filters. Present technologies do not utilize either of these devices in combination or on their own to create a dynamic polarization-sensitive filter. As such, the devices and methods which have led to the creation of the dynamic metamaterial polarizer will be described. In particular, metamaterial split ring resonators, metamaterial fishnet patterns, and metamaterial split wire pairs operating at relevant wavelengths will be compared. Also, this section will discuss present research into dynamic metamaterial devices. Finally, the incorporation of these devices into a dynamic metamaterial polarizer will be described.

As described in Section 2.2 the first true metamaterial devices were known as split ring resonator (SRR) devices. Although they initially operated exclusively at GHz frequencies, there has been many recent research projects utilizing electron beam lithography in order to create devices compatible with visible and infrared frequencies.^[169-176] It should be noted that the previous cited papers provide a good overview of the field; however, are only a small fraction of the over 8,000 papers published on the SRR metamaterial design over the past 3 years. Of particular note are a few papers describing small split ring resonator devices operating in the near-IR.^[169-173] These papers discuss a very small scale SRRs while providing a large resonance effects, as shown in Figure 3.4.1.1.^[172]

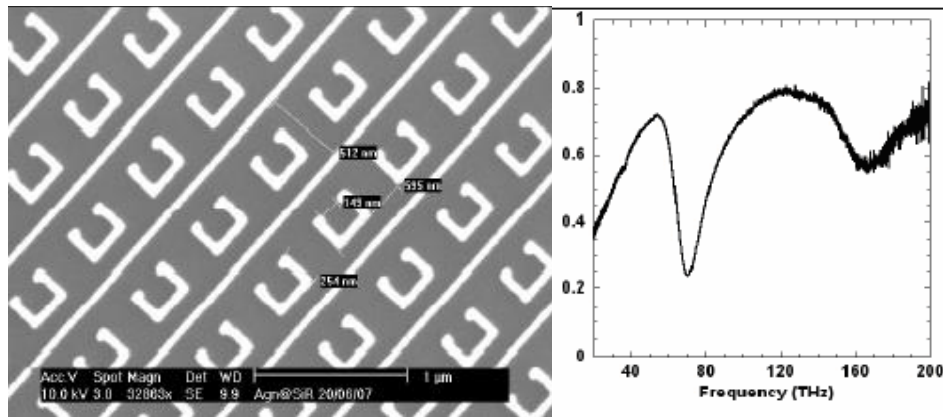


Figure 3.4.1.1: Left: SRR patterns produced at scales under 1μm in length. Right: resonance response of these small SRR devices.^[172]

The evolution of this work has led to comparisons between these small split ring resonators and their individual components. For example, a work by Husnik *et al*, describes small SRR design for use as nano-scale resonance antennas.^[169] These SRR designs are incrementally modified and effectively compared to repeating patterns of nano-bars, shown in Figure 3.4.1.2. The nano-

bars are of particular interest to this work and will be described in more detail as split wire pair SWP MMs.

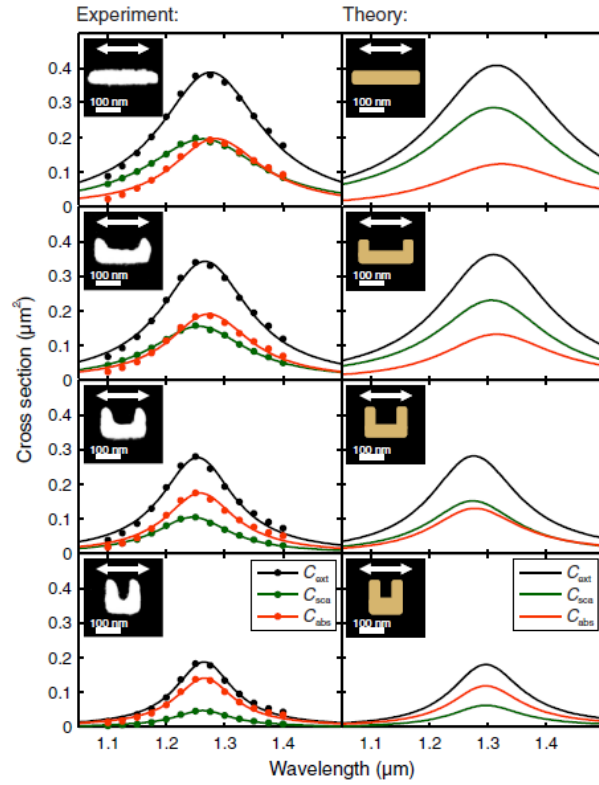


Figure 3.4.1.2: Incremental modification of a SRR device into thin nano-bars. These structures provide the bases for the split wire pair MM structure. ^[169]

A second enabling technology for the dynamic MM polarizer is a type of MM structure known as an optical fishnet. These devices utilize two metallic layers with a dielectric spacer. Repeating patterns of circular or square holes are then etched completely through the structure, shown in Figure 3.4.1.3. ^[177-182]

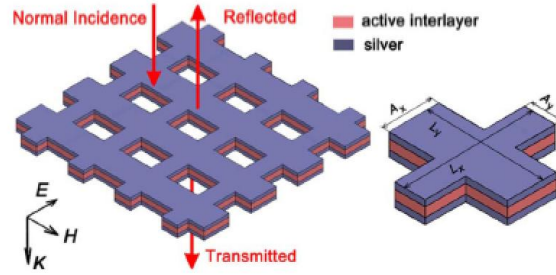


Figure 3.4.3: A fishnet MM devices consisting of two metallic layers with a dielectric spacer^[178]

As with nano-sized SRR designs, fishnet MM devices have shown very strong and narrow resonance peaks at specific frequency ranges, shown in Figure 3.4.1.4.

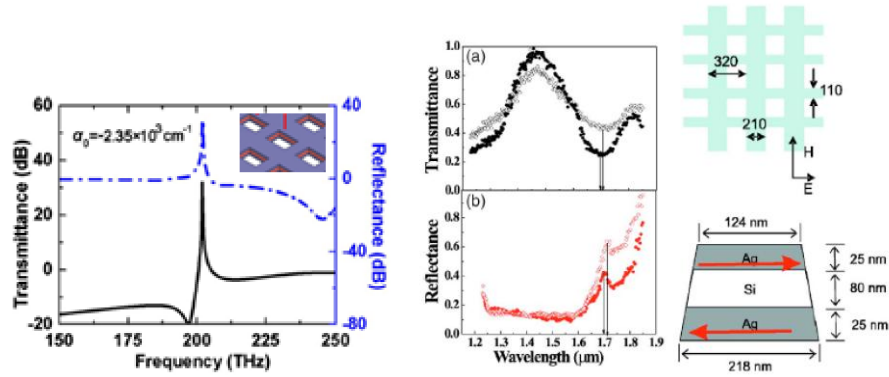


Figure 3.4.1.4: *Left:* simulated transmission and reflection characteristics for a silver MM fishnet structure.^[178] *Right:* Experimentally obtained reflection and transmission characteristics for a silver and silicon fishnet design.^[179]

Initially, two design characteristics must be taken into consideration to produce a dynamic metamaterial polarizer with the correct optical properties. First, there must be a distinct transmission characteristic for each polarization of incident light. This design constraint is easily satisfied through the usage of anisotropic structure. However, the second constraint is more difficult to produce: The metamaterial device must be “off” in the unbiased condition. To

satisfy this condition, when no bias is applied, the MM must allow equal transmission of all polarizations. This condition will allow the device to operate at a lower power, as well as provide continued functionality if there is a single layer grid failure.

While considering these design constraints, a third type of metamaterial was examined, the split wire pair (SWP).^[183-188] These devices operate similar to the nano-bars, described previously. For example, it is the interaction between metallic elements which create the resonance phenomena. However, unlike the fishnet patterns in Figure 3.4.1.4, wire pair metamaterials operate as notch filters with a high transmission window and large absorption at resonance, shown in Figure 3.4.1.5.

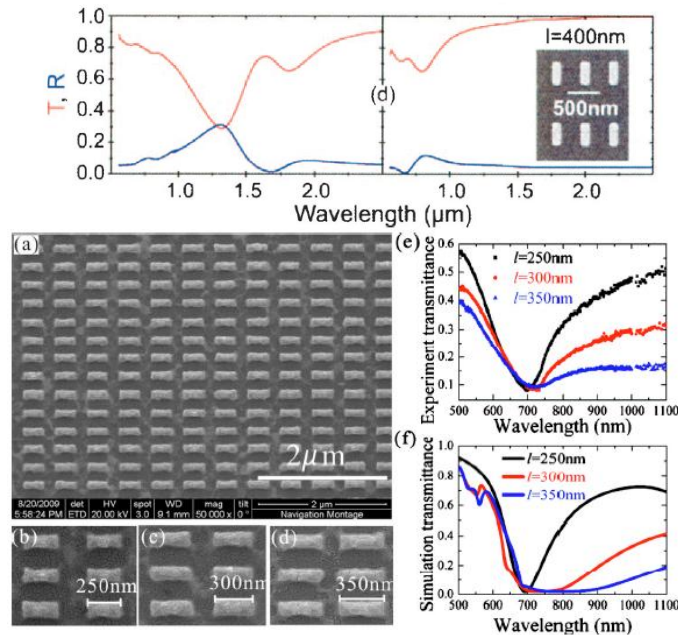


Figure 3.4.1.5: Top: Transmission and reflection of a SWP MM.^[183] Bottom: SEM image of a SWP MM along with experimental and simulated transmission results. Notice the notch filter type transmission obtained with the SWP structure.^[184]

SWP metamaterial device structures are useful to the design of a dynamic polarization grid as they maintain a high transmission value with a resonance narrow response. At the same time, this structure provides polarization sensitivity of similar quality to metallic gratings typically used for polarization sensitive photodetectors, shown in Figure 3.4.1.6.^[189-191]

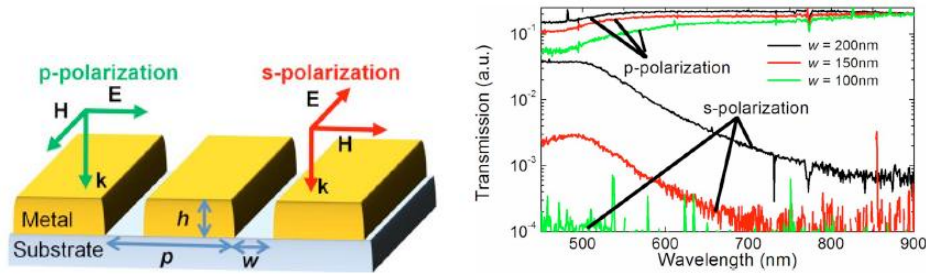


Figure 3.4.1.6: *Left:* cross-sectional image of a typical metallic grating polarization filter. *Right:* transmission of each polarization, notice the large transmission for p-polarized light and large reflection for s-polarized light at all frequencies.^[191]

The combination of these three MM devices allowed the conception of the dynamic MM device proposed in Chapter 5. This unique structure utilizes the parallel metallic bands of a split wire pair MM, the ring resonator design of SRR, and the repeating “+” of a fishnet pattern (right side of Figure 3.4.1.3). The expected result is a well-established MM resonance from the anisotropic SRR, high transmission and polarization sensitivity of the SWP, and low transmission polarization sensitivity from the fishnet pattern. These properties would allow for a high transmission of both polarizations in the “off” position. Also, if the resonance conditions of the SRR and fishnet can be altered, the resonance peak will shift, effectively turning “on” the polarizer and only allow transmission of

one polarization. Figure 3.4.1.7 describes the position of each MM structure in the polarizer as well as the expected response for the resulting structure. The characterization of this device alone represents a new leap forward in MM technologies as it incorporates multiple design elements and, to date, no similar device has been previously investigated.

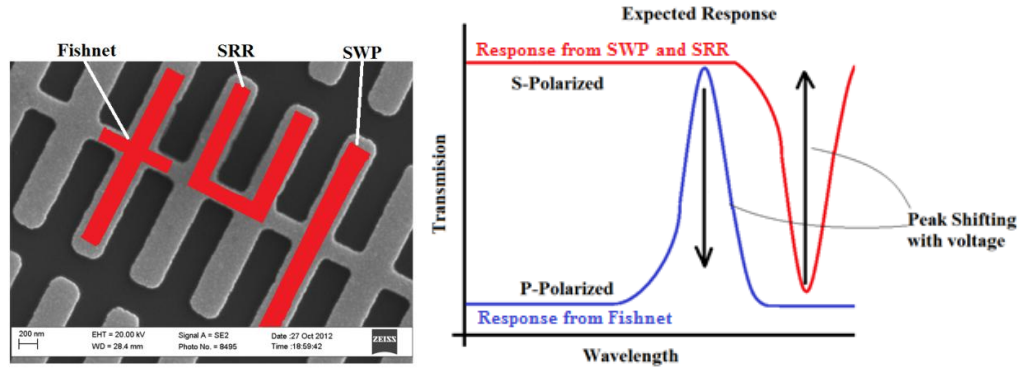


Figure 3.4.1.7: *Left:* Each MM structure in the polarizer device. The SRR and SWP utilize the semiconductor and the split-gap and the fishnet is made up of the semiconductor/Schottky barrier/metal stack as opposed to the traditional metal/dielectric/metal stack. *Right:* expected transmission response of the polarization grid. The SWP and SRR act as a notch filter and the fish-net structure acts as a band pass filter.

3.4.2 Dynamic Metamaterials

Despite recent interest in dynamic metamaterials, the field remains relatively unexplored. The largest strength of a dynamic MM is the ability to combine the resonances of MMs with an external energy source. This energy source then causes the MM response to be tuned in some form. Dynamic metamaterials typically fall into one of two categories, optically tunable or voltage tunable.^{[192-205][64]} As explained in Section 2.2.2, these device operate by increasing or decreasing the carrier concentration across the split gap of a MM. However, achieving the desired response can prove to be extremely difficult. This

section will describe current methods for optical and electrical tuning. Then, the approach used to provide dynamic tuning to the MM polarizer described in Section 3.4.1 will be discussed.

The first, and most common, method of creating a dynamic MM is to use laser in order to optically pump excited charge carriers into a highly doped semiconductor. The semiconductor is located at, or below the metamaterial pattern, and its conductivity is increased due to the optical pumping. The result is an altered response. Two such structures can be seen in Figure 3.4.2.1.

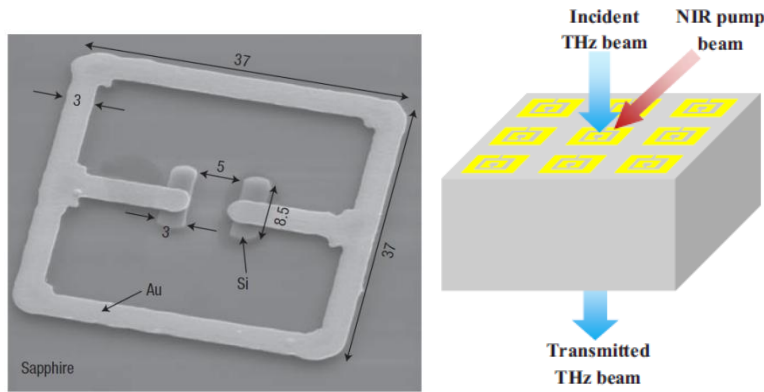


Figure 3.4.2.1: *Left:* a split ring resonator with highly doped Si located at the split-gap, optical pumping increases the carrier concentration in the Si. The result is a larger capacitance across the split gap and an altered MM response.^[64] *Right:* A SRR on a highly doped substrate the optically excited charge carriers “short” the split gap, altering the MM response.^[195]

When the pump laser strikes each structure of Figure 3.4.2.1, there is a unique optical response. For example, the structure on the right of Figure 3.4.2.1 will obtain an alter resonance frequency as the silicon fingers gain charge carriers.^[64] However, when light strikes the substrate on the right of Figure 3.4.2.1, an electrical pathway forms across the split gap, resulting in the removal of the MM resonance.^[195] The experimental results are shown in Figure 3.4.2.2.

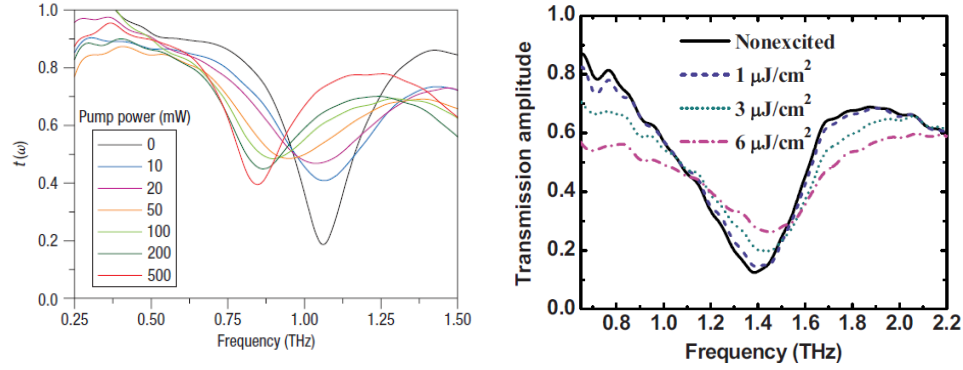


Figure 3.4.2.2: *Left:* As the Si gains charge carriers, the resonance frequency of the MM structure is shifted.^[64] *Right:* as the split gap is “shorted” the MM resonance is removed, not simply shifted to another frequency.^[195]

It should be noted that the relatively low change in transmission amplitude is common in most dynamic metamaterials. The largest percent change in transmission percentages tend to be on the order of 40% for both optical and voltage tunable MM devices.^{[196][200]} However, as will be explained later, there are a few new techniques being used to increase these percentages. Also, the response and structure on the left of Figure 3.4.2.2 should be noted.^[64] This device utilizes a highly insulating substrate (sapphire) and a very thin layer of semiconductor (600 nm). Using this structure, the photogenerated electrons are confined to the surface of the MM. The result is an especially strong resonance not commonly seen in dynamic MM devices.^[64]

The second type of dynamic MM device utilizes an external bias in order to alter the conductivity of the MM split gap. As with optically pumped dynamic MMs, these devices can be created to either reduce a response or alter transmission percentages. Two structures are shown in Figure 3.4.2.3 and 3.4.2.3.

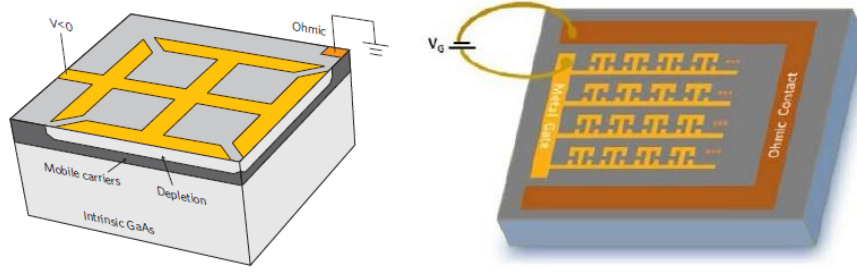


Figure 3.4.2.3: *Left:* voltage controlled SRR MM structure designed to increase resonance by depleting the split-gap region.^[200] *Right:* voltage controlled SRR MM designed to alter the capacitance of the split gap (not creating a short) in order to alter the resonance frequency.^[203]

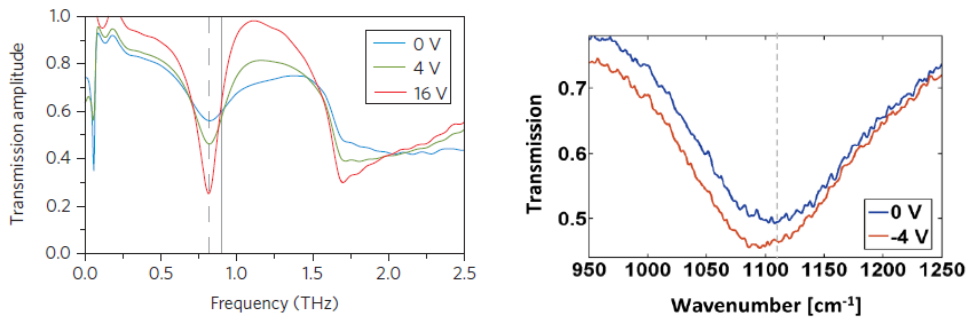


Figure 3.4.2.4: *Left:* Applied voltage used to increase the MM resonance by creating a charge depleted region in a doped semiconductor. Resulting in increased transmission.^[200] *Right:* Applied voltage used to shift the MM response using a charge depletion region.^[203]

As opposed to optically pumped dynamic MMs, most voltage dependent MMs operate by removing charge carriers from the split-gap by creating a charge depleted region.^{[192-209][64]} However, both optically pumped MMs and voltage controlled responses are increased when there is a highly insulating substrate, as in the left side of Figures 3.4.2.3 and 3.4.2.4.^[200] Although some of these devices are polarization sensitive, the structures were created to maximize properties such as phase modulation or simply show that specific structures can act in a dynamic fashion.^{[192-209][64]} However, some of the design constraints mentioned do improve device performances. In particular, moderate semiconductor doping levels have

been shown to create the best current profiles within the MM.^{[201]-[206]} Also, a SiN_x insulation layer is recommended to create the largest possible bias over the MM and not the contact pads.^[203]

In order to achieve a level of completeness two other types of dynamic MMs will be briefly mentioned. The first is a device which utilizes temperature effects in order to create a dynamic response.^[206-208] The second is created with microelectromechanical systems (MEMS) where the resonance is tuned by physically altering the structure.^[209] However, these tuning methods are not applicable to the applications of this work as they cannot be integrated monolithically or individually tuned. These structures are shown in Figure 3.4.2.5.

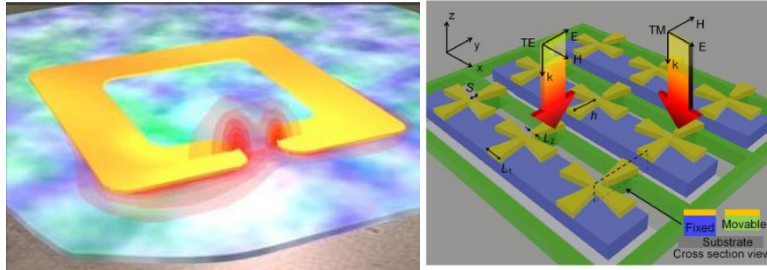


Figure 3.4.2.5: *Left:* Thermally tuned dynamic MM, the optical split gap can be “shorted” using thermally generated charge carriers.^[206] *Right:* MEMS MM structure, one arm of the cross can be altered physically to change the resonance frequency.^[209]

These previous studies led to the design of a dynamic MM polarizer tested experimentally in Chapter 5. This device uses the pattern described in Section 3.4.1, and was constructed with various optimizations shown to be effective in the above mentioned body of work. In particular, this dynamic device implemented a highly insulating sapphire substrate, a thin GaAs semiconducting layer of

moderate doping levels, and a SiN_x layer grown under the Schottky contact pad. However, there is an additional design optimization which is not considered in literature: as seen in Section 2.2.2., the ratio of current to voltage effects the resonance frequency of the MM. In literature, all voltage controlled MMs utilize a reverse biased Schottky diode to create this effect. This work proposes to create a similar effect using a forward biased Schottky diode. The result will be similar to optically pumped MMs which utilize an increased carrier density to alter the MM response. The new forward bias dynamic response is predicted to allow lower applied voltages as a large depletion width is not needed to create the dynamic effect. Therefore, this device will also operate using unique principles not shown in literature.

Chapter 4

Materials and Methods

This section is designed to give a brief background on specific tools used to create the devices proposed in Chapter 3. These tools include simulation methods, fabrication tools, and testing equipment. The tools and methods in this section will then be employed to create the devices described in Chapter 5.

List of abbreviations - Chapter 3

MM - metamaterial	GaAs - gallium arsenide	CVD - chemical vapor deposition
TPV - thermophotovoltaic	GaSb - gallium antimonide	ALD - atomic layer deposition
PhC - photonic crystal	Z - impedance	RIE - reactive ion etching
PV - photovoltaic	T - transmission	IR - infrared
FDTD - finite difference time domain	r - reflection coefficient	PECVD - plasma enhanced chemical vapor deposition
FIT - finite integral technique	t - transmission coefficient	n - refractive index
\mathbf{E} - electric field	IPA - isopropyl alcohol	\mathbf{n} - optical mode
\mathbf{H} - magnetic field	DI - deionized	λ - wavelength
EBL - electron-beam lithography	MIMs - monolithically interconnected module	FTIR - Fourier transform infrared spectroscopy
ϵ - permittivity	σ - conductivity	PL - photoluminescence
μ - permeability	ND - neutral density	EL - electroluminescence
SEM - scanning electron microscope	PVD - physical vapor deposition	IMF - interfacial misfit array

4.1 Simulation Methods

Simulation methods refer to the types of algorithms and numerical methods utilized by the simulation software in this work. In particular, the simulation software for photonic crystals (PhC), metamaterial (MM) resonance (FDTD software), and MM permittivity and permeability characterization (MATLAB) will be examined. This section does not go into actual device simulation, only the methods each solver uses to predict experimental results will be discussed.

4.1.1 Finite Difference Time Domain

The finite difference time domain method (FDTD) is commonly used to understand the propagation of electromagnetic waves in a semiconductor material. This method uses Maxwell's Equations to find the strength of the electric or magnetic field components in one, two, or three dimensions at discrete moments in time. The propagation of the electromagnetic wave can be described by continuing the calculation at another moment of time (next time step). The Lumerical software package, used in this project, employs this method to determine the electric field intensity at any moment in time.^[210] It is important to note that CST Microwave Studio, also used in the project, utilizes the Finite Integral Technique (FIT).^[211] The FIT, however, is identical to the FDTD method when using the transient solver; which was employed in this work.

The FDTD begins with Maxwell's Equations, Equations 4.1.1.1 and 4.1.1.2,

$$\nabla \times \mathbf{E} = -\mu \frac{d\mathbf{H}}{dt} \quad \dots 4.1.1.1$$

$$\nabla \times \mathbf{H} = \sigma \mathbf{E} + \epsilon \frac{d\mathbf{E}}{dt} \quad \dots 4.1.1.2$$

where \mathbf{E} is the electric field, and the auxiliary field, \mathbf{H} , is defined as $(1/\mu)\mathbf{B}$, \mathbf{B} is the magnetic field or the “magnetic flux density”, σ is defined as the conductivity, μ is the material permeability, ϵ is the permittivity of the material, and c is the speed of light in a material (defined as $\mu \cdot \epsilon$).^[212] In cartesian coordinates, these two equations can then be broken into six partial differential equations, three equations (4.1.1.3, 4.1.1.4, and 4.1.1.5) from Equation 4.1.1.1,

$$\frac{dE_z}{dy} - \frac{dE_y}{dz} = -\mu \frac{dH_x}{dt} \quad \dots 4.1.1.3$$

$$\frac{dE_z}{dx} - \frac{dE_x}{dz} = -\mu \frac{dH_y}{dt} \quad \dots 4.1.1.4$$

$$\frac{dE_y}{dx} - \frac{dE_x}{dy} = -\mu \frac{dH_z}{dt} \quad \dots 4.1.1.5$$

and three equations (4.1.1.6, 4.1.1.7, and 4.1.1.8) form from Equation 4.1.1.2,

$$\frac{dH_z}{dy} - \frac{dH_y}{dz} = \sigma E_x + \epsilon \frac{dE_x}{dt} \quad \dots 4.1.1.6$$

$$\frac{dH_z}{dx} - \frac{dH_x}{dz} = -\sigma E_y - \epsilon \frac{dE_y}{dt} \quad \dots 4.1.1.7$$

$$\frac{dH_y}{dx} - \frac{dH_x}{dy} = \sigma E_z + \epsilon \frac{dE_z}{dt} \quad \dots 4.1.1.8$$

These six equations are next made into difference equations. To accomplish this task, one must visualize the locations of the six field components in a finite area, shown in Figure 4.1.1.1.

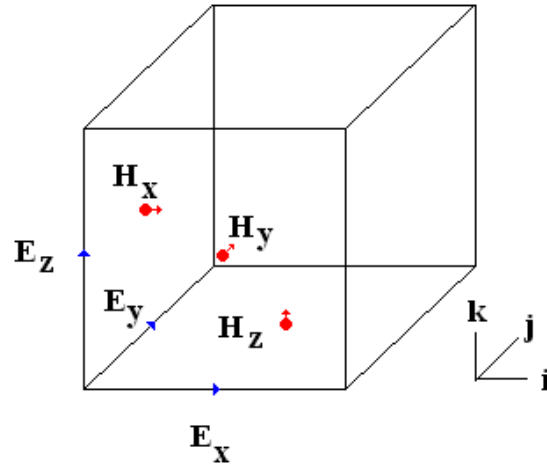


Figure 4.1.1.1: Yew Square with the electric field vectors located in the center of the edges in the direction of the blue arrows. The magnetic field vectors are located in the center of the faces and in the direction towards the middle of the cube.

Each of the components is located in the center a face or line. Also, an arrow designates the direction of the vector.

In order to find the left half of the difference equation, one must also locate the previous and next electric field components in space, for example the next components in the x -direction are shown in Figure 4.1.1.2 (as $i+1$ to symbolize one cell over in the x - or i -direction).

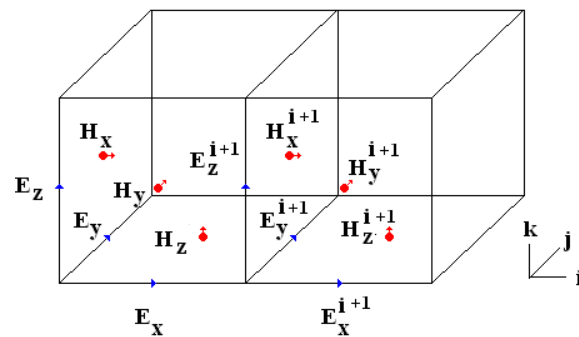


Figure 4.1.1.2: Original vectors and the vectors located one unit step to the right. If the unit cell was one above (in the k -direction) or behind (in the j -direction), then the k - and j -units would be indexed by one.

A partial derivative is the change in one variable with respect to another variable, or in the case of Equation 4.1.1.3,

$$\frac{dE_z}{dy} - \frac{dE_y}{dz} = -\mu \frac{dH_x}{dt} \dots 4.1.1.3$$

becomes Equation 4.1.1.9,

$$\frac{E_z^{j+1} - E_z}{\Delta y} - \frac{E_y^{k+1} - E_y}{\Delta z} = -\mu \frac{dH_x}{dt} \dots 4.1.1.9$$

which represents the change in the electric field divided by the change in the y-direction or z-direction (the previous definition of a derivative). The reason **j**+1 and **i**+1 are used is to center the difference at H_x (located on the right half of the equation), which one can see is between the **j** and **j**+1 values for E_z and also between the **i** and **i**+1 values for E_y . This process works the same for both electric and magnetic field components with respect to x, y or z. The right half of the equation, however, is in the time domain so a different method must be used to find the full difference equation.

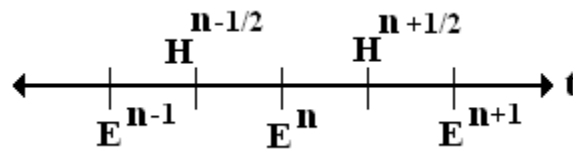


Figure 4.1.1.3: The electric and magnetic field vectors in time. The variable **n** represents the current time; therefore **n**+1 represents a future time step and **n**-1 represents a past time step.

The time domain can be represented as in Figure 4.1.1.3, where E^n is the current time (and also the time of the left half of the equation) and each value of

$\frac{1}{2}$ is a half of a discrete time step. To find the change in \mathbf{H} with respect to time, one can simply use the future magnetic field component (in time), $H^{n+1/2}$, subtract the past magnetic field component one time step away, $H^{n-1/2}$, and divide by the change in time, Δt , allowing Equation 4.1.1.9 to be represented as Equation 4.1.1.10,

$$\frac{E_z^{j+1}-E_z}{\Delta y} - \frac{E_y^{k+1}-E_y}{\Delta z} = -\mu \frac{H_x^{n+1/2}-H_x^{n-1/2}}{\Delta t} \dots 4.1.1.10$$

The partial derivatives of the electric fields can be treated in the same way. As for the E_x , E_y , and E_z components of Equations 4.1.1.6, 4.1.1.7, 4.1.1.8 respectively, one can simply add the present electric field, E^n , and the future electric field, E^{n+1} , and divide by two. Finally, the six partial differential equations become six difference Equations 4.1.1.11, 4.1.1.12, 4.1.1.13, 4.1.1.14, and 4.1.1.15;

$$\frac{E_y^{i+1}-E_y}{\Delta x} - \frac{E_x^{j+1}-E_x}{\Delta y} = -\mu \frac{H_z^{n+1/2}-H_z^{n-1/2}}{\Delta t} \dots 4.1.1.11$$

$$-\left(\frac{E_x^{k+1}-E_x}{\Delta z} - \frac{E_z^{i+1}-E_z}{\Delta x}\right) = -\mu \frac{H_y^{n+1/2}-H_y^{n-1/2}}{\Delta t} \dots 4.1.1.12$$

$$-\left(\frac{H_z-H_z^{i-1}}{\Delta x} - \frac{H_x-H_x^{k-1}}{\Delta z}\right) = \sigma \frac{E_y^n-E_y^{n+1}}{2} + \varepsilon \frac{E_y^{n+1}-E_y^n}{\Delta t} \dots 4.1.1.13$$

$$\frac{H_z-H_z^{j-1}}{\Delta y} - \frac{H_y-H_y^{k-1}}{\Delta z} = \sigma \frac{E_x^n-E_x^{n+1}}{2} + \varepsilon \frac{E_x^{n+1}-E_x^n}{\Delta t} \dots 4.1.1.14$$

$$\frac{H_y-H_y^{i-1}}{\Delta x} - \frac{H_x-H_x^{j-1}}{\Delta y} = \sigma \frac{E_z^n-E_z^{n+1}}{2} + \varepsilon \frac{E_z^{n+1}-E_z^n}{\Delta t} \dots 4.1.1.15$$

with the sixth equation being 4.1.1.10, where the left half of the equations are at the n time step of Figure 4.1.1.3. Using a computer algorithm, such as Lumerical or CST Microwave Studio transient solver, these equations can be used to solve the electric field and magnetic field components at the next time step, E^{n+1} or $H^{n+1/2}$. The process can then be repeated to solve at the next time step using the same equations. The resulting E and H values are used to describe the propagation of the electromagnetic wave through space and time. It is important to note that one needs only the initial E and H fields at each i , j , and k locations; the permittivity of the material, ϵ ; the permeability of the material, μ ; and the conductivity, σ . All of these values can differ from cell to cell; however, they all must be initially known.

4.1.2 Effective Permeability and Permittivity Calculator

A second form of numerical analysis was used to calculate the effective optical constants of a MM interface. This MATLAB program utilizes real and imaginary reflection and transmission data (usually simulated) in order to calculate the effective optical constants over a wide wavelength range. This calculator was created specifically for this research using published articles by Xudong Chen *et al* and Smith *et al*.^{[213][214]}

The first step in determining the effective optical constants of a metamaterial is to calculate the real and imaginary optical impedance. This feat is accomplished using a reflection coefficient, r , and transmission coefficient, t ,

where the system reflection is equal to r , and t is related to the system transmission, T , by Equation 4.1.2.1.^[213]

$$t = T e^{ikd} \dots 4.1.2.1$$

where k is the wavenumber of the incident wave in free space, and d is the metamaterial thickness. The impedance, Z , can be found using Equation 4.1.2.2.^[213]

$$Z = \pm \sqrt{\frac{(1+r)^2 - t^2}{(1-r)^2 - t^2}} \dots 4.1.2.2$$

This is where the first of many root errors may occur. In order to correct these errors, one must determine the correct sign for each wavelength. This can be accomplished using a few assumptions about the system. One such assumption is that the real part of Equation 4.1.2.2 will determine the sign of the imaginary part of the impedance. For example, all materials have a positive real impedance, therefore, $\text{Re}(Z)$ must always be greater than zero. However, if Equation 4.1.2.2 expresses a negative $\text{Re}(Z)$, the $\text{Im}(Z)$ must be less than zero. After this correction is made then the $\text{Re}(Z)$ must be made positive.^[213]

The next effective optical property of a metamaterial which can be calculated is the imaginary index of refraction, solved for using Equation 4.1.2.3^[214]

$$\text{Im}(n) = \pm \text{Im} \left(\frac{\cos^{-1} \left(\frac{1}{2t} [1 - r^2 + t^2] \right)}{kd} \right) \dots 4.1.2.3$$

Then the real part of the index of refraction can be also be found using Equation 4.1.2.4^[214]

$$Re(n) = \pm Re\left(\frac{\left(\frac{\cos^{-1}\left(\frac{1}{2t}[1-r^2+t^2]\right)}{kd}\right)}{kd}\right) + \frac{2m\pi}{kd} \dots 4.1.2.4$$

where m is a integer used to correct a branch error. The correct value of m can be found by using multiple small values MM thicknesses, d , and by observing that consistent values of n are obtained.^[214] Alternatively, the following constraints can also be used to determine the m value. Equations 4.1.2.5, 4.1.2.6, and 4.1.2.7, represent boundary conditions on the impedance, index of refraction, permittivity, and permeability.^[213] The lowest integer to satisfy these three equations is the generally accepted branch mode.^[213]

$$|Re(n)Im(Z)| \leq Im(n)Re(Z) \dots 4.1.2.5$$

$$Im(\mu) \geq 0 \dots 4.1.2.6$$

$$Im(\varepsilon) \geq 0 \dots 4.1.2.7$$

A second important note in relation to root errors is that the imaginary portion of the index of refraction, Equation 4.1.2.3, must always be positive. This creates a unique solution for the imaginary index of refraction; but, the real index of refraction can be positive or negative.^[213] Due to multiple possible signs in the $Re(n)$, discontinuities can clearly be seen when the permittivity and permeability are plotted. Correcting $Re(n)$ can be done manually by analyzing $Re(n)$ in order to make it continuous, or with an iterative Taylor series as shown by Chen *et al.*^[213]

The final step in calculating the permeability and permittivity can be done using Equation 4.1.2.8 and Equation 4.1.2.9.

$$\mu = nZ \quad \dots 4.1.2.8$$

$$\varepsilon = n/Z \quad \dots 4.1.2.9$$

These equations result in a complex permittivity and permeability, which can be used to optically characterize a metamaterial device. Also, it can clearly be seen that altering the permittivity and permeability of a material has a direct effect on both the index of refraction and the impedance of a surface. Using this information it becomes more clear that altering the conductivity of the metamaterial will have a direct effect on the permeability and permittivity of a surface, as discussed in Section 2.2.2.2. The code created to accomplish this calculation can be found in Appendix 4.1.

4.2 Processing Techniques

This section is designed to give a basic overview of different fabrication techniques ranging from wafer cleaning, to lithography, to metallization. While this section may contain information on how a device made using each tool or recipe, it is not meant to fully describe any particular fabrication process. The full procedures for each specific device can be found in Appendixes 5.1-5.4. This section is designed to introduce the tools of fabrication and provide examples for prospective.

4.2.1 Wafer preparation

There are many types of chemical processing used for many unique applications. However, in the scope of this work, the two main chemical

processing techniques are nitride etching and surface preparation, mainly consisting of oxide removal. For example, an Epi-ready wafer must first be cleaned to remove any surface material, ranging from air contaminates to oxide growth. Surface preparation procedures should be performed before any type of deposition; this includes metallization as well as oxide or nitride deposition. The goal is to provide the cleanest possible surface in order to achieve the best possible adhesion between two different materials. This section will describe the general procedure for performing a chemical clean, as well as the chemical cleans used for the silicon (Si), gallium arsenide (GaAs), and gallium antimonide (GaSb) substrates.

Regardless of the end device, wafer cleaning techniques are always performed at three specific process steps. These steps are: *before* metal deposition (after photolithography), *before* any chemical vapor deposition, and *before* spinning of electron beam photoresist. The chemicals needed for each clean are surface specific and are shown in Figure 4.2.1.1

Material	Chemicals	Time
Silicon	Sulfuric Acid (H ₂ SO ₄):Hydrogen Peroxide (H ₂ O ₂) [1:1]	5 min
GaAs	Hydrochloric Acid (HCl) : DI Water [1:1] Hydro Fluoric Acid (HF) : DI Water [1:9]	45 sec 30 sec
GaSb	Hydrochloric Acid (HCl) : DI Water [1:1]	75 sec
Si₃N₄	Hydrochloric Acid (HCl) : DI Water [1:1]	30 sec
Al₂O₃	Acetone Isopropyl Alcohol (IPA)	1 min under ultrasonication rinse

Figure 4.2.1.1: Substrate oxide chemical cleaning list.

The cleaning procedures in Figure 4.2.1.1 are all preceded by an acetone ultrasonication for 30 sec, IPA rinse, and DI water rinse. These solvents are used to remove any particles that may have settled on the sample before surface

cleaning. The chemicals in Figure 4.2.1.1 are then used to remove oxide growth while limiting chemical reactions with the surface and/or photoresist. The resulting surfaces have shown improved structural adhesion and electrical properties.

There is a large field of research dedicated to chemically etching the semiconductors and dielectrics used in this research. However, for the most part these wet etches were avoided due to their highly isotropic nature. The exception is the use of HF:DI water [1:9] to etch silicon nitride (Si_3N_4) on GaAs. For this application an isotropic etch was not necessary and a wet etch was used to increase fabrication simplicity.

4.2.2 Photolithography

All devices fabricated in this research require some form of nanostructures. The standard procedure used to fabricate these structures is known as photolithography, which uses light to pattern a polymer material. The resulting patterned polymer allows location-sensitive material etches and material depositions. Photolithography is one of the most common fabrication techniques in this work and is used approximately five times to fabricate a monolithically interconnected modules (MIMs) structured photodiode, four times to fabricate a standard photodiode, and three times for an active metamaterial polarizer. This section discusses the use of negative photoresist polymers in which areas exposed to optical energy are able to be chemically dissolved. Positive-type photoresist were not used in this work and as such are not discussed.

The first step in photolithography is known as resist spinning. The sample is first placed on a rotating vacuum chuck, and the photoresist polymer is spun onto the samples using a four step spin processes. The rotation speed is ramped to 500 rpm in less than 4 seconds. This speed is then maintained for 10 second in order to spread the photoresist. The next steps vary based on the type of photoresist, sample type, and desired photoresist thickness; however, there is always a ramp to the final spin speed, and 45 seconds with a spin speed of 3000 rpm to 5000 rpm. Depending on the type of resist a pre-exposure bake maybe required prior to photoresist exposure.

The next step is known as exposure. In order to expose the photopolymer, one must use a mask aligner. Two typical mask aligners used in this work are the OAI Model 204IR Mask Aligner (shown on right of Figure 4.2.2.1) and Suss MJB4 Mask Aligner. A mask aligner operates by exposing the sensitive polymer (photoresist) to a mercury lamp light source.^{[215][216]} The lamp is tuned to the mercury I-line, which corresponds to a wavelength of 365 nm, and operates at an intensity between 20 mW/cm² and 35 mW/cm². It should be noted that exposure time is directly related to lamp intensity, and the exact intensity is tool specific; for example, the OAI Model 204IR, operates at 20 mW/cm² (the I-line). Most exposure times, are based both on the photoresist used and atmospheric conditions such as temperature and humidity. However, the type of photoresist used is application specific and based on the presence of any nanostructured trenches, thickness of future deposition layers, or future etch depths. The variable range in both photoresist type and thickness creates the need for different exposure times

between different processes. This means that the optimal exposure times for a given mask process often must be empirically determined.

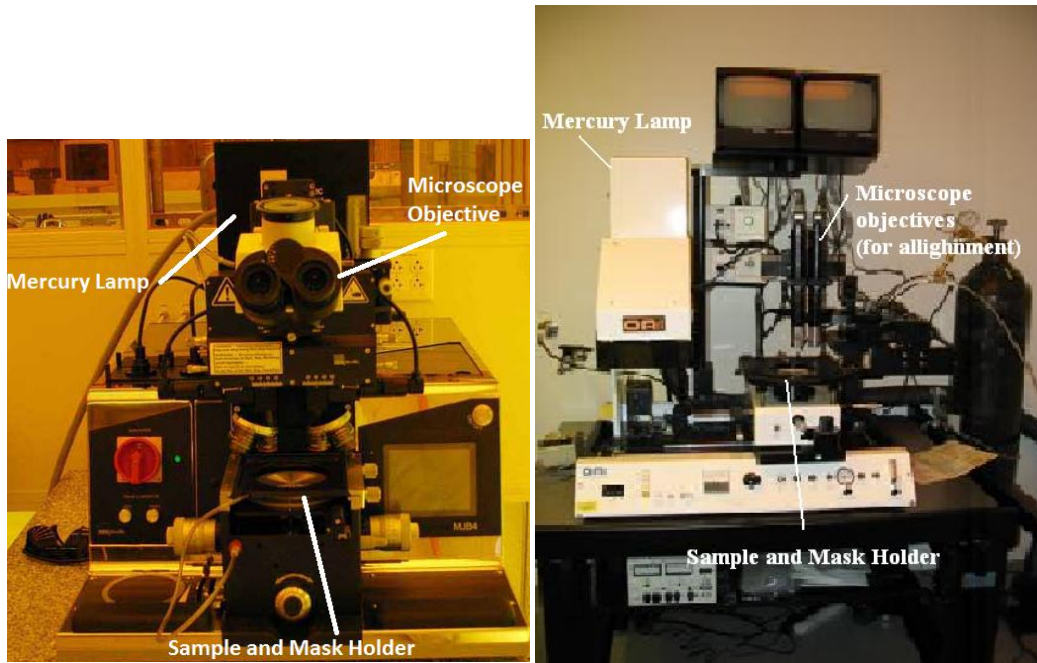


Figure 4.2.2.1: *Left:* A Suss MJB4 Mask Aligner. *Right:* The OAI Model 204IR Mask Aligner. Shown are the microscope objectives and monitors for mask alignment. Also, the mercury lamp and sample/mask holder are shown. ^{[215][216]}

During exposure, a soda lime glass mask coated with a thin layer of patterned chrome is used to block light from interacting with specific areas of the photoresist (shown on left of Figure 4.2.2.2). Photoresist which is covered by the chrome is protected from the high energy photons of the mask aligner, and no chemical reaction occurs in the photoresist. However, the areas that are exposed to the mercury lamp are chemically altered, and can be dissolved in a specific development agent. Using this process, photoresist allows for reliable, repeatable, and highly accurate patterning of small features (from mm scale to $2\mu\text{m}$).

The correct use of a mask aligner is the key to achieving good results using photolithography. When using a mask aligner, the sample is placed within a

sample holder and brought into soft contact with the chrome mask. Soft contact is used to eliminate any air wedges between the wafer and the mask, increasing feature resolution. A ball joint, below the sample, is then locked to keep the sample in position. Soft contact can then be broken in order to align structural features on the sample to the chrome mask. In order to align, the sample can be moved in the x-, y-, and theta-directions using fine control adjustment knobs.

Due to the fragile nature of most of the substrates used, features such as hard contact, vacuum contact, and backside N₂ pressure are not used. However, for completeness, the next step would involve initiating hard contact, vacuum contact, and/or N₂ pressure. Hard contact forces the mask and the sample into contact to eliminate any residual air wedge and improve the exposure resolution, vacuum contact applies a vacuum between the sample and mask further increasing resolution, and N₂ pressure applies an upward force of nitrogen gas behind the sample. The mask and sample are then exposed to the mercury lamp for a predetermined amount of time.

After exposure, the photoresist is placed in a developer to chemically remove photoresist exposed to the mercury lamp. Each photoresist requires a different developing agent. Also, the thickness of the photoresist along with the surface area exposed effects the develop time. However in all cases the chemical reaction of the developer/photoresist must be quenched with DI Water. Figure 4.2.2.2 shows a patterned negative resist ring on a Si substrate and Figure 4.2.2.3 contains general processing notes for all photoresists utilized in this body of work.

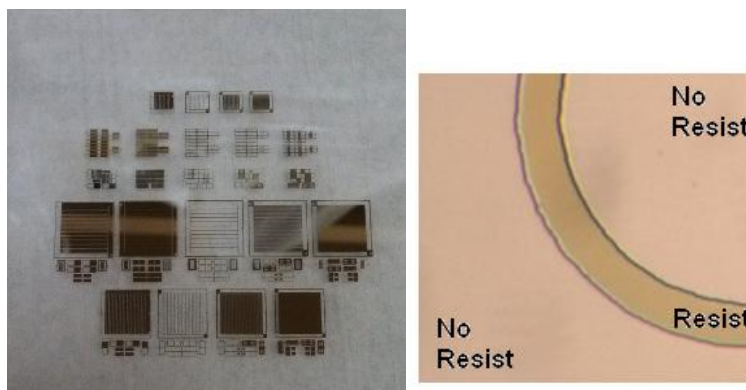


Figure 4.2.2.2: *Left:* example of a photolithography mask chromium is represented as black. *Right:* Positive photoresist (circle) after exposure and development.

Photoresist	Spinning Speed/ Time	Pre-exposure bake time/ temp.	Exposure Dose/ Time	Development Time	Ending thickness
S1813	4000 rpm/ 30 sec	75 sec/ 115 C	20mW/cm ² / 4.5 sec	25 sec	1.6 μm
AZ9245	3500 rpm/ 45 sec	120 sec/ 115 C	22 mW/cm ² / 40 sec	5 min 15 sec	4.8 μm
S1822	3000 rpm/ 45 sec	75 sec/ 115 C	24 mW/cm ² / 8 sec	55 sec	2.7 μm

Figure 4.2.2.2: General processing notes for all photoresists use. Note that all development times are using MF-CD 26 developer

After development is complete, metal deposition can occur using a sputter tool or thermal evaporator, or the substrate can be chemically or physically etched. If the substrate is to be etched, the resist must be thick enough to not be etched away in the process. After etching, a brief sonication in acetone is sufficient to remove the residual photoresist. For metallization, the general rule of thumb for resist thickness is 1:3 [metal:photoresist] . After metallization, the sample must undergo a process known as lift-off, described below.

During metallization, most lithographic features are completely surrounded by deposited material. By increasing the resist thickness, the deposited material becomes thinner at the barrier (shown in Figure 4.2.2.4). The

thinner the deposited barrier material becomes, the easier it becomes to remove the photoresist.

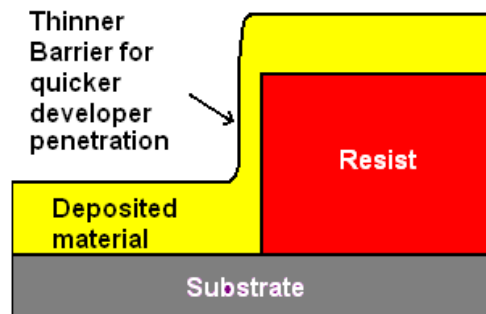


Figure 4.2.2.4: A thicker resist allows easier penetration of the lift-off agent.

Lift-off is the process of removing the photoresist underneath a deposited substance using a chemical known as a remover. There are numerous removers with different compositions, however, acetone is sufficient to create lift-off when using the photoresist shown in Figure 4.2.2.3. In all cases, the remover penetrates the thin metal region at the edge of photoresist patterns. The remover then dissolves the photoresist under the deposited material. The metal, previously attached to photoresist, separates from the wafer leaving behind a patterned wafer, shown in Figure 4.2.2.5.



Figure 4.2.2.5: Metallization patterned using photolithography. Light pattern is gold, darker pattern is the GaSb semiconductor substrate after removal of photoresist.

4.2.3 Electron Beam Lithography

Electron beam lithography (EBL) is a useful tool in semiconductor nanofabrication. This process is very similar in purpose to that of photolithography. The largest differences are processing time and feature sizes. EBL is a serial process and can take from hours to days to create a pattern; where standard photolithography is a parallel process and can be completed in under half an-hour. However, EBL can create feature sizes much smaller than standard photolithography (on the order of 10s of nm). It is for this reason that EBL was used to fabricate MM emitters, PhCs, and MM polarization grids.

EBL follows the same processing pattern as standard photolithography: spinning of resist, exposing of pattern, development, and lift-off. However, where photoresist is composed of a photosensitive polymer, electron beam resist is typically a plastic known as polymethyl methacrylate (PMMA). As in photoresist, PMMA can be spun at any speed; however, for MM polarization grids, PMMA-C6 series e-beam resist was used at a spin speed of 2500 rpm, and

for MM emitters, PMMA-C2 series e-beam resist was used at a spin speed of 4000 rpm. Both resist were used with a 5min pre-exposure bake at 180 °C . The resulting PMMA thicknesses were approximately 650 nm and 180nm respectively.

In order to pattern e-beam resist, the sample is placed inside of a scanning electron microscope (SEM). More information on the SEM is located in Section 4.3.1. The high energy electron beam then scans along the surface of the PMMA exposing (breaking the molecular bonds of the PMMA) any pattern loaded into the SEM control software. As such, the feature size is limited only by the ability to focus the e-beam of the SEM. In this work, we limit our smallest features to approximately 100 nm; however, features can typically reach 10s of nanometers.

As with photolithography, exposure dose ($\frac{\mu A \cdot sec}{cm^2}$) has a very large effect on pattern quality. The dosing value can change greatly with resist thickness and feature sizes, for example, PhC patterns required an exposure dose of 465 $\mu As/cm^2$, MM polarization grids require 440 $\mu As/cm^2$, and the MM emitter requires 475 $\mu As/cm^2$. The effects of a wrong exposure are quite noticeable; too large an exposure dose will cause shapes to expand and lose their sharp edges, but too low a dose will create only partial patterns, or no pattern. However, the limiting factor in e-beam lithography is a prohibitively long writing time. As such, the largest patterns generated in this work are all less than 1mm². The Raith 150 electron beam lithography system used in this work is shown in Figure 4.2.3.1.



Figure 4.2.3.1: Raith 150 electron beam lithography system. The system includes software controlled pattern generator, field effect scanning electron microscope, and 20 keV electron source.^[217]

After the pattern is exposed within the SEM, the sample must be developed. PMMA-C series e-beam resist is developed in methyl-isobutyl ketone (MIBK) : IPA [3:1] for one min. This is immediately followed by a 30 sec bath of IPA and N₂ gas drying. The roll of the MIBK is to break the molecular bonds damaged by the electron beam, and the IPA dissolves the damaged polymer. The result is a small well defined pattern ready to be used in a physical vapor deposition system for metal deposition. The developed electron beam resist is easily dissolved in acetone; as such lift-off can be done in an acetone bath, resulting in a nanosized metallic pattern.

4.2.4 Electron-Beam Thermal Evaporation

For all photonic applications used in this research, some form of metallization is necessary. This research utilizes metal ohmic contacts (defined later in this section) to photodiodes, metallic photonic crystals, Schottky barrier

diodes (defined in Section 2.2.2), and metallic split ring resonators for polarization and emitter technologies. In order to produce these devices, a very uniform and low contamination metallic film must be created. This task was accomplished using electron-beam thermal evaporation.

Electron-beam thermal evaporation is a subset of deposition techniques known as physical vapor deposition (PVD). PVD consists of two distinct deposition subsets: thermal evaporation and sputtering. Sputter deposition utilizes a high energy plasma in order to bombard a material with ions. Under ion bombardment, the material ejects atoms onto the intended growth surface. Sputtering systems tend to have much higher deposition rates and lower anisotropy than thermal evaporation process. As such, thermal evaporation was the primary metal deposition method used in this work.

In a thermal evaporation process, the deposition rate can easily be controlled by reducing or increasing the temperature of the metal, thereby altering the rate of evaporation. It should also be noted that thermal evaporation techniques are line of sight deposition techniques, so a curved sample will result in uneven film thicknesses and shading. However, line of sight deposition will result in easier lift-off if photoresist patterning is used as lithographic sidewalls will not be coated with metal. This allows a solvent, such as acetone, to dissolve the lithographic polymers with much greater ease.

PVD is generally performed under vacuum conditions. For example, typical base pressures within the deposition chamber of an E-beam thermal evaporation system are on the order of 1×10^{-7} torr. It is important to note that the

base pressure of a system has a direct deterministic effect on material purity. For example, a system at 8×10^{-8} torr allows the aggregation of approximately 0.03 monolayers per second of contamination. A large contamination rate requires one to use a deposition rate significantly faster than the contamination rate in order to maintain high film quality. Also, pauses in deposition can cause adhesion or barrier issues within material layers. It is for these reasons that the low base pressure of a thermal E-beam evaporator is used and not other higher pressure PVD units, such as traditional thermal evaporators.

Electron-beam thermal evaporation implements a high-energy beam of electrons to heat a metal slug in order to produce a steady rate of gaseous metal evaporate. The plum of metal then projects into the vacuum chamber with the standard cosine-square law distribution, where they come into contact with both the chamber sidewalls and the sample. Deposition occurs at a very slow (0.1-0.2 nm/sec) rate in order to maintain very uniform film qualities. The exact deposition rate is determined by the temperature of the metal slug, which is controlled by the electron beam current. E-beam thermal evaporation does not damage the sample through ion impacts or high-energy material impacts as in other PVD techniques, which further improves film quality. However, the sample may experience heating due to the incident high-temperature evaporate. As such, only temperature insensitive devices should be used in an E-beam thermal evaporator.

The electron beam can be produced in many ways, but in all cases, the electrons are accelerated and focused onto the metallic slug using an applied

voltage. As stated above, the temperature of the metal is directly related to the current created in the electron beam. Therefore, altering the electron beam current alters the deposition rate. A common setup for an E-beam deposition system includes a target, located at the bottom of the vacuum chamber, and the sample suspended from the top of the chamber. The Denton E-beam thermal evaporator used in this work is shown in Figure 4.2.4.1



Figure 4.2.4.1: Denton E-beam evaporator. The sample chamber, target chamber, and connector are indicated. ^[218]

The E-beam thermal evaporator was used to deposit three different types of metallic films; these were ohmic contacts, Schottky barriers, and thin films for MM applications. An ohmic contact is a direct electrical contact to a semiconductor in which electrons can travel into the semiconductor (and back out) with extremely little resistance. Ohmic contacts were used for photodiode

applications as well as for a ground contact of the dynamic MM polarizer. A Schottky barrier was used to form a Schottky barrier diode within the MM dynamic polarizer, the physics of which were discussed previously in Section 2.2.2. The electrical properties of these two contact types are shown in Figure 4.3.4.2. Finally, non-electrical metallic thin films were used in MM emitter applications. Figure 4.2.4.3 summarizes the metals, type of film, and thicknesses used for each application.

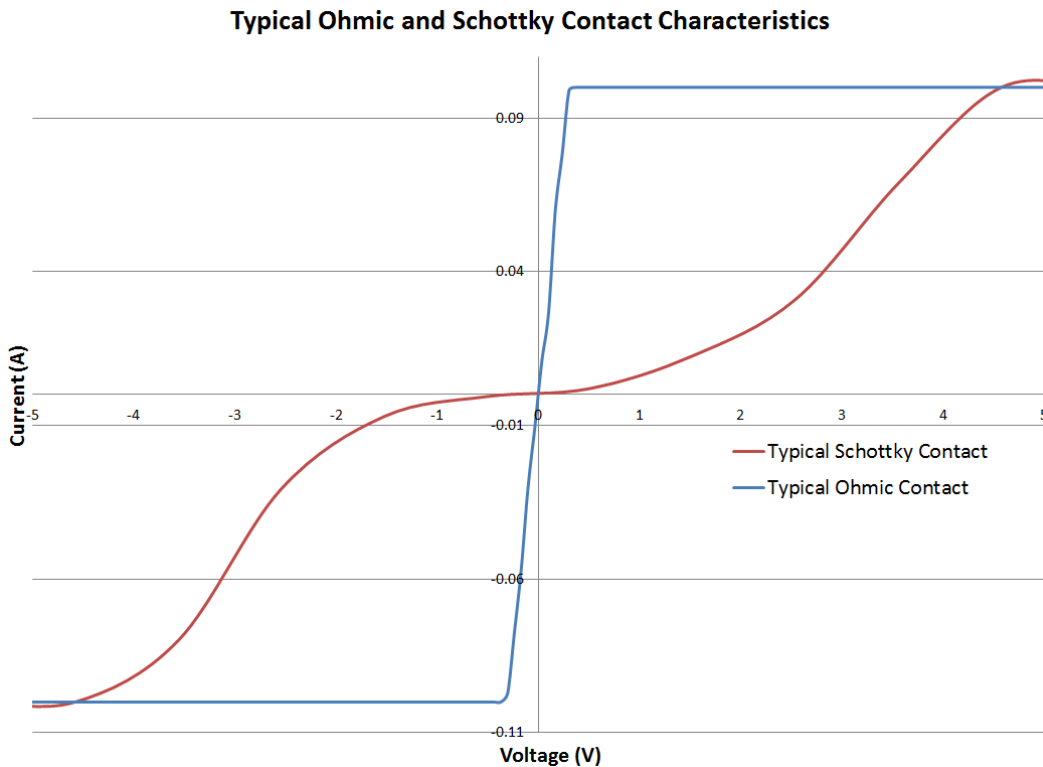


Figure 4.3.4.2: Typical Schottky and ohmic contact characteristics. Schottky contacts prevent current flow due to a conduction band barrier, as an external bias is applied, this barrier shrinks, allowing greater current flow as well as a non-linear response. Ohmic contacts are designed to have very little barrier between the semiconductor and metallization, the result is high current flow and little electrical resistance.

Structure or Material	Materials	Thickness	Film Type
Silicon n-type/p-type	Cr / Au	12nm / 150nm	Ohmic Contact
Silicon p-type	Al / Au	100nm / 50nm	Schottky Barrier
GaSb n-type / p-type	Ti / Pt / Au	50nm / 50nm / 200nm	Ohmic Contact
GaAs n-type	Ge / Au / Ni / Au	26nm / 54nm / 14nm / 100nm	Ohmic Contact
GaAs n-type	Ti / Au	6nm / 84nm	Schottky Barrier
PhC	Ti / Au	50nm / 400nm	N-type GaSb ohmic contact
MM emitter	Pt Pt	100nm 35nm	Base Absorber Film MM Pattern
MM polarizer	Ti / Au	12 / 140nm	High voltage contact pad

Figure 4.2.4.3: E-Beam thermal evaporator metallization recipes used.

4.2.4 Chemical Vapor Deposition

Chemical vapor deposition (CVD) is the process of depositing a material, usually, a dielectric. This research utilizes CVD technology to deposit two materials, Al_2O_3 for MM perfect emitters, and Si_2N_3 for photodiode surface passivation. In particular, two different types of CVD devices were used, atomic layer deposition (ALD) for Al_2O_3 , and plasma-enhanced chemical vapor deposition (PECVD) for Si_3N_4 . It is the aim of this section to describe both of these tools and how the materials deposited are used within the aims of this work. As an important aside, CVD units combine high temperatures and very uniform coatings. This information implies that patterned photoresist should never be used inside of a CVD, the photoresist pattern will lose integrity and the uniformly deposited dielectric will prevent lift-off from occurring.

ALD is particularly useful at depositing very thin dielectric films (less than 100 nm) very accurately. This precision was required for the MM emitter

applications, where dielectric (Al_2O_3) layers of exact thicknesses, 10-20nm, had to be fabricated. However, thick films are simply not practical to grow in ALD as the deposition process occurs one atomic monolayer at a time.

The ALD growth process utilizes a vacuum chamber which is filled with a precursor gas in the form of a quick pulse. In the case of Al_2O_3 this gas is trimethylaluminum, $\text{Al}(\text{CH}_3)_3$. The precursor gas forms a one monolayer thick film on the surface of the sample. The ALD chamber is then purged of excess gas. A second precursor gas is then introduced to the chamber in the form of a second pulse. For Al_2O_3 , the second precursor gas is H_2O . The second precursor gas reacts with the one monolayer film forming a single molecular layer of the desired film, in our example this is Al_2O_3 . In order to finish the cycle, the chamber is once again purged of the secondary precursor gas, and the first precursor gas is once again pulsed. The process is known as a “pulse-purge” cycle, and each pulse is separated by large purge time. Typical growth rates for ALD tend to be between 0.3-0.6 nm/min.

PECVD operates in a similar manner to ALD; however, with some fundamental differences. As opposed to ALD, both precursor gases are always in the growth chamber during PECVD growth. As the name implies, an AC plasma, usually between 10 and 600 W, is also present in PECVD growth chambers. To describe the general operation of the tool, the growth method of Si_3N_4 , used for TPV surface passivation, will be described. As with ALD, the first precursor gas silane (SiH_4), bonds to the surface of the sample. Ions from the plasma are used to dissociate the hydrogen, leaving a film of silicon. The second precursor gas, a

mixture of ammonia (NH₃ - 1%) and Nitrogen (N₂ - 99%), can then bond to silicon film resulting in a thin film of Si₃N₄. The PECVD growth process is much faster than ALD, because it lacks the pump-purge cycle. The growth reaction is continuous resulting in a growth of Si₃N₂ between 10nm/min and 45nm/min depending on the plasma's frequency and power.

There is, however, a trade-off to using PECVD over ALD. PECVD lacks ALD's precise control over material thickness. Also, with ALD, the precise material composition is always known. For example, PECVD growth of Si₃N₄ produces a hydrogenated form of the dielectric. Hydrogen atoms that are not completely dissociated from the silicon become trapped under new growth. The result is not a pure Si₃N₄ film. However, as mentioned before, thicker films, even on order of only 100s of nm, cannot be realistically grown on an ALD system. PECVD can provide thicker and very uniform films in a relatively short timeframe, making this process ideal for large scale and throughput processing.

CVD is a very useful tool in semiconductor and metamaterial fabrication. As mentioned previously, ALD growth was used for MM emitters to provide exact control over dielectric film thickness (Al₂O₃), and PECVD was used for sidewall and surface passivation of photodiodes (Si₃N₄). Although the general processes are alluded to above, Figure 4.2.4.1 summarizes the process parameters.

Material	Method	1 st Precursor	2 nd Precursor	Process Pressure	Process Temperature	Plasma Power/Type	Growth Rate
Si ₃ N ₄	PECVD	SiH ₄ 40sccm	N ₂ 1960sccm NH ₃ 55sccm	900 mT	300C-plasma 250C- samp.	20W / N ₂	10 nm/min
Al ₂ O ₃	ALD	Al(CH ₃) ₃	H ₂ O	~1Torr pulses	250C - Chamber	--	0.55 nm/min

Figure 4.2.4.1: Process parameters summarized for CVD applications.

4.2.5 Reactive Ion Etching

While the previous section focused on the tools used for depositing material, the precise removal of material is also a necessary. The semiconductor mesa etch is one common microfabrication technique needed to produce a photodiode. There are generally two possible avenues to obtain the mesa, a wet etch or dry plasma etch. This work utilizes the plasma etch as it tends to be more anisotropic and, therefore, provides near vertical sidewall profiles. The difficulty of a plasma etch is that it tends to etch all materials within the chamber. Therefore, thick layers of photoresist are required, and material selective etches are not always possible. To mitigate this effect, reactive ion etching (RIE) is often used. This work utilized RIE to etch two materials, Si_3N_4 and GaSb.

RIE operates by introducing a reactive chemical to the etching plasma. This chemical is chosen as it strongly reacts with the material to be etched, and weakly with the photoresist. When the reactive chemical bonds with the exposed layer, it lowers the bond strength of the atoms within the substrate. Low energy ions from the plasma then impart energy to this new bond, breaking away material, and are then purged from the chamber. In the RIE etch processes used by this work; the plasma gas is also the reactive gases. The RIE process is depicted in Figure 4.2.5.1.

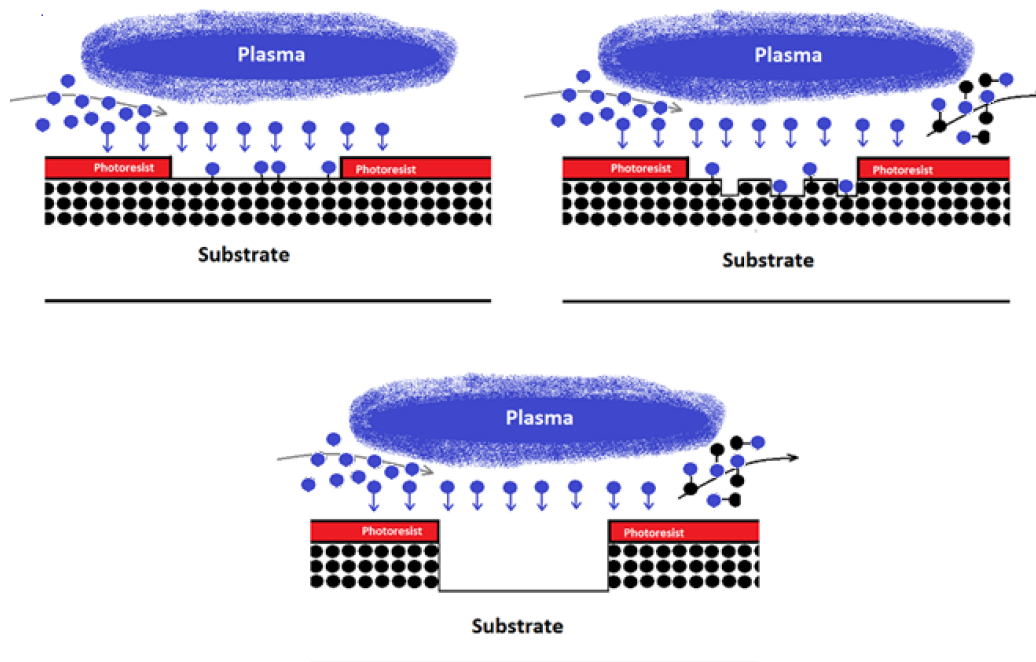


Figure 4.2.5.1: Reactive ion etching. *Top Left:* Reactive gases are introduced to the chamber and a plasma is created using these gases. The gases then react with the surface of the sample. *Top Right:* The plasma imparts enough energy to the reacted chemicals to allow the reactive chemicals to bond to the substrate and then are released as gas molecules to be removed from the chamber. *Bottom:* the process is continued until the desired etch depth is reached. The resulting trench is very anisotropic due to an applied voltage between the substrate and plasma.

The operation of an RIE remains the same regardless of etched material; however, the reactive ions and plasma type often change. There is an additional type of RIE that is often useful in nanofabrication. This process is not an etch, but known as a photolithography descumb. In general, the descumb is used to remove organic polymers utilizing an oxygen plasma. The oxygen plasma clean can remove exposed resist (not removed during the development process) by exposing the sample to a short, low powered oxygen plasma. This plasma clean has the advantage of not damaging or etching a substrate, but removes organic

contaminates from the substrate surface. Figure 4.2.5.2 summarizes the reactive gases and plasma characteristics for the two etch types used in this work.

Material Etched	Plasma Type	Reactive Gas (also plasma type)	Plasma Power	Etch Rate
GaSb	ICP	Cl – 5sccm BCl ₃ – 15sccm Ar – 7.5sccm N ₂ – 3.8sccm	500 W (100W bias power)	~15 nm/sec
Si ₃ N ₄	CCP	SF ₆ - 12sccm O ₂ - 6sccm	150 W	~110nm/min
Organic polymers	DC	O ₂ – 10sccm	100 W	45 sec. timed etch

Figure 4.2.5.2: Etch parameters used during device fabrication.

4.3 Testing Techniques

This section is dedicated to the various pieces of equipment used to image and test the devices created using the fabrication tools of Section 4.2. The testing devices range from electron microscopy, to optical characterization, to electrical characteristics. The goal of this section is to build various methods for which multiple devices can be characterized and evaluated in order to provide a path for optimization.

4.3.1 Scanning Electron Microscope

Scanning electron microscopes are useful for imaging nanosized features. SEM images are needed to analyze the structural information of MMs in the near- and mid-IR. SEMs can resolve features sizes below 10 nm. Accordingly, we employed SEM to image MM emitters and MM polarization grids, as well as for material quality analysis of fabricated photodiodes.

A SEM is a focused electron source located within a vacuum. The device operates by bombarding the surface of a sample with a narrow beam of high-energy electrons. The electrons penetrate into the surface of the sample and excite other electrons within the sample. These newly excited *secondary electrons* then have enough energy to break free of the semiconductor where they are collected by a detector. A depiction of the process is shown in Figure 4.3.1.1.

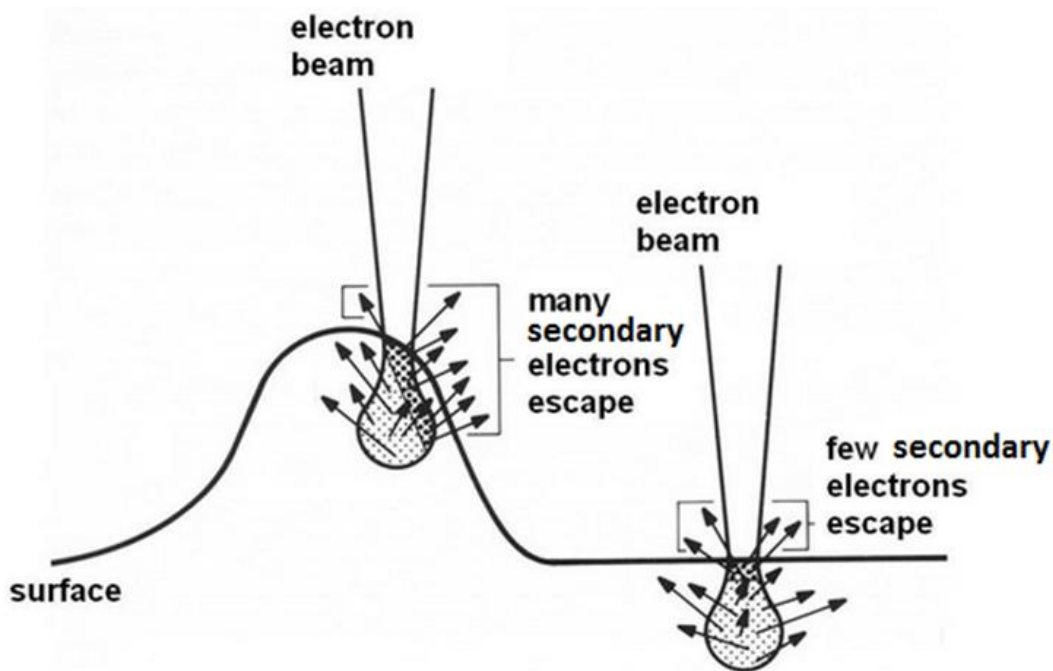


Figure 4.3.1.1: The process from which features are resolved using an SEM backscatter detector. There are many more secondary electrons produced at surface features resulting in more electron flux on the detector. Thus an image is produced. ^[219]

Once the secondary electrons are free of the material surface, they are collected using two types of detectors, a secondary electron detector (SE2) or an inlens detector. Each detector has its own benefits and drawbacks: the inlens detector, for example, is physically located isotropically around the electron beam. Because of the location, the inlens detector is able to easily determine

changes in material composition due to different work functions. Conversely, the SE2 detector is not as useful for determining material quality; however, the SE2 detector can image topographic features much more clearly. It is also possible to take advantage of both detectors by mixing the signal from the SE2 and inlens detectors. Figure 4.3.1.2 shows the same features using the inlens and SE2 detectors.



Figure 4.3.1.2: *Left:* inlens detector used to image a GaSb aperture surrounded by Au. *Right:* SE2 detector used to image the same aperture.

Within an SEM, the electron beam itself is controlled in order to acquire a clear image. There are four primary controls: magnitude, focus, aperture align, and stigmation.^{[219] [220]} The magnitude and focus options adjust the scan range, electron beam size, and focus point in order to achieve a clear image of the correct size. The aperture align alters the location of the “virtual” aperture within the electron beam column. If the virtual aperture is out of alignment, altering the focus will also move the image location. The stigmator corrects for demagnification of the condenser lens (usually the result of particle contamination). When the stigmator is out of alignment there are astigmatism effects when the image is not in correct focus, and when in focus, the image is not as clear. Figure 4.3.1.3 displays the relative locations of each of the pieces of the SEM.^{[219][220]}

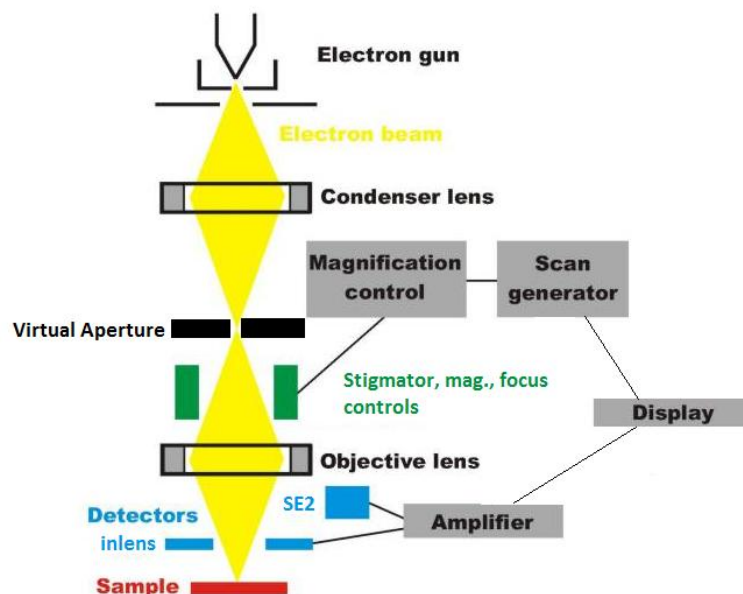


Figure 4.3.1.3: Diagram of an SEM with both inlens and SE2 detectors, stigmator and focusing controls, lenses, apertures, and controls software.^[220]

4.3.2 Fourier Transform Infrared Spectroscopy

The most common way to experimentally investigate an IR MM is through a device known as a Fourier transform infrared spectrometer or FTIR. The FTIR is especially useful when analyzing the absorption, transmission, and reflection of IR MM emitters device and dynamic MM polarizes. To this end, two types of FTIRs were implemented, shown in Figure 4.3.2.1. The first utilizes a transmission stage, the second, a microscope objective to record absorption. However, the inner workings of both devices remain identical.



Figure 4.3.2.1: Two types of FTIRs. *Left:* Jasco Microscope reflection FTIR using a cassegrain lens allowing for reflection measurements averaged at angles from 25 degrees to 45 degrees.^[221] *Right:* Thermoscientific FTIR allowing for normal incident transmission measurements and near normal reflection measurements (10 degrees).^[222]

A FTIR operates by pulsing a wide spectral band of infrared radiation into a sample, and then recording the transmission or reflection. In order to achieve spectral resolution, two separate things must happen. First, multiple pulses must be measured, each with a slightly different spectrum. Second, the measured pulses must be compared to a background scan with no sample present. The result is a reflection or transmission characteristics of a sample corrected for atmospheric effects such as water vapor absorption.

The key component to the FTIR is the ability to alter a broad band source to create a wavelength spectral resolution. In order to do this, each FTIR contains a Michelson Interferometer. The Michelson interferometer, shown in Figure 4.3.2.1, consists of an optical source, a beam splitter, one stationary mirror,

and one moving mirror. The condition for destructive interference for the Michelson interferometer is governed by Equation 4.3.2.1,

$$n\lambda = 2d,$$

where λ is the wavelength of light, n is the mode, and d is the distance the mirror is from the home position. Because of Equation 4.3.2.2, at any mirror location d , every wavelength of light has an altered spectrum due to constructive or destructive interference.

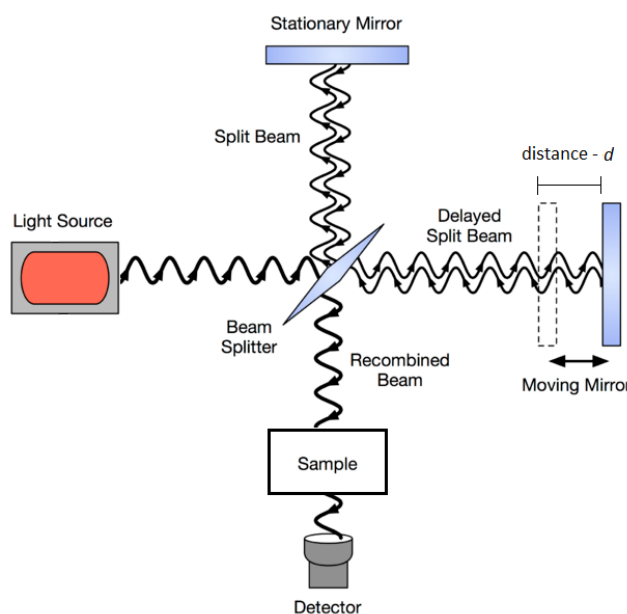


Figure 4.3.2.2: The Michelson interferometer of an FTIR. The interference pattern formed due to the light source and moving mirror allows for wavelength resolution through frequency domain measurements.

By using the Michelson interferometer it is possible to create a plot of optical intensity based on mirror location as well as the rate of change of mirror location (a function of time). However, this data is generally desired to be in frequency or wavelength form and not as a function of time. To accomplish this task, the data points based on mirror velocity can undergo a Fourier transform,

resulting in a plot of optical intensity for each frequency. This data is then compared to a background scan in order to determine the optical percent transmission or percent reflection through the only the sample.

4.3.3 Solar Simulation I-V Characterization

As mentioned in Section 2.1.5 many of the important characterization mechanisms of photodiodes are obtained through I-V curves. A solar simulator presents the unique opportunity to obtain consistent results over multiple trials to compare relative photodiode efficiencies. In order to obtain this data, a Newport Corporation 1600 W (10 sun) solar simulator is used in conjunction with an Oriel source meter, shown in Figure 4.3.3.1.

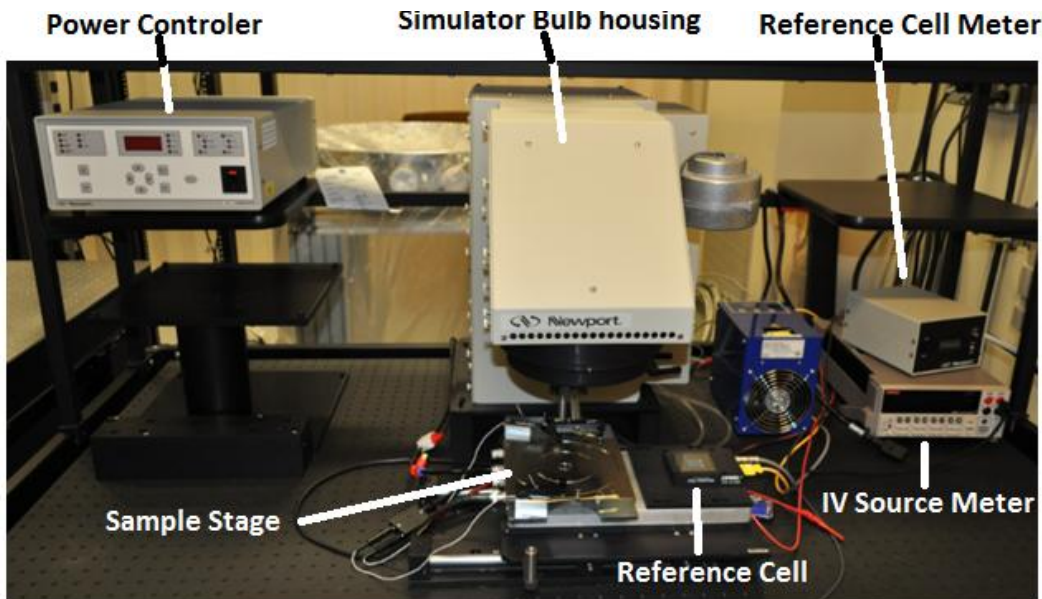


Figure 4.3.3.1: Solar simulator capable of optical intensities from 1-10 suns calibrated using a reference cell. The I-V measurement is then obtained using the source meter.

The Newport 1600 W solar simulator has an optical spectrum corresponding to 10 suns at AM1.5. In order to operate at 1 sun, an optically flat 10% ND filter can be implemented directly above the sample. Before testing occurs, the spectrum intensity is measured with an Oriel reference cell assure continuity between sample tests.

Measurements are taken by exposing a sample to either a specific optical illumination and applying a range of voltages to the sample. The Oriel source meter scans a pre-determined range of applied voltages, recording the current resulting from each applied voltage. All outputs are then plotted graphically in LabView.

The solar simulator is equipped with a probe station and is useful for both obtaining dark and light I-V curves as well as general I-V curves for testing metallization contacts. The probe station is shown in Figure 4.3.3.2. Using the same LabView software as the solar simulator, it is possible to plot I-V curves for ohmic contacts as well as Schottky contacts, the results of which can be seen in Section 5.3.

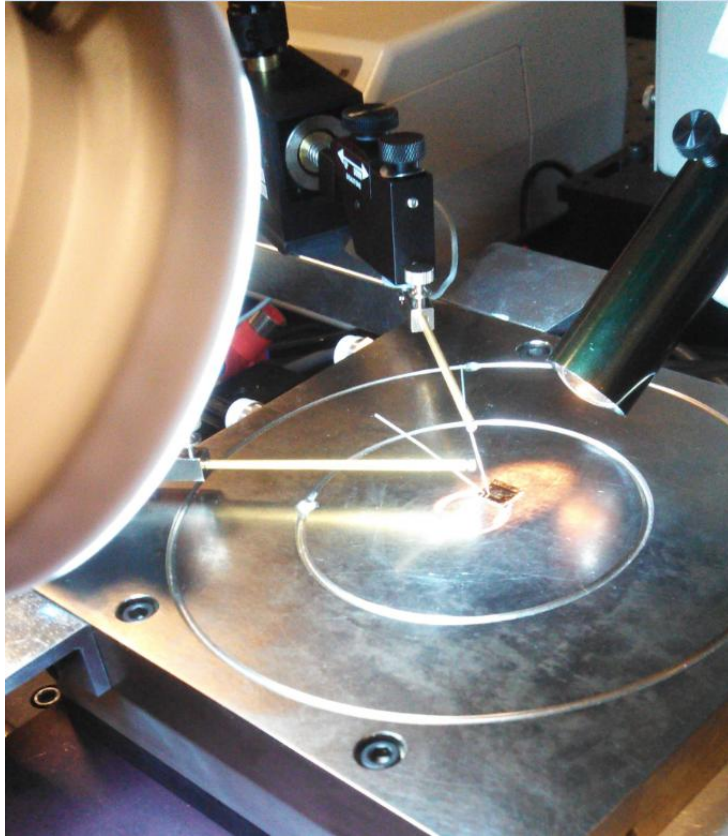


Figure 4.3.3.2: The sample stage of the solar simulator where a PV or TPV diode can be connected to the source meter using micro-manipulators.

4.3.4 Photoluminescence

There are many metrics to characterize the material properties of a semiconductor. One of these ways is through photoluminescence (PL). Photoluminescence allows one to obtain specific information on relative crystal quality, bandgap energy, and defect mapping. PL can also be important in determining relative photodiode performance; in particular, it is used to determine the quality of the interfacial misfit array photodiodes. Perhaps the largest benefit of PL over characterization techniques is the ability to characterize materials without the need for metallization (as in electroluminescence).

Photoluminescence uses light of a specific known energy, greater than the sample's band gap, to excite electrons within a sample into the conduction band. The electron/hole pair then recombines, emitting photons in process. These photons correspond to the energy of the sample's bandgap.

The primary PL setup, shown in Figure 4.3.4.1, uses a HeNe laser (632.8 nm) guided through a neutral density (ND) filter to limit the power incident on the sample. The beam can then be guided through a beam splitter in order to measure the incident intensity on the sample. In order to remove background noise from the PL response, a chopper is integrated with a LabView controlled lock-in amplifier. Using this design, only a signal frequency matched to the chopper is recorded by the software analysis package. Of particular note is the sample mapping stage, which can be used to plot PL intensity over a sample, effectively plotting defect areas. Other parts of the PL setup include a monochromator to control the wavelength of light incident on the detector, two lenses focused on the sample, and one lens focused on the monochromator.

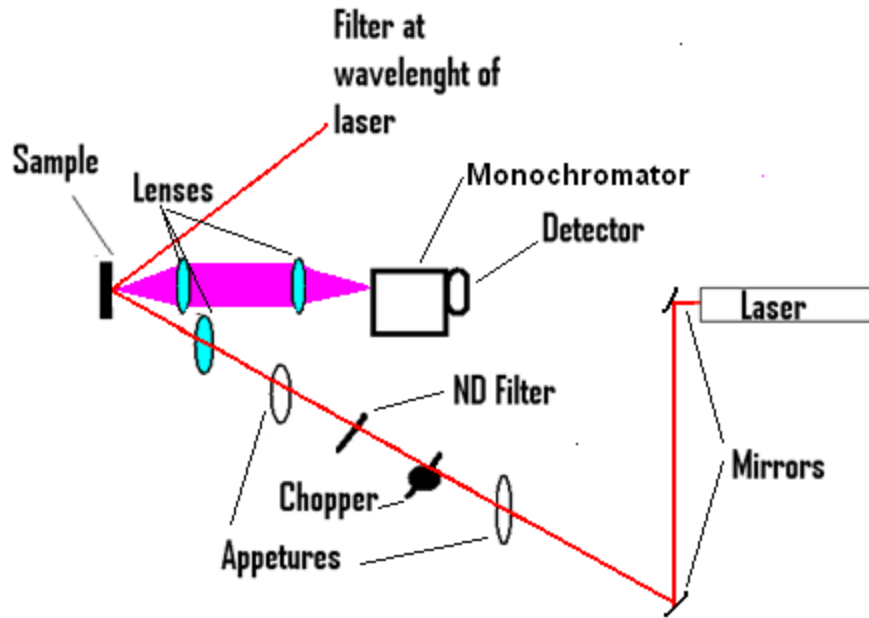


Figure 4.3.4.1: Photoluminescence setup. Light emitted from the HeNe laser is first chopped. Then the incident intensity can be altered with a neutral density filter and focused onto the sample using a lens. Any photoluminescence from the sample is collected by another lens and focused on the monochromator. The monochromator allows only one wavelength through to the detector at any moment. The signal is then recorded by the detector.

4.3.5 Electroluminescence

Electroluminescence (EL) operates in a very similar manner to photoluminescence. Using EL it is possible to measure semiconductor crystal quality, bandgap, and carrier lifetime, however, as opposed to PL, the EL is investigated by applying a bias to a semiconductor photodiode. The bias excites the electrons from the valence band to the conduction band, and when recombination occurs, a photon is emitted. It is with these properties that EL was used to characterize GaSb IMF layers.

The electroluminescence setup (shown in Figure 4.3.5.1) operates in the following manner. A square wave is applied to the sample with a function generator. The square wave causes a “pulse” of excited carriers within the semiconductor, resulting in photons generated at the semiconductor bandgap. This signal is then chopped, and collected by a collimating lens. The collimated signal is then focused onto a monochromator which cycles through a predefined frequency range. Finally, the intensity at each wavelength is recorded by a photodetector, which only detects frequency matched radiation through a lock-in amplifier.

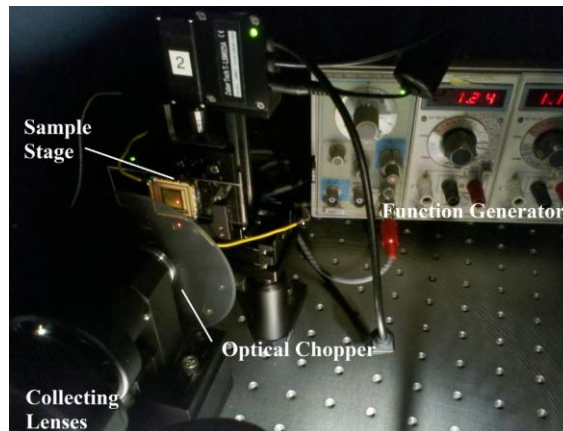
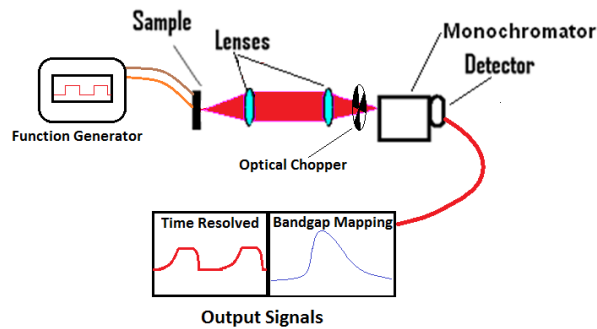


Figure 4.3.5.1: Electroluminescence setup. The sample is excited using a function generator. The resulting electroluminescence is collected by lenses and optically chopped. A monochromator then scans through a set wavelength range with a photodetector collecting the electroluminescent signal.

It is also important to note that EL has a few benefits as well as disadvantages when compared to PL. First, it becomes much easier to determine overall carrier lifetimes with EL as the exponential decay of carriers can be seen with each pulse of the function generator. Also, the signal obtained from EL can be many times stronger than PL. However, the disadvantages of EL included decreased mapping resolution as the entire sample is excited simultaneously. Also, EL requires good electrical contacts to the sample necessitating sample fabrication before characterization.

4.3.6 Ellipsometer

The ellipsometer, depicted in Figure 4.3.6.1, is a useful spectroscopic tool to determine material properties in the visible and near IR frequency range. An ellipsometer operates by detecting a change in light polarization due to optical reflections. To successfully use an ellipsometer for material characterization, either the index of refraction or the approximate thickness of a material must be known. However, in this work ellipsometry was primarily used to obtain reflection data at near normal incidence (23 degrees from the surface normal).

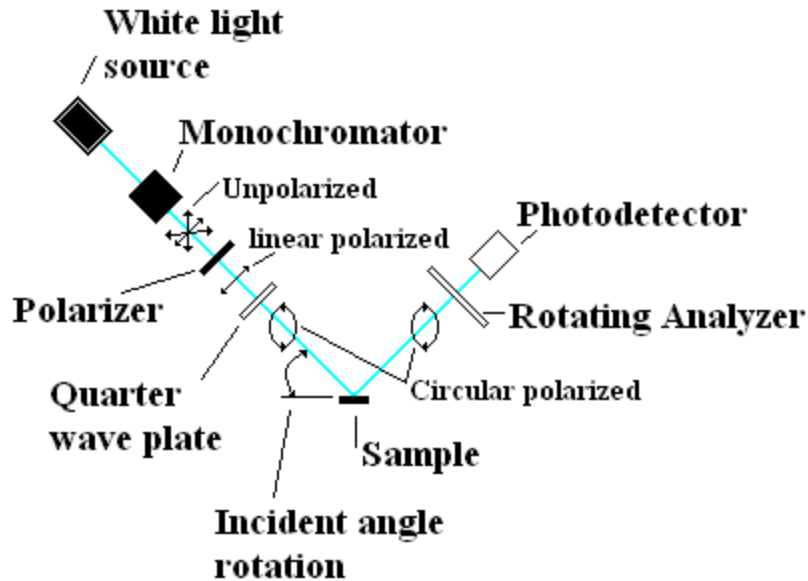


Figure 4.3.6.1: Depiction of a variable wavelength ellipsometer. White light is filtered with a monochromator to a specific wavelength. The light is then linearly polarized and guided through a quarter wave plate resulting in circularly polarized light. The circularly polarized light is incident on the sample which causes a polarization change dependent on the sample's properties.

The J. A. Woollam Spectroscopic Ellipsometer, shown in Figure 4.3.6.2, has the option to vary both the incident wavelength and the angle of incidence. A white light source is guided through a monochromator (the J.A Woollam Spectroscopic Ellipsometer has a range from 193 – 1700 nm) and then is linearly polarized. The polarized light is incident on a quarter wave plate to create a circularly polarized beam of monochromatic light. Reflection off of a sample alters the circular polarization based on the angle of incidence, wavelength of light, layer thickness, layer material, and substrate material. The polarization change is recorded by the photodetector (usually an avalanche photodiode).

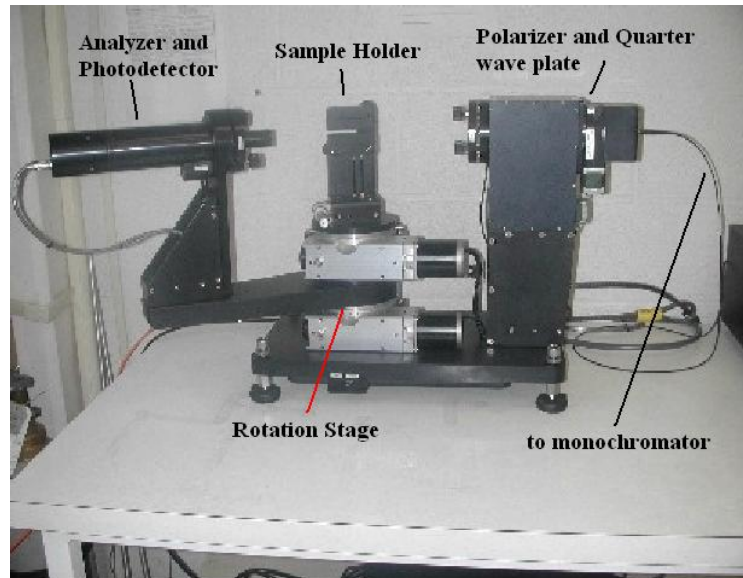


Figure 4.3.6.1: The J. A. Woollam Spectroscopic Ellipsometer. Shown is the sample holder, rotation stage, polarizer, quarter wave plate, analyzer, and photodetector.^[223]

As the circularly polarized light becomes incident on the rotating analyzer, there are specific moments in time when the rotating analyzer completely destructively interferes with the circularly polarized light. At these points, the photodetector records zero intensity. A graph can be made comparing the wave vector to incident angle by comparison of the zero crossings. The ellipsometer can be used to find reflectance and transmittance measurements, electric permittivity, index of refraction, multiple layer thicknesses, and various other properties. The general method to determine these properties is always similar, comparing the change in polarization to existing data files to determine material properties.

This chapter has described the various simulation, fabrication, and testing techniques used to design, create, and optimize the items proposed in Chapter 3. It was the purpose of this chapter to describe how each technique operates, and

when each is best utilized. Chapter 5 will describe how each of these techniques was used and the individual results obtained during testing.

Chapter 5

Design and Results

This section is dedicated to specific results obtained for each topic subset. A brief research purpose will be reiterated, followed by the project's design constraints, simulation results, and experimental results. The knowledge gained and conclusions drawn maybe alluded to in this section; however, the results in comparison to the stated goals will be reserved for discussion in Chapter 6.

List of Abbreviations - Chapter 5

MM - metamaterial	EL - electro luminescence
TPV - thermophotovoltaic	MBE - molecular beam epitaxy
PhC - photonic crystal	ARC - antireflective coating
GaSb - gallium antimonide	PECVD - plasma enhanced chemical vapor deposition
GaAs - gallium arsenide	IMF - interfacial misfit array
FDTD - finite difference time domain	XRD - x-ray diffraction
FIT - finite integral technique	TLM - transfer length method
SEM - scanning electron microscope	FTIR - Fourier transform infrared spectroscopy
ALD - atomic layer deposition	DSP - double side polished

5.1 Metamaterial High Temperature Emitter

Present MM perfect emitter devices have standard limitations in temperature robustness. To this end, high temperature materials were considered based on conductivity, melting point, and Drude coefficients. Once a potential material was selected, the MM absorber/emitter was simulated, fabricated, and tested.

As described in previous sections, a metamaterial requires two properties, a metallic element and a nanostructure. However, the high temperature conditions of many TPV emitters cause many commonly used MM metals undergo a phase change. To this end, multiple metals were investigated for their potential use in high temperature emitter technologies; this list is shown in Figure 5.1.1.

Metal	ω_p [1/cm]	ω_p [rad/s]	ω_t [1/cm]	ω_t [1/s]	Melting Pt. [°C]	Conductivity [S/m]	Thermal Exp. [$\mu\text{m}/^\circ\text{C}$]
Al	119000	2.24E+16	660	1.97E+13	660	3.546E+7	23.1
Co	32000	6.03E+15	295	8.84E+12	1495	1.603E+7	13
Cu	59600	1.12E+16	73.2	2.19E+12	1085	5.96E+7	16.5
Au	72800	1.37E+16	215	6.44E+12	1064	4.52E+7	14.2
Fe	33000	6.22E+15	147	4.40E+12	1538	1.00E+7	11.8
Pb	59400	1.12E+16	1630	4.88E+13	327	4.55E+6	28.9
Mo	60200	1.13E+16	412	1.23E+13	2620	2.00E+07	4.8
Ni	39400	7.42E+15	352	1.05E+13	1453	1.43E+07	13.4
Pd	44000	8.29E+15	124	3.71E+12	1555	1.00E+07	11.8
Pt	41500	7.82E+15	558	1.67E+13	1770	9.43E+06	8.8
Ag	72700	1.37E+16	145	4.34E+12	961	6.301E+7	18.9
Ti	20300	3.82E+15	382	1.14E+13	1670	2.38E+06	8.6
V	41600	1.25E+15	489	1.46E+13	1910	5.00E+06	8.4
W	51700	1.55E+15	487	1.45E+13	3422	2.00E+07	4.5
Al ₂ O ₃	-	-	-	-	2072	-	5.3

Figure 5.1.1: A list of potential materials for use in a high temperature TPV emitter. The five most promising metals and the standard dielectric material (Al₂O₃) are highlighted in grey.^[224]

The initial goal was to create a high-temperature MM emitter for use with GaSb, with a bandgap energy of 0.7 eV. This bandgap corresponds to a blackbody radiator centered at 1600 °C; therefore, only metals with a melting point greater than 1600 °C were considered. Initially, molybdenum (Mo) was considered as a viable solution; however, Mo and W are known to oxidize readily when heated. Therefore, platinum (Pt) was chosen as it demonstrates a high plasma frequency as well as a high conductivity, both of which are required in a successful MM material.

Emitter models were then designed and simulated based on work described in Section 3.1. These emitters incorporate a large Pt grounding plane, a thin alumina insulating layer to create a capacitance, and a small Pt circular MM absorber pattern, shown in Figure 5.1.2.

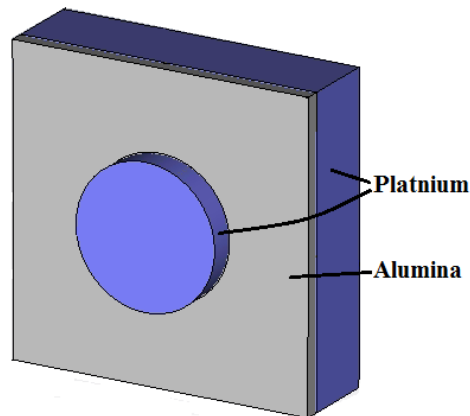


Figure 5.1.2: MM emitter structure: circular Pt MM features, alumina dielectric spacer, and Pt back grounding plane.

Simulations were performed in CST Microwave studio. The FIT transient solver was used, which operates identically to FDTD simulations described

previously in Chapter 3.1. A Drude model was used to describe the two metal layers, and a standard dielectric model was used for the thin alumina layer. Using this simulation method it was possible to design an initial MM test structure. This device was designed to operate between 0.7 μm and 1.6 μm ; however, was not optimized to create a perfect absorption spectrum. The lower conductivity of Pt, as compared to the field standard of Au, requires a thin alumina layer in order to achieve high absorption. Alumina layers were chosen on the order of 10-20 nm for ease of fabrication as well as device robustness. These layer thicknesses were chosen to allow for chemical cleaning of the Al_2O_3 surface without fear of film penetration.

In order to form a comparison to present MM perfect absorber technologies, collaborators at Boston College constructed a MM perfect absorber based on the Au/Alumina/Au stack described in Section 3.1 and shown in Figure 5.1.3. This structure was constructed with: a 930 nm lattice constant, a 50 nm thick alumina spacer, and a 310 nm Au square MM pattern, stacked on an Au back grounding plane. We then tested the initial absorption of this structure using ellipsometry; the results are shown in Figure 5.1.3

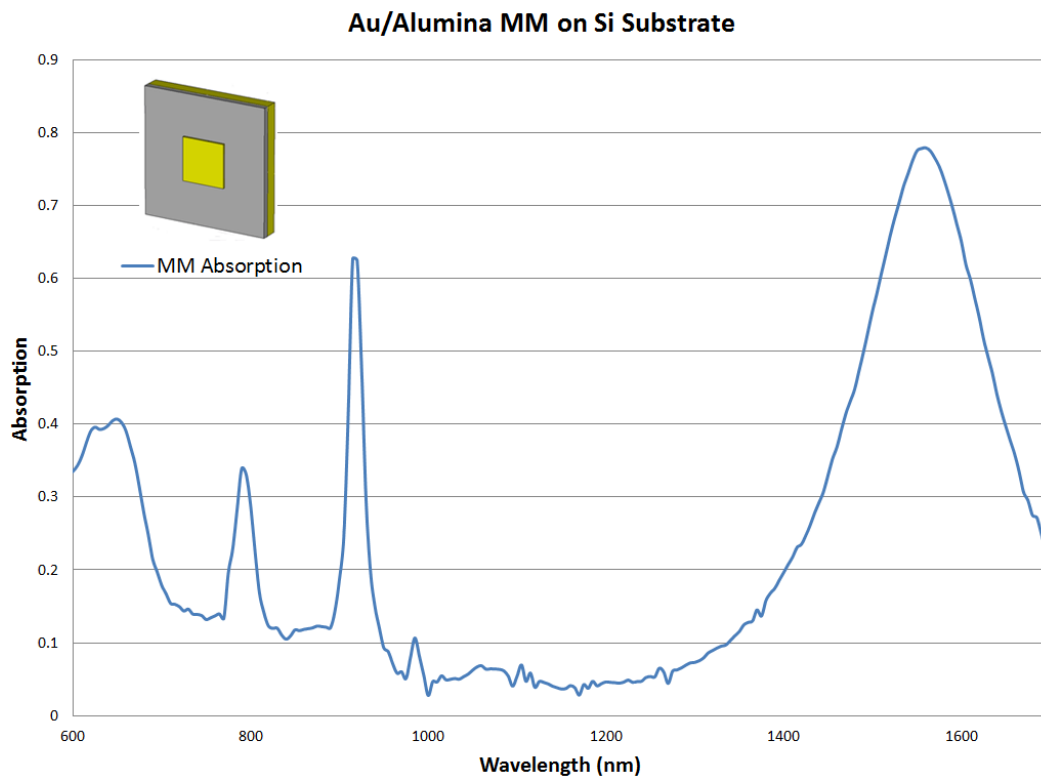


Figure 5.1.3: An Au MM absorber constructed to operate at a wavelength of 1550 nm. Absorption was tested at room temperature using an ellipsometer at 15 degrees from normal incidence. *Inset:* MM design.

The gold and alumina MM was then heated to 360 °C at which point discoloration was observed on the surface of the Au. The sample was then examined in an SEM, shown in Figure 5.4.

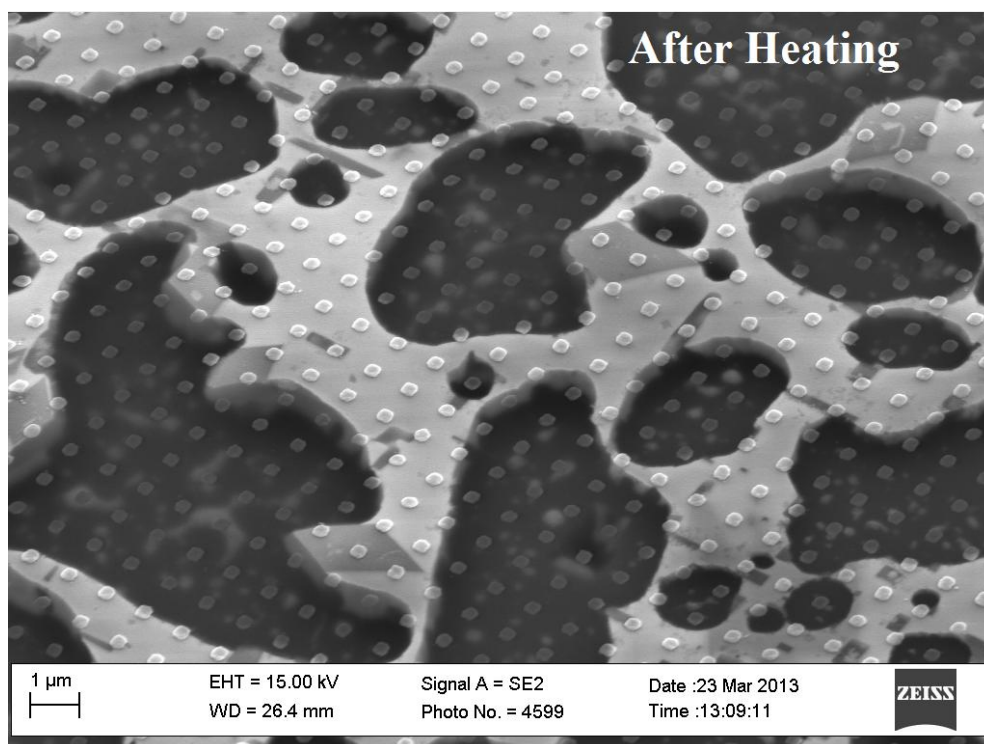
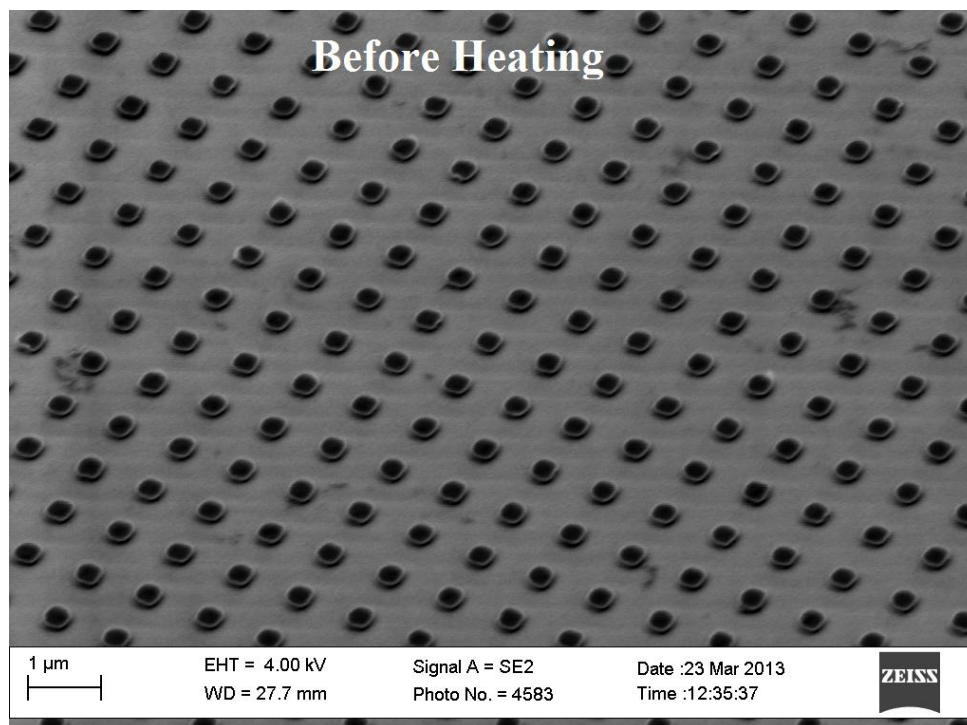


Figure 5.1.4: *Top:* Au MM pattern before heating to 360 °C. *Bottom:* MM pattern after heating to 360 °C. The dark shapes represent areas where the gold and silicon combine in an eutectic.

In order to determine the effect of heating on the MM absorption, the sample was once again examined in the ellipsometer. The results are shown in Figure 5.1.5.

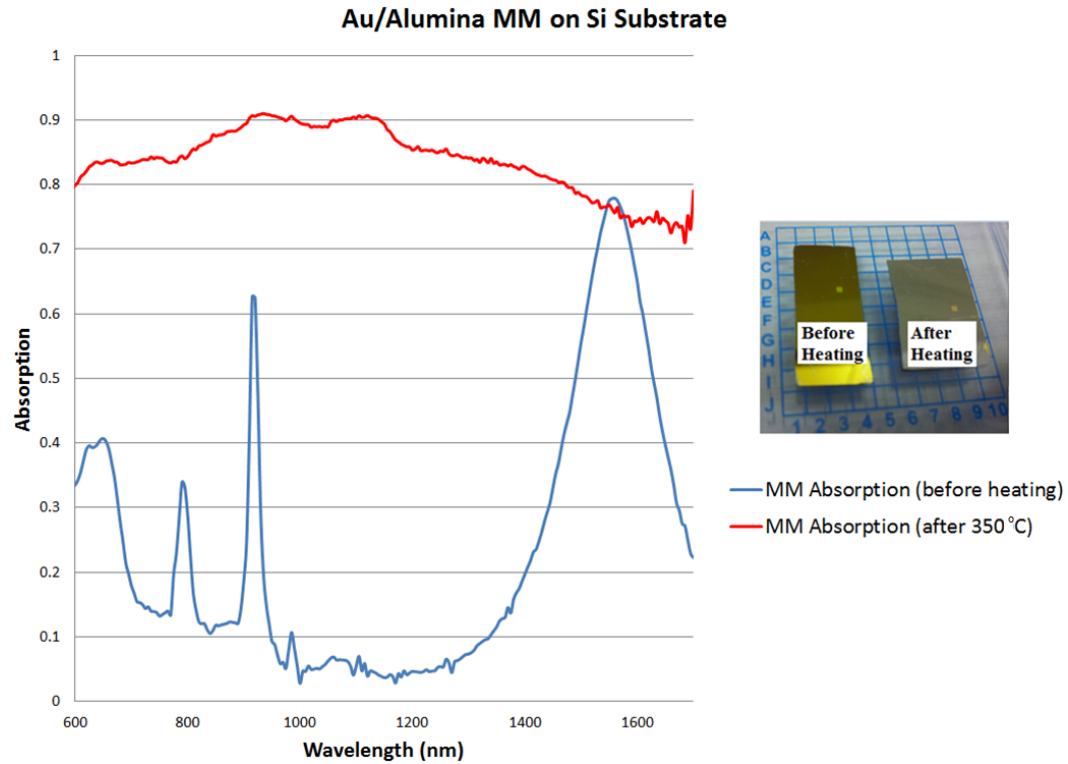


Figure 5.1.5: *Left:* Absorption measured before and after heating. The formation of the eutectic causes a complete loss of MM absorption even though the patterned elements are present. *Right:* Optical image of MM patterned samples with and without heating.

This work shows the need of an alternative material device even when temperatures are only a few hundred degrees Celsius as gold and silicon form an eutectic at a temperature of 360 °C; and as seen from Figure 5.1.3, eutectic formation can cause a catastrophic failure of the MM emitter.^[225] To this end, the Pt/Alumina/Pt stack of Figure 5.2.1 was simulated and constructed. A full fabrication procedure for all metamaterial emitters is described in Appendix 5.1.

Initial device simulations predicted MM absorption on the order of 88% at a wavelength of 800 nm, as shown in Figure 5.1.6. The narrow absorption peak

implied through simulation data shows enough proof of concept to allow fabrication of a high temperature MM emitter.

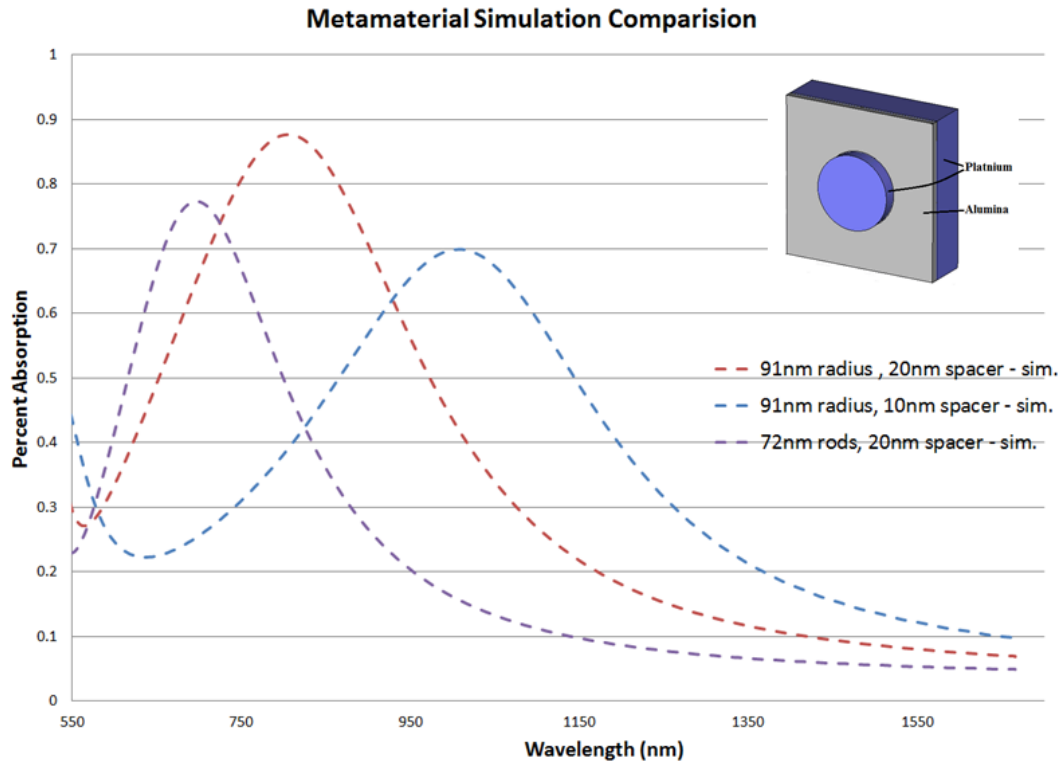


Figure 5.1.6: Simulated results of a Pt MM absorber. *Inset:* model of structure.

Simulation results also yielded the E-field and H-field vectors for the MM absorber of Figure 5.1.2. These vectors were found at various points in the MM absorber in order to track the surface current as well as E-field propagation. These results are shown in Figure 5.1.7 and 5.1.8.

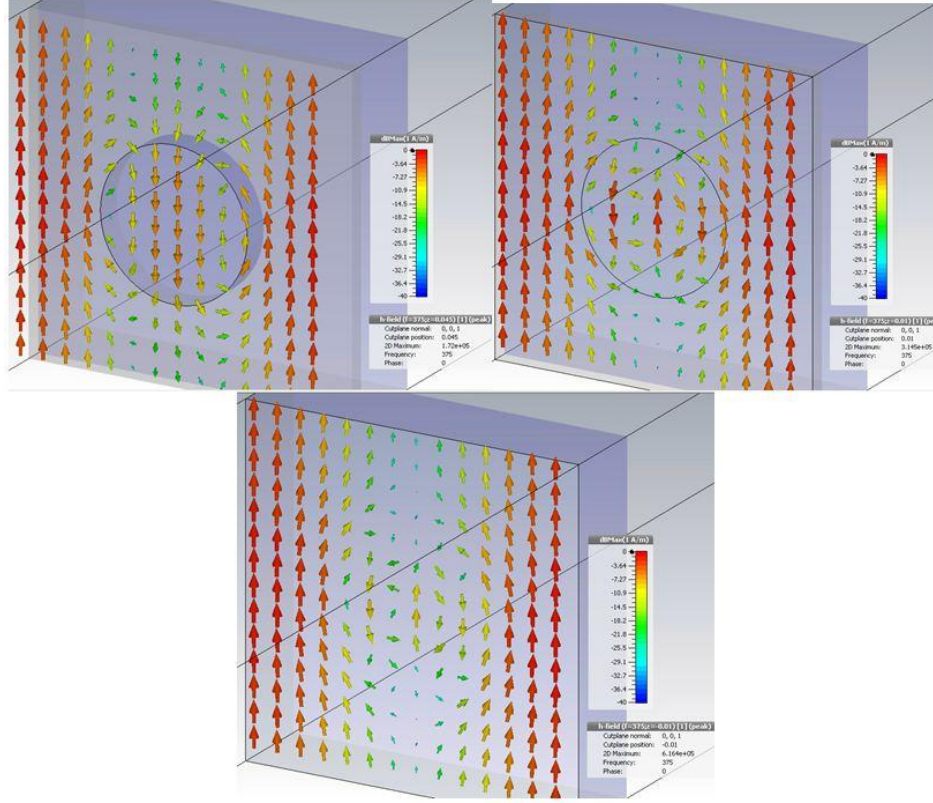


Figure 5.1.7: Surface current at three points in the Pt perfect absorber stack at resonance ($8\ \mu\text{m}$). *Top Left:* the top of the Pt rod. *Top Right:* the Pt rod/ Al_2O_3 interface. *Bottom Middle:* the Al_2O_3 /Pt grounding plane interface.

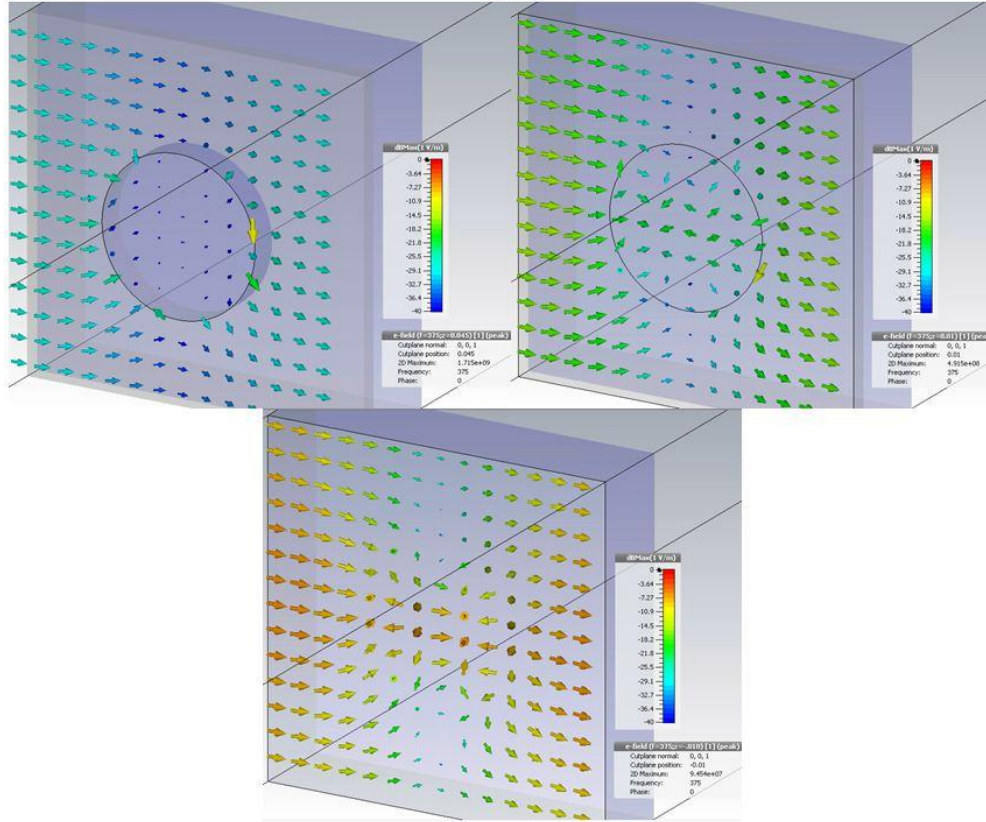


Figure 5.1.8: The E-field at three points in the Pt perfect absorber stack at resonance (8 μm). *Top Left:* the top of the Pt rod. *Top Right:* the Pt rod/Al₂O₃ interface. *Bottom Middle:* the Al₂O₃/Pt grounding plane interface.

One-hundred nanometers of Pt were then deposited on an Epi-ready Si wafer to act as a back grounding-plane and assure no transmission through the structure. The Pt was then coated with 20 nm of Al₂O₃ deposited by ALD and thickness confirmed with an ellipsometer. Finally, E-beam lithography was used to create a MM pattern (91 nm radius and 400 nm lattice constant); followed by a 35 nm Pt metallization, using e-beam thermal evaporation. The resulting structure can be seen in Figure 5.1.7. This same process was then repeated for a

second structure using rods of 72 nm radius with 20 nm Al_2O_3 and a third structure with 10 nm Al_2O_3 and rods of 91 nm radius.

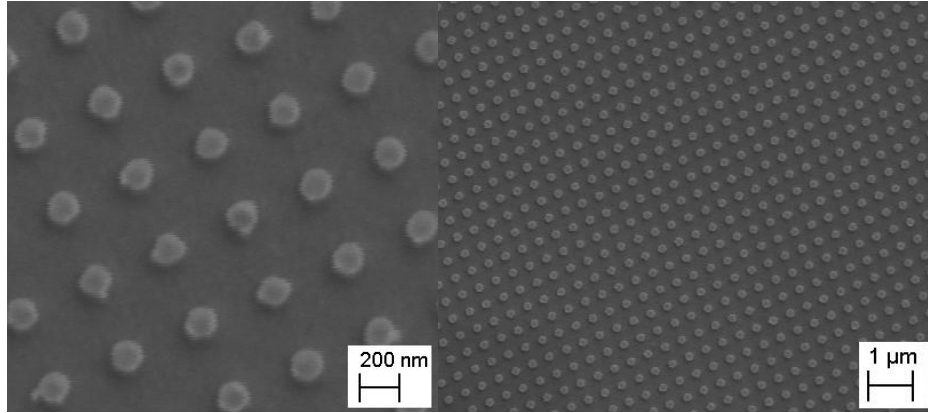


Figure 5.1.7: Pt nano-rods deposited on 20 nm of Al_2O_3 with a 100 nm Pt grounding plane.

Reflection measurements were then taken on these samples to confirm absorption at the desired wavelength. An example of a metamaterial response as compared to an unpatterned platinum surface can be seen in Figure 5.1.8. This data was taken with an ellipsometer at 23 degrees from the surface normal.

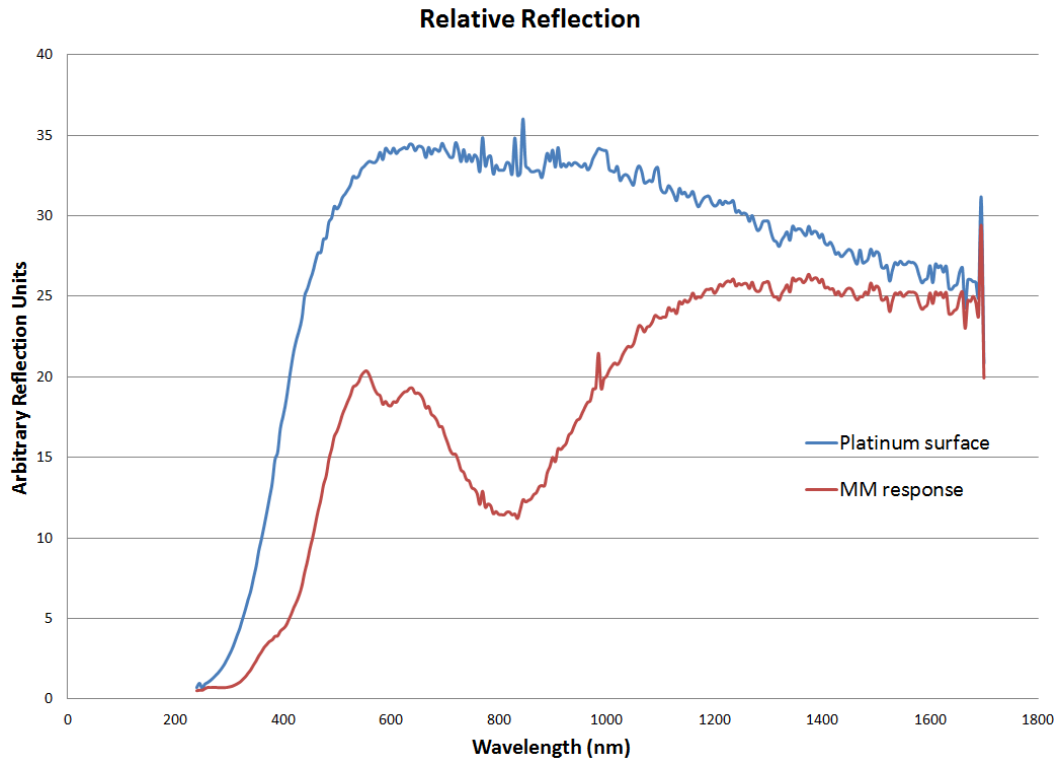


Figure 5.1.8: Reflection data taken from the Pt perfect absorber MM of figure 5.1.4.

When the two curves of Figure 5.1.5 are compared, it is possible to determine the total absorption of the MM pattern, as shown in Figure 5.1.9.

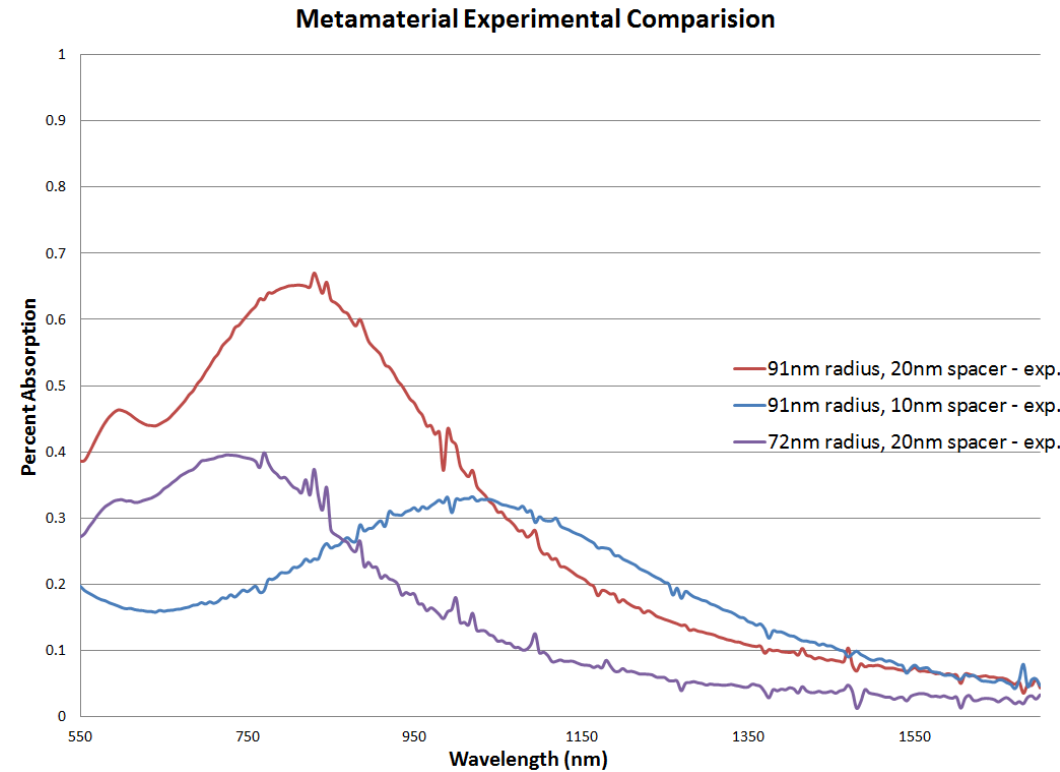


Figure 5.1.9: Absorption measurements for three MM structures with varying radius and spacer thicknesses. Notice the read peak at 800 nm.

The next step in this work is to obtain emissivity data for this MM emitter. To this end, a ceramic heating element was attached to the backside of the substrate, and the sample was placed in an EL tester. This measurement was not the standard EL test described in Section 4.3.5. The emission was due to the applied heating element, as opposed to an applied bias, shown in Figure 5.1.10.

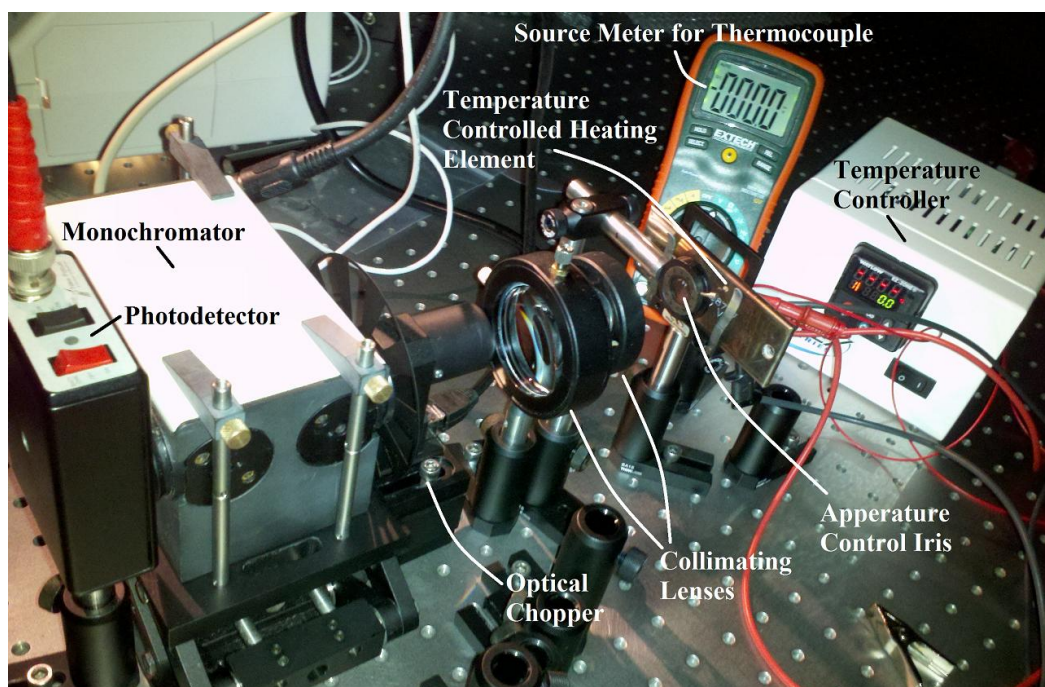


Figure 5.1.10: Emissivity testing setup. The sample is heated using a temperature controller; the emission is then collected using collimating lenses and optically chopped. The chopped signal is filtered with a monochromator and then collected with a photodetector.

The Pt metamaterial of 91 nm radius rods and a 20 nm thick layer of Al_2O_3 (red of Figure 5.1.9) was heated to a temperature of 500 °C. The spectral emission of the sample was then measured and is shown in Figure 5.1.11.

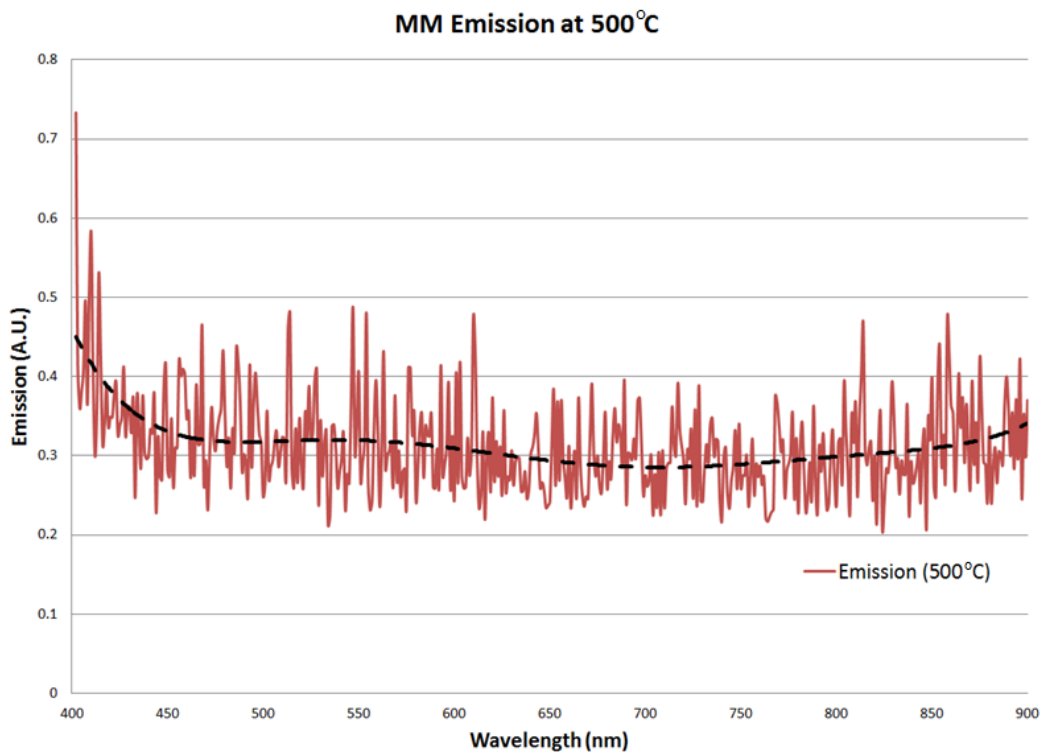


Figure 5.1.11: Emission at 500 °C. This temperature does not contain large quantities of energy in the visible and heating caused structural defects, as such no signal is observed.

As the emission test of Figure 5.1.11 resolves mostly noise, the MM pattern was then examined. After heating to a temperature of 500 °C the MM was observed to undergo a strong discoloration. The post-heating sample was then re-tested using an ellipsometer and exhibited a significantly modified absorption, shown in Figure 5.1.12.

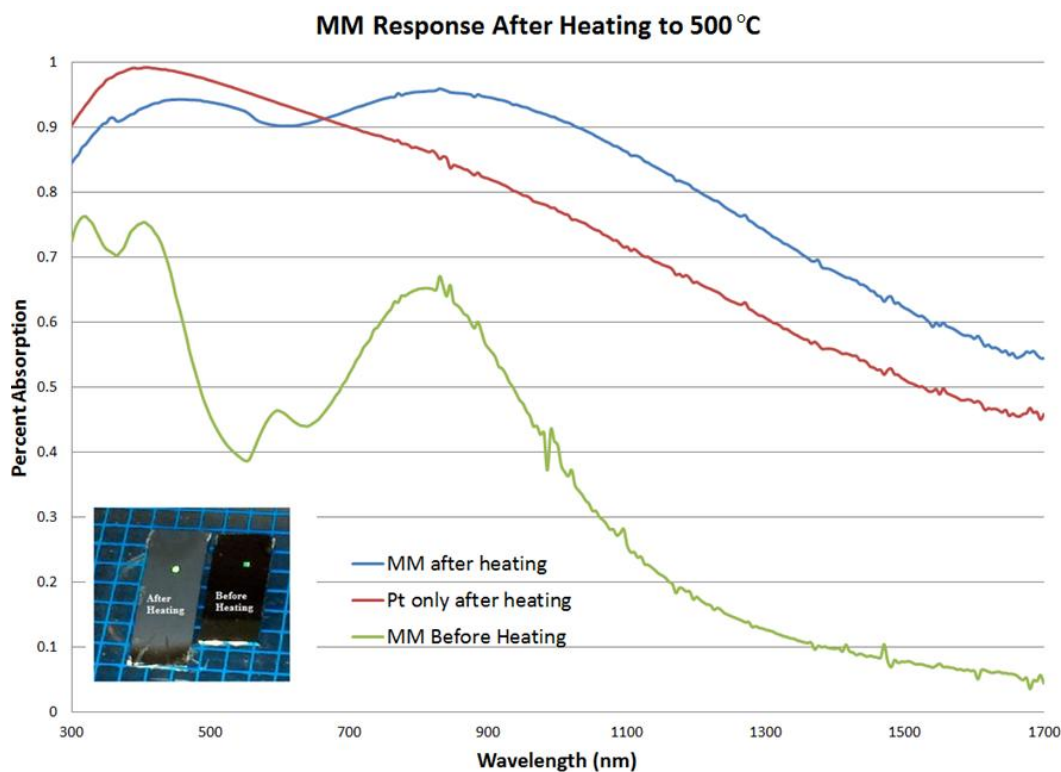


Figure 5.1.12: MM response before and after heating. A temperature of 500 °C caused an altered absorption pattern with and without a MM pattern as well as strong discoloration in the sample.

The sample was then examined with a SEM in order to determine if heating cause structural degradation in the MM sample, shown in Figure 5.1.13.

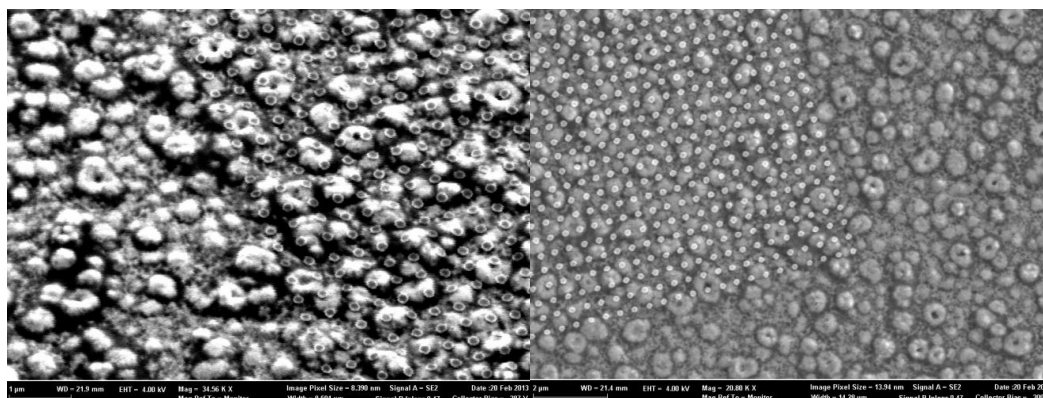


Figure 5.1.13: After heating the MM pattern is intact, however there appears to be significant damage to the thin Al_2O_3 layer.

In order to rectify the heat damage, the Pt MM was next constructed on a sapphire (Al_2O_3) substrate. This MM was designed to operate at a wavelength of $1\ \mu\text{m}$. and consisted of $104\ \text{nm}$ radius dielectric rods on $20\ \text{nm}$ of Al_2O_3 . The new MM stack was then measured using an ellipsometer at 15° from the surface normal and heated to a temperature of 650°C . The simulated response as well as the experimental response (before and after heating) is shown in Figure 5.1.14.

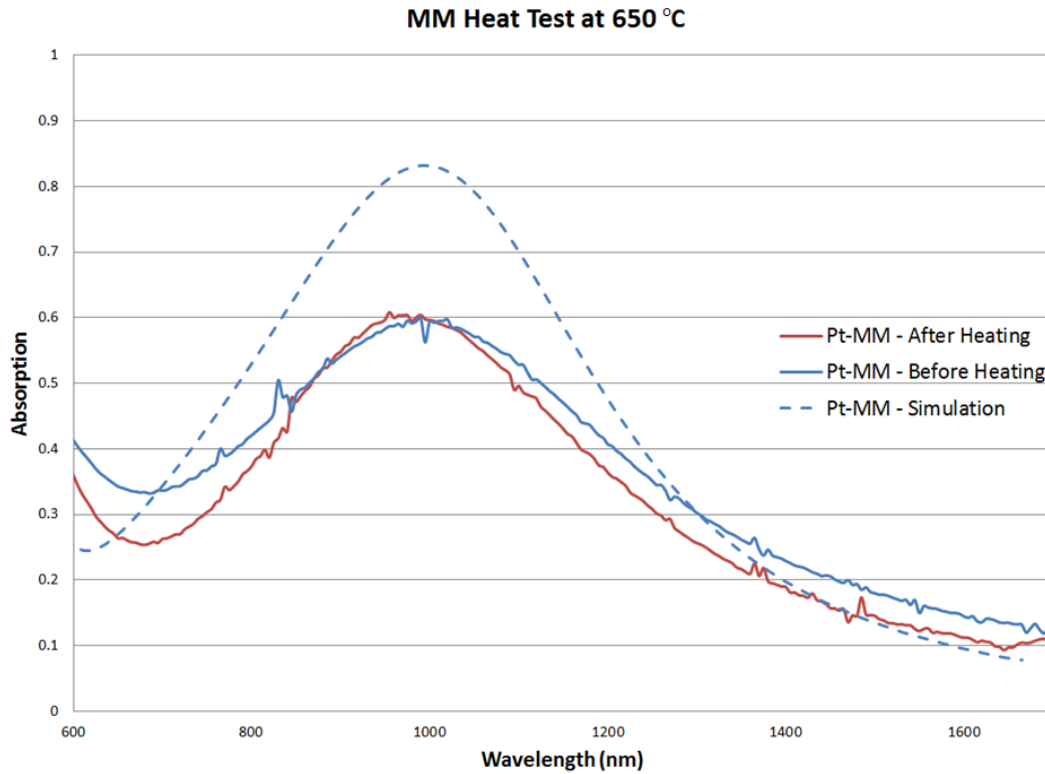


Figure 5.1.14: Absorption results from the Pt/ Al_2O_3 /Pt on sapphire MM structure. *Blue Dash:* Simulated absorption results. *Blue Line:* Absorption at 15° from normal incidence before heating to 650°C . *Red Line:* Absorption at 15° from normal incidence after heating to 650°C .

The MM sample was then examined under an SEM in order to confirm that structural integrity was maintained. These images are shown in Figure 5.1.15.

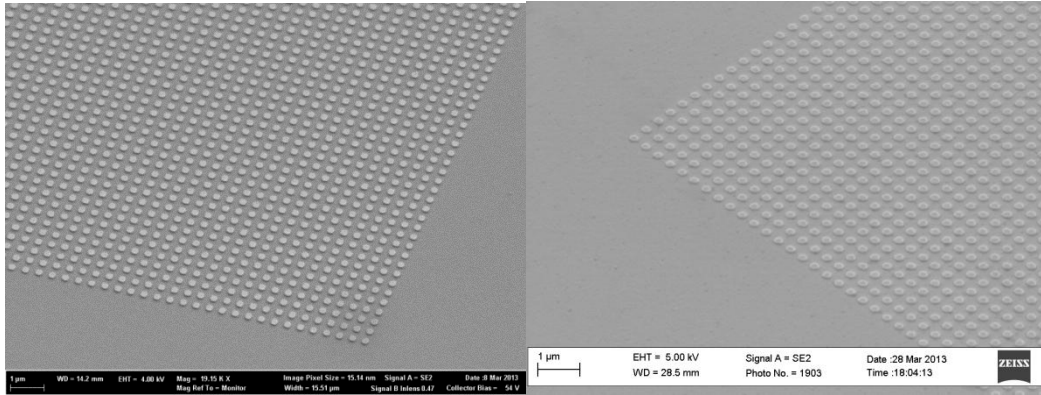


Figure 5.1.15: Pt/Al₂O₃/Pt on sapphire MM structure. *Left:* Before heating. *Right:* after repeated heating to 650 °C.

In order to test spectral emission from these MM devices, they were once again tested using the emission tester of Figure 5.1.10. In order to obtain emission independent of the photodetector spectral response, the emission was normalized to that of a Pt substrate without a MM pattern. The emissivity was measured at various temperatures in order to assure consistency between measurements as well as reduce noise. Figure 5.1.16 shows the resulting emissivity as well as the measured absorption using the ellipsometer.

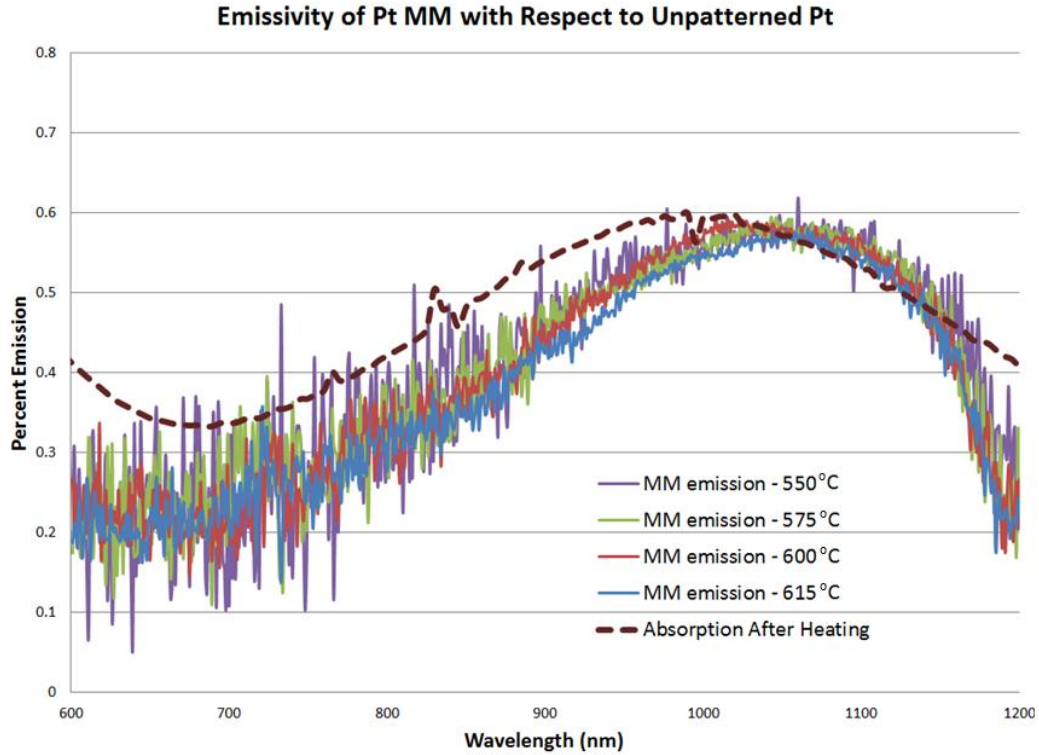


Figure 5.1.16: Emissivity as a function of wavelength as well as absorption obtained using an ellipsometer after repeated heating.

5.2 Metallic Photonic Crystal Filters

As discussed in previous sections, photonic crystals (PhCs) can have unique applications as a front side filter for a photodiode. In particular, a metallic PhC was created in order to provide filtering and light trapping for a GaSb photodiode. This PhC device was taken from conception to performance simulations using Lumerical FDTD software; and finally into experimental trials using GaSb photodiode, e-beam resist patterning, and electron beam thermal evaporation for metal deposition.

Lumerical FDTD simulation software was first used to model a physically viable structure to trap photons incident on a TPV diode. This program uses a modeled optical source in order to provide a realistic base line for comparison. Then, the PhC surfaces were added to the model and various computations were performed to compare models.

Pure undoped GaSb has a band gap energy of 0.726 eV which corresponds to a photon of wavelength 1.7 μm . In order to create an electron/hole pair an incident photon must have a wavelength shorter than 1.7 μm . Therefore, a plane wave pulse was injected into the sample with a peak intensity at 1.3 μm . Figure 5.2.1 shows the input plane wave source as a function of time and as a function of wavelength content.

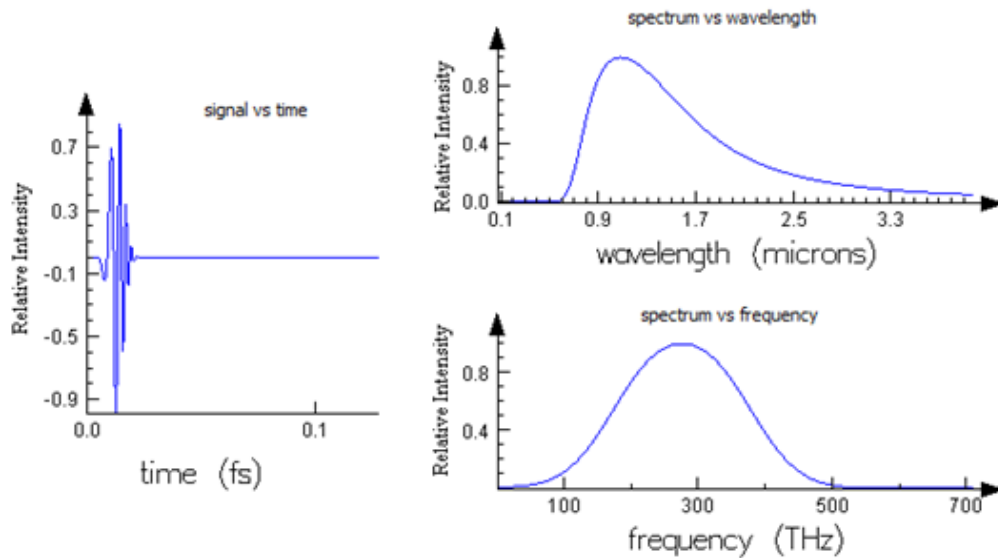


Figure 5.2.1: Spectral content and pulse time of the Lumerical Simulation Source. *Top:* pulse intensity as a function of time. *Middle:* Intensity of E-field as a function of wavelength content (notice black body curve and peak wavelength of 1.3 μm). *Bottom:* Intensity of E-field as a function of frequency content.

Lumerical FDTD was then used to simulate the GaSb substrates as well as any surface patterns or materials. To correctly simulate the material properties of GaSb, the real and imaginary index of refraction as a function of wavelength was taken from Djurišić, *et al.*^[226] Material constants were also obtained through experimental ellipsometer data. However, the optical constants for GaSb p-n photo diode were shown to be relatively invariant and, therefore, the photodiode was modeled as a pure GaSb substrate.

Three different designs were used to determine an optimum geometry for an enhanced GaSb thermophotovoltaic design. A pure GaSb substrate was first simulated for a control. Then, a PhC pattern was added as a gold top contact layer. To provide further enhancements, the effects of an antireflective coating (Si_3N_4) were simulated, and a bottom Au vertical confinement layer was added (all shown in Figure 5.2.2). The results are measured in optical absorption. Physically, an increase in optical absorption corresponds to a larger electron/hole pair population and increased conversion efficiencies.

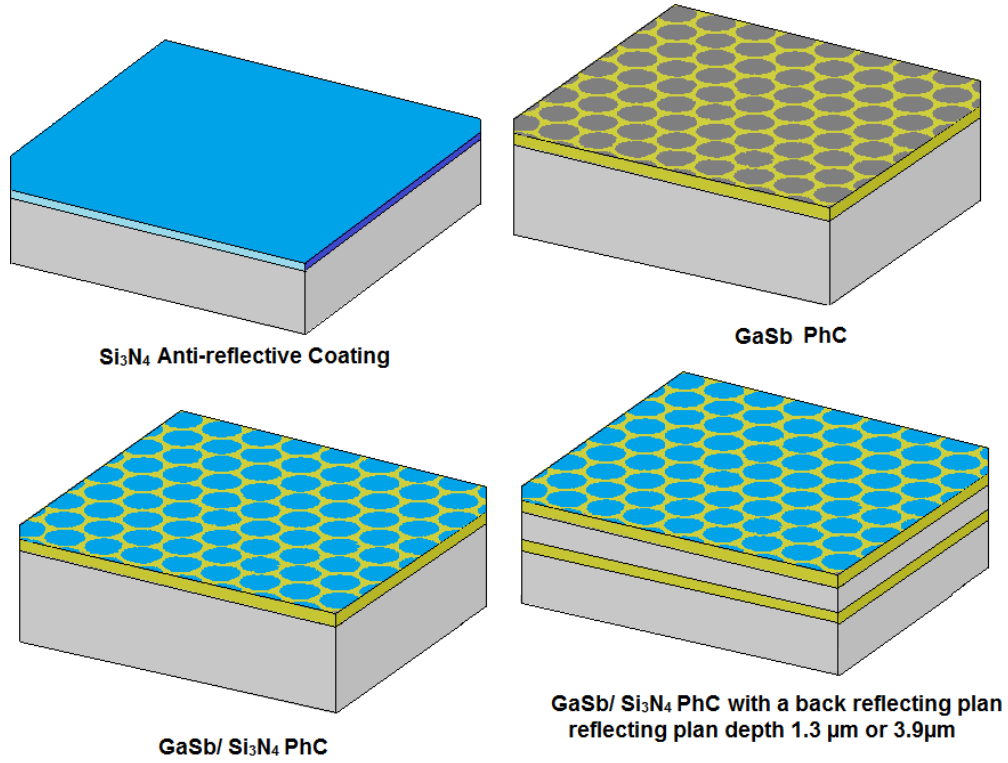


Figure 5.2.2: Representative structures tested in this section. Only Si₃N₄ as an ARC, a GaSb PhC, and GaSb/Si₃N₄ PhC were fabricated and tested.

Control absorption measurements were simulated on bulk GaSb with no PhC pattern and a GaSb substrate with a Si₃N₄ antireflective coating. All PhC simulations were done in Ti/Pt/Au (50 nm/50 nm/350 nm) ohmic contact material on a GaSb substrate. Also, all PhC patterns had a height of 0.45 μm . All results are analyzed over a wavelength range of 0.7 μm to 1.7 μm due to both the bandgap limitations of GaSb and the quickly decaying absorption shown later in Figure 5.2.4 and Figure 5.2.5.

PhC absorption simulations were performed on an PhC/ air-rod pattern with a lattice constant of 1.7 μm and a hole radius of 0.75 μm . Absorption measurements were also simulated for a PhC patterns with Si₃N₄ rods. The Si₃N₄ rod simulations utilized a lattice constant of 1.7 μm and a rod radius of 0.75 μm to

create an enhancement at a wavelength of 1.3 μm . To create the largest amount of absorption around the band gap of GaSb, a black body centered at 1.3 μm was used for these absorption simulations, shown in Figure 5.2.1. This wavelength was chosen so that most of the blackbody curve contains enough energy to excite charge carriers within GaSb while at the same time limiting phonon creation. Tailoring the PhC/air rod pattern to the black body source, or the black body source to PhC/air rod pattern decreased the absorption within the cavity. Therefore the same source and pattern was used for all reported absorptions.

The first two absorption simulations performed were to establish a baseline for future measurements. A GaSb substrate and a GaSb substrate with a thin layer of Si_3N_4 (to act as an antireflective coating and provide surface passivation) served this purpose, shown in Figure 5.2.2. The results showed a marked increase in the optical absorption within the GaSb active region when Si_3N_4 was added, shown in Figure 5.2.3.

PhC absorption measurements were performed and the absorption was measured over the entire GaSb region as a function of wavelength. To provide an optimized PhC pattern the air-rods were replaced with Si_3N_4 rods. The Si_3N_4 PhC pattern acts as a surface passivation layer to decrease surface recombination as well as an antireflective coating. This new PhC increased absorption by 9% over the air PhC pattern, and increased absorption by 81.81% over the GaSb control substrate.

As a segue to possible future work with PhC resonance cavities, a back reflecting layer was added at a depth of 1.3 μm or 3.9 μm to the PhC/ Si_3N_4

sample. With this sample, the absorption was shown to decrease by 47% and 29% respectively. This was surprising, as the increased optical path length was thought to increase absorption opportunities within the region. A full table showing the relative absorption (from 0.7 μm to 1.7 μm) within the active p-n region of all designs is shown in Figure 5.2.3.

Trial	Absorbed Power	Percent Increase	Loss with Reflector
Control	85.27	--	N/A
Control +Si ₃ N ₄	99.41	16.57	N/A
Back Side reflector at 3.9 μm	66.76	-29.20	18.52
PhC/ Air holes	142.2	66.73	N/A
PhC/ Si ₃ N ₄	155.0	81.81	N/A
PhC/ Si ₃ N ₄ holes 1.3 μm reflector	40.38	-47.36	115.2
PhC/ Si ₃ N ₄ holes 3.9 μm reflector	118.8	39.31	36.82

Figure 5.2.3: Predicted absorption increases using FDTD simulation software. Notice the lack of improvement with the addition of a back reflecting plane.

Although the addition of a PhC backside reflector decreased optical absorption, the effect was also closely examined in comparison to the presence of only a PhC, shown in Figure 5.2.4.

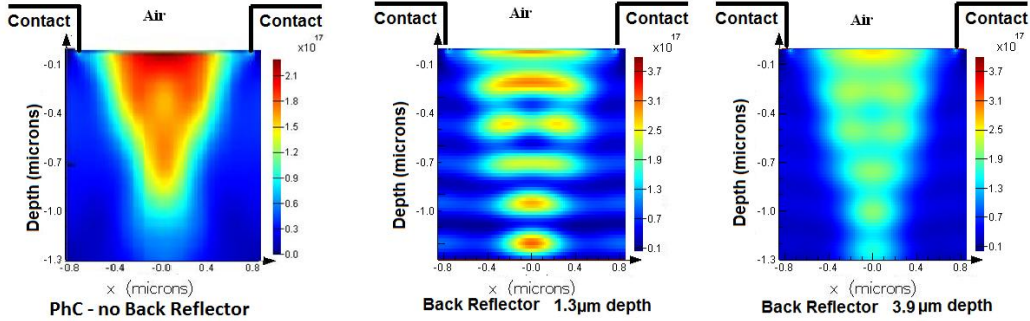


Figure 5.2.4: Comparison of absorption with the addition of a back reflector. The resulting interference pattern decreases absorption as shown in Figure 5.2.3.

Using this promising simulation data, fabrication procedures were initiated for construction of a PhC on a GaSb photodiode. Devices were constructed on MBE grown samples (growth number R9-86) which had previously undergone standard diode processing, to be described in more detail in Chapter 5.4. The full PhC fabrication procedures, created specifically for this work, can be found in Appendix 5.2.1. Each fabricated device, see example in Figure 5.2.5, was tested before PhC fabrication, and after fabrication in order to provide the most accurate comparison.

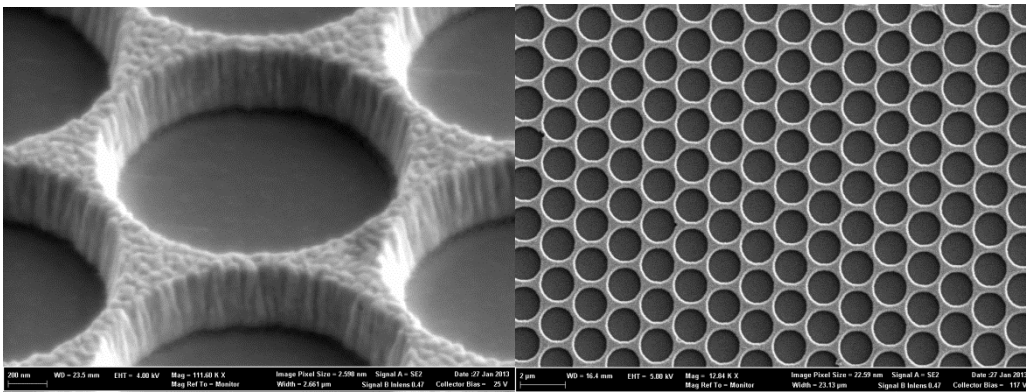


Figure 5.2.5: Fabricated PhC pattern shown under scanning electron microscopy.

Reflection tests on these PhC patterns were performed on an ellipsometry system from 500 nm to 1700 nm. The minimum reflection angle possible on this system is 15 to 23 degrees from the surface normal. This was expected to reduce maximum recordable coupling efficiency at resonance as PhC are very sensitive to angle of incidence. The resulting absorption spectrum is shown in Figure 5.2.6.

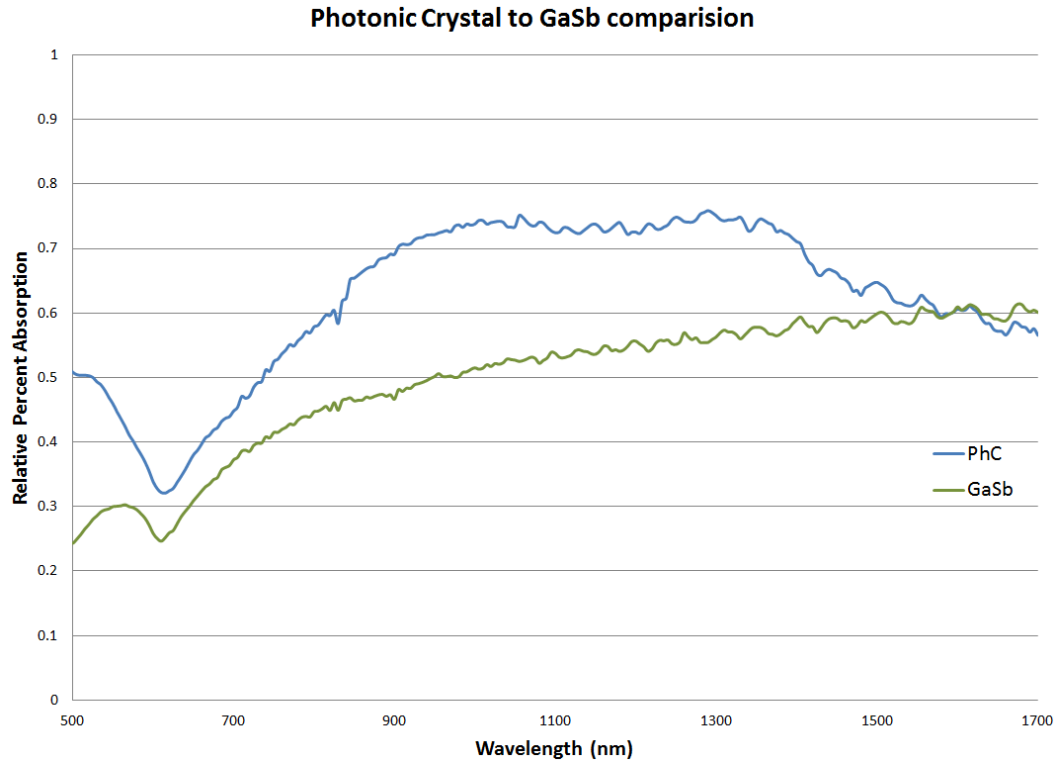


Figure 5.2.6: Absorption data of substrates with no ARC determined from ellipsometry at an angle of 23 degrees from the surface normal. The y-axis represents relative absorption as feature sizes were much smaller the measured background spectrum causing errors in absolute magnitude.

Figure 5.2.6 shows an increased absorption of approximately 26.5% at an angle of 23 degrees from the surface normal when a PhC is present on the surface as compared to pure GaSb. A 110 nm thick antireflective coating was then added to the surface of the PhC and GaSb and absorption was measured at 15 degrees from the surface normal. The results are shown in Figure 5.2.7.

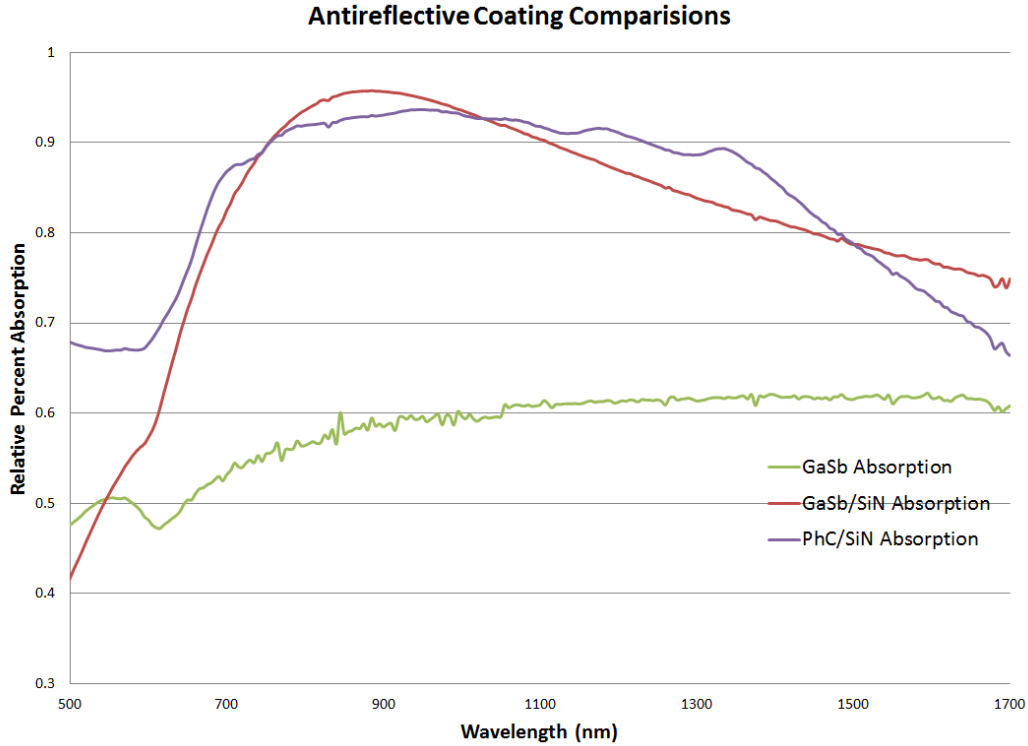


Figure 5.2.7: Absorption data of substrates with SiN_x ARC determined from ellipsometry at an angle of 15 degrees from the surface normal. The y-axis represents relative absorption as feature sizes were much smaller the measured background spectrum causing errors in absolute magnitude.

Due to the limited usefulness of testing off-angle measurements for PhC, further testing was confined to diode efficiency measurements. However, it should be noted that the PhC pattern from Figure 5.2.7 shows a 1% improvement in absorption over an antireflective coating and a 67% improvement over GaSb even when measured at 15 degrees from the surface normal. To this end, A PhC was then fabricated on a GaSb photodiode (structure shown in Figure 5.2.7) using electron beam lithography, shown in Figure 5.2.8. The PhC was fabricated using a Ti/Pt/Au (50 nm/50 nm/350 nm) ohmic contact recipe.

R9-86			
GaSb/GaSb			
7	GaSb	p-type $2 \times 10^{19} \text{ cm}^{-3}$ (Be)	10nm
6	$\text{Al}_{0.4}\text{Ga}_{0.6}\text{Sb}$	p-type $2 \times 10^{19} \text{ cm}^{-3}$ (Be)	50nm
5	GaSb	p-type $2 \times 10^{18} \text{ cm}^{-3}$ (Be)	50nm
4	GaSb	p-type $2 \times 10^{16} \text{ cm}^{-3}$ (Be)	200nm
3	GaSb	NID	1500nm
2	GaSb	n-type $2 \times 10^{16} \text{ cm}^{-3}$ (Te)	3500nm
1	GaSb	n-type $2 \times 10^{18} \text{ cm}^{-3}$ (Te)	400nm
0	GaSb substrate N+		

Figure 5.2.7: Diode structure used with a metallic PhC structure.

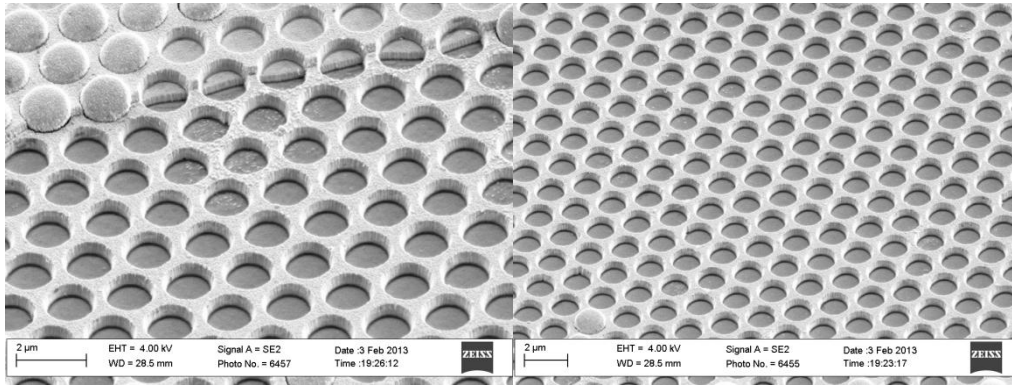


Figure 5.2.8: SEM image of PhC enhanced diode. *Left:* the edge of the aperture is shown and the PhC acts as a continuation of the ohmic contact. *Right:* PhC pattern over the center of the photodiode.

I-V curves were taken for the photodiode under three conditions: no PhC and an ARC, a PhC and no ARC, and a PhC and an ARC. The ARC was constructed from 100 nm of SiN_x deposited using a PECVD. The I-V curves, shown in Figure 5.2.9, were taken using an AM 1.5 solar simulator at 10x concentration.

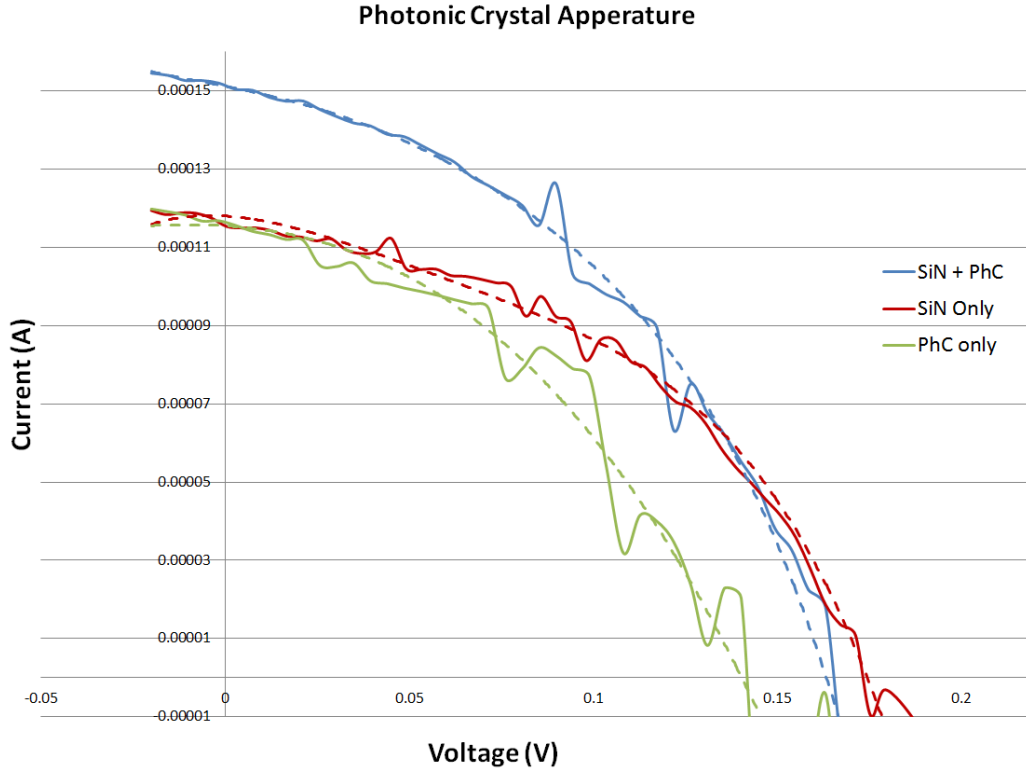


Figure 5.2.9: I-V curve of a GaSb photodiode with and without a PhC. This data was taken from the same diode in order to maintain consistency with processing and I-V characteristics.

Figure 5.2.8 was then analyzed in order to determine the effect of a PhC cavity on diode conversion efficiency. The results are shown in Figure 5.2.10.

	I_{sc} (mA)	V_{oc} (mV)	FF(%)	Max Power (μ W)	CE (%)
SiN_x - ARC	.115	175	64	9.06	4.38
PhC - No ARC	.115	142	73	7.63	3.69
PhC - ARC	.150	165	62.5	10.5	5.08

Figure 5.2.10: The resulting performance metrics of the PhC enhanced GaSb TPV diode stage. Of particular note is the I_{sc} , max power, and conversion efficiency, which result from an increased number of photogenerated excitations.

It is important to note that various diodes were processed along with the PhC diodes. These diodes were passivated with SiN, and then underwent all of the same processing steps as the PhC diodes (with the exception of e-beam

lithography writing). The purpose was to show that it was the PhC pattern which enhanced the photodiode, not the additional processing. After processing, only PhC enhanced diodes showed any increase in performance. The I-V curves of four of the sixteen representative unenhanced photodiodes are shown in Appendix 5.2.2 for reference if desired.

5.3 Interfacial Misfit Array (IMF) Photodiodes

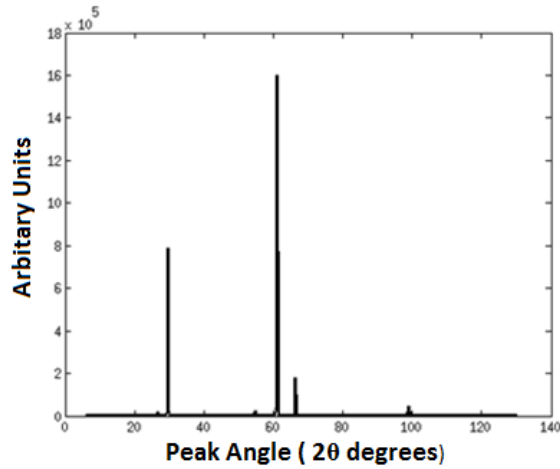
The aim of this work is to compare the efficiencies of two types of GaSb photodiodes. Theoretically, there should be no difference between the active region of these photodiodes. The only ways in which these structures differ is substrate material. Sample 1 (R9-86), is a standard GaSb photodiode grown on a GaSb substrate. Sample 2 (R9-81) is a standard GaSb photodiode grown on a GaAs substrate with the addition of an IMF layer. These two structures are both shown in Figure 5.3.1.

R9-81			
GaSb/GaAs			
8	GaSb	p-type $2 \times 10^{19} \text{ cm}^{-3}$ (Be)	10nm
7	$\text{Al}_{0.4}\text{Ga}_{0.6}\text{Sb}$	p-type $2 \times 10^{19} \text{ cm}^{-3}$ (Be)	50nm
6	GaSb	p-type $2 \times 10^{18} \text{ cm}^{-3}$ (Be)	50nm
5	GaSb	p-type $2 \times 10^{16} \text{ cm}^{-3}$ (Be)	200nm
4	GaSb	NID	1500nm
3	GaSb	n-type $2 \times 10^{16} \text{ cm}^{-3}$ (Te)	3500nm
2	GaSb	n-type $2 \times 10^{18} \text{ cm}^{-3}$ (Te)	400nm
1	GaAs	n-type	50nm
0	GaAs substrate N+		

R9-86			
GaSb/GaSb			
7	GaSb	p-type $2 \times 10^{19} \text{ cm}^{-3}$ (Be)	10nm
6	$\text{Al}_{0.4}\text{Ga}_{0.6}\text{Sb}$	p-type $2 \times 10^{19} \text{ cm}^{-3}$ (Be)	50nm
5	GaSb	p-type $2 \times 10^{18} \text{ cm}^{-3}$ (Be)	50nm
4	GaSb	p-type $2 \times 10^{16} \text{ cm}^{-3}$ (Be)	200nm
3	GaSb	NID	1500nm
2	GaSb	n-type $2 \times 10^{16} \text{ cm}^{-3}$ (Te)	3500nm
1	GaSb	n-type $2 \times 10^{18} \text{ cm}^{-3}$ (Te)	400nm
0	GaSb substrate N+		

Figure 5.3.1: Two structures grown using molecular beam epitaxy. *Top:* R9-81 is a GaSb junction grown on GaAs with a IMF layer. *Bottom:* R9-86 is an identical junction grown on a GaSb substrate.

These two samples were initially compared using XRD. The IMF layer is expected to allow the lattice constant of R9-81 to be that of GaSb grown on GaSb. However, if the lattice constant measured for R9-81 is not that of GaSb, the IMF growth is not compensating for the change in lattice constant, and defects will result. The XRD measurements are shown in Figure 4.3.2.



Strain Mitigation Successful:

Measured lattice constant GaAs/GaAs:
– 5.622 Angstroms

Measured lattice constant GaSb/GaSb:
– 6.056 Angstroms

Measured lattice constant with IMF:
– 6.056 Angstroms

material (order of interference)	peak angle, 2θ (degrees)	lattice constant (Å)	average lattice constant (Å)
GaSb (n=1)	29.60	6.0361	6.0558 ± 0.0278
GaSb (n=2)	61.00	6.0754	
GaAs (n=2)	66.33	5.6370	5.6370

Figure 5.3.2: XRD data for the IMF layer. The measured lattice constant for the R9-81 was consistent with a GaSb on GaSb junction.

To compare the efficiencies of these samples, they were processed into photodiode mesas and aperture arrays. The full fabrication procedure is found in Appendix 5.3.1. However, a brief process overview is given in Figure 5.3.3.

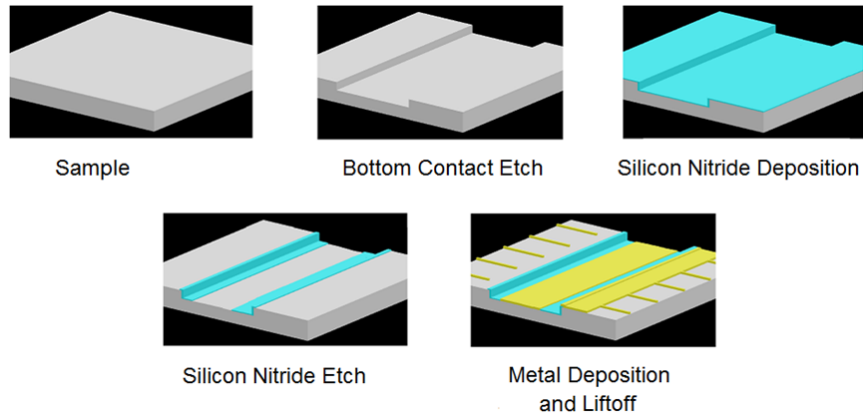


Figure 5.3.3: photodiode fabrication process. The sample is first etched to the bottom contact and then coated with Si_3N_4 . The Si_3N_4 is then etched leaving behind a layer of sidewall passivation. Finally the contacts are metalized to create a photosensitive structure.

In order to insure that efficiency measurements were accurate between fabrication runs, contact resistances were tested on IMF top contacts in order to assure an ohmic response. Ohmic I-V curves were observed and are shown in Figure 5.4.4 along with a linear transfer length method (TLM) pattern.

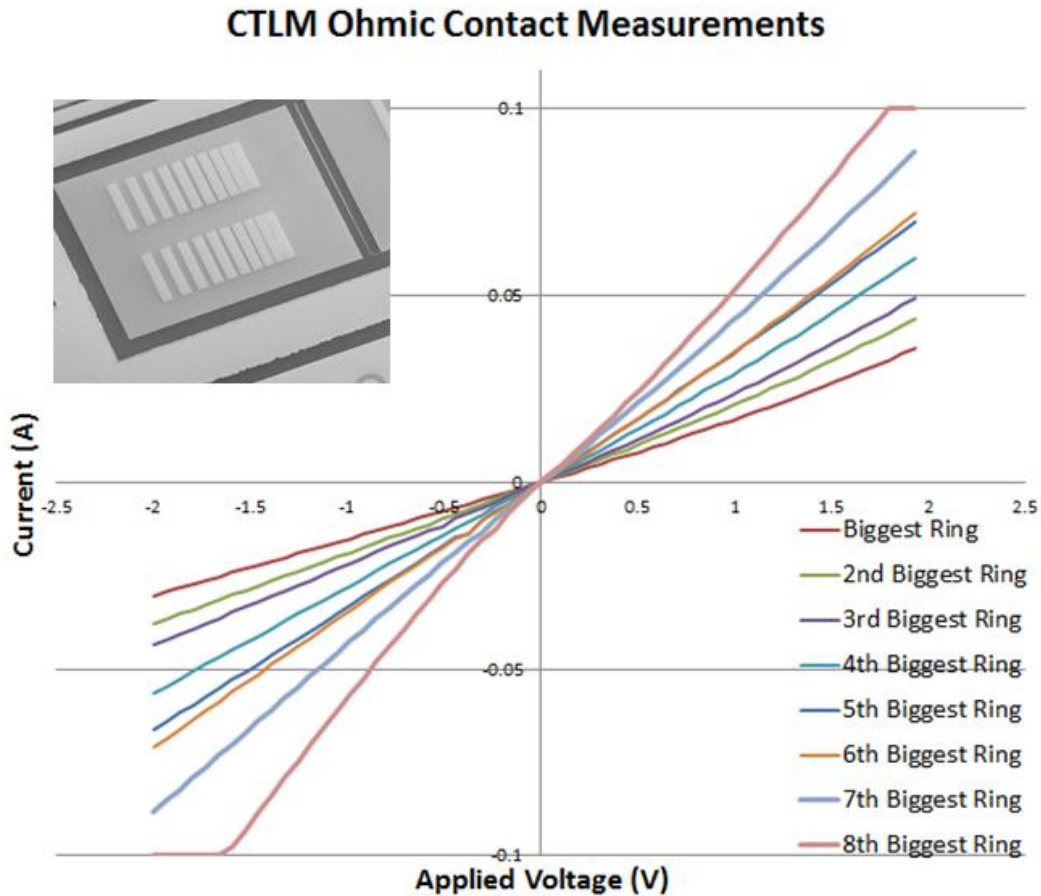


Figure 5.3.4: *Insert:* Image of a TLM pattern on the top contact layers. *Bottom:* Ohmic contact I-V curves for R9-81 top contacts using various circular TLM patterns.

Both samples, R9-86 and R9-81, were fabricated into a standard photodiode mesa, shown in Figure 5.4.5. The samples were then tested using the solar simulator in order to produce I-V curves. The resulting curves are shown in Figure 5.3.6.

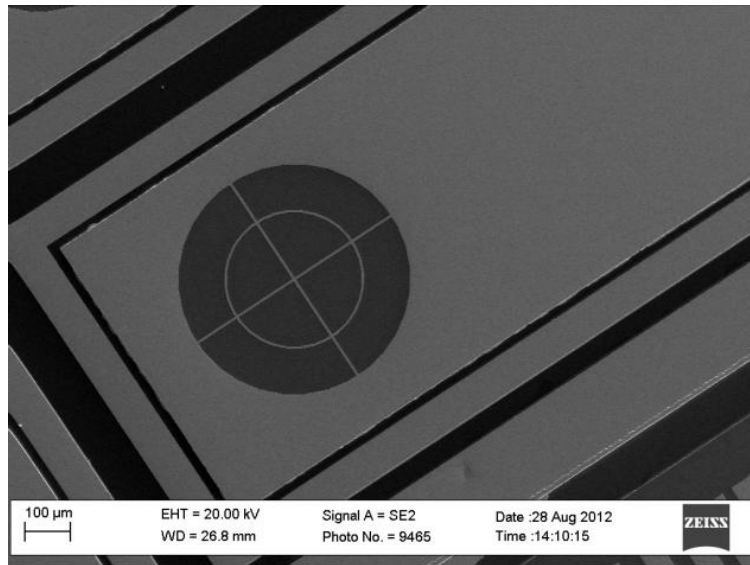


Figure 5.3.5: Standard photodiode mesa patterns.

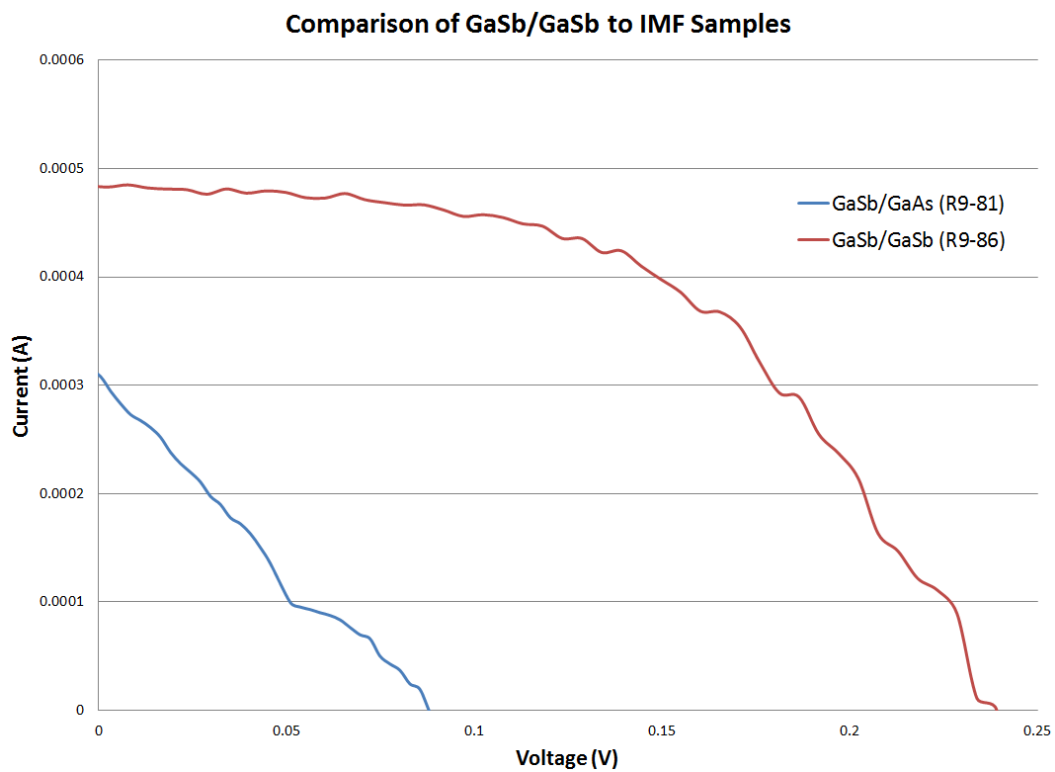


Figure 5.3.6: *Left:* comparison of the R9-86 photodiode and R9-81 photodiode. *Right:* relative I-V characteristics.

In order to compare recombination rates, the samples were also fabricated into sets of aperture patterns. These patterns consist of ten different size apertures ranging from 30 μm to 240 μm , as shown in Figure 5.3.7.

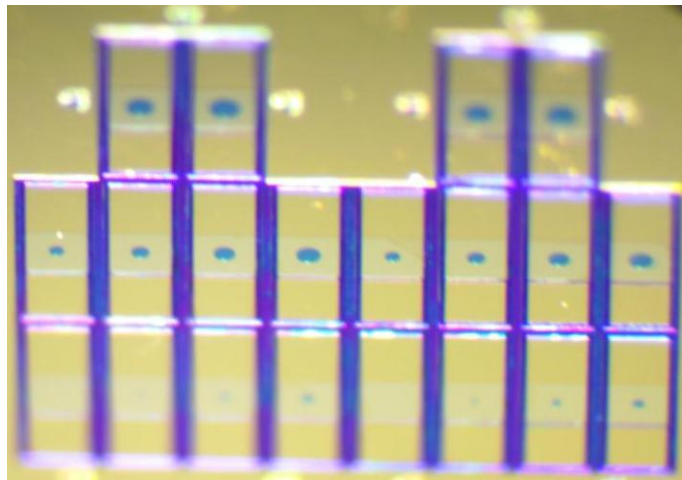
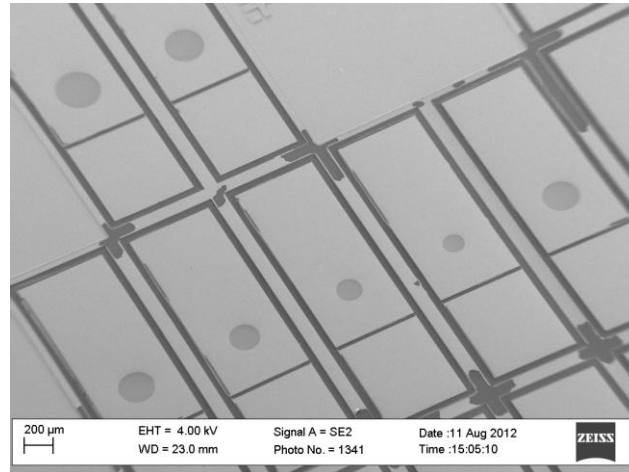


Figure 5.3.6: Apertures ranging from 30 μm to 300 μm fabricated to test relative surface recombination rates.

Comparing the relative I-V curves of all apertures, allows one to determine surface defect density by comparing relative efficiencies with aperture size. If no defect density exists, then the increase in aperture size will result in a proportional increase in efficiency. However, if defect densities are larger, then the increase in aperture size will also increase defects present. This will result in a lower

proportional efficiency. The I-V curves for R9-81 and R9-86 are shown in Figure 5.3.7.

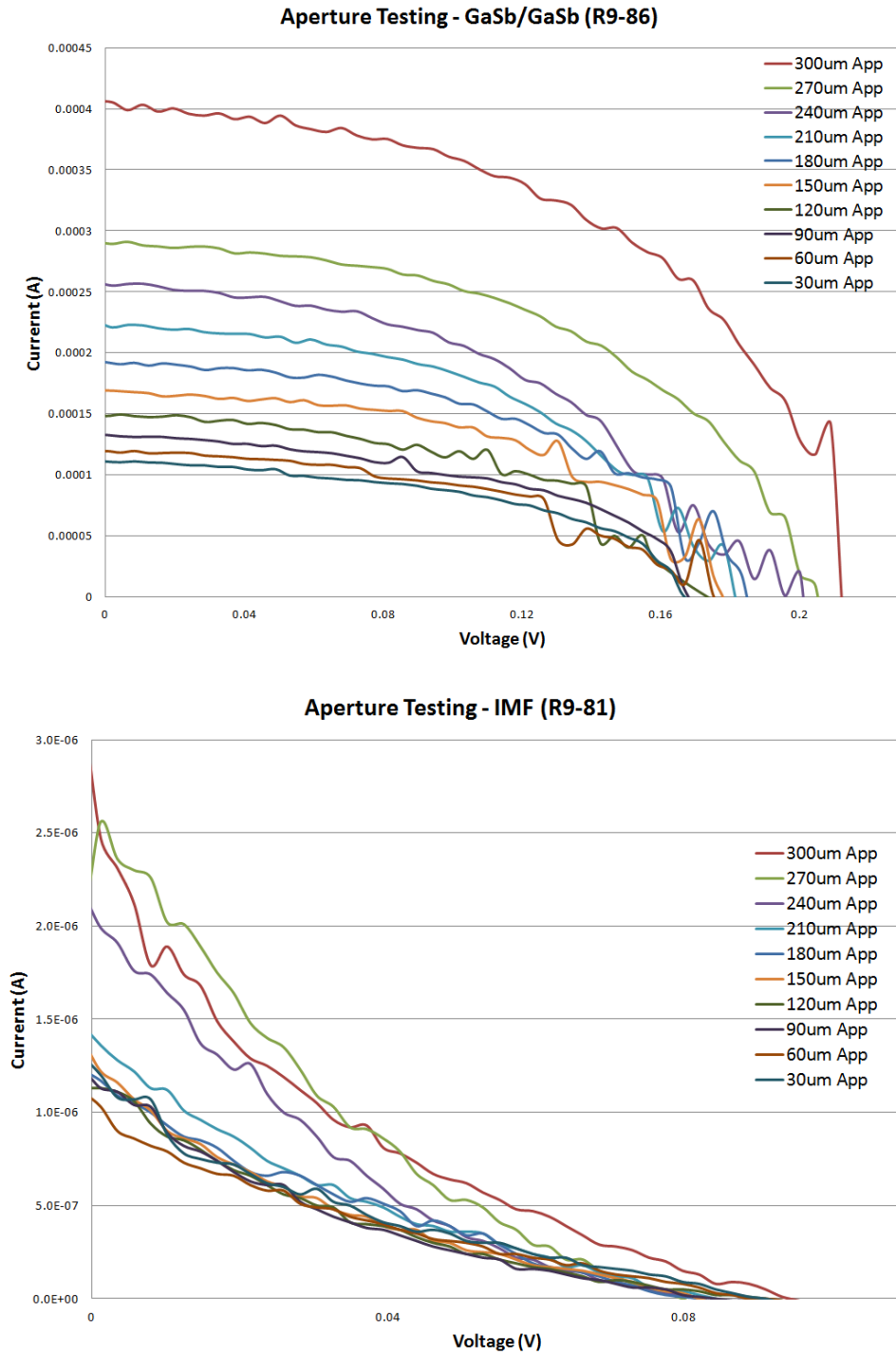


Figure 5.3.7: *Top:* Aperture I-V curves obtained for the GaSb on GaSb R9-86 sample. *Bottom:* I-V curves obtained for the GaSb on GaAs with IMF layer.

These initial growths showed inconsistency between expected efficiency for the IMF sample (R9-81) in comparison to the control GaSb/GaSb sample (R9-86). In order to determine potential defects within the IMF structure, the short circuit current densities were plotted with respect to aperture size. These currents are shown in Figure 5.3.8. Finally, in order to better characterize IMF TPV diodes, three optimized structures were then grown based on Figure 5.3.9.

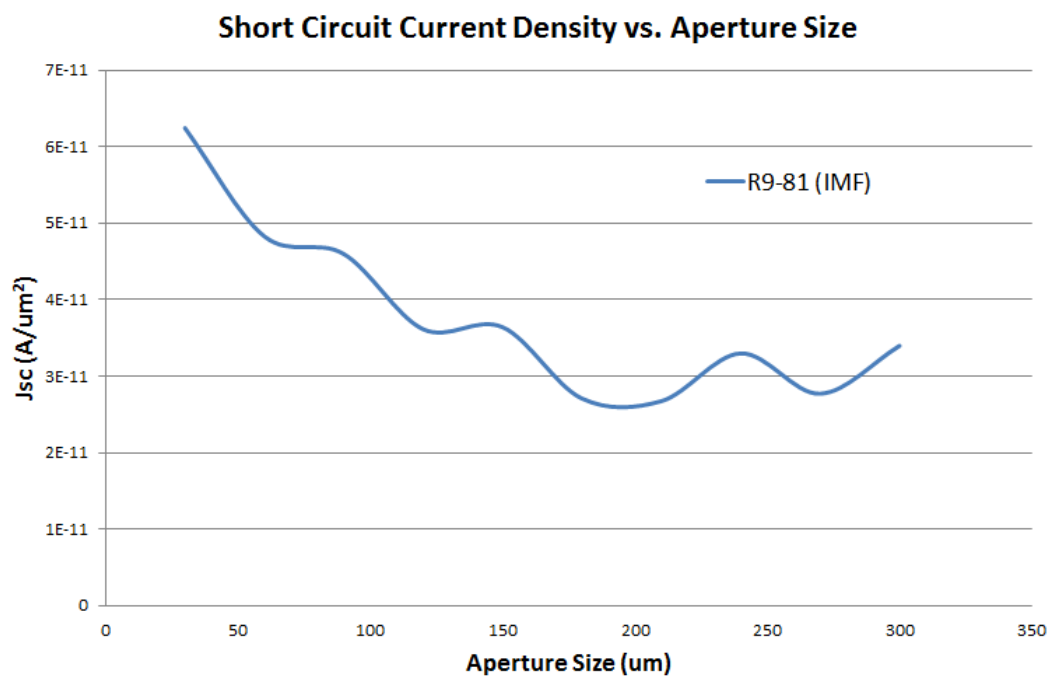
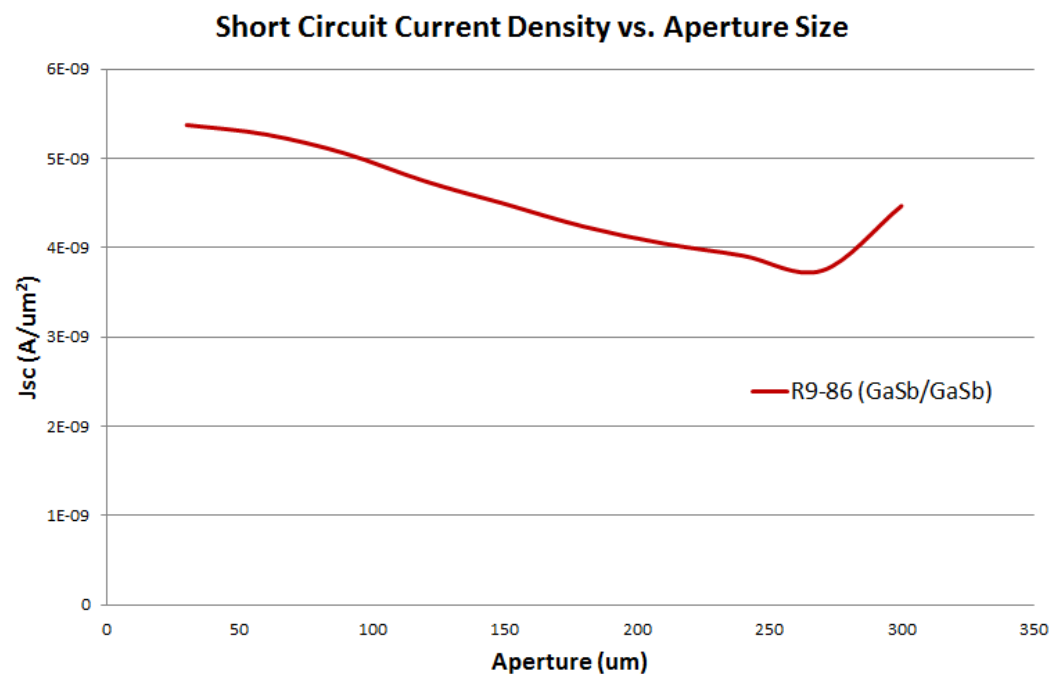


Figure 5.3.8: Current densities obtained from the apperture diode set for the R9-86 (*Top*) and R9-81 (*Bottom*) sample set.

These samples then underwent post fabrication quality control tests including spectral response and electroluminescence. Spectral response is a useful metric in determining the optimum wavelengths absorbed for each cell as well as crystal quality. For this reason, the spectral response of the IMF and GaSb/GaSb samples were measured for two wavelength ranges, 800 nm to 2000 nm (Figure 5.3.9). Electroluminescence was also measured and is shown in Figure 5.3.11.

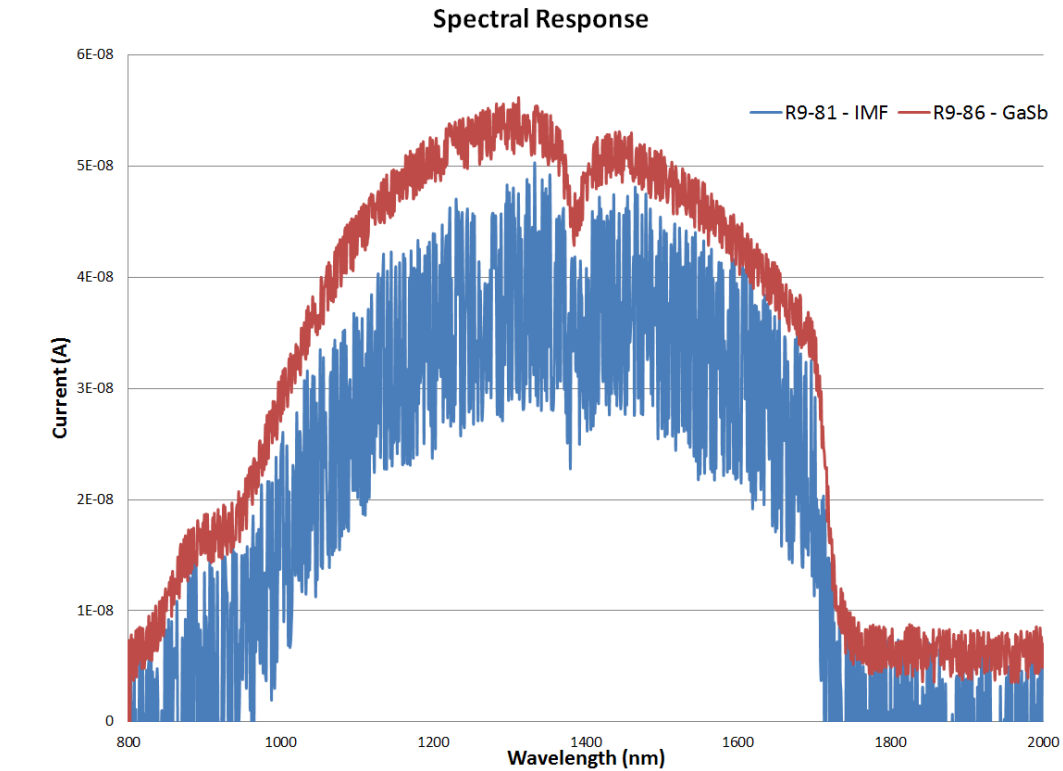


Figure 5.3.9: Spectral response from 800 nm to 2000 nm, the high noise is due to low optical transmission in the filtering grating of the monochromator.

Due to the relatively low efficiencies observed in both the GaSb/GaSb (R9-86) and IMF (R9-81) samples, three new TPV diode structures were proposed and are shown in Figure 5.3.10. Structure 1 is shown in Figure 5.3.10. Structure 2 adds an IMF layer between layer 0 and layer 1, and Structure 3 is

formed by replacing layer 0 of Figure 5.3.10 with GaSb. The expected improvement was also simulated using Sentarus by Synopsis, and is shown in Figure 5.3.11. This new structure is expected to improve efficiency through optimized layer thicknesses as well as a decreased n-type doping in layer 1. The decreased doping is expected to lower the short circuit current density; however, it will also improve crystal quality throughout the structure.

Layer	Material	Doping	Description	Thickness
6	GaSb	p-type 2×10^{19} (Be)	Top Contact	10 nm
5	$\text{Al}_{0.3}\text{Ga}_{0.7}\text{Sb}$	p-type 2×10^{19} (Be)	Window Layer	50 nm
4	GaSb	p-type 2×10^{18} (Be)	Buffer Layer	50 nm
3	GaSb	p-type 2×10^{16} (Be)	Absorber	1500 nm
2	GaSb	n-type 2×10^{16} (Te)	Emitter	500 nm
1	GaSb	n-type 2×10^{17} (Te)	Back Contact	400 nm
0	Substrate			

Figure 5.3.10: Optimized Structure to further test benefits of using an IMF layer. These designs consist of a three sample group. Sample 1 is shown above. Sample 2 adds a IMF layer between layer 0 and 1. Sample 3 replaces layer 0 with a GaSb substrate.

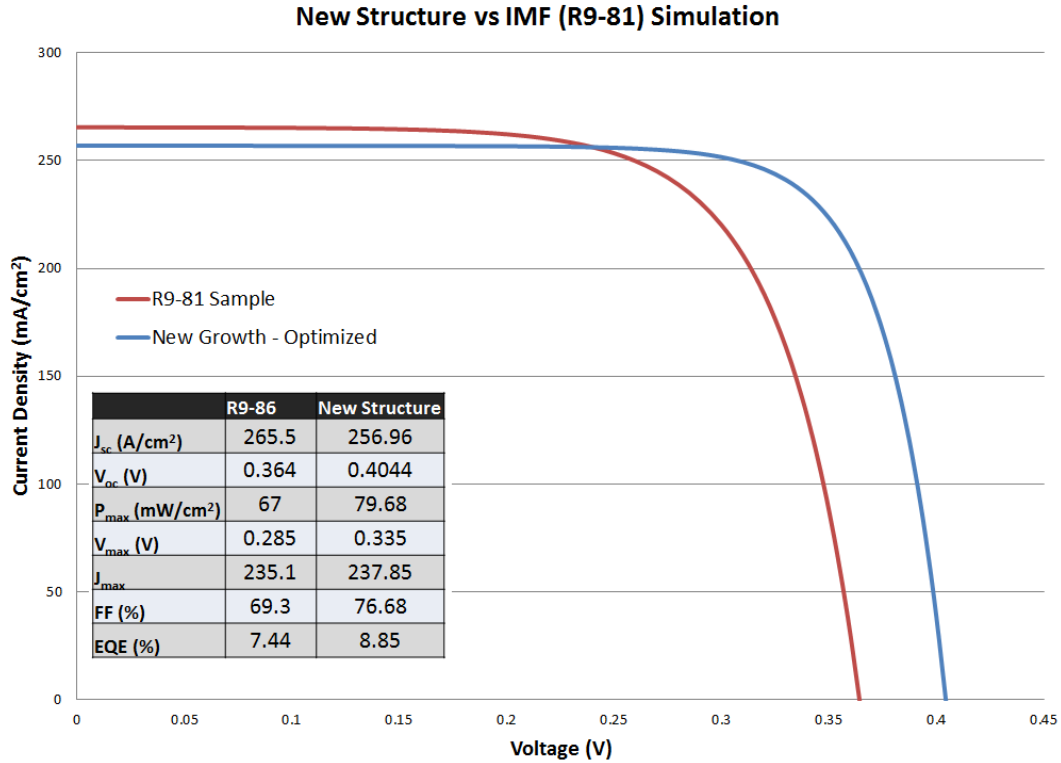


Figure 5.3.11: Optimized growth is simulated to perform with a higher efficiency as well as provide better crystal quality due to a lower doped n-type contact region.

5.4 Metamaterial Polarization Grid

The creation of a new metamaterial device follows a general process flow: device conception, simulation, fabrication, and testing. However, the creation of a dynamic metamaterial polarization sensitive device may cause this process flow to become overly complicated. To simplify this results section, information will be provided in the following manner: Static simulation results, device fabrication, dynamic simulation results, dynamic device fabrication. It is important to note however, the results were not obtained in this chronological order. For example,

both dynamic and static simulations were performed before any device fabrication. However, for simplicity, this section is broken up into two sections: static results and dynamic results.

5.4.1 Static Results

As described in Chapter 3, there are problems easily converting any of the existing polarization sensitive MMs into dynamic polarization filters. The two greatest challenges are to maximize transmission and to maintain MM resonance when a contact metallization is applied.

CST Microwave Studio was used to simulate the MM structures in the section. The design itself utilizes a sapphire substrate to maximize signal transmittance (tested at 80% transmission from 2 μm to 6 μm when utilizing a 500 μm thick substrate). However, as the substrate has no impact on the MM response, sapphire was not included in the simulations.

Perhaps one of the more important variables in creating a dynamic MM is semiconductor thickness. This layer must be thick enough to allow good electrical conduction when an external bias is applied. If this layer is too thick, the trade-off is a severely reduced MM response as well as a large reduction in overall transmission percentage. To this end, a compromise of 400nm GaAs layer was utilized. The MM pattern used is a thin gold rectangle and a very thin contact bar. The capacitive element is the area between rectangles in the repeating pattern. The metamaterial pattern was then constructed on the GaAs layer, shown in Figure 4.4.1.1.

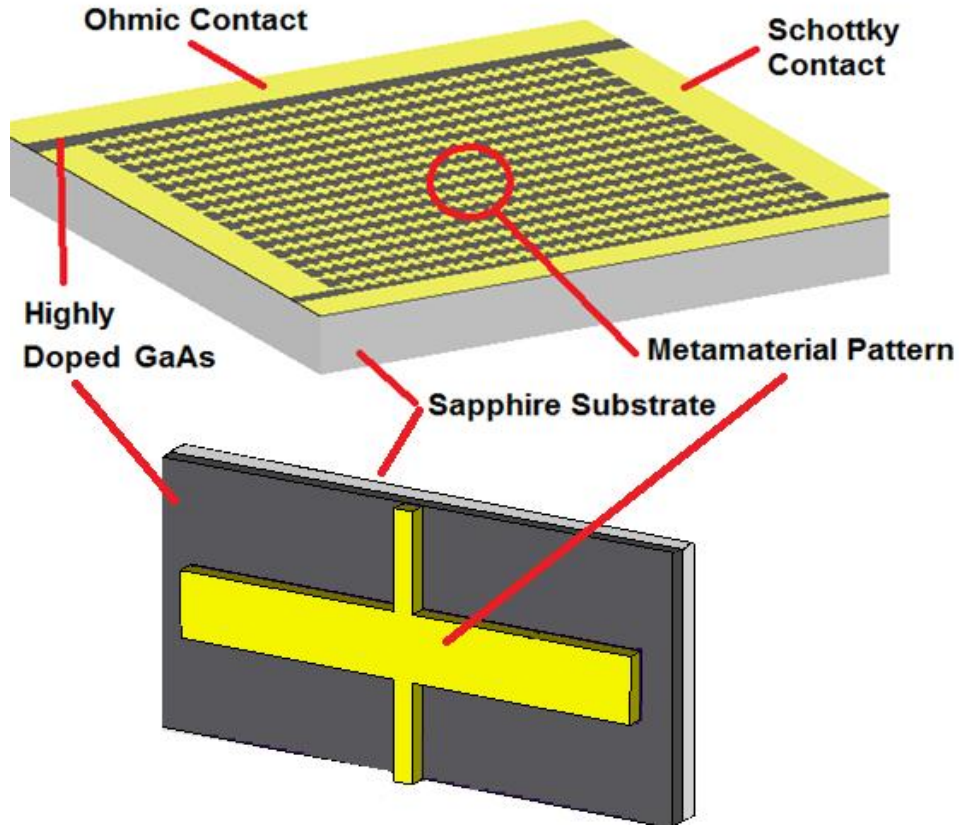


Figure 5.4.1.1: Metamaterial pattern, substrate, and semiconductor layer used to create a dynamic MM response.

Initial simulation utilized the Drude model for the Au metamaterial and lightly doped GaAs (n-type, carrier concentration around $1 \times 10^{14} \text{ cm}^{-3}$). In order to determine polarization sensitivity, the structure was exposed to x-polarized and y-polarized light. The resulting transmission curves are shown in Figure 5.4.1.2.

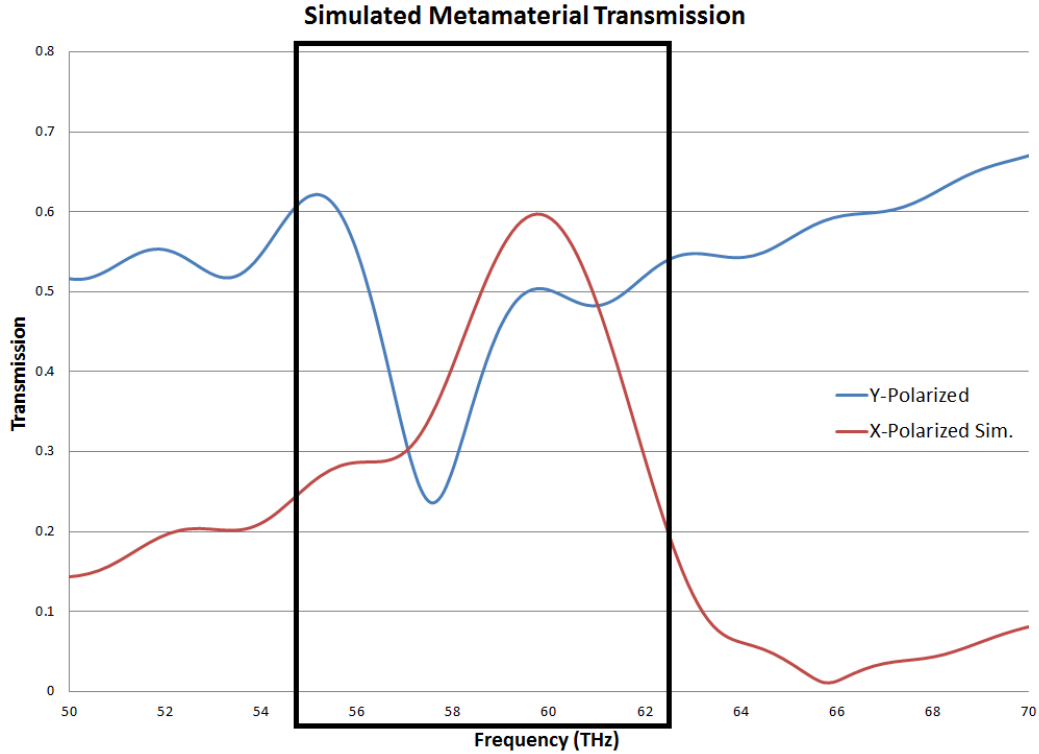


Figure 5.4.1.2: Simulated transmission characteristics of the MM polarization grid. Purple is the S-polarized transmission and green is the Y-polarized transmission. Highlighted in a black square is the resonance frequency of the MM for each polarization.

Of particular note in Figure 4.4.1.2 is the area from 55 THz to 63 THz. This region corresponds to $4.28 \mu\text{m}$ to $4.68 \mu\text{m}$, and is the range of note for this dynamic polarizer. These signals were analyzed in the static case at a frequency of 61 THz. Ideally, in a non-biased case, the horizontal to vertical polarization ratio should be 1:1; at 61 THz and 57 THz, this is in fact the case. In order to determine the E-field response and surface currents created in these structures, CST Microwave studio was also used to measure these properties at various points within the structure. A few select examples are shown in Figure 5.4.1.3 and Figure 5.4.1.4.

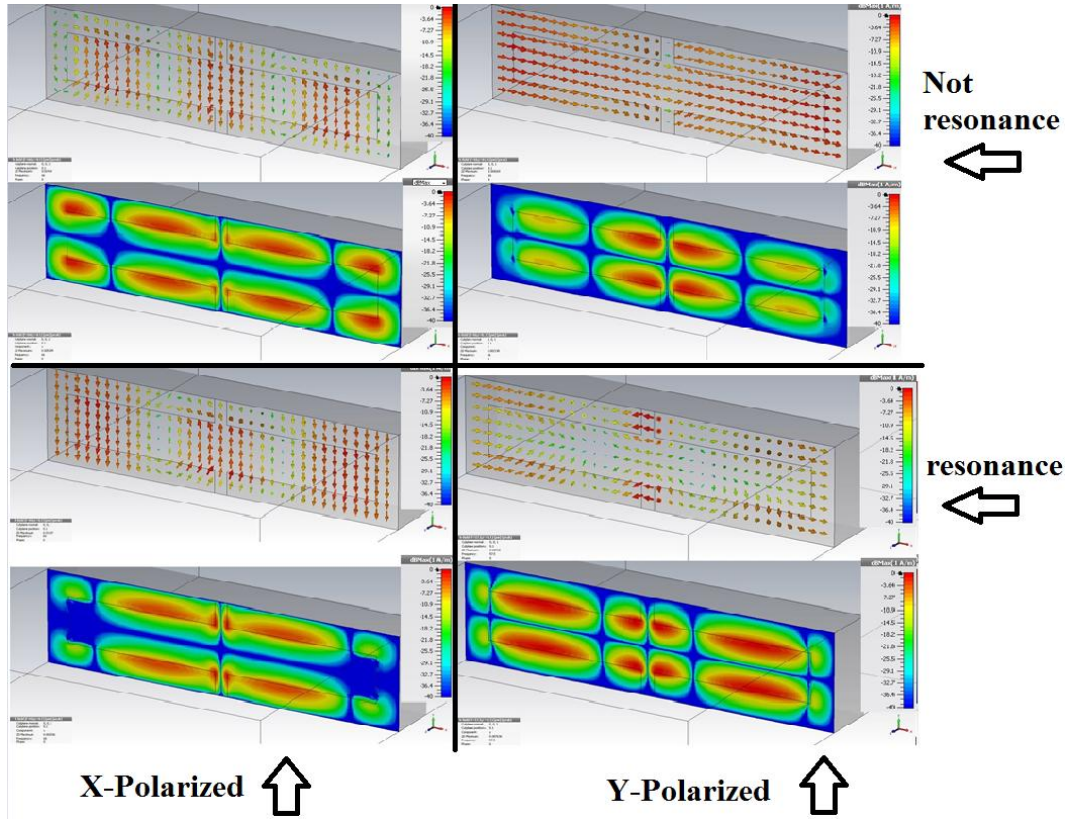


Figure 5.4.1.3: Magnetic field and surface current at the Au/GaAs interface. For each pair, top images are vector and bottom images are magnitude. *Top Left:* Off resonance (66 THz) X-polarized surface current direction and H-field magnitude. *Top Right:* Off resonance (66 THz)Y-polarized surface current direction and H-field magnitude. *Bottom Left:* X-polarized surface current direction and H-field magnitude at resonance (60 THz). *Bottom Right:* Y-polarized surface current direction and H-field magnitude at resonance (57.5 THz).

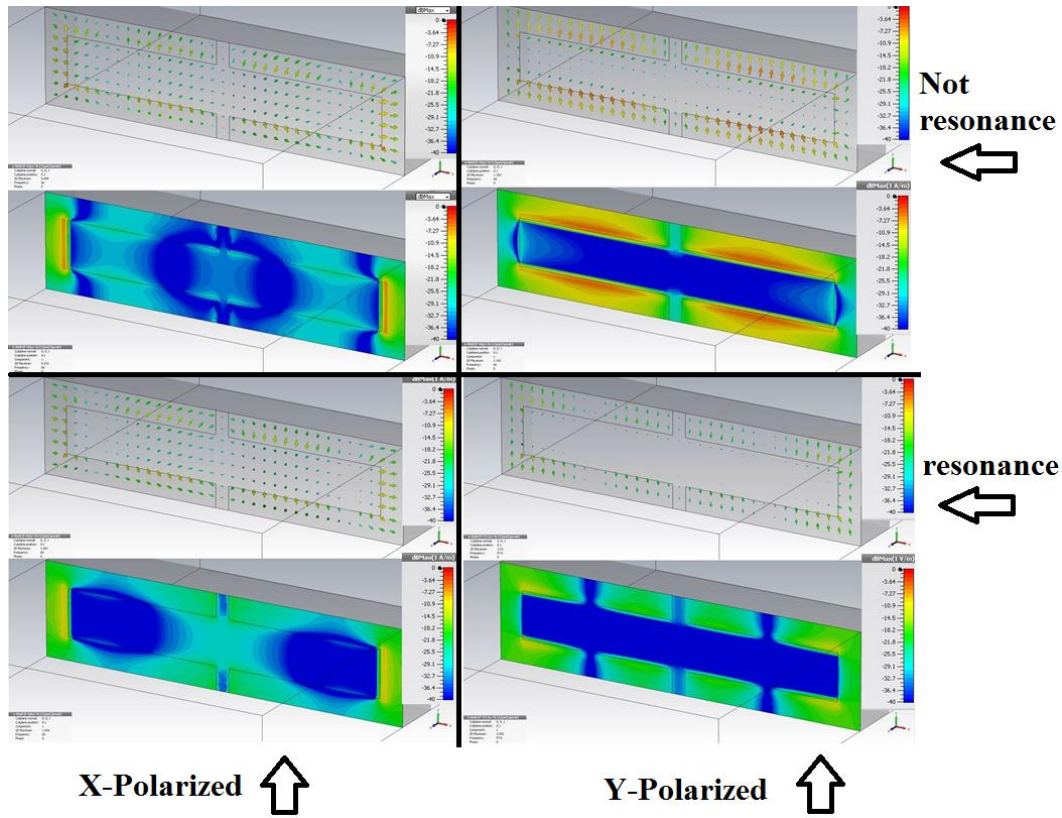


Figure 5.4.1.4: Electric Field at the Au/GaAs interface. For each pair, top images are vector and bottom images are magnitude. *Top Left:* Off resonance (66 THz) X-polarized surface current direction and H-field magnitude. *Top Right:* Off resonance (66 THz) Y-polarized surface current direction and H-field magnitude. *Bottom Left:* X-polarized surface current direction and H-field magnitude at resonance (60 THz). *Bottom Right:* Y-polarized surface current direction and H-field magnitude at resonance (57.5 THz).

The sample was then fabricated using r-plane sapphire (0112) and lightly doped GaAs grown using molecular beam epitaxy. The MM pattern was fabricated using electron beam lithography and electron beam thermal evaporation. A detailed fabrication procedure can be found in Appendix 5.4.1 and the resulting MM pattern is shown in Figure 5.4.1.5.

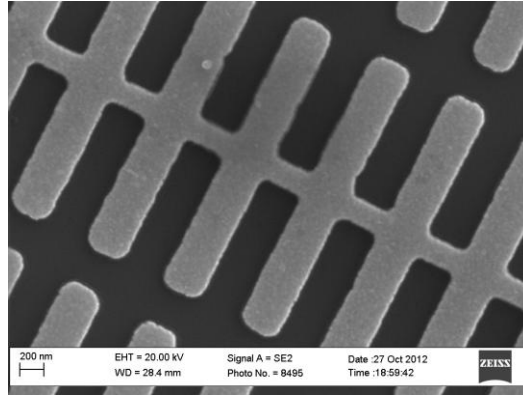


Figure 5.4.1.5: SEM image of a Au MM pattern fabricated on GaAs.

Testing was then performed using Fourier transfer infrared spectroscopy (FTIR), and a sapphire/GaAs substrate with no MM pattern as the background. The resulting transmission characteristics are shown in Figure 5.4.1.6.

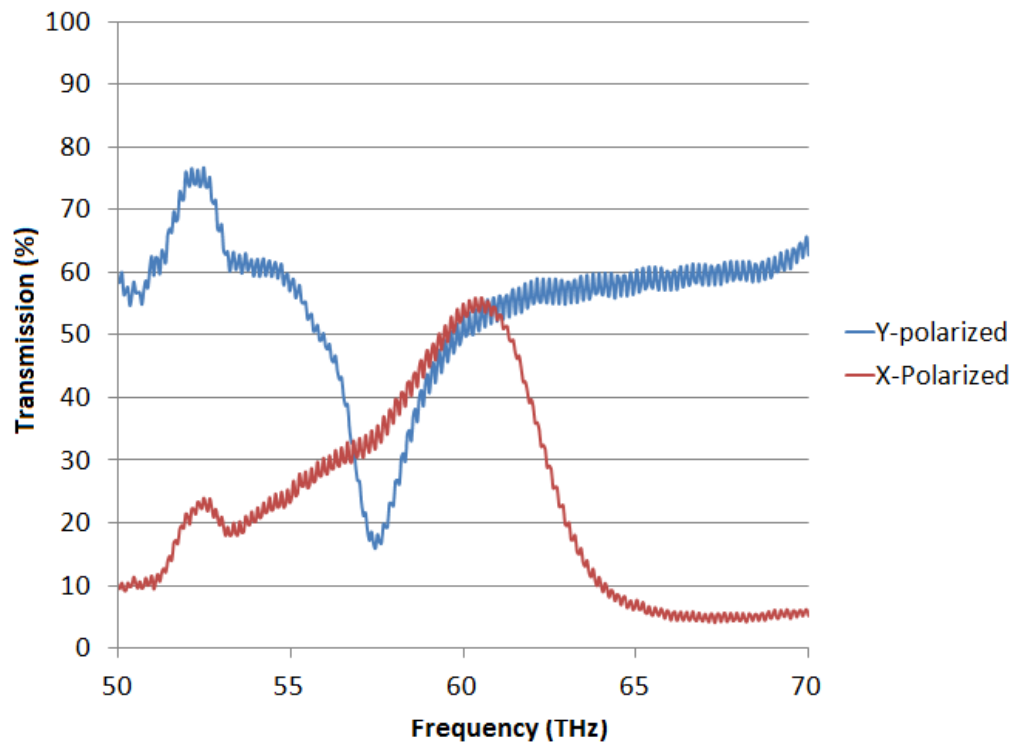


Figure 5.4.1.6: Experimental transmission for X and Y-polarized light obtained using FTIR data.

As can be seen from Figure 4.4.1.6, the transmission characteristics resemble those of Figure 5.4.1.2. Also, there is a 1:1 ratio of horizontal: vertical polarized light at 60THz (5um). Figure 5.4.1.7 summarizes data for the static case.

Ratio [Static]	Simulation (Frequency)	Experimental (Frequency)
Polarization - H:V	1:1 (61 THz)	1:1 (61 THz)

Figure 5.4.1.7: Static transmission Characteristics comparing simulation and experimental data at the resonance frequency (61 THz).

In order to further characterize the static dynamic polarizers, the effective optical constants were calculated for each polarization case. These results are shown for the X-Polarization in Figure 5.4.1.8, Y-polarization in Figure 5.4.1.9.

X- Polarization Characterization

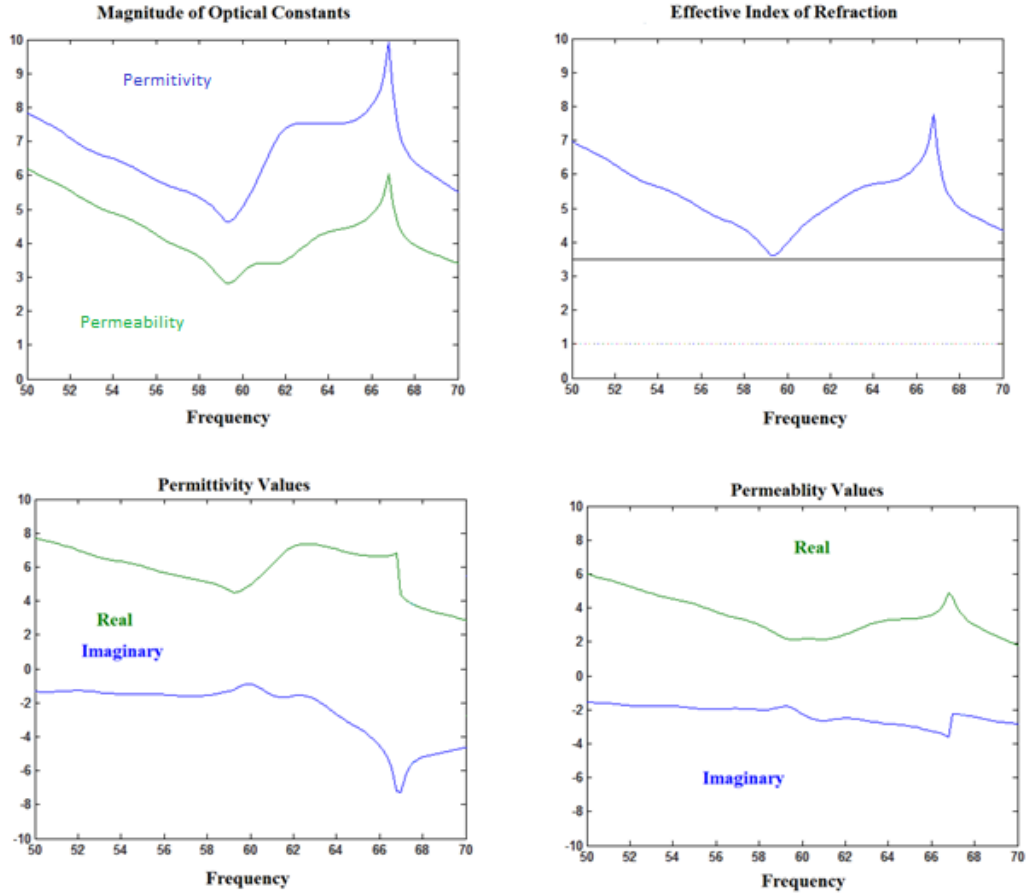


Figure 5.4.1.8: *Top Left:* effective permeability and permittivity. *Top Right:* the effective index of refraction of the MM. *Bottom Left:* Real and imaginary permittivity values. *Bottom Right:* Real and imaginary permeability values.

Y- Polarization Characterization

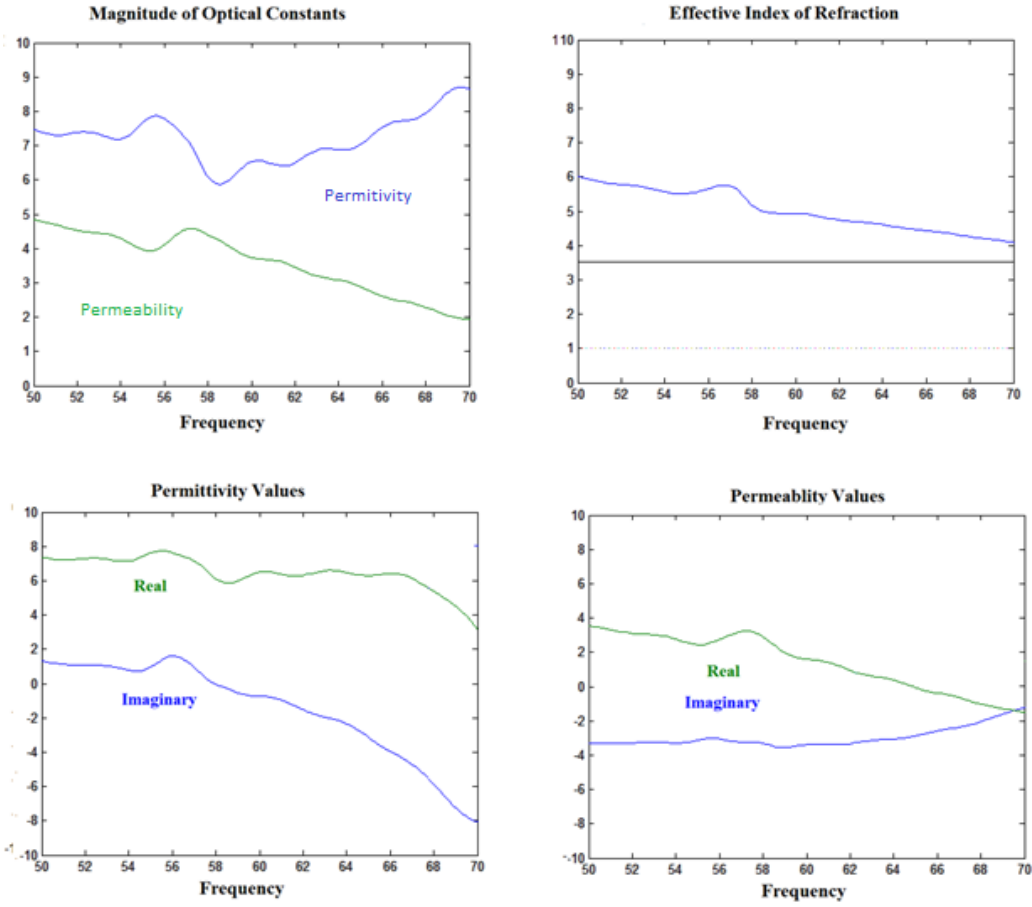


Figure 5.4.1.9: *Top Left:* effective permeability and permittivity. *Top Right:* the effective index of refraction of the MM. *Bottom Left:* Real and imaginary permittivity values. *Bottom Right:* Real and imaginary permeability values.

A study was also undertaken to explore the wavelength scalability of a metamaterial polarization grid. To this effect, the metamaterial pattern was increased in size by 100 nm in the X-direction and 200 nm in the Y-direction. This was done to show the orthogonality of the metamaterial response in relation to structure size. From simulation data, it is expected that the Y-transmission

peak will experience a larger blue-shift when structure size is altered. The results are shown in Figure 5.4.1.10.

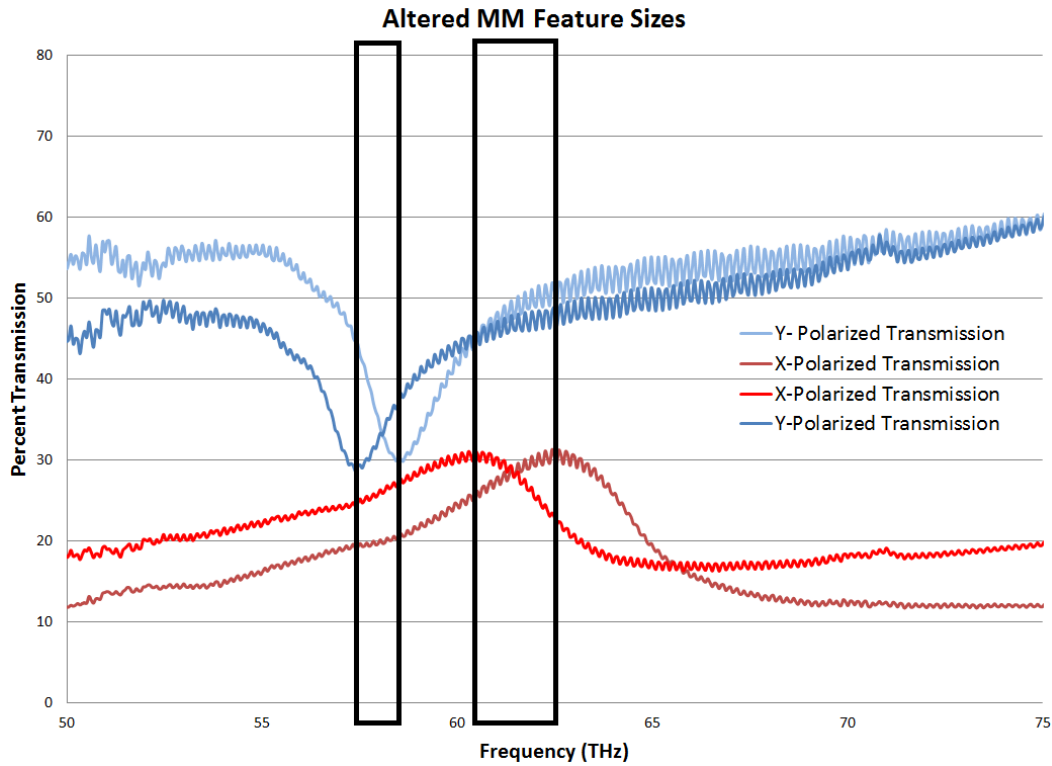


Figure 5.4.1.10: Experimental demonstration of MM scalability. When the pattern size is in one direction, the corresponding polarization resonance peak is also altered.

Work was also done in order to determine if the GaAs on a sapphire substrate was an influence on the MM response. In order to verify the necessity of a highly insulating substrate, the MM structure was constructed on lightly doped n-type GaAs DSP substrates. These results, both experimentally as well as in simulation do not exhibit the strong MM response of the GaAs on sapphire substrate, shown in Figure 5.4.1.11. Therefore, the construction of a dynamic MM polarizer must utilize only a thin semiconductor layer and an insulation layer to create a MM response.

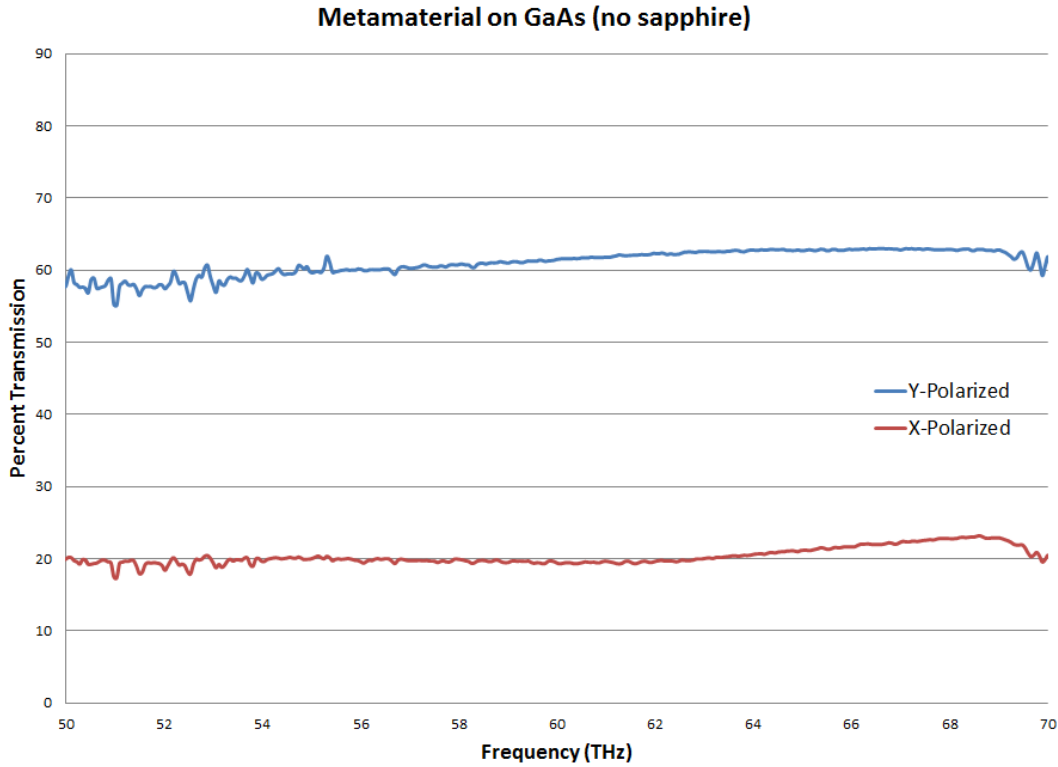


Figure 5.4.1.11: The MM response is removed as the thickness of the GaAs layer is increased.

The effect of the semiconductor doping level on the metamaterial resonance response was also investigated. The MM sample was fabricated on GaAs/sapphire using three doping levels (Te doped - $1 \times 10^{16} \text{ cm}^{-3}$, $1 \times 10^{17} \text{ cm}^{-3}$, and $1 \times 10^{18} \text{ cm}^{-3}$). It was expected that the increased conductivity of the doped GaAs would cause a decrease in MM response and a blue shift. As can be seen from Figure 5.4.1.12, both effects were observed. The MM resonance experience a blue-shift of approximately 3THz and a significant decrease in transmission as doping concentration increased.

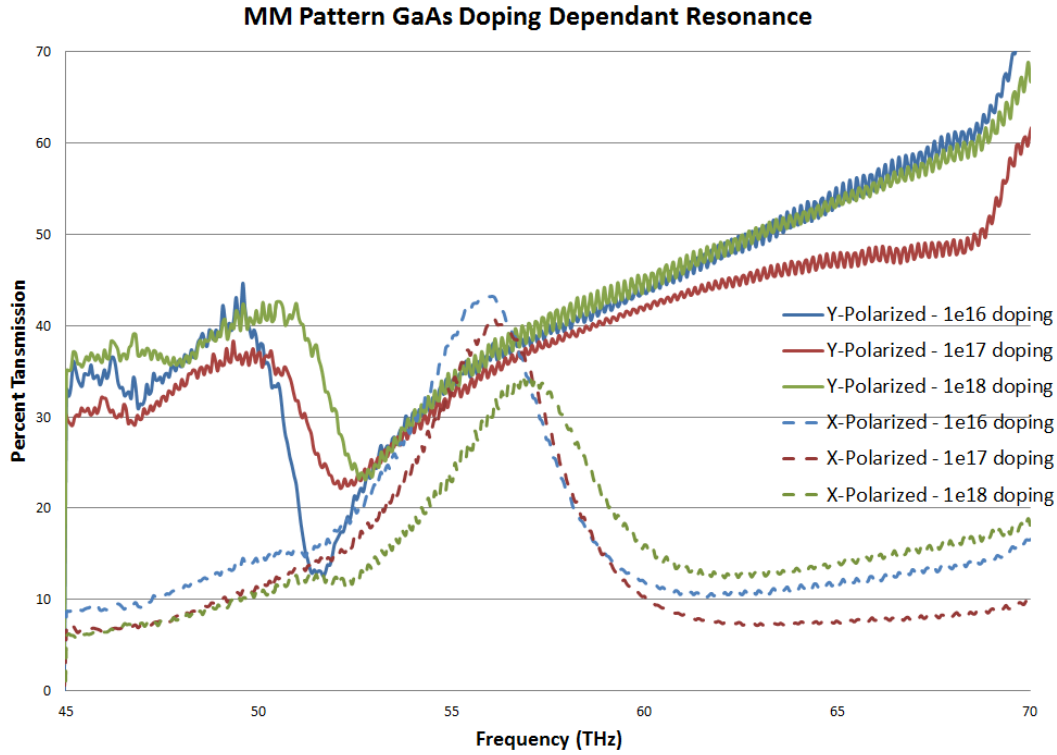


Figure 5.4.1.12: Doping dependence of MM response. There is a blue-shift experienced with increased doping levels, as well as a decrease in transmission consistent with higher conductivity.

5.4.2 Dynamic Results

The structure described in Section 5.4.1 was designed with the ability to operate with an applied bias. In order to simulate this response, the conductivity of the GaAs layer was increased. As shown in Chapter 2, altering the conductivity of the dielectric has a direct impact on the MM transmission. The simulation results for various GaAs conductivities are shown in Figure 5.4.2.1.

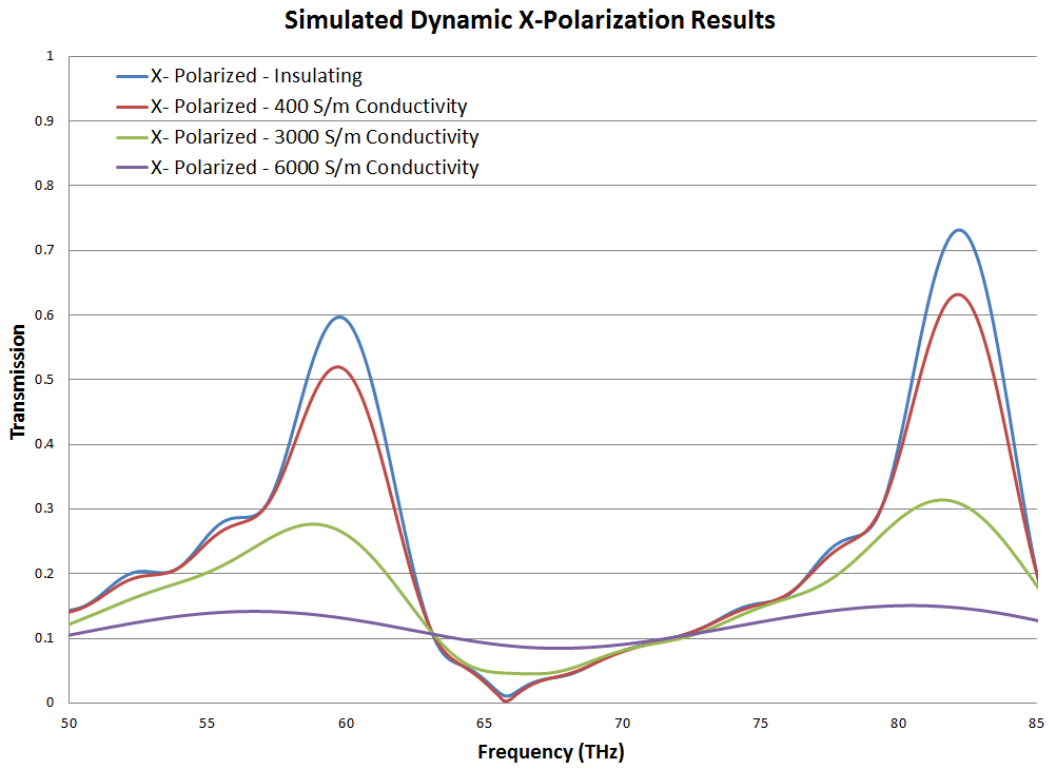
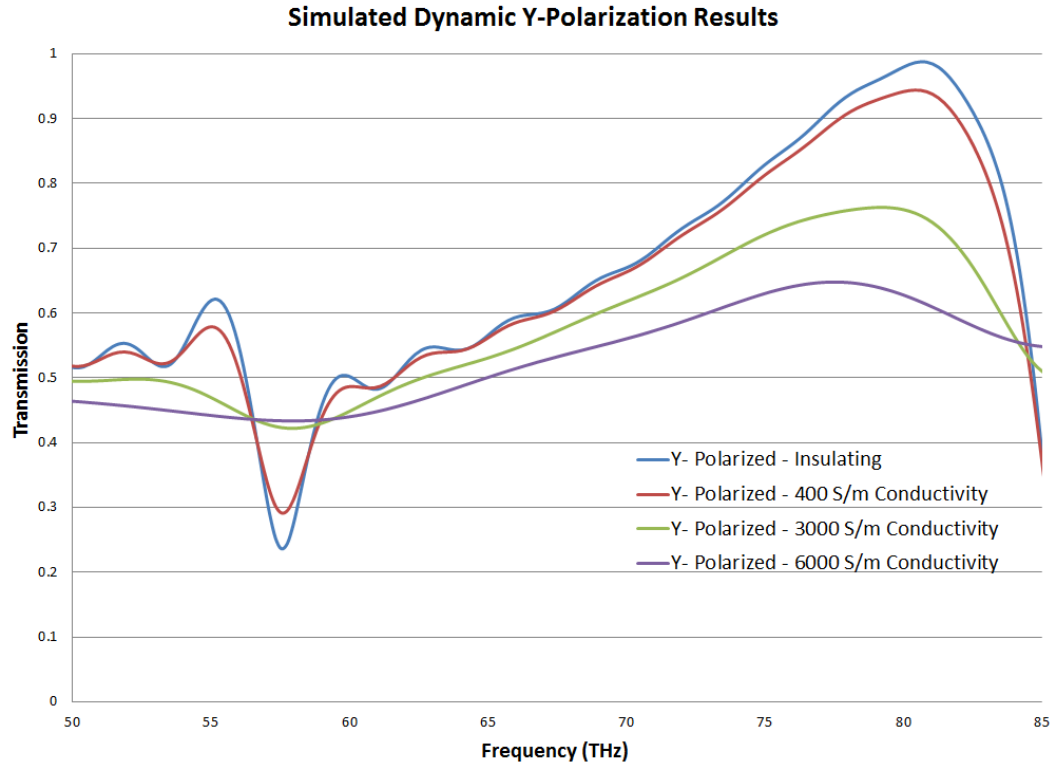


Figure 5.4.2.1: Dynamic Simulation results obtained by altering the conductivity of the GaAs layer. *Top:* Y-polarization. *Bottom:* X-polarization.

Using this simulation data, the expected on/off ratios and horizontal: vertical polarization ratios (at 60 THz or 5 μm) are described in Figure 5.4.2.2.

Bias	Actual Horizontal Pol. (Ideal)	Actual % Vertical Pol. (Ideal)
No / on	12 (0)	50 (100)
Yes / off	60 (100)	45 (100)

Ratio	Actual Horizontal Pol. (Ideal)	Actual Vertical Pol. (ideal)
On/Off	1:5 (0:100)	10:9 (1:1)

Ratio	Actual On (Ideal)	Actual Off (Ideal)
Polarization - H:V	1:2 (0:100)	12:9 (1:1)

Note: Off represents transmission of all polarizations

Figure 5.4.2.2: Simulated and ideal on/off and polarization ratios at 60 THz.

The next step was MM fabrication on the correctly doped semiconductor. It was already determined that GaAs would provide a very good optical transmission window for this work. However, three factors must be addressed before device fabrication could occur. The first was creating an efficient ohmic contact. The next was creating a Schottky contact which could create a high current to applied voltage ratio. The third factor was choosing the correct doping level to allow a high conductivity change, at the same time, maintaining the correct contact characteristics.

The standard ohmic contact recipe for n-type GaAs is Ge/Au/Ni/Au (26nm/54nm/14nm/100nm). This recipe was tested on four substrates with doping levels of: $<1 \times 10^{15} \text{ cm}^{-3}$, $5 \times 10^{16} \text{ cm}^{-3}$, $1 \times 10^{18} \text{ cm}^{-3}$, and intrinsic GaAs on sapphire. The resulting I-V curves are shown in Figure 5.4.2.3, where the more vertical the step height around $V=0$, the more ohmic the contact.

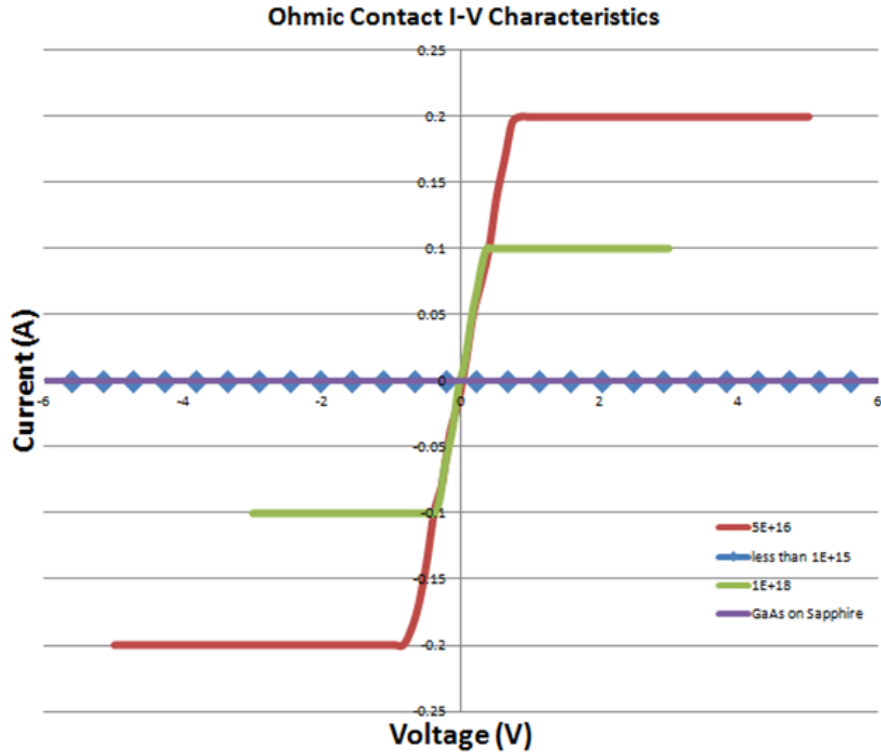


Figure 5.4.2.3: Ohmic contact measurements for four potential substrates with doping levels of $<1 \times 10^{15} \text{ cm}^{-3}$, $5 \times 10^{16} \text{ cm}^{-3}$, $1 \times 10^{18} \text{ cm}^{-3}$, and intrinsic GaAs on sapphire.

A Schottky contact pad was then fabricated in order to determine which doping levels allow for the greatest change in I/V. These Schottky diodes (12 nm -Ti, 86 nm -Au) are shown in Figure 5.4.2.4.

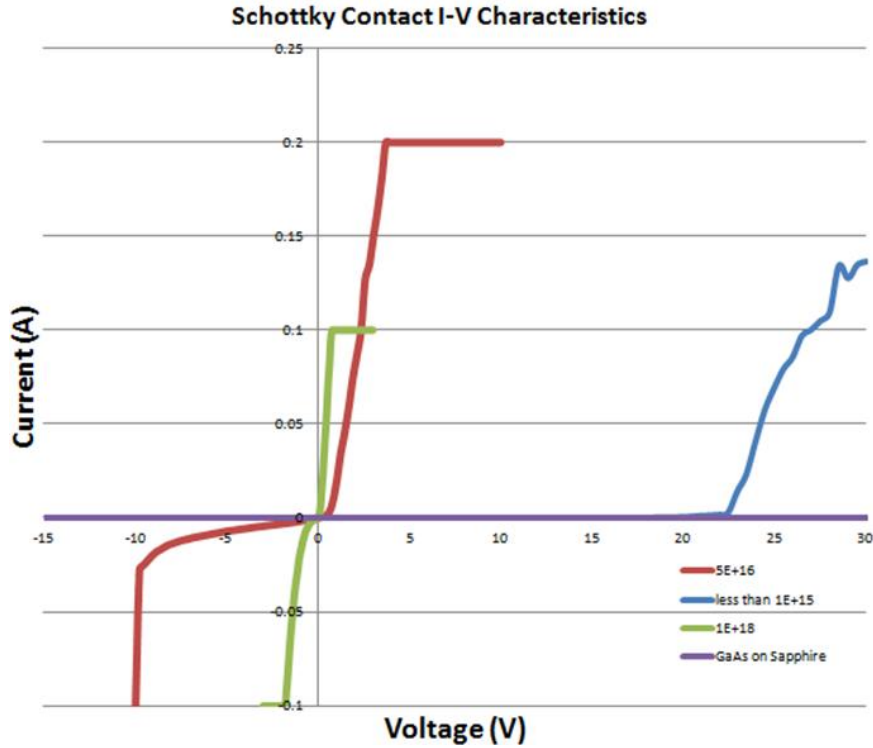


Figure 5.4.2.4: Schottky contacts fabricated on three substrates with doping levels of $<1 \times 10^{15} \text{ cm}^{-3}$, $5 \times 10^{16} \text{ cm}^{-3}$, $1 \times 10^{18} \text{ cm}^{-3}$, and intrinsic GaAs on sapphire.

Through these contact tests and with the simulated conductivities from Figure 5.4.2.1, it was determined a doping profile of approximately $5 \times 10^{15} \text{ cm}^{-3}$ - $5 \times 10^{16} \text{ cm}^{-3}$ would provide the best trade-offs between low initial conductivity and optimum contact characteristics. For completeness, Figure 5.4.2.5 shows testing of ohmic contacts using circular TLM patterns as well as Schottky diode testing using large contact pads.

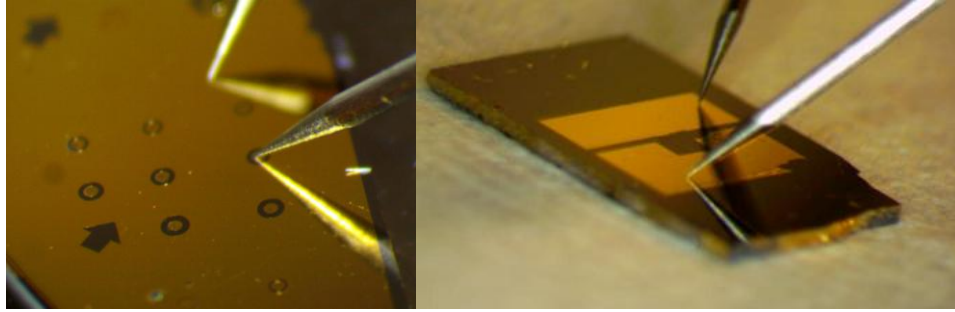


Figure 5.4.2.5: *Left:* linear TLM patterns used to test ohmic contact recopies. *Right:* top square is the Schottky diode and bottom “U” is the ohmic contact pad. This structure was used to test the Schottky response.

The metamaterial pattern was then constructed within the two contact pads (physically connected to the Schottky contact), using electron beam lithography. The two contacts with the metamaterial pattern can be seen in Figure 5.4.2.6. The large U-shaped ohmic contact pad was constructed in such a way to reduce noises when testing within the FTIR. With this unique contact pad geometry, the entire transmitted signal is processed through the MM pattern, increasing the signal to noise by approximately 75%.

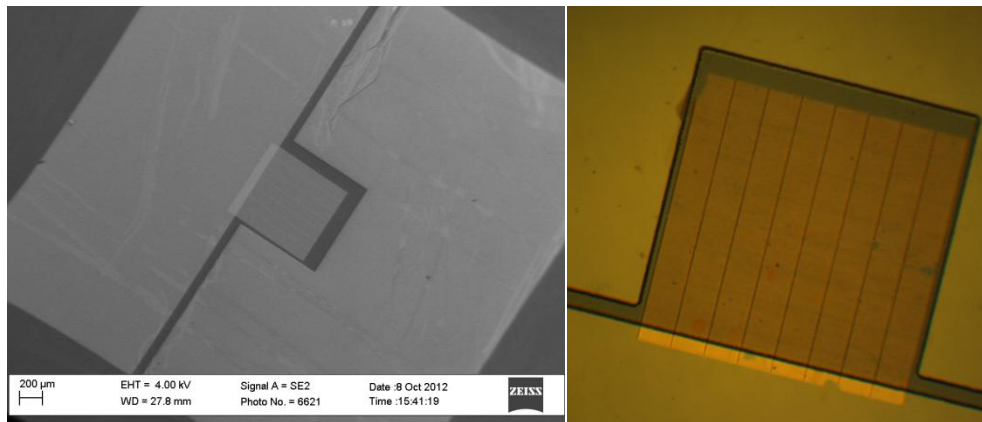


Figure 5.4.2.6: MM pattern with Schottky contact and ohmic contact pad. The structure was constructed in such a way as to reduce noise when transmission measurements were performed.

Initial prototypes of the MM dynamic polarizer underwent a process known as “arc-welding” between the Schottky and ohmic contact pads. The result was an electrical short between the two pads, shown in Figure 5.4.2.7.

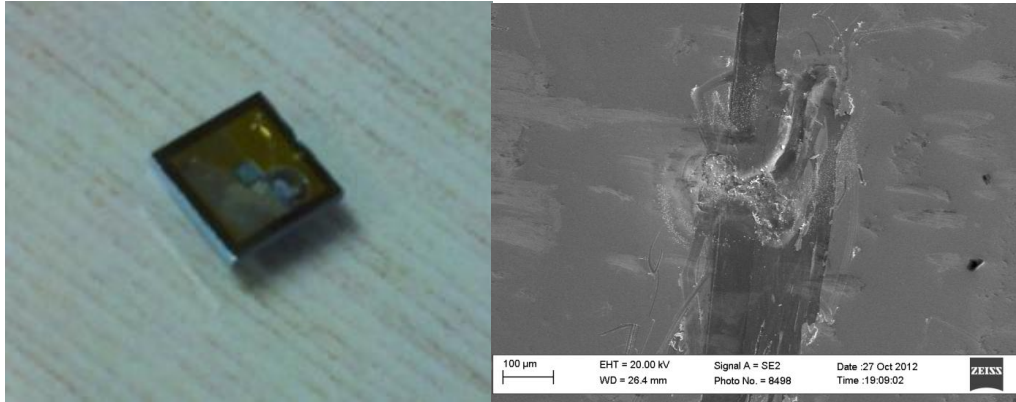


Figure 5.4.2.7: Left: image of the arc-welded sample after testing. Right SEM image of the two contact pads and short formed due to the weld.

This process, although destructive to the sample, provides valuable insight into the physical location of current travel. In order to counteract this problem, a 150 nm thick layer of Si_3N_4 was added under the Schottky contact pad, shown in Figure 5.4.2.8. This insulating layer forces current to travel through only the MM pattern. As an added benefit, no more arc-welding was observed.

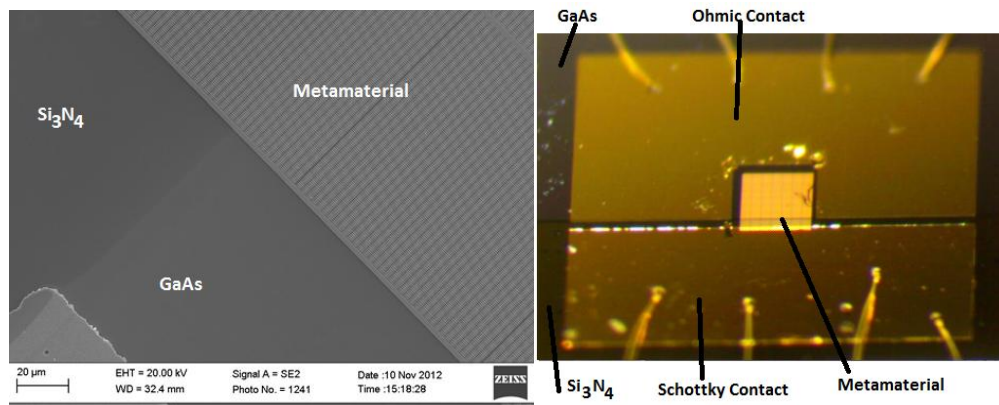


Figure 5.4.2.8: The addition of Si_3N_4 to the MM pattern. *Left:* SEM image showing the Si_3N_4 , metamaterial, and exposed GaAs. *Right:* fully constructed MM pattern with Si_3N_4 layer, metamaterial, GaAs layer, and contact pads.

The I-V characteristics of the dynamic GaAs/sapphire MM patterns were then tested for varying GaAs doping concentrations. The results were quite surprising as little to no current was generated even at very high voltages, as shown in Figure 5.4.2.9. This is data proved in sharp contrast to previous GaAs I-V characteristics obtained from bulk materials, Figure 5.4.2.4.

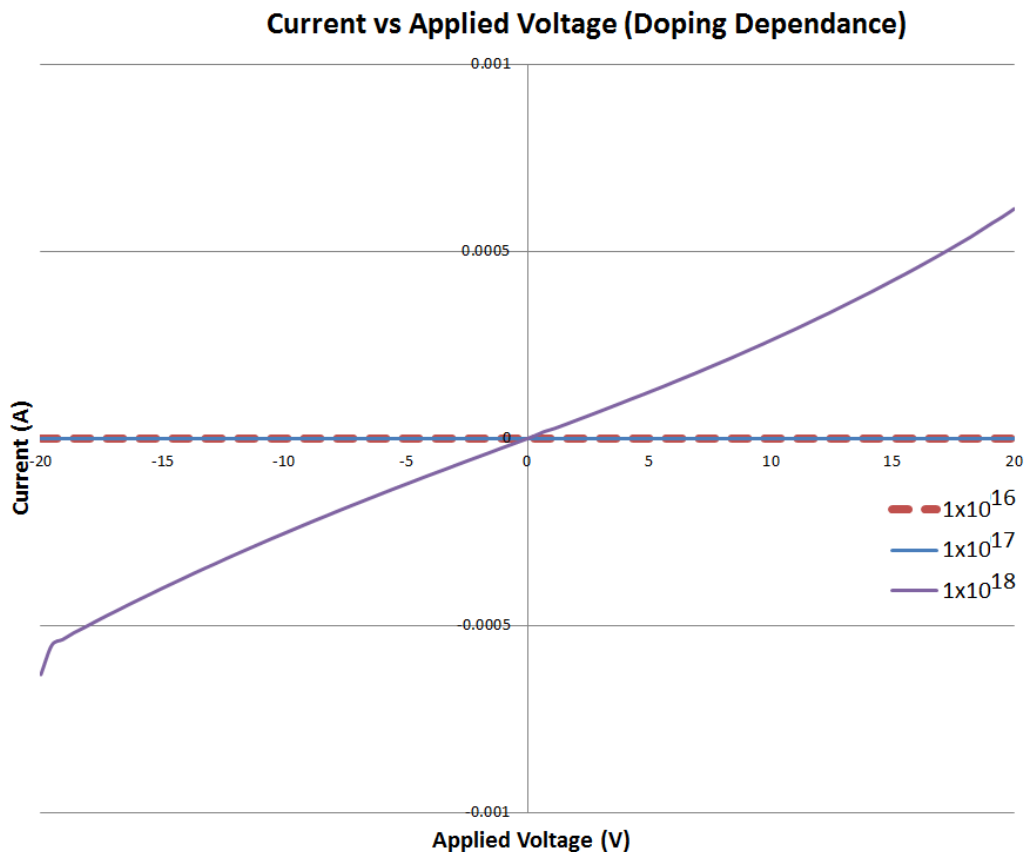


Figure 5.4.2.9: Current-Voltage characteristics for three highly doped n-type GaAs thin films grown on a sapphire substrate. At an applied voltage of 20 V the max current obtained is 0.5 mA.

Due to the poor contacts obtained in Figure 5.4.2.9, a study was undergone to determine if other contact recipes would improve the generated current within the GaAs layer. Various contact recipes were tested including typical ohmic contacts

such as Ge/Au/Ni/Au (26 nm/54 nm/14 nm/100 nm) and Schottky contacts such as Ti/Au (14 nm/136 nm). The I-V characteristics observed are shown in Figure 5.4.2.10.

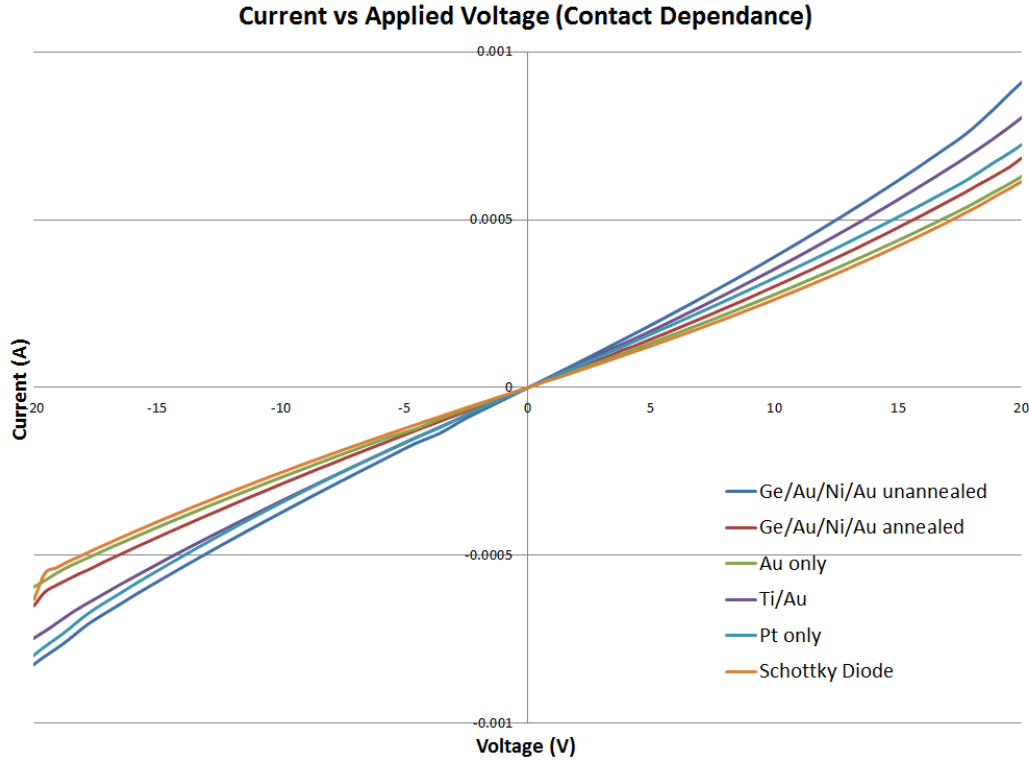


Figure 5.4.2.10: Contact tests for thin film GaAs epitaxially grown on sapphire. At an applied voltage of 20 V, the maximum current generated is 0.8 mA and is generally consistent between all contact recipes attempted.

Due to the consistent nature of the I-V curves with both Schottky and ohmic contacts, the substrate's photoluminescence was tested, for which no luminescence was observed. Also, the surface was examined using both focused ion beam cross sections and scanning electron microscopy. As seen in Figure 5.4.2.11, sever surface defects were observed on the GaAs/sapphire substrates. Due to the poor material quality, the maximum current expected to be obtained during transmission testing is around 1 mA.

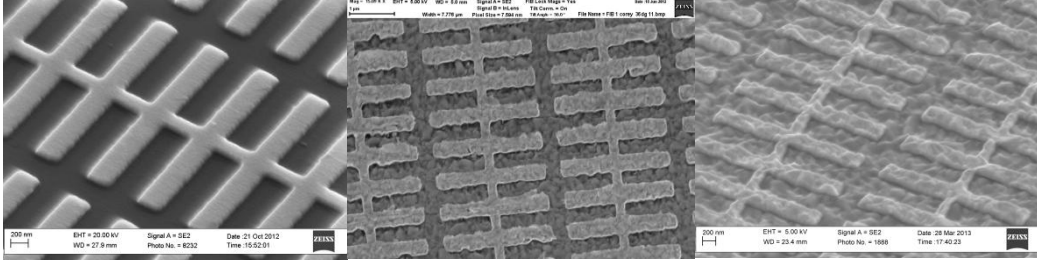


Figure 5.4.2.11: SEM images of the MM surface after identical processing techniques. *Left:* Bulk GaAs commercially obtained wafer. *Middle:* Undoped GaAs grown using MBE on sapphire. *Right:* Highly doped ($1 \times 10^{18} \text{ cm}^{-3}$ doping) GaAs grown using MBE on sapphire. Both Middle and Right surfaces should be smooth as shown in the Left image.

The sample was then mounted to a chip carrier and the contacts wire bonded to leads, as shown in Figure 5.4.2.12. The chip carrier was designed to allow transmission through the sample and through the chip carrier using a 1/8 inch hole in the center. To allow continued use of the chip carrier an acetone soluble adhesive was used to mount the sample.

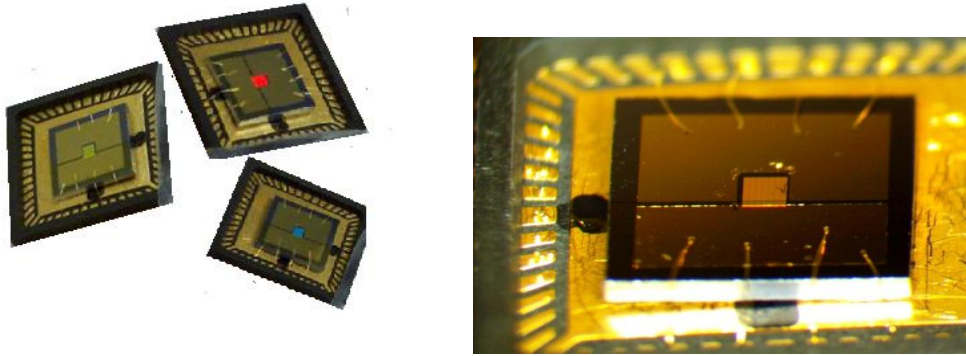


Figure 5.4.2.12: Metamaterials mounted in the chip holder and wire-bonded to the outside contacts.

The $1 \times 10^{18} \text{ cm}^{-3}$ doped sample was then mounted vertically onto a transmission FTIR. Leads were connected to the sample, and an external bias was applied. Figure 5.4.2.13 shows a mounted sample, and Figure 5.4.2.14 depicts obtained

transmission data at no applied bias and at 20 V applied bias (0.8 mA generated current).

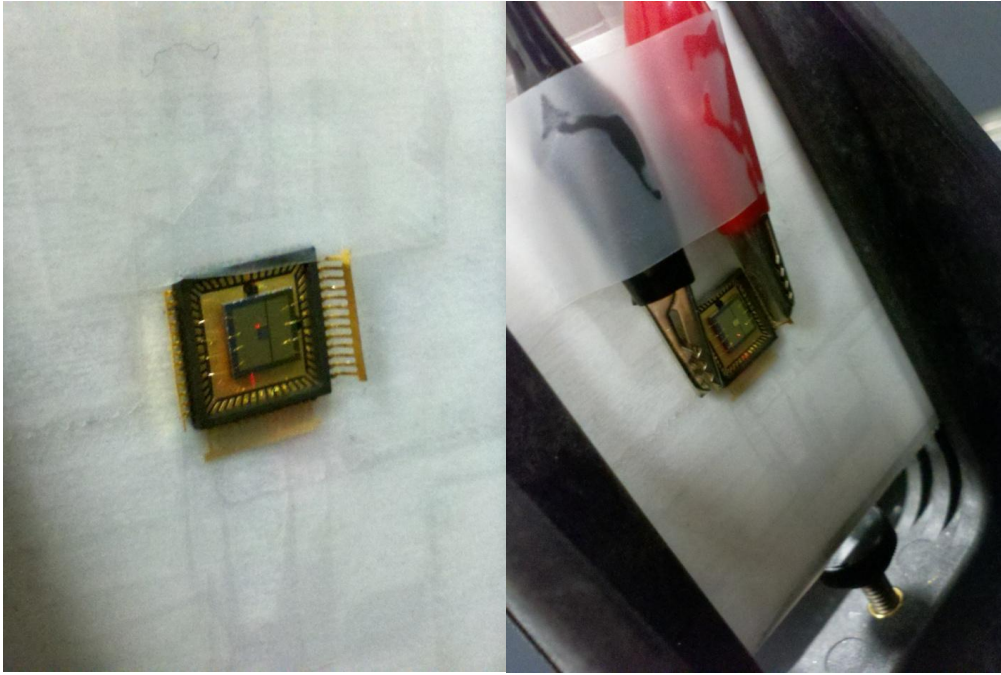


Figure 5.3.2.13: *Left:* Fully mounted MM in the FTIR. *Right:* leads are attached to the ohmic and Schottky contact pads and an external bias is applied.

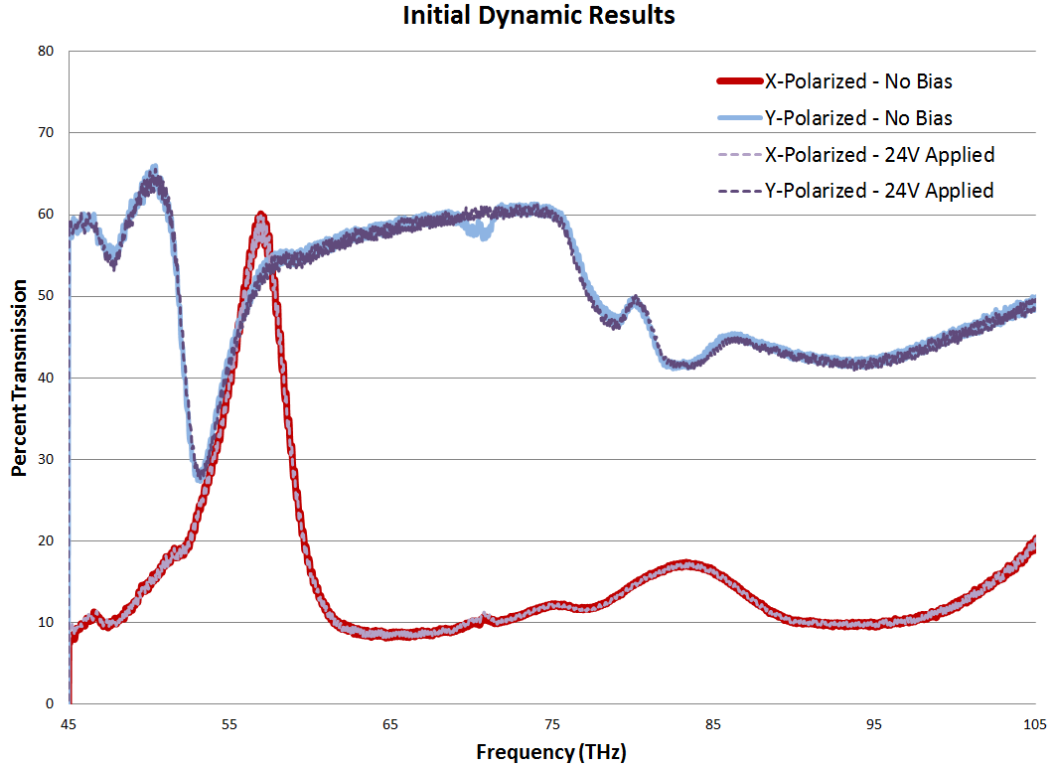


Figure 5.4.2.14: Dynamic results obtained using very high resistance contacts to highly doped GaAs on Sapphire.

The low generated current obtained in these highly doped substrates is expected to directly relate to the absent decrease in transmission with applied voltage. For this reason, the MM pattern was once again constructed on a DSP GaAs substrate with a doping concentration of $5 \times 10^{16} \text{ cm}^{-3}$, and transmission measurements were obtained for various applied biases, shown in Figure 5.4.2.15.

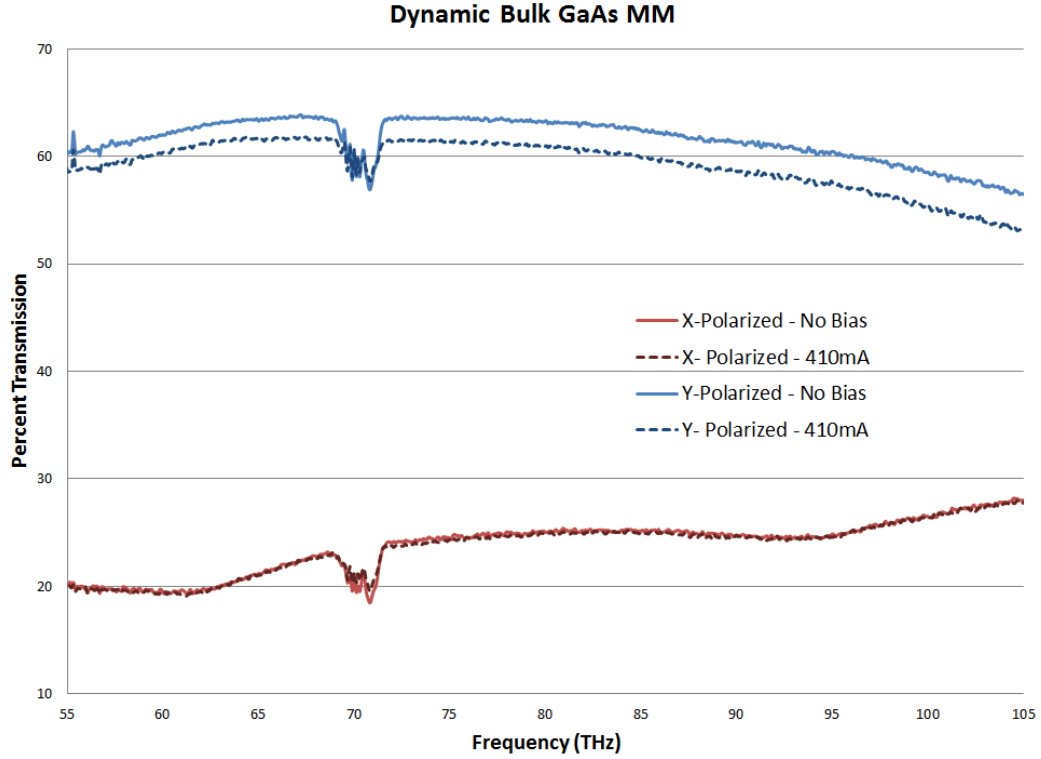


Figure 5.4.2.15: Dynamic results obtained using $5 \times 10^{16} \text{ cm}^{-3}$ doped DSP GaAs with a MM pattern. The results demonstrate dynamic transmission characteristics (3% decreases in transmission) for materials not at resonance wavelengths.

The results obtained for this experiment conclusively demonstrate a change in percent transmission when an external bias is applied to the MM pattern. This data demonstrates a transmission decrease of approximately 3% for bulk for a non-resonant MM pattern. When compared to bulk transmission change in conductivity of MM simulations, this response is equivalent to a 3,000 S/m shift in conductivity, as shown in Figure 5.4.2.16.

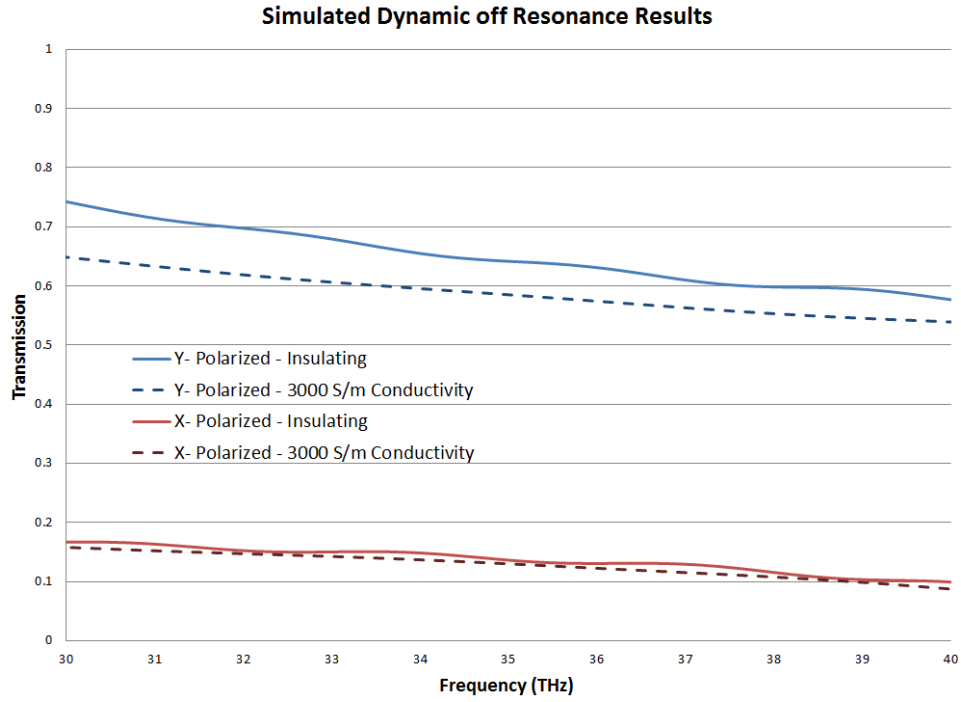


Figure 5.4.2.16: Simulated alteration in conductivity needed for the GaAs on sapphire metamaterial to achieve a 3% drop in conductivity at wavelengths demonstrating bulk properties and not MM resonant frequencies. Using this data the expected change in conductivity with an applied bias is 3,000 S/m.

This chapter described the experimental process and results obtained for each device proposed in Chapter 3. The impact of these results was alluded to; however, an in depth analysis will be discussed later in Chapter 6. For this reason Chapter 5 was dedicated to experimental procedure, device fabrication, and testing.

Chapter 6

Discussion

This chapter provides a more in-depth look at the results obtained in Chapter 5. Each section begins with a look into the most important data of Chapter 5. Then this chapter describes why the device produced such results and how each device can be best used. The sections then conclude by recommending further work which can optimize each device.

List of Abbreviations - Chapter 6

MM - metamaterial	IMF - interfacial misfit array
PhC - photonic crystal	ARC - antireflective coating
TPV - thermophotovoltaics	FWHM - full width half max
MIMs - monolithically interconnected modules	VECELs - vertical-external-cavity surface emitting lasers
I_{sc} - short circuit current	GaAs - gallium arsenide
V_{oc} - open circuit voltage	SRR - split ring resonator
FF - fill factor	SWP - split wire pair
MPP - max power point	SLS - strain-layer superlattice
GaSb - gallium antimonide	

6.1 Metamaterial High Temperature Emitter

This section examines the fabrication and testing of a MM emitter created from materials designed with stand temperatures greater than 1100 °C. For this purpose, various materials and structural designs were evaluated. A successful design was determined to be an absorption peak of approximately 70%, a resonance at a wavelength less than 1.6 μm , a full-width-half-max (FWHM) of less than 1 μm , and designed to withstand temperatures exceeding 1600 °C.

To this end, a circular metamaterial pattern was chosen for ease of fabrication; and platinum was chosen the metallic component due to its high melting point and e electrical conductivity. The MM device was then simulated in CST Microwave studio for three device geometries, shown in Figure 6.1.1. These three devices all show similar resonance peaks, shown in Figure 6.1.2.

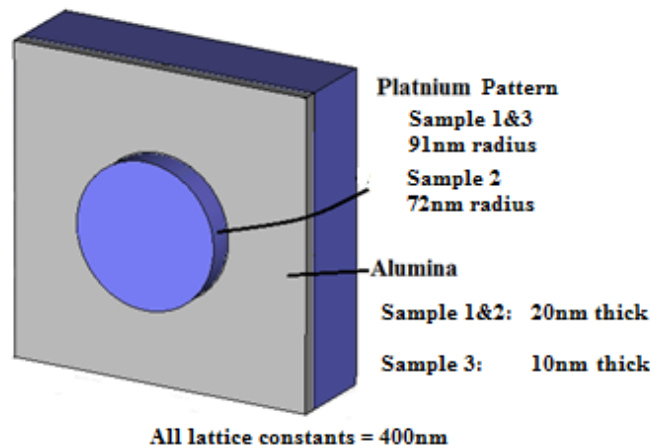


Figure 6.1.1: Design of the high temperature thermal emitter. Three designs were constructed and tested. *Sample 1:* Pt radius of 91 nm, Al_2O_3 of 20 nm. *Sample 2:* Pt radius of 72 nm, Al_2O_3 of 20 nm. *Sample 3:* Pt radius of 91 nm, Al_2O_3 of 10 nm.

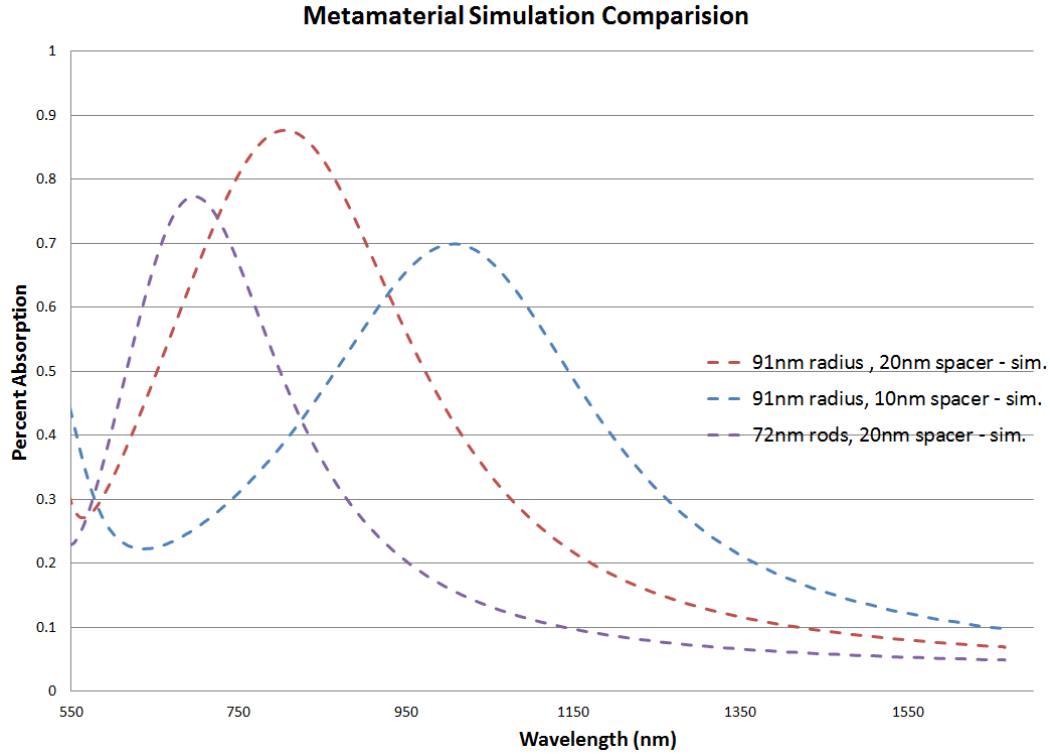


Figure 6.1.2: Simulated Absorption. *Purple:* Absorption of 72 nm radius Pt rods with 20 nm of Al_2O_3 . *Red:* Absorption of 91 nm radius Pt rods with 20 nm of Al_2O_3 . *Blue:* Absorption of 91 nm radius Pt rods with 10 nm of Al_2O_3 .

In order to determine that resonance of Figure 6.1.2 was due to a MM response, and not due to other plasmonic effects, the E-field and surface currents of the MM were measured at various points. As can be seen from Figure 6.1.3, at resonance there is a surface current forming two closed loops within the MM structure. These loops alter the H-field response into a Z-plane direction. Also, there is an induced E-field in the +/- Z-plane. The resulting effect, as explained in Chapter 2.2.1, is a metamaterial response and an altered permittivity and permeability.

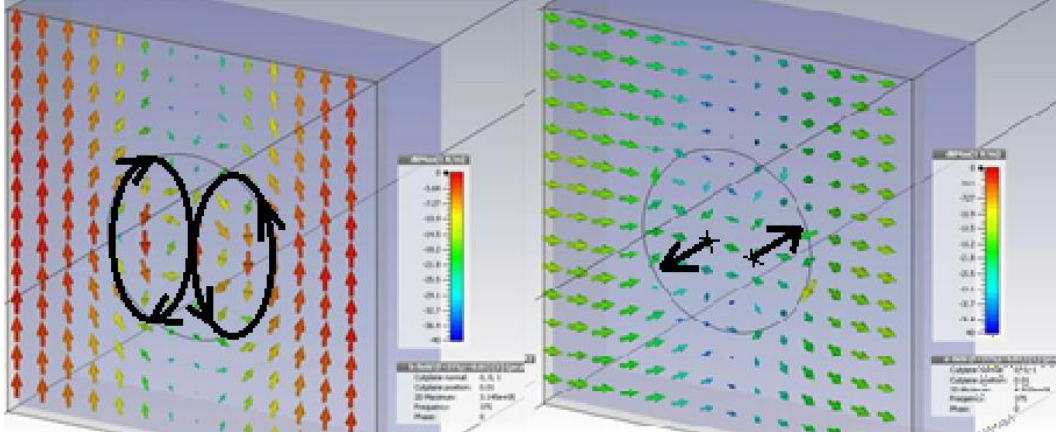


Figure 6.1.3: *Left:* the incident radiation creates a surface current in the metamaterial structure. This current is isotropic as to effect all incident polarizations. *Right:* the electric field within the structure is also altered in the Z-direction. The effect of both characteristics is an altered permeability and permittivity.

These metamaterial three structures were then fabricated using electron beam lithography and are shown in Figure 6.1.4. It should be mentioned that the structures in Figure 6.1.4 do not form perfect cylinders as can be seen more clearly from a 45 degree angle in Figure 6.1.5. Due to the irregular shape of the MM pattern, we expect there to be a magnitude reduction in the resulting resonance peaks. This effect was verified experimentally in reference [86] for metallic PhC emitters. The absorption was then measured experimentally using an ellipsometer at 23 degrees from the surface normal. The absorption for each structure as well as two regions of interest, is shown in Figure 6.1.6.

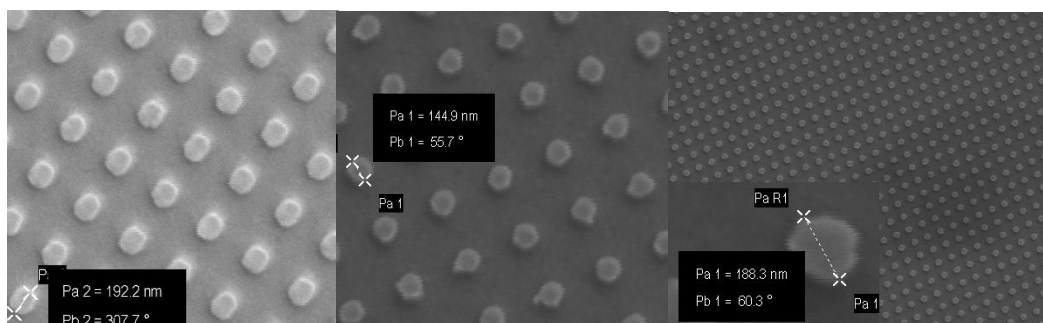


Figure 6.1.4: Fabricated devices. *Left:* 10 nm Al_2O_3 insulation layer. *Middle:* 20 nm Al_2O_3 insulation layer. *Right:* 20 nm Al_2O_3 insulation layer (scale inset).

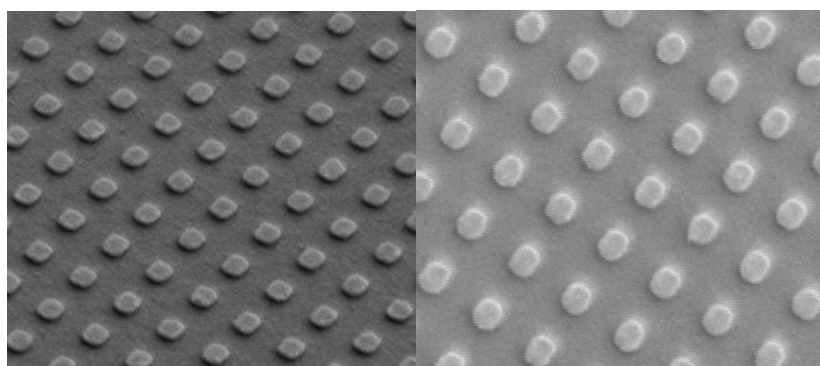


Figure 6.1.5: *Left:* 45 degree angle of 10nm thick Al_2O_3 sample. *Right:* top view of same sample.

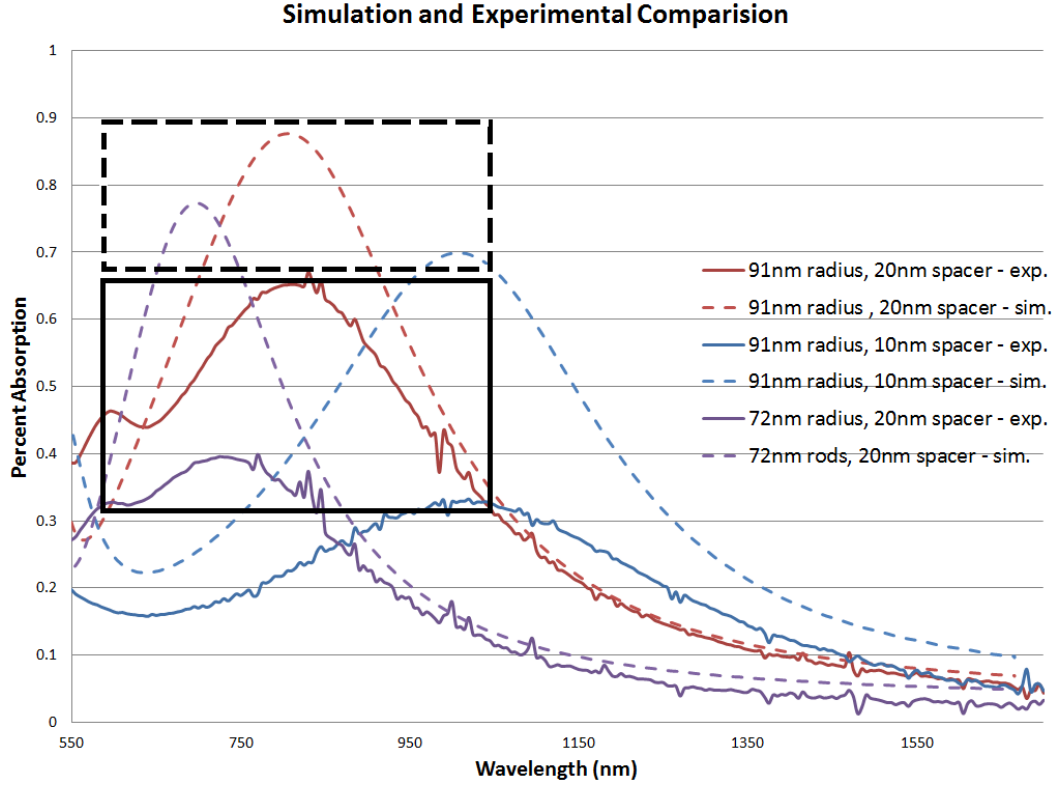


Figure 6.1.6: Experimental Absorption. *Black Check Box:* simulated absorption peaks obtained for all MMs, of note is the relative intensity for each peak. *Black Box:* Experimental absorption for each structure. The relative intensity as well as resonance wavelengths, matches that of the simulated results.

The experimental results showed a reduced optical response, as compared to the simulated results. It is expected that this degraded response is due to fabrication irregularity as well as measuring at 23 degrees from the surface normal. However, this effect corroborates with similar results found in literature.^[86] It is important to note that the relative peak intensities between samples remain consistent from simulation results to experimental results.

The proposed structure (Pt, 91nm radius, 20 nm Al_2O_3) was then to be examined at temperatures of 480 °C to 650 °C, in order to examine the design robustness. Lower temperatures around 500 °C would allow for initial device

robustness testing, and 650 °C would allow for emissivity testing, as black body radiators at this temperature begin to release photons at 800 nm in a measurable quantity. The MM structure was heated and the emissivity was examined at 500 °C. As expected, the resulting emission curve contained little signal and a large amount of noise. However, the MM sample underwent severe discoloration during heating. The effect on higher temperature emission was in question, therefore the device was re-examined in the ellipsometer. The absorption characteristics and emission characteristics can be seen in Figure 6.1.7.

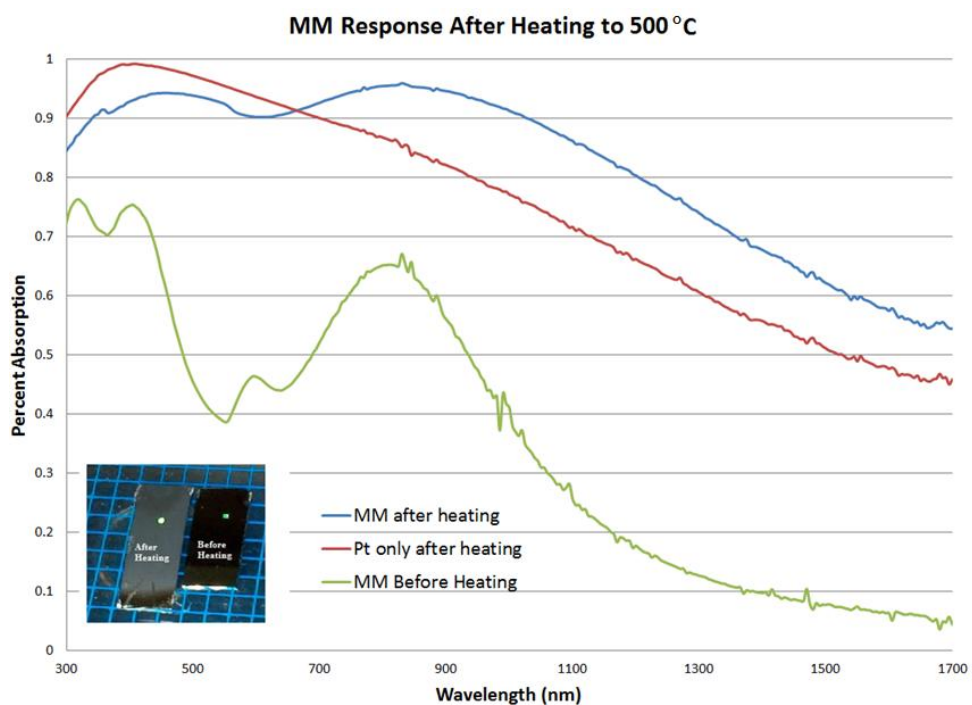
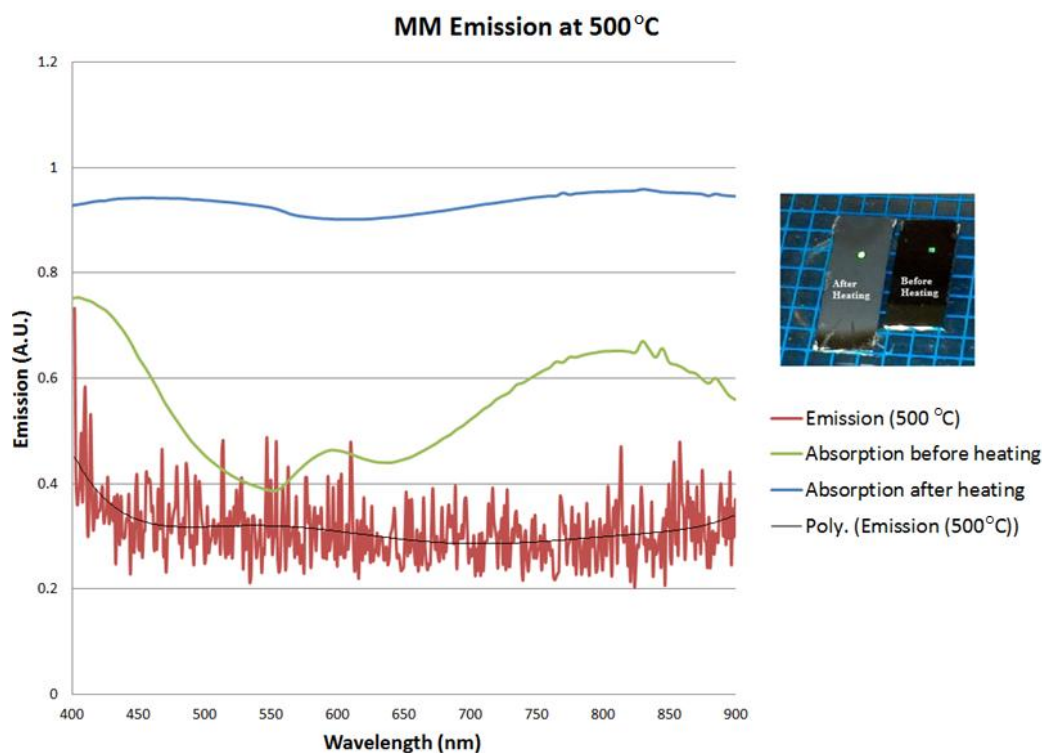


Figure 6.1.7: *Top:* Emission testing results at 500 °C. It is unclear if noisy signal was completely due to low thermal energy density or of if heating damage reduced signal quality. *Bottom:* Absorption response before and after heating of MM to 500 °C.

The sample was examined with scanning electron microscopy (SEM) in order to determine if the MM structure itself was altered at 500 °C. The resulting images for heated and unheated sample are shown in Figure 6.1.8.

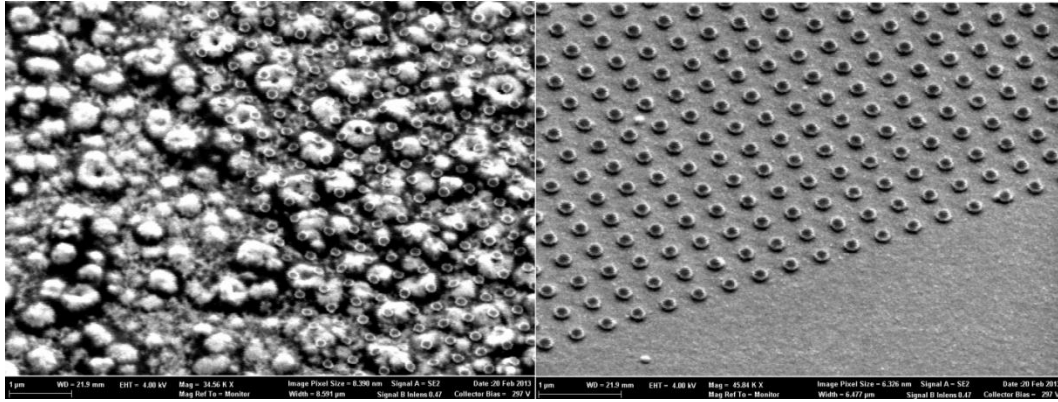


Figure 6.1.8: Left: SEM image after heat testing to 500 °C. Right: Same structure before heat testing.

These results show no deformation to the Pt MM itself. However, there is significant damage to the 20 nm Al_2O_3 dielectric spacer. As alumina has a significantly high melting point (~2000 °C), and the damage appears to be a “bubbling” effect, we conclude that two effects may have occurred. First, at high temperatures, Si readily oxidizes becoming Si-O. The substrate used in this test was Si, as such, Si-O may have formed and then evaporated through the thin Pt and alumina layers. Secondly, in order to determine the likelihood of this event, the Pt/ Al_2O_3 structure was constructed on a sapphire substrate.

The Pt/ Al_2O_3 /Pt MM was constructed to operate at 1050 nm, and underwent heat/cooling cycling between 80 °C and 650 °C in order to demonstrate device robustness at high temperatures. After four complete cycles the structure was testing using an ellipsometer at 15 degrees from the surface normal, the results are shown in Figure 6.1.9. The MM was then observed under

an ellipsometer in order to determine if material defects were forming due to heat/thermal expansion issues. A comparison of the structures is shown in Figure 6.1.10. It was determined that heating may cause adhesion issues due to thermal expansion, as shown in Figure 6.1.11; however, as Figure 6.1.9 demonstrates, this has little effect on device performance.

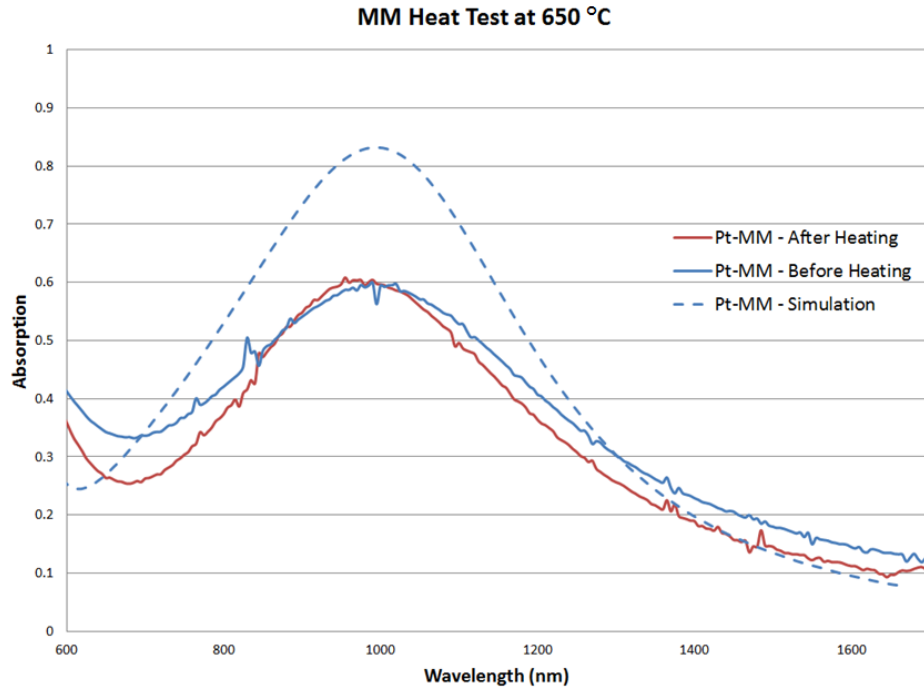


Figure 6.1.9: Measured absorption before heat cycling and after 4 cycles to temperatures exceeding 600 °C, the simulated MM response is also shown.

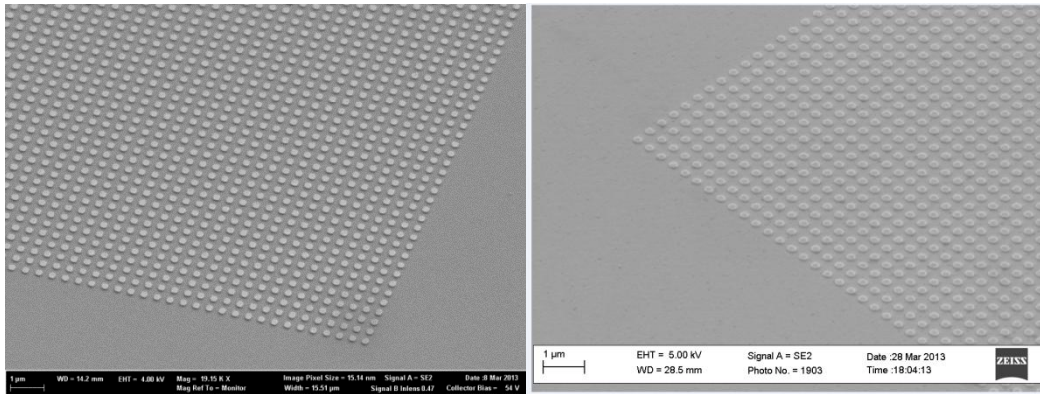


Figure 6.1.10: *Left:* Metamaterial structure before heating. *Right:* Same structure after repeated heating to 650 °C.

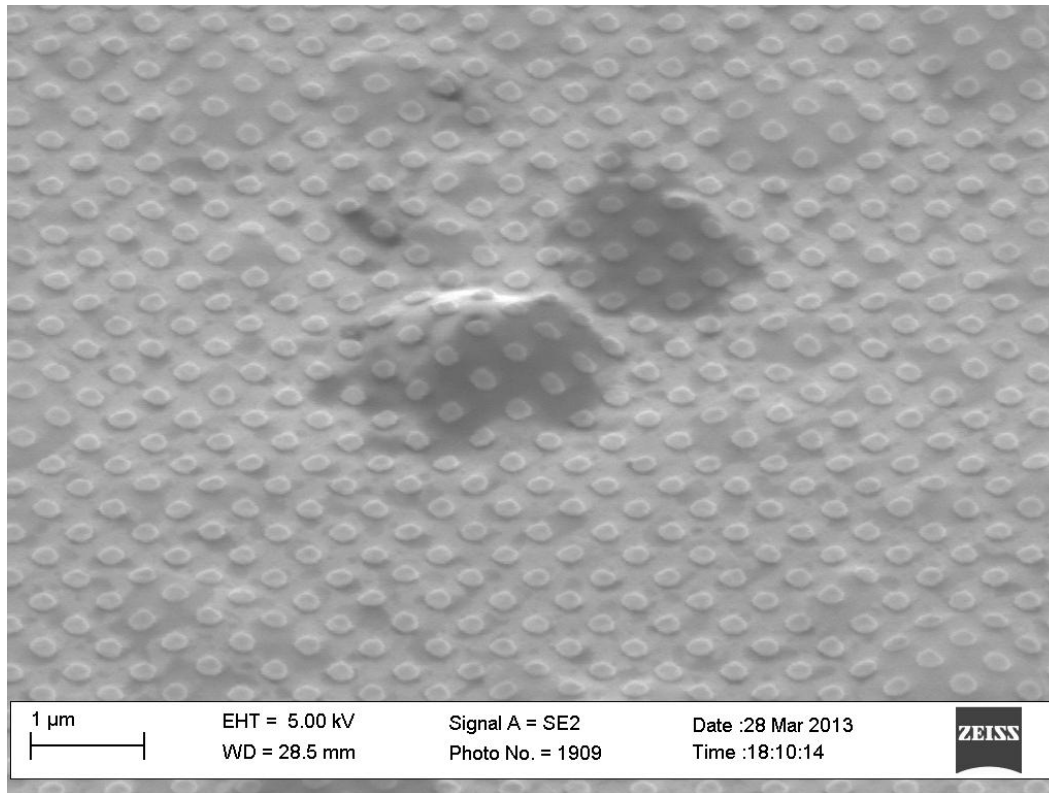


Figure 6.1.11: Deformation due to repeated heating, these defects are worth noting, however, they have been shown to have little effect on pattern emission or absorption.

Once device robustness was observed, the MM emission was then tested at multiple temperatures in order to determine the emissivity of the structure. In order to create consistency between measurements, the emissivity was measured relative to the emissivity of a Pt surface. As shown in Figure 6.1.12, the measured ellipsometry results match the device emissivity for a variety of temperatures.

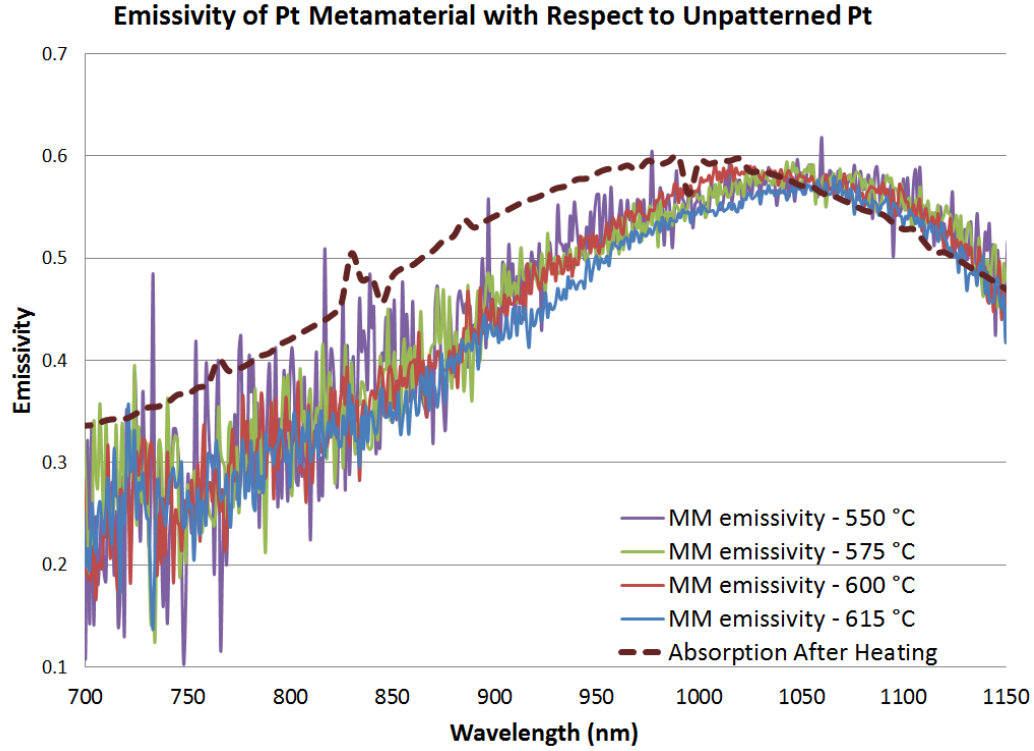


Figure 6.1.13: MM emissivity normalized with respect to the emission of Pt. The emissivity was measured independently at a variety of temperatures. Increasing the temperature was found to decrease the noise present; however, in all cases the resonance peak remained unchanged.

Using Figure 6.1.13, it becomes possible to determine the spectral emission of the MM when even warmer temperatures are utilized. Figure 6.1.14 demonstrates device emission at temperatures ranging from 1400 °C to the maximum operating temperature of 1700 °C. As the temperature reaches closer to 1700 °C, the MM becomes more spectrally sensitive. The result is a larger spectral control as the temperature increases, thereby increasing the efficiency of a TPV diode by limiting the energy lost to diode heating.

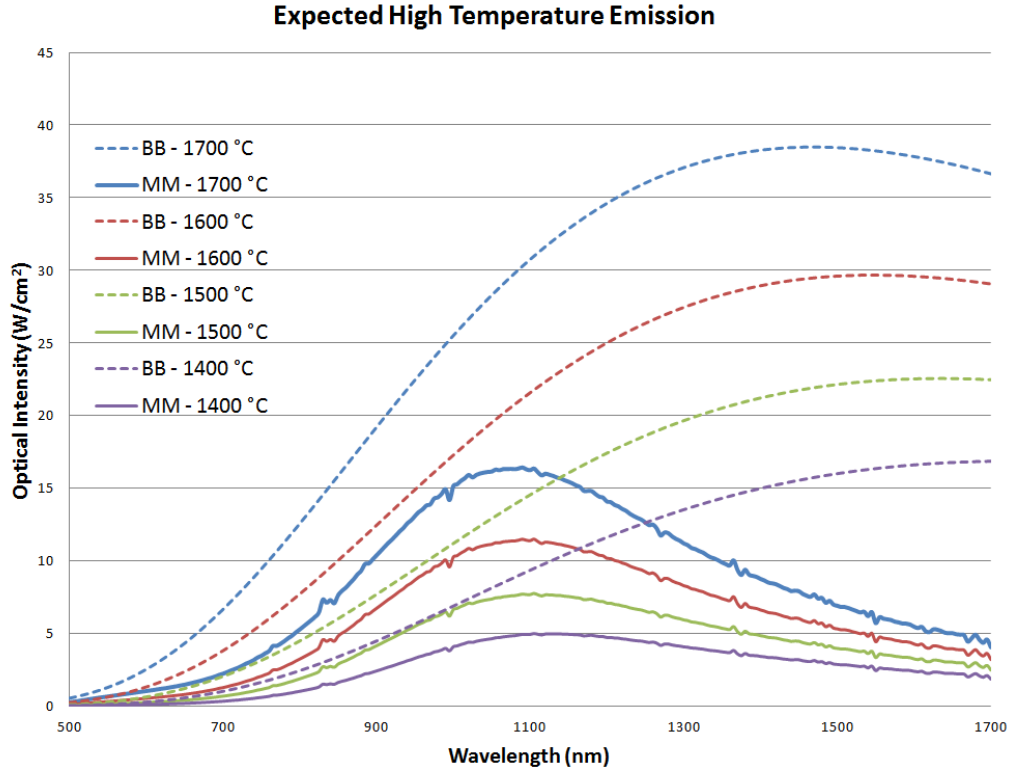


Figure 6.1.14: The expected emission of the MM at temperatures greater than 1400 °C. This data is based on the experimentally obtained emissivity from Figure 6.1.15.

In order to determine the final parameters of the MM polarizer in comparison to the field, the 91 nm radius and 20 nm Al_2O_3 (red line of Figure 6.1.6) will be considered. The initial design parameters require a device which operates at resonance below 1.5 μm , has peak absorption approaching 70%, a FWHM of less than 1 μm , and fabricated from materials able to operate at temperatures greater than 1,050 °C. The proposed device was constructed from platinum which has a melting point of 1,770 °C so can inherently operate at temperatures greater than 1,050 °C. The fabricated device has a measured absorption of 70% at a wavelength of 1050 nm. Also, the FWHM of the experimental structure is approximately 500 nm, relatively narrow in terms of

MM emitter devices. This resonance peak can be enhanced further with higher resolution electron beam lithography, which would create a much narrower band emission peak. This device was also shown to withstand multiple heating cycles to temperatures exceeding 600 °C. The emissivity was also able to be measured at these temperatures and matched experimentally obtained data. The MM emitter was shown to have a strong emission peak, and is expected to operate at greater spectral selectivity as the device temperature is increased. A MM emitter was also shown to exhibit a narrower emission spectrum than traditional photonic crystal emitters; and this spectrum can be tuned with much greater accuracy to the spectral response as shown in Figure 6.1.15. To this end, the initial design goals of this project were met, and a new type of MM emitter technology can now be explored and implemented in high temperature TPV applications.

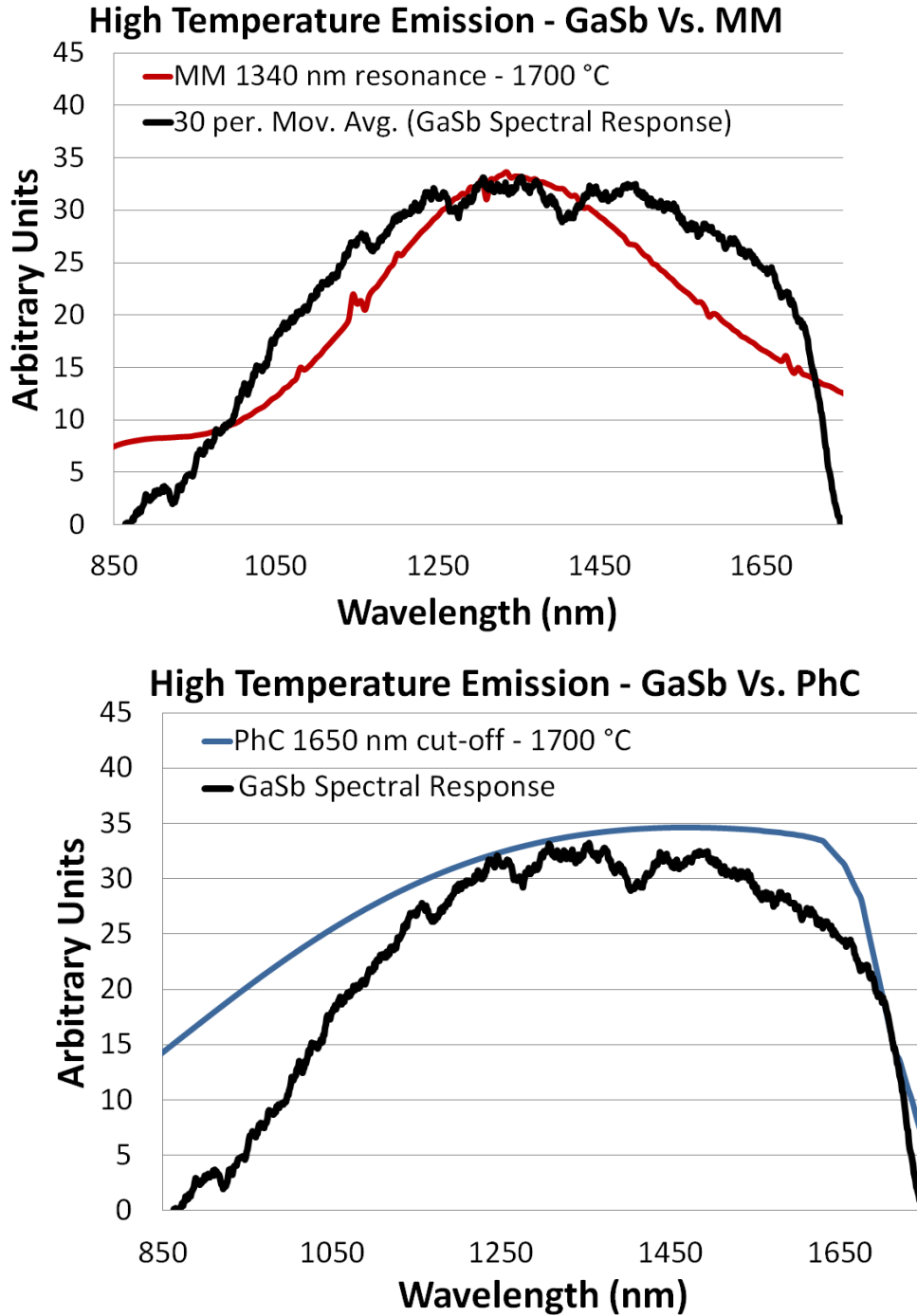


Figure 6.1.15: *Top:* High Temperature MM absorber centered at 1350 nm. *Bottom:* PhC with cut-off frequency of 1650nm based on the emissivity of Ref. [84]. The MM emitter follows the spectral response of a GaSb photodiode much more closely than the PhC emitter. Both structures are based on emissivity data at a temperature of 1700 °C.

Beyond the work reported in this thesis, this project will undergo a two phase plan. First, the metamaterial resonance will be optimized for Pt in order to increase emissivity to between 90 and 100 percent. This will allow specific band gap matching while providing a simplified emitter model expected to operate up to 1700 °C. Secondly, an alternative material study will occur in order to optimize the system for increasing operational temperatures. In particular, the issue of coefficient of expansion must be examined. For this reason, a tungsten MM (coefficient of expansion equal to $4.5 \mu\text{m}/^\circ\text{C}$) pattern will be examined on an Al_2O_3 dielectric (coefficient of expansion equal to $5.3 \mu\text{m}/^\circ\text{C}$). In order to mitigate the oxidation issues described for tungsten in Chapter 3.1, the structure will then be encapsulated in Al_2O_3 . We expect this new structure to maintain structural integrity up to 2000 °C due to the high melting points of the individual components.

6.2 Metallic Photonic Crystal Filter

A metallic photonic crystal pattern was constructed on a GaSb TPV diode. The metrics for success were determined to be an increase in I_{sc} , max power, and conversion efficiency. As a supplemental method to characterize the PhC enhancement, ellipsometry measurements were obtained and analyzed. The data was then compared to simulation results to determine the effect of the photonic crystal.

Simulation data was measured as power absorbed at the interface of the GaSb with an ideal incident spectrum. This was done in order to provide a constant point of measurement through all simulations and maximum possible enhancement. For this same reason, absorbed power was only measured to a depth of 2 μm , as the electric field of the confined PhC was negligible after this point. The location of the simulated power monitors, at the GaSb interface, seems to have introduced a false blue shift in PhC resonance when compared to ellipsometry data as will be shown in Figure 6.2.1.

Photonic crystals are also extremely dependent on normal incident light, which not an issue for TPV applications. However, the ellipsometer utilized for these measurements had a maximum incident angle of 23 degrees from the surface normal. This was expected to decrease the observable PhC response at resonance. However, the PhC pattern was still observed to increase absorption as display the defining characteristics shown in simulations.

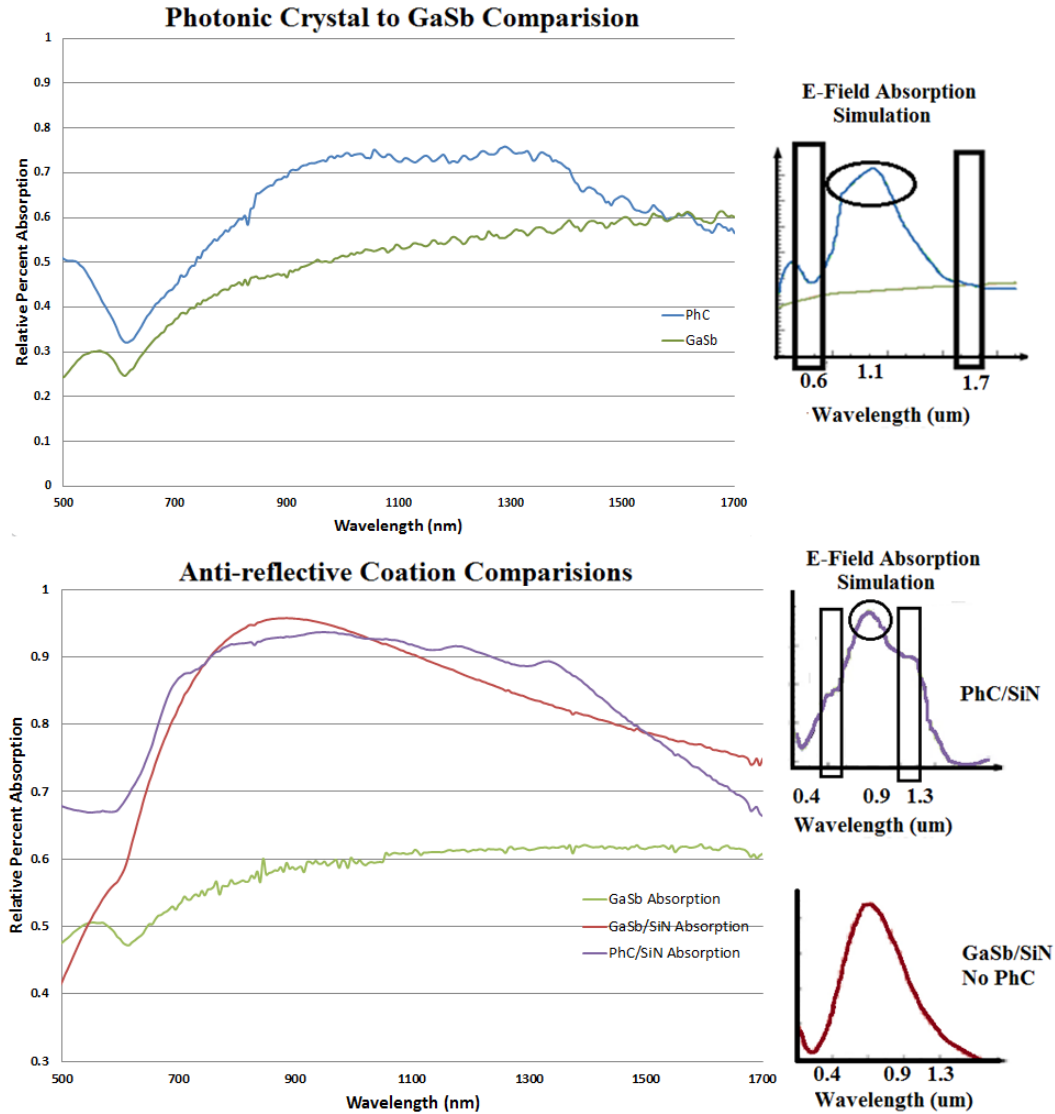
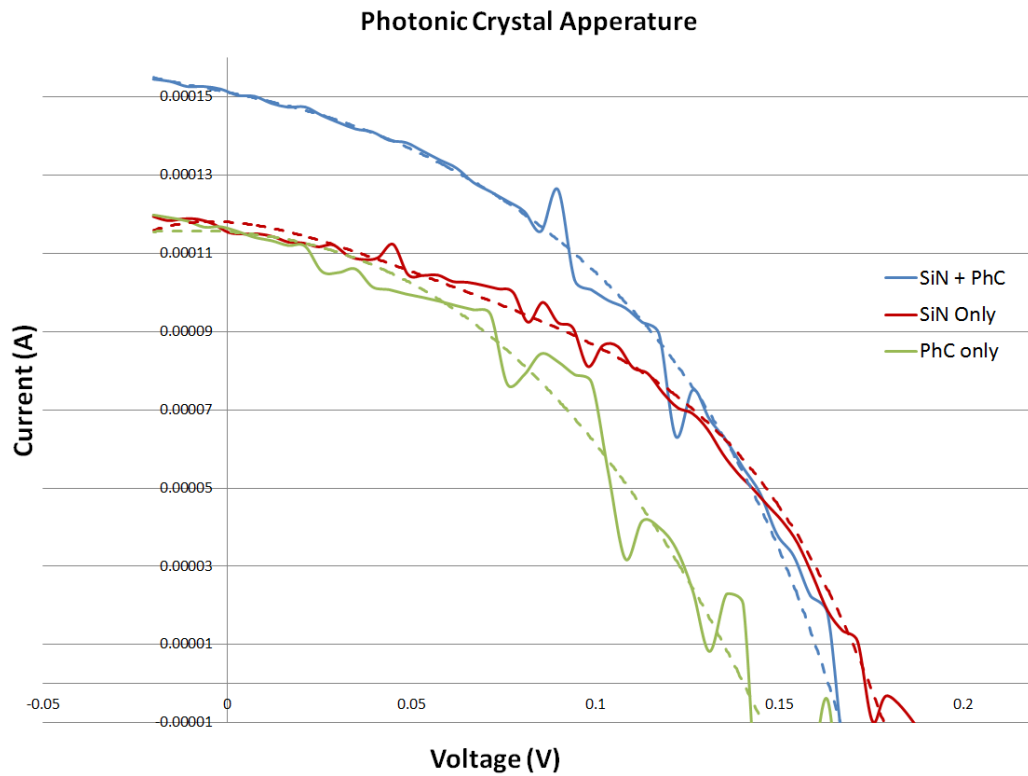


Figure 6.2.1: Simulated and experimental absorption. Experimental absorption was taken at an angle of 23 degrees from the surface normal leading to decreased observable absorption at resonance (black circles). *Top:* PhC with no ARC compared to GaSb with no ARC. The characteristic responses of the PhC are shown as black squares. *Bottom:* PhC with an ARC, GaSb with an ARC, and GaSb without an ARC. The characteristic PhC responses are shown within the black squares.

The ellipsometry measurements shown in Figure 6.2.1 do display the defining characteristics implied through simulations. If the absorption of the PhC was calculated, based only on the data of Figure 6.2.1, it was determined that the

off-angle absorption of a PhC would increase by 23 percent when no ARC was present and by 1 percent when both structures utilized an ARC layer. This data provides evidence that there will be optical effect due to the photonic crystal and this effect will in fact be positive towards device performance. To this effect an unoptimized photodiode was constructed, and a PhC was fabricated over the active aperture region, the result is the I-V characteristics shown in Figure 6.2.2.



	I_{sc} (mA)	V_{oc} (mV)	FF(%)	Max Power (μ W)	CE (%)
SiN_x ARC	.115	175	64	9.06	4.38
PhC No ARC	.115	142	73	7.63	3.69
PhC and ARC	.150	165	62.5	10.5	5.08

Figure 6.2.2: I-V curve characteristics. *Top:* I-V curves obtained for the samples at a solar concentration of 10 suns. *Bottom:* the defining characteristics obtained from the I-V curves including short circuit current, open circuit voltage, fill factor, max power, and conversion efficiency.

These PhC devices were fabricated with other photodiodes in order to compare effects of performance with and without increased processing steps. All devices experienced some form of performance degradation after processing with the exception of those fabricated with complete PhC/ARC enhancements. The photonic crystal with an ARC did in effect show an increase across all expected characteristics, with exception to fill factor and open circuit voltage.

An important note must be considered before analysis of results. The diodes used for this experiment were not optimized for a PhC enhancement. Therefore the increase in generated current can be improved by changing the layer thicknesses of the diodes shown in Figure 4.1.7. In particular, Figure 6.2.3 shows the optimum intrinsic area for enhancement due to a PhC is located at a depth of less than 1.5 μm . However, the intrinsic region used for absorption in this structure is at a depth of 300 nm to 1.8 μm leaving an area of 300 nm unutilized. The unoptimized structure leaves around 20% of the active diode region unutilized by the PhC. This is one reason that the experimental enhancements are around 50% of the simulated absorption increases. A second reason is the use of a solar simulator for testing as opposed to the frequency selective emitter used in simulations. The effect of the alternative spectrum, however, is less quantifiable as the photodiode structure. None the less, it is expected that the incident spectrum influences device performance in relation to simulated results.

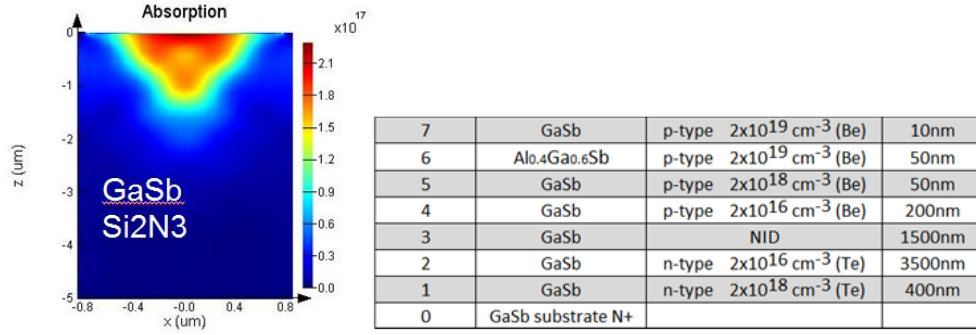


Figure 6.2.3: *Left:* Region of optical enhancement for a PhC is limited to a depth of approximately $1.5 \mu\text{m}$. *Right:* the structure of the photodiode used in the measurement. The absorber layer is located at a depth of 300 nm to $1.5 \mu\text{m}$. The result is a 20% smaller absorption region compared to simulated results.

Further analysis will begin with the PhC/air pattern. The low V_{oc} experienced by the air/PhC is typically due to an increase in series resistance. To this effect, the PhC must have a larger contact resistance than the ohmic contact pads, reducing the V_{oc} . We also expect there to be a lower V_{oc} due to increased trap states on the unpassivated surface. However, it should be noted that there is not the decrease in I_{sc} that one would typically expect with increased surface recombination (due to no Si_3N_4 passivation layer). The consistent I_{sc} implies that there are more photogenerated charge carriers which, to some extent, overcame the increased surface recombination rate. The increased recombination could not be taken into account through simulations or ellipsometry but is observed in actual devices leading to a lower than expected PhC enhancement.

When a Si_3N_4 layer was added to the PhC, an increase was observed in I_{sc} , max power, and conversion efficiency. This implies that there were more photogenerated charge carriers to produce the current, and a larger percentage of these carriers reached the contacts, increasing the conversion efficiency. The

improved diode characteristics confirm that a metallic PhC pattern in conjunction with a Si_3N_4 layer will increase the efficiency of a TPV diode. A summary of the PhC enhancements for simulations, ellipsometry, and TPV applications are shown in Figure 6.2.4.

	Simulated Enhancement	Ellipsometry Enhancement 15° off-angle	I_{sc} Enhancement	Max Power Enhancement	CE Enhancement
SiN_x ARC	16.57%*	30%*	--	--	--
PhC no ARC	66.73%*	23%*	0% [#]	-15.8% [#]	-15.8% [#]
PhC and ARC	81.81%*	32%*	30% [#]	17% [#]	16% [#]

Figure 6.2.4: The metrics used to determine the quantitative effects of applying a metallic PhC as a front side filter enhancement to a TPV diode. As a TPV diode without a SiN layer is not feasible, the leftist three metrics use this structure as a baseline. *Denotes compared to unaltered GaSb. [#]Denotes compared to GaSb with SiN_x

There are also other important conclusions to be drawn from the V_{oc} and fill factor in the PhC/ Si_3N_4 case. These two parameters are most affected by an increase in series resistance, typically caused by an increase in contact resistance. This leads one to believe that the PhC is also acting as a front contact grid; as other contact resistances remain constant and the surface is passivated with SiN_x to remove trap states. The V_{oc} must then be reduced due to a barrier at the contact, which is likely due to a thin insulating layer creating during the PhC processing. As such, it follows that with the correct process optimization, the enhancement of a metallic photonic crystal should be even further increased.

Further work with metallic PhCs for TPV applications should include the replacement of existing TPV front contact grids. This can be done for various photodiode geometries ranging from traditional geometries to monolithically interconnected modules (MIMs). Figure 6.2.5 depicts a MIMs designed photodiode along with three mesa's each utilizing a different front contact method. By integrating a MIMs structure utilizing only PhCs with SiN_x (Left most mesa of Figure 6.2.5), a much higher efficiency can be generated than by using only traditional contacts and ARCs (right side of Figure 6.2.5).

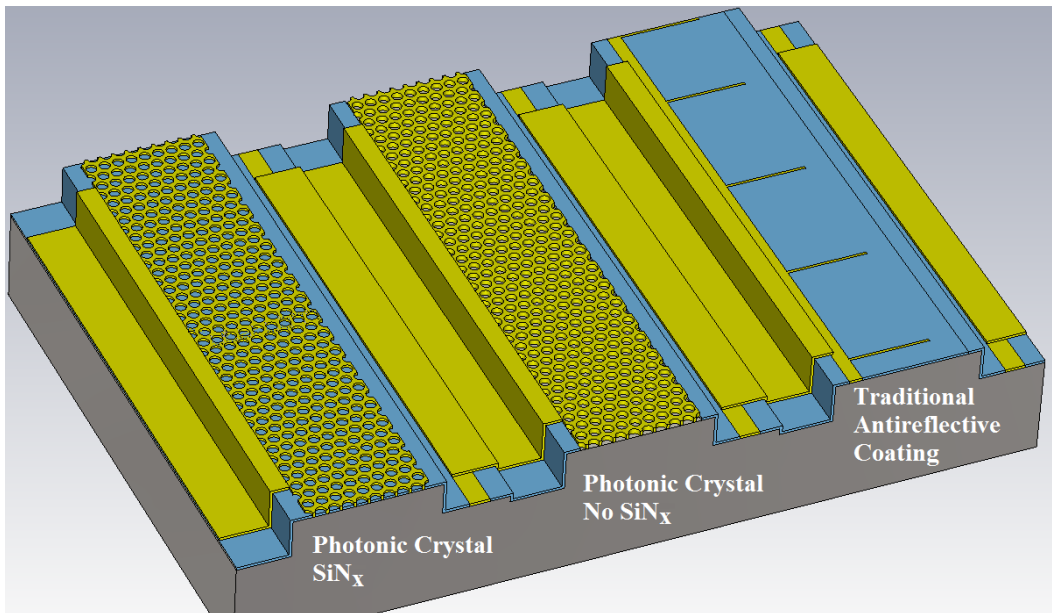


Figure 6.2.5: Potential Future applications of metallic PhCs. These devices can be used as a combination front contact and antireflective coating replacing traditional contacts (right mesa). This figure shows a MIMs diode geometry which is a diode geometry which can be improved by employing a metallic PhC front side contact.

This work has shown that the metallic PhC acts as a surface enhancement as well as a material contact. In comparison to other TPV filter technologies the PhC front-side filter has a much narrower bandwidth (see Chapter 3.2 for

additional information) and can, therefore, be better matched to a photodiode stage. In addition, the proposed metallic PhC can be used to replace both metallic front contacts (which completely block light) and transparent conducting oxides (which are typically poor ohmic contacts). The resulting device would incorporate the best of both devices, effective optical transparency with very low contact resistances, and no downside to device performance. It is the hope that this study emphasizes the importance of PhC technologies to next generation TPV devices and allows for research into yet unexplored areas of PhC applications.

6.3 IMF Photodiode

This section aimed at providing a means to combine lattice mismatched materials into one high efficiency photodiode. The method implemented was to grow a gallium antimonide (GaSb) photodiode on a gallium arsenide (GaAs) substrate, thereby reducing substrate costs. As described in Section 3.3, this process has been shown to be effective when producing a variety of devices including VECELs, but has yet to be utilized for TPV.^[136-144] To this purpose, the structures of Figure 6.3.1 were fabricated into both test diodes and varying aperture arrays in order to test for both relative efficiency values as well as possible material defects.

R9-81			
GaSb/GaAs			
8	GaSb	p-type $2 \times 10^{19} \text{ cm}^{-3}$ (Be)	10nm
7	$\text{Al}_{0.4}\text{Ga}_{0.6}\text{Sb}$	p-type $2 \times 10^{19} \text{ cm}^{-3}$ (Be)	50nm
6	GaSb	p-type $2 \times 10^{18} \text{ cm}^{-3}$ (Be)	50nm
5	GaSb	p-type $2 \times 10^{16} \text{ cm}^{-3}$ (Be)	200nm
4	GaSb	NID	1500nm
3	GaSb	n-type $2 \times 10^{16} \text{ cm}^{-3}$ (Te)	3500nm
2	GaSb	n-type $2 \times 10^{18} \text{ cm}^{-3}$ (Te)	400nm
1	GaAs	n-type	50nm
0	GaAs substrate N+		

R9-86			
GaSb/GaSb			
7	GaSb	p-type $2 \times 10^{19} \text{ cm}^{-3}$ (Be)	10nm
6	$\text{Al}_{0.4}\text{Ga}_{0.6}\text{Sb}$	p-type $2 \times 10^{19} \text{ cm}^{-3}$ (Be)	50nm
5	GaSb	p-type $2 \times 10^{18} \text{ cm}^{-3}$ (Be)	50nm
4	GaSb	p-type $2 \times 10^{16} \text{ cm}^{-3}$ (Be)	200nm
3	GaSb	NID	1500nm
2	GaSb	n-type $2 \times 10^{16} \text{ cm}^{-3}$ (Te)	3500nm
1	GaSb	n-type $2 \times 10^{18} \text{ cm}^{-3}$ (Te)	400nm
0	GaSb substrate N+		

Figure 6.3.1: Two structures grown using molecular beam epitaxy. Top: R9-81 is a GaSb junction grown on GaAs with a IMF layer. Bottom: R9-86 is an identical junction grown on a GaSb substrate.

The I-V curves obtained for these two samples provided valuable information about the material growth and quality. For example, the relative I-V curves and efficiencies for the GaSb/GaAs (R9-81) and GaSb/GaSb (R9-86) were noticeably different, as shown in Figure 6.3.2.

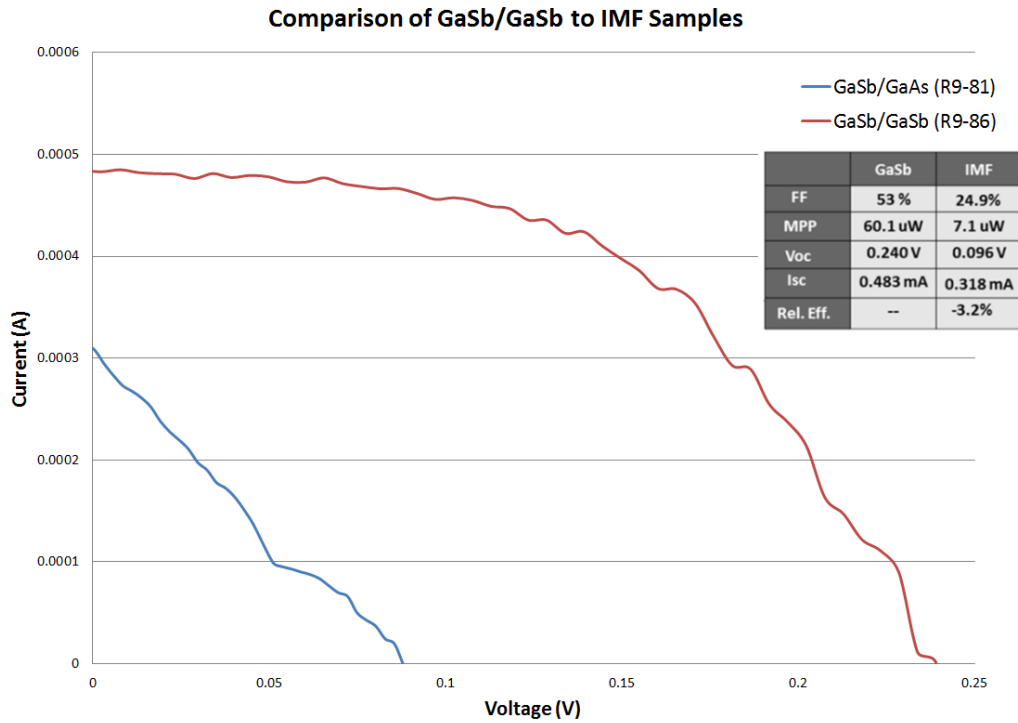


Figure 6.3.2: Current-Voltage characteristics as well as diode characterization metrics discussed in Section 2.2.4. The data shows a marked decrease in performance of an IMF p-n junction in comparison to a GaSb on GaSb junction.

It is expected that the noticeable decrease in FF, MPP, V_{oc} , I_{sc} and efficiency is due to an increase in trap states. The two diodes were grown and fabricated in an identical manner, therefore, it is expected that IMF layer was not completely successful in eliminating threading dislocations and other strain induced dislocations. For this reason, the shift of this study was altered from optimal device configuration, to material analysis. For this reason, multiple

varying sized aperture structures were fabricated in order to determine the effect of IMF layers on surface recombination events. The I-V curves for these aperture sets can be seen in Figure 6.3.3.

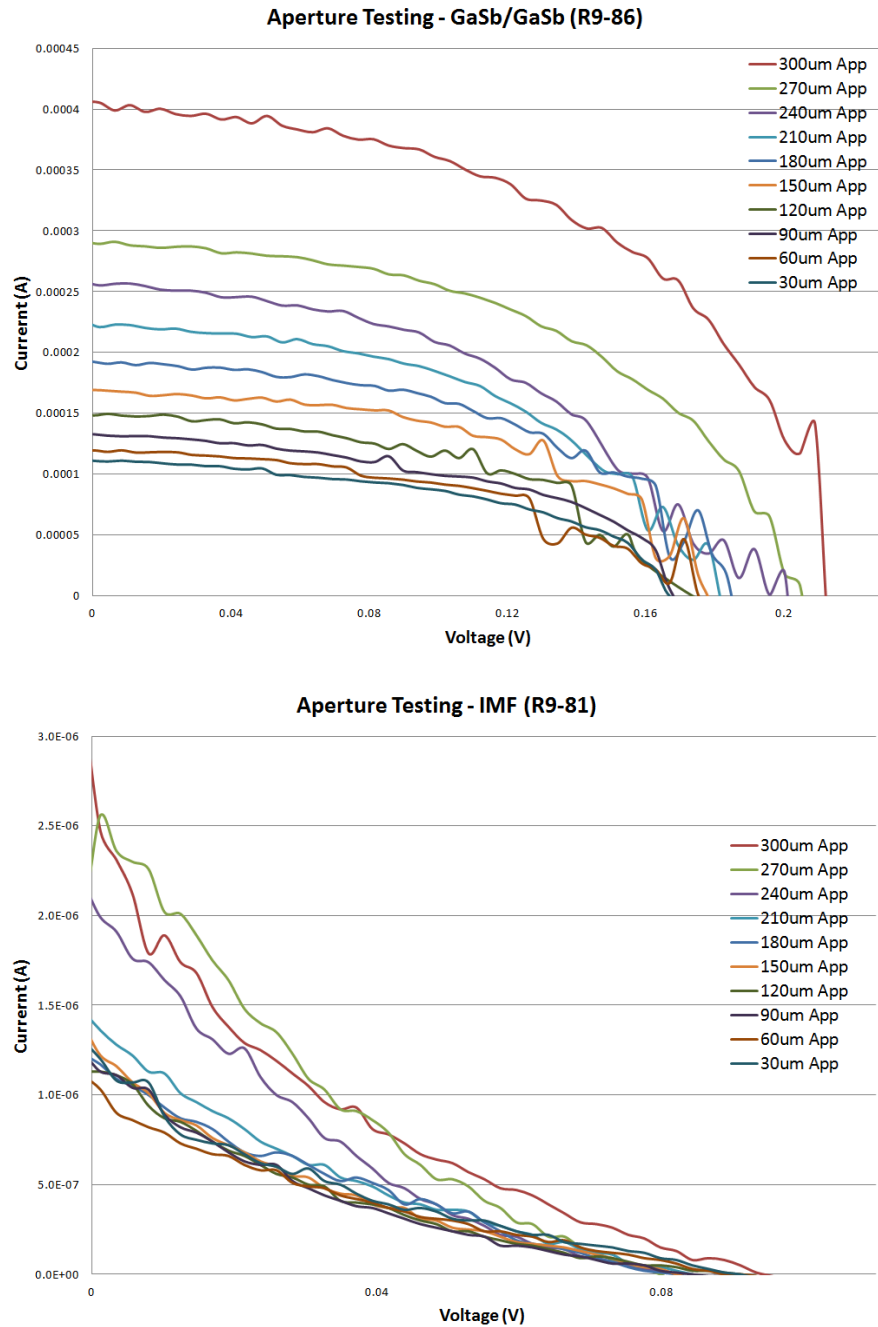


Figure 6.3.3: I-V curves obtained for arrays of varying size aperture diodes. The current obtained from each aperture should decrease proportionately to aperture surface area. *Top:* GaSb on GaSb array of apertures. *Bottom:* IMF aperture array.

The aperture tests of Figure 6.3.3 allow for the creation of current density vs aperture size, shown in Figure 6.3.4. However, another interesting note can be obtained from examination of Figure 6.3.3. The IMF sample experiences an exponential decay in the I-V characteristics. We believe that this can come from one or a combination of two events: a large defect density within the material or a Schottky electrical contact.

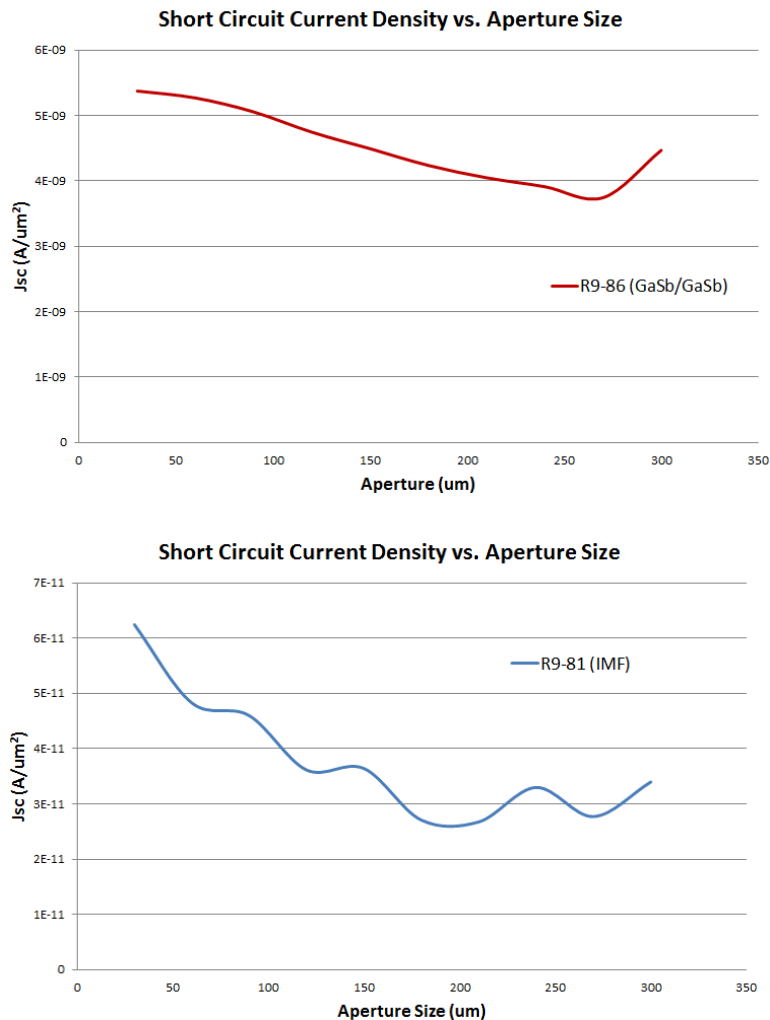


Figure 6.3.3: Current density obtained from varying aperture diodes. Ideally the current densities should be linear; however, variables such as surface recombination and ideal contact spacing may influence the current density. *Top:* GaSb on GaSb samples. *Bottom:* IMF sample.

The short circuit current densities observed in Figure 6.3.3 should be a relatively flat line, with a slight downward slope do to increase contact separation. This is more-or-less the case for both samples; however, the IMF sample does experience an increased slope leading to the conclusion that there is an increase in surface recombination. The observed effect, however, would not account for the significantly altered FF, V_{oc} , I_{sc} , and efficiency observed. For this reason, it is believed that there is an increase in defects related to the GaSb/GaAs lattice mismatch; and not loss of efficiency due to a surface recombination effect.

The spectral response of the R9-86 and R9-81 was then tested in order to determine crystal quality and wavelength selectivity. The two experimental structures were also compared to a large area commercially obtained diffusion doped GaSb TPV diode. The relative spectral responses are shown in Figure 6.3.4.

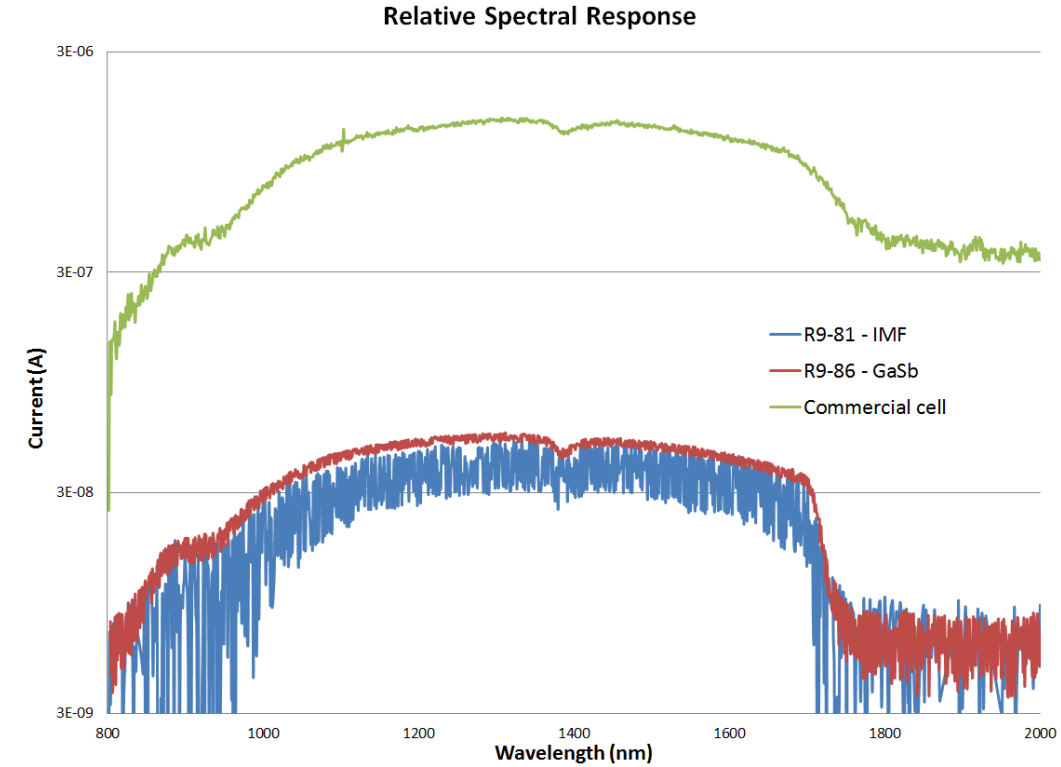


Figure 6.3.4: Spectral Response of both the GaSb on GaSb (R9-86) and IMF (R9-81) samples compared to the spectral response of a commercially available GaSb TPV diode. Although the commercial cell shows better efficiency, the sharper cut-off frequency of the R9-86 and R9-81 samples allude to higher general crystal quality.

Due to Figure 6.3.4 it becomes evident that a high quality p-n junction was obtained for both the GaSb/GaSb (R9-86) and IMF (R9-81) samples. In particular, the cut-off frequency off both samples was much sharper than the commercially available GaSb diode. However, the current obtained through the commercial cell was orders of magnitude greater than both experimental samples. It is for this reason that the low current is predicted to be due to poor electrical contacts causing a barrier impeding current flow.

Closer examination of the electrical reviled some interesting information not previously observed. As shown in Figure 6.3.5, the top contacts of both

samples displayed highly resistive ohmic characteristics, which do explain some of the decreased efficiencies. However, more concerning was the bottom contacts which demonstrated Schottky diode characteristics until an applied voltage approaching 3 V. This contact material was obtained through photodetector research and as such was typically operated at an applied voltage. As TPV photodiodes do not use an applied voltage, a new ohmic contact material must be explored for high-efficiency cells.

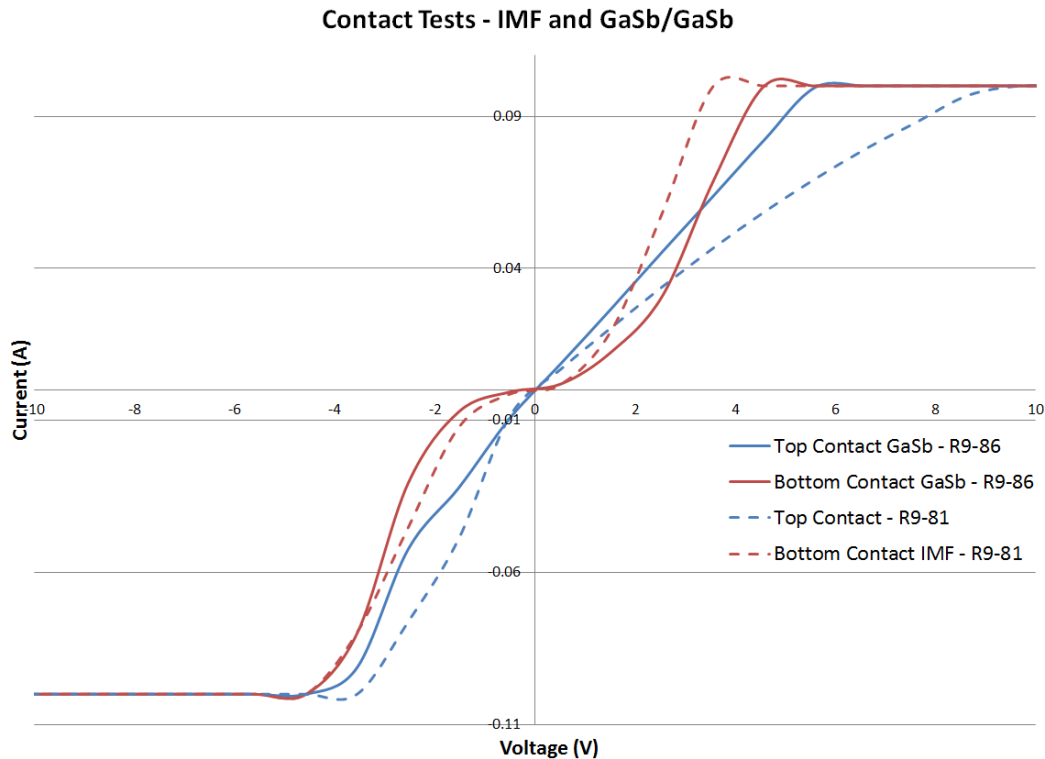


Figure 6.4.5: I-V characteristics of the GaSb on GaSb (R9-86) and IMF (R9-81) contact materials. Neither top nor bottom demonstrated ideal ohmic behavior; however, the top contacts did show highly resistive ohmic results. Bottom contacts for both the R9-81 and R9-81 were shown to be Schottky contacts until an applied voltage of approximately 3 V. These samples typically operate at voltage of less than 1 V making these common contact materials non-ideal for TPV applications.

The poor contact materials, however, do not sufficiently explain the decreased efficiency experience between the IMF photodiode and GaSb/GaSb cells. There are many possible reasons for the decreased efficiencies with the presence of an IMF layer. The most common issue is expected to be due to poor IMF layer isolation leading to dislocations which then propagate vertically through the TPV structure. To this end, a second batch of IMF type TPV diode devices was designed, shown in Figure 6.4.6. These layers utilize a new structure in order to optimize the device efficiency and will also implement improved contact recipes. Furthermore, the bottom contact layers will be grown with a decreased doping concentration in hopes of improving crystal quality. The new structures were simulated by Sentarus by Synopsys and the simulated I-V curves are shown in Figure 6.4.7.

Layer	Material	Doping	Description	Thickness
6	GaSb	p-type 2×10^{19} (Be)	Top Contact	10 nm
5	$\text{Al}_{0.3}\text{Ga}_{0.7}\text{Sb}$	p-type 2×10^{19} (Be)	Window Layer	50 nm
4	GaSb	p-type 2×10^{18} (Be)	Buffer Layer	50 nm
3	GaSb	p-type 2×10^{16} (Be)	Absorber	1500 nm
2	GaSb	n-type 2×10^{16} (Te)	Emitter	500 nm
1	GaSb	n-type 2×10^{17} (Te)	Back Contact	400 nm
0	Substrate			

Figure 6.4.6: Optimized Structure to further test benefits of using an IMF layer. These designs consist of a three sample group. Sample 1 is shown above. Sample 2 adds a IMF layer between layer 0 and 1. Sample 3 replaces layer 0 with a GaSb substrate.

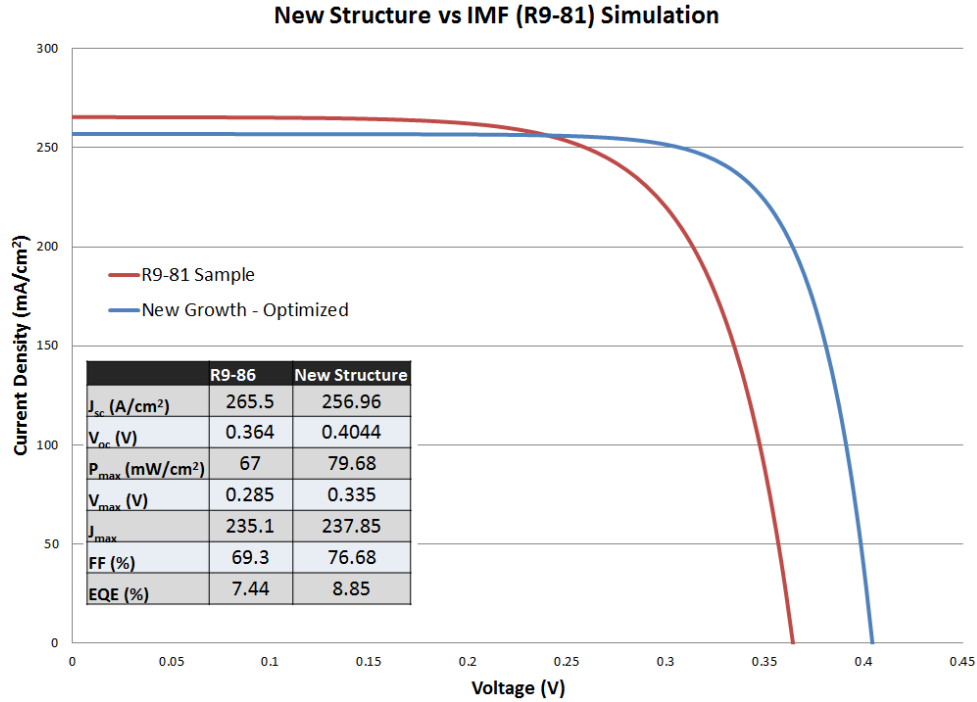


Figure 6.4.7: The proposed IMF layer produces a lower I_{sc} , however, the device was designed to operate using a bottom contact layer of decreased doping concentration. This is hoped to reduce potential defects related to highly doped material growths allowing IMF analysis based on lattice mismatched strain with reduced effects due to other mechanisms.

These new structures utilize features beyond optimized layer thickness. The structures include a diode isolation layer allowing for monolithically integrated modules (MIMs) to be fabricated on chip, as well as a layer thickness which take full advantage of the metallic photonic crystals designed in Chapter 6.2.

It is important to mention that IMF layers have not been studied as optical absorber materials in existing literature. The bulk of IMF studies examine optical and structural characteristics, or photon emitter applications, as described in Chapter 3.4.^[133-157] It is for this reason that any study of an IMF layer demonstrating photovoltaic power generation is a significant step forward in IMF research, and opens the door to improving previously uninvestigated technologies.

In order to provide increase the efficiency IMF absorbers, more work must to be done in order to understand exciton recombination and carrier transport issues; which may cause the decreased IMF performance in relation to traditional GaSb photodiodes. Some of these design issues have been addressed, such as decreasing back contact doping concentration as well as decreased total device thickness. It is hoped that these improvements allow for a diode efficiency approaching that of a traditional sample. As mentioned in Chapter 3.3, this would provide a breakthrough to allow many other IMF material combinations such as SLS structures, leading to an entirely new field of custom bandgap multijunction TPV diodes.

6.4 Metamaterial Polarization Grid

The metamaterial polarization grid is specifically designed to be used to provide multiple polarization sensitive photodetector measurements without reducing pixel count. To accomplish this, the device must operate dynamically, i.e. altering between single polarization sensitivity, and an all polarization transmission phase. This section is broken into two parts: the static polarizer and the dynamic polarizer. The static polarizer represents a new type of metamaterial structure which provides polarization sensitivity as well as an “all-pass” polarization phase. Following the static case, the dynamic MM polarizer will be examined. This device is designed to operate with an applied bias in order to reduce the MM resonance and produce only single polarization transmission.

6.4.1 Static Polarizer

The goal of the static polarization grid was to create a device which produced polarization sensitivity, however, at resonance allowed equal transmission of all polarizations. This proved to be a challenge in that it required the integration of two different types of MM resonance, a notch filter and a band pass filter, at near the same wavelength. In order to accomplish this, three types of MM patterns were combined in order to produce a response similar to that of Figure 6.4.1.1

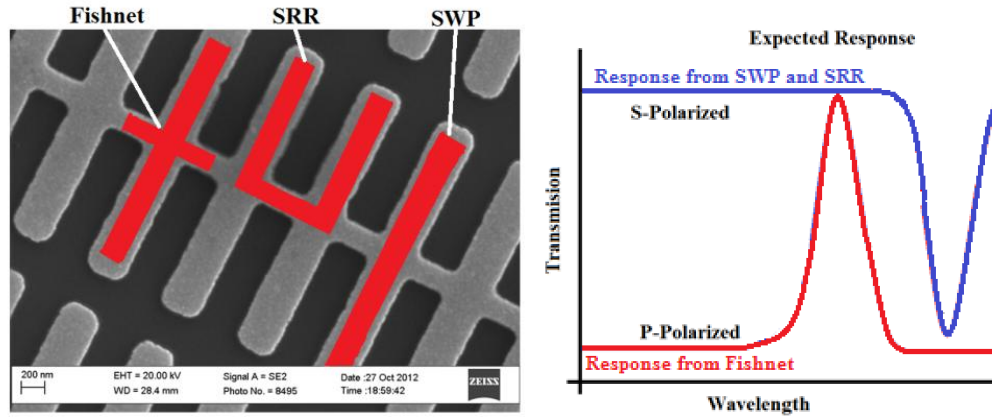


Figure 6.4.2.1: *Left:* structure created in order to produce the unique MM response seen on the Right. This structure combines properties of Fishnet, SRR, and SWP type metamaterials. *Right:* the expected response of the MM polarizer grid shown on the Left. This structure uses two polarization sensitive MM resonance peaks.

This unique structure utilizes the parallel metallic bands of a split wire pair MM, the ring resonator design of SRR, and the repeating “+” of a fishnet pattern. This device was predicted to have both a high transmission and polarization sensitive band as well as a low transmission polarization band. The characterization of this new device represents a new leap forward in MM technologies as it incorporates multiple design elements and no similar device has been previously investigated. In order to determine the surface currents and electric fields generated in this new MM, the surface currents and E-field was examined using CST Microwave studio.

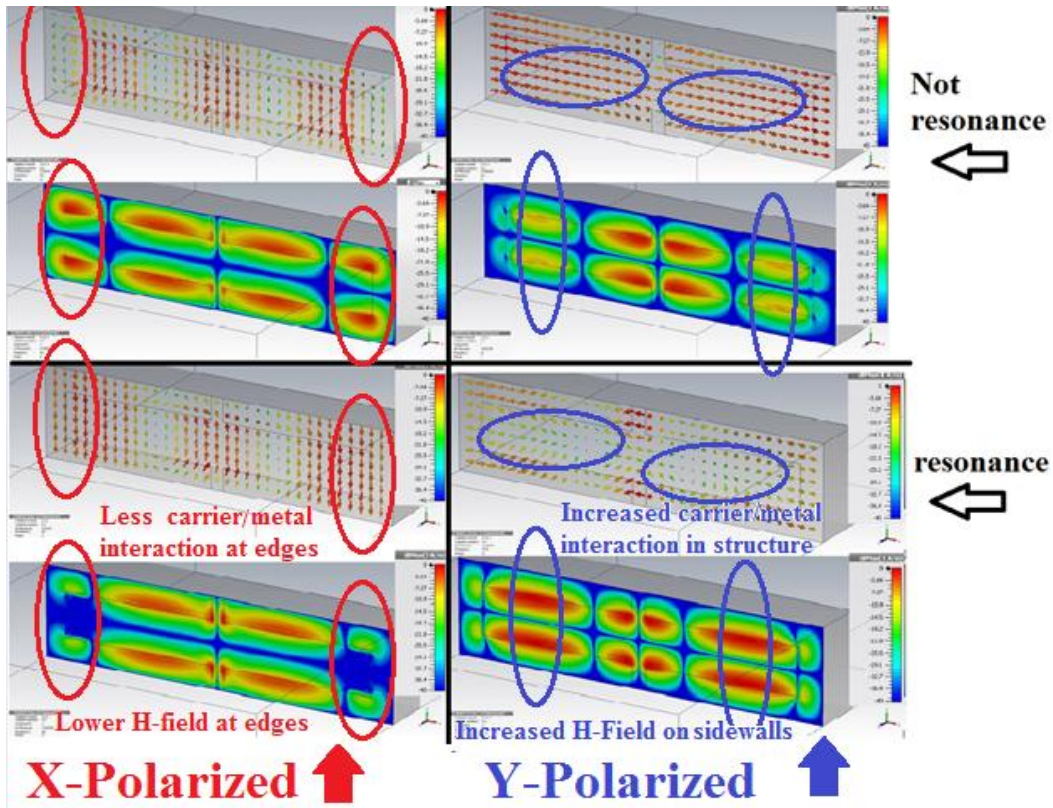


Figure 6.4.1.2: Surface current and H-field vector. *Top Left:* X-polarized radiation not at resonance. There is a surface current across the splitgap causing the MM to act as a traditional polarization bar. The result is decreased transmission. *Top Right:* Y-polarized radiation not at resonance. There is little surface current interaction between the Y-splitgap. The result is an unaffected transmission. *Bottom Left:* X-polarization at resonance. The interaction across the X-splitgap is removed, the result is a transmission pass-band. *Bottom Right:* Y-Polarization at resonance. Surface current begins to flow across the Y-splitgap resulting in a decreased transmission.

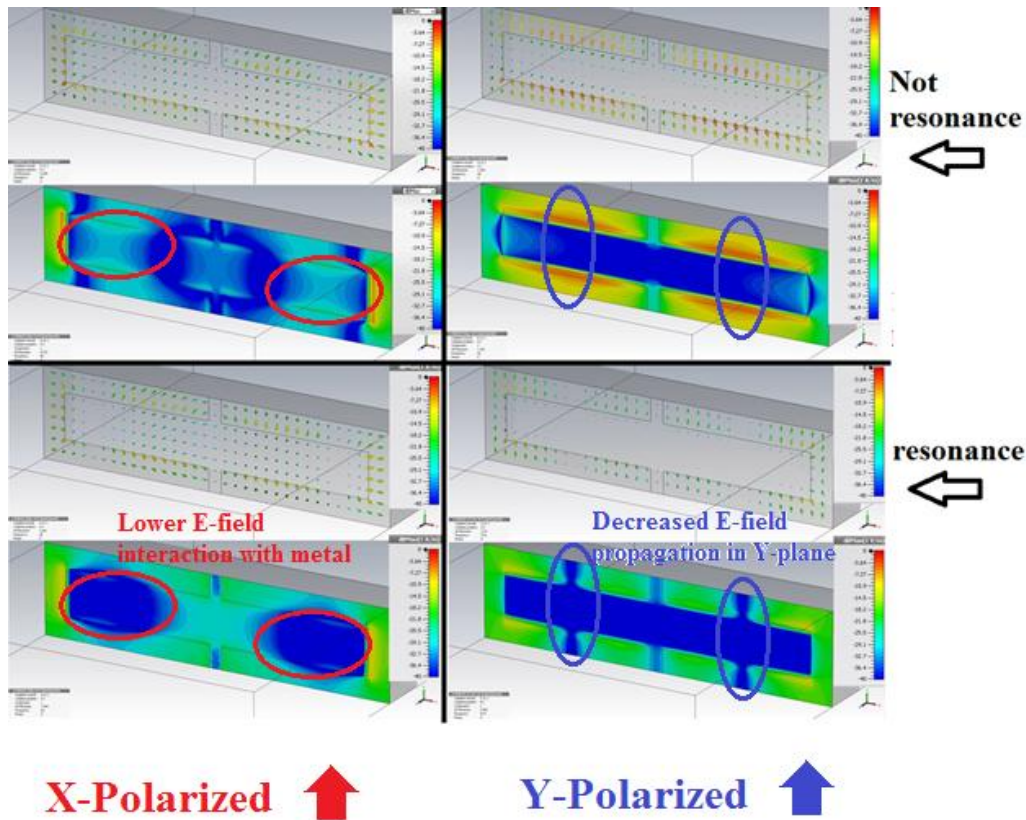


Figure 6.4.1.3: E-field vector and magnitude. *Top Left:* X-polarized light not at resonance. There is a stronger Z-direction E-field within the metallic elements creating the surface current. *Top Right:* Y-polarization in the E-field is directed in the Y-plane therefore orthogonal to the incident radiation. *Bottom Left:* X-polarized light at resonance. The E-field is now directed in the X-plane and therefore orthogonal to the incident radiation. *Bottom Right:* The E-field begins to interact in the Z-plane and not Y-plane resulting in a transmission dip due to loss of orthogonality.

The E-field, surface current, and H-field provide valuable information about the interaction of photons with the MM structure. For example, Y-polarized light is effectively absorbed at resonance. Figure 6.4.1.3, shows a decreased E-field between parallel elements in the Y-plane, whereas Figure 6.4.1.2 expresses an increased in carrier flow. This can be attributed to an E-field interaction with surface charges at resonance which creates current flow, and alters the H-field in

the Z-plane, as one might expect in a SRR device. The result is a decreased transmission.

For the X-polarization at resonance, there is a lower interaction between the E-field across the X-plane split gap. At this frequency, the E-field interaction shifted to the center of the “cross-shaped” pattern. Also, the surface current at the edges of the MM is drastically decreased (decrease in H-field). The combination of these resonance properties causes one to expect an increase in transmission at resonance, as experienced in fishnet patterned MMs. ^[177]

This device was fabricated, tested, and compared to simulation software, shown in Figure 6.4.1.4. In order to verify the response is due to the combination GaAs/sapphire substrate, this metamaterial was also constructed on a 450 μm thick GaAs substrate. The effect is the loss of carrier confinement near the surface of the GaAs and the uncoupling of the thin film MM effect. As shown in Figure 6.4.1.4, the resulting structure acts as a polarization grid common to most photodetectors (see Figure 3.4.1.6 of Chapter 3).

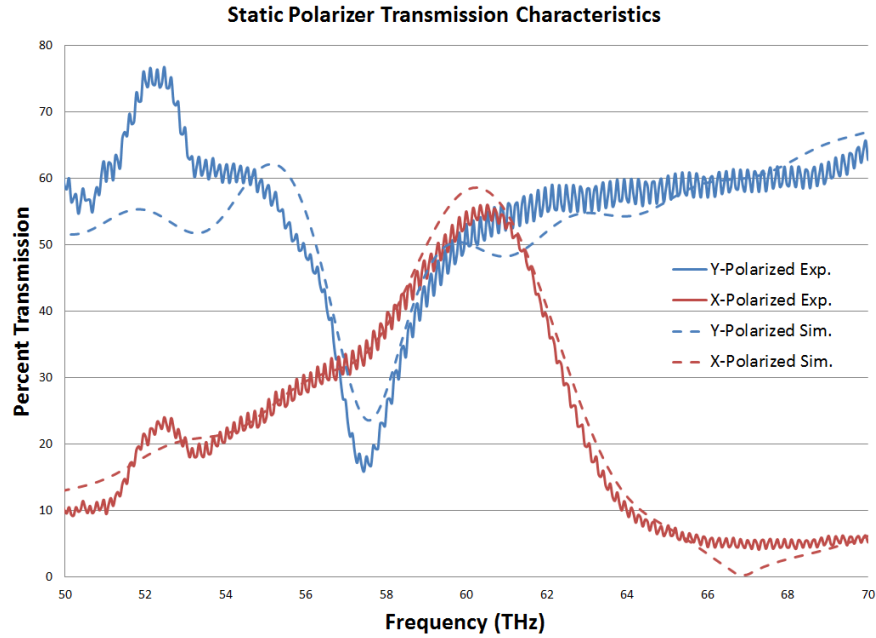


Figure 6.4.1.4: Experimental and simulation data for both optical polarizations. Dashed lines are simulation results and solid curves were obtained experimentally. Blue results are Y-polarized light and Red lines are X-polarized cases.

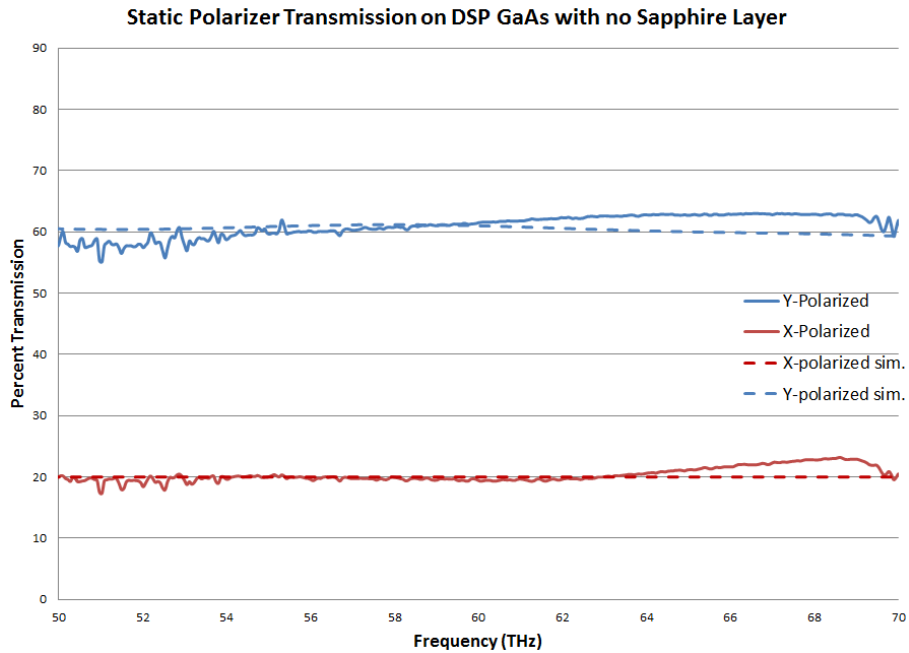


Figure 6.4.1.4: MM structure constructed on a 450 μm thick doped GaAs substrate, the result is loss of carrier confinement and a transmission response similar to that of a common photodetector polarization grid.

It was also determined that altering the MM gap spacing in the X and Y direction uniquely affects the MM response, Figure 6.4.1.5. This effect has unique applications in altering each polarization's resonance frequency independently. When optimized, this can allow for designer regions of unity transmission, effectively allowing one to increase or decrease the frequencies of operation.

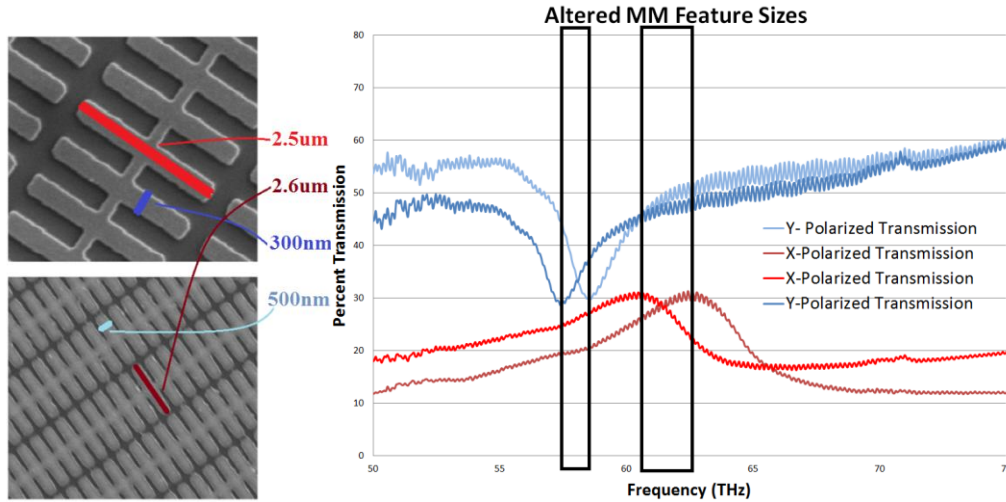


Figure 6.4.1.5: Independent manipulation of X and Y feature parameters allows for independent shifts in X and Y resonance peaks. *Left:* SEM images of two unoptimized structures. *Right:* Corresponding polarization sensitive transmission for each structure.

Further analysis of simulated data also concluded that both optical polarizations experience an altered effective index of refraction, Figure 6.4.1.6. This effective index experiences a dip at the location of the X-polarization transmission window, resulting in decreased reflection. This dip is to the approximate value of GaAs; and perhaps not so coincidentally, bulk GaAs and the MM polarizer (at resonance) have the same percent transmission. Also, the metamaterial experiences a slight increase in the effective index for Y-polarized light at resonance. However, this effect does not completely explain the large

transmission changes experienced experimentally. Therefore, it is assumed that there is a large optical loss in the Y-polarized MM response at resonance, as would be expected from a SWP or SRR metamaterial.

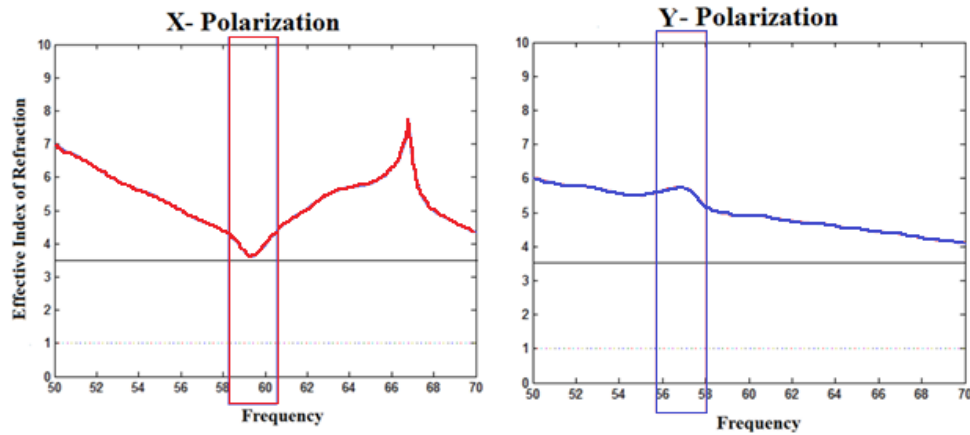


Figure 6.4.1.6: *Left:* Effective index for X-polarized light. There is a large dip in magnitude at resonance to the same value as GaAs. *Right:* Effective index for Y-polarized light. There is a slight increase at resonance, however, not a large enough value to explain the decreased transmission.

Multiple GaAs doping concentrations were also examined in order to provide some base for potential dynamic results. High doping concentrations are also expected to alter the optical properties of the GaAs surface leading to a change in resonance wavelength. The result is expected to be a decrease in transmission as well as an optical blue-shift in resonance frequency, as shown in Figure 6.4.1.7.

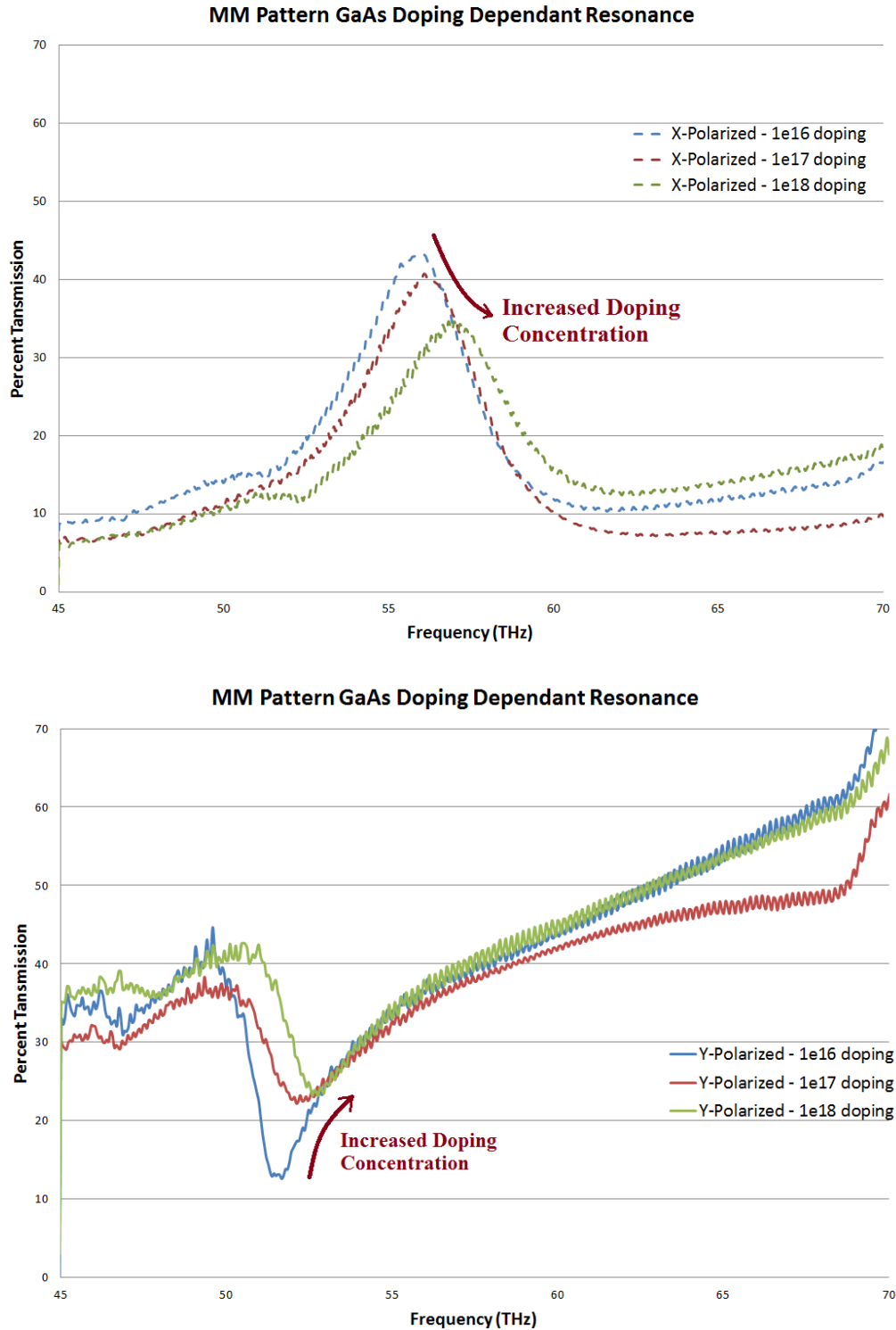


Figure 6.4.1.7: Effect of doping concentration on total percent transmission as well as resonance wavelength. Higher doping concentrations increase the material permittivity thereby creating a blue shift in resonance. Also, higher doping levels coincide with larger conductivities resulting in a decreasing resonance peak. *Top:* X-Polarization. *Bottom:* Y-Polarization.

Within this section, a MM polarization sensitive device was simulated, constructed, and analyzed. This device produced high transmission with a notch filter effect for Y-polarized light, and a low transmission with a band pass effect for X-polarization. The unique structure was fabricated by combining existing MM structures in a novel approach. Also, the sapphire/GaAs/metallization was confirmed to be producing the MM effect. The loss of either the sapphire substrate or alteration of the metallization was determined to directly affect the optical response. This metamaterial structure produces 1:1 transmission for both polarizations at a frequency of 61 THz (4.9 μm). Also, the effect of increased conductivity on metamaterial response was demonstrated via increased GaAs doping concentration. The metamaterial transmission characteristics can also allow this device to be implemented in conjunction with a dynamic MM contact grid in order to produce bias dependent transmission characteristics.

6.4.2 Dynamic Polarizer

The dynamic metamaterial polarizer was initially simulated in CST microwave studio using an increase in conductivity to simulate an applied voltage/ increased current flow through the GaAs layer. These simulated results provided a baseline for the necessary conductivity increases to initiate a sufficiently altered metamaterial response. The simulated dynamic transmission characteristics are shown in Figure 6.4.2.1

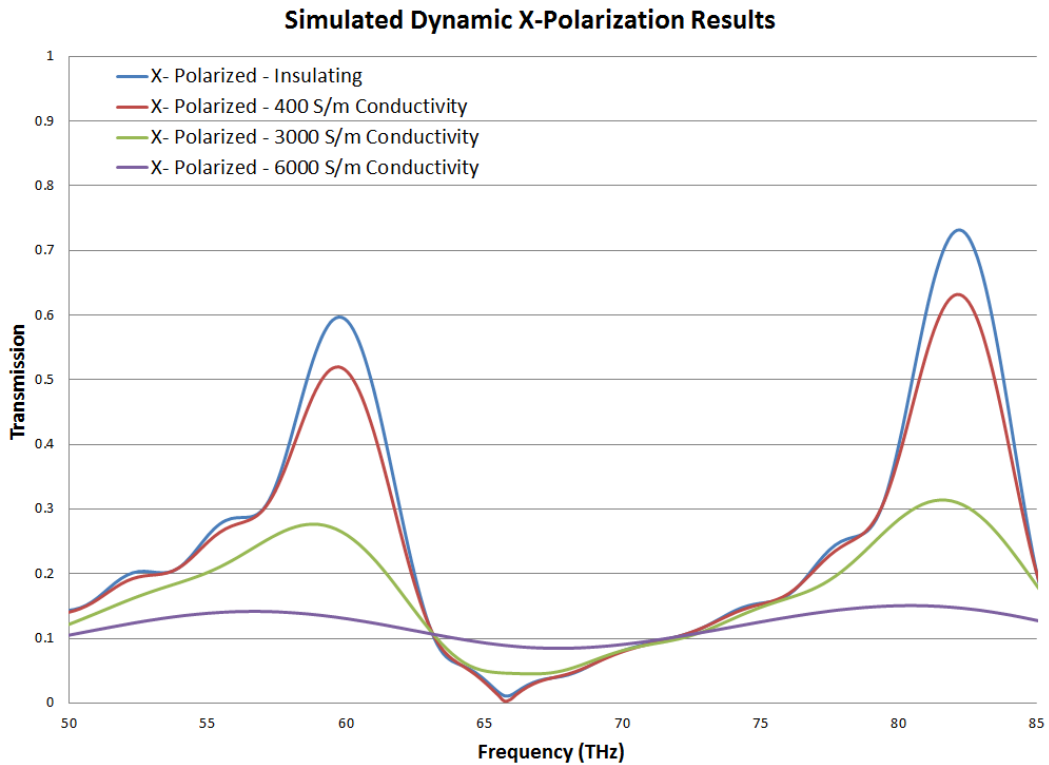
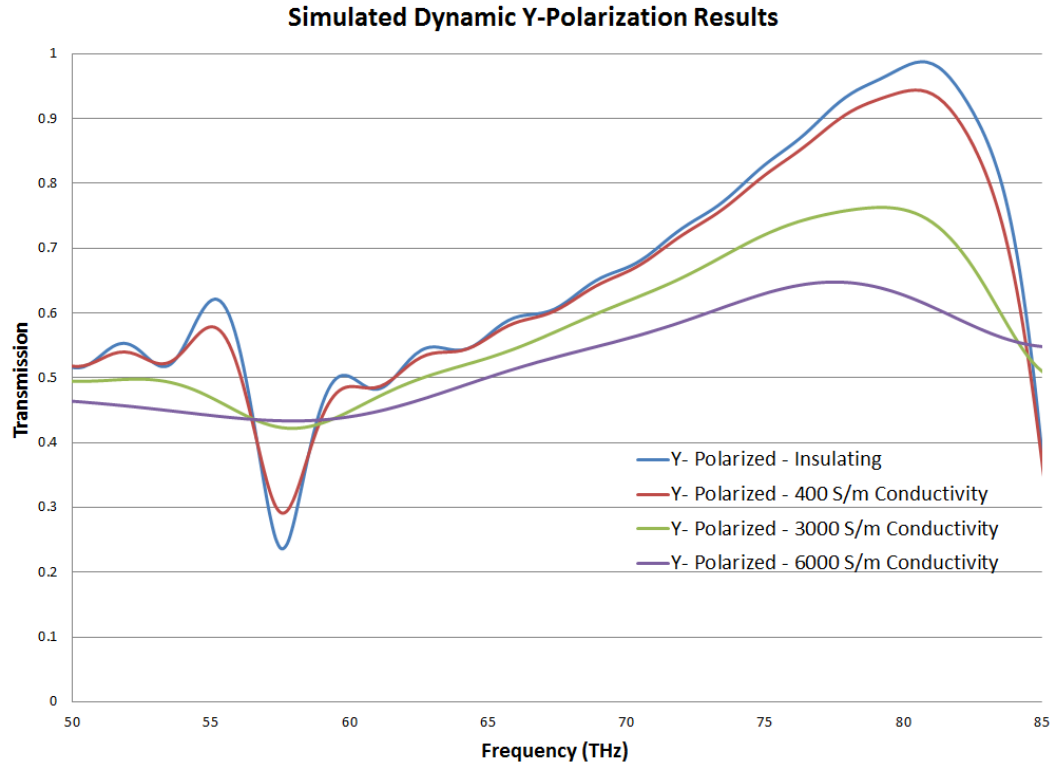


Figure 6.4.2.1: Dynamic metamaterial response due to an increase in GaAs conductivity ranging from 0 S/m to 10,000 S/m. This MM is designed to operate at 60THz. *Top:* Y-Polarization. *Bottom:* X-Polarization.

As shown in Figure 6.4.2.1, a minimum change in conductivity of 3,000 S/m is necessary to provide a dramatic change in optical transmission. With this minimum change in conductivity, optical filter characteristics were determined, and are shown in Figure 6.4.2.2.

Bias	Actual Horizontal Pol. (Ideal)	Actual % Vertical Pol. (Ideal)
No / on	25 (0)	50 (100)
Yes / off	60 (100)	48 (100)

Ratio	Actual Horizontal Pol. (Ideal)	Actual Vertical Pol. (ideal)
On/Off	5:12 (0:100)	25:24 (1:1)

Ratio	Actual On (Ideal)	Actual Off (Ideal)
Polarization - H:V	1:2 (0:100)	15:14 (1:1)

Note: Off represents transmission of all polarizations

Figure 6.4.2.2: Initial simulated dynamic MM filter characteristics for a conductivity change of 10,000 S/m

The metamaterial was constructed on a bulk GaAs substrate, ohmic and Schottky contact materials were deposited, and dynamic transmission characteristics were obtained. These characteristics, shown in Figure 6.4.2.3, are sufficient to provide a baseline for the current necessary to create a 3,000 S/m conductivity change within the substrate. This relatively simple experiment determined that a current injection of at least 410 mA is needed in order to provide a sufficient change in substrate conductivity.

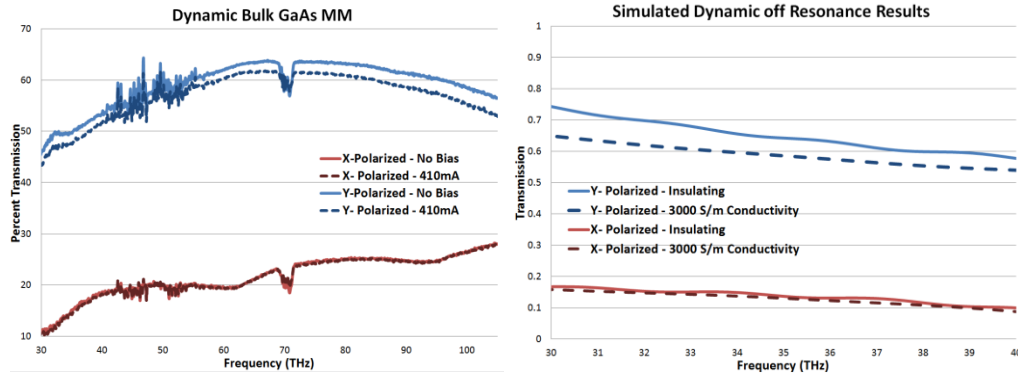


Figure 6.4.2.3: *Left:* Experimental dynamic results for a MM patterned on bulk GaAs. An external bias of 5 V and injection current of 410 mA was applied over the MM structure. The bulk GaAs removes the MM resonance response; however the bulk response due to an applied voltage can still be determined. *Right:* Simulated response of a MM structure patterned on a bulk GaAs substrate and the conductivity change (3,000 S/m) needed near the surface to obtain a bulk transmission loss of 3%.

These results indicate that we needed to determine material combinations which yield high currents through the GaAs layer. To this end, the traditional ohmic contact recipes (used for the structure in Figure 6.4.2.3) as well as a variety of Schottky contacts were deposited on highly doped GaAs on sapphire ($1 \times 10^{18} \text{ cm}^{-3}$ doping). Both Schottky contacts and ohmic contacts resulted in the same general current flow through the metamaterial, shown in Figure 6.4.2.4. For this reason, it was determined that there was a material flaw within the GaAs, and not an issue forming an electrical contact.

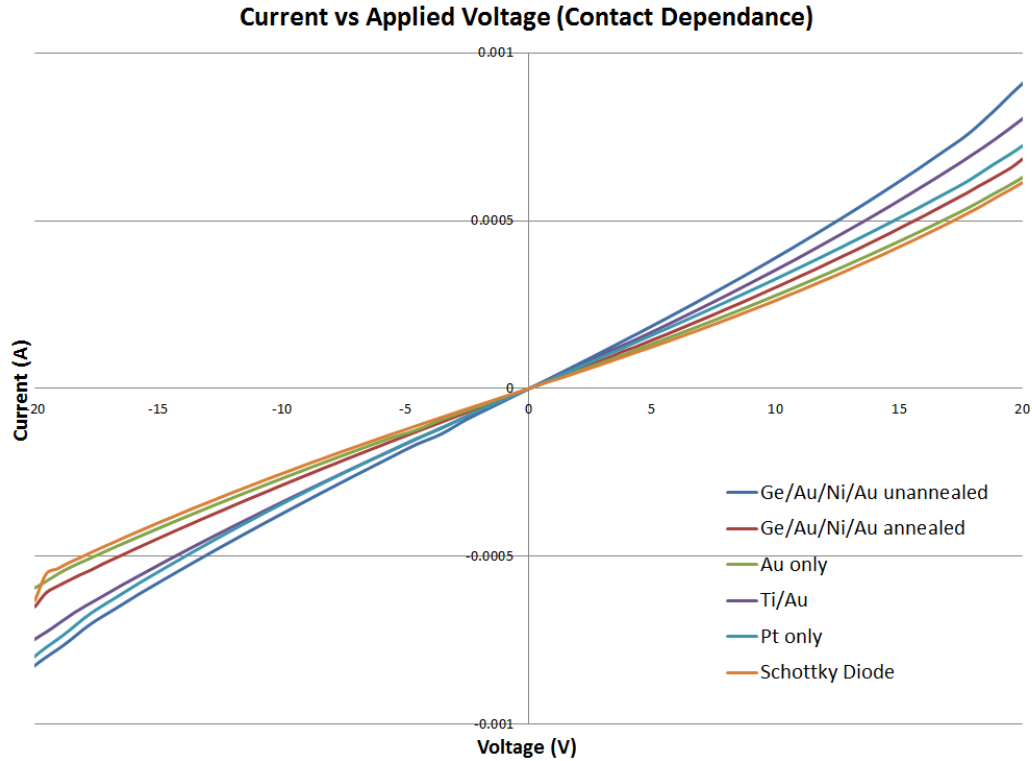


Figure 5.6.2.4: A variety of contact recipes used on a 400 nm thick GaAs on sapphire wafer. All contacts performed relatively consistently whether it was a traditional ohmic contact (annealed Ge/Au/NiAu) or a traditionally Schottky contact (Ti/Au). This leads one to believe that material quality is not sufficient to support high quality electrical contacts.

Under closer examination, the GaAs layer was identified to be of lesser than optimal quality. For example, Figure 5.6.2.5 shows a typical bulk GaAs substrate and a GaAs on sapphire substrate. The bulk GaAs is extremely smooth even after chemical cleans and MM fabrication. The GaAs on sapphire, however, has visible pits and ridges. These surface defects are characteristic of poor growth quality. Also, due to the nature of the MM pattern's dependence on the GaAs layer, it would not be unexpected to find a decrease in device performance due to these defects.

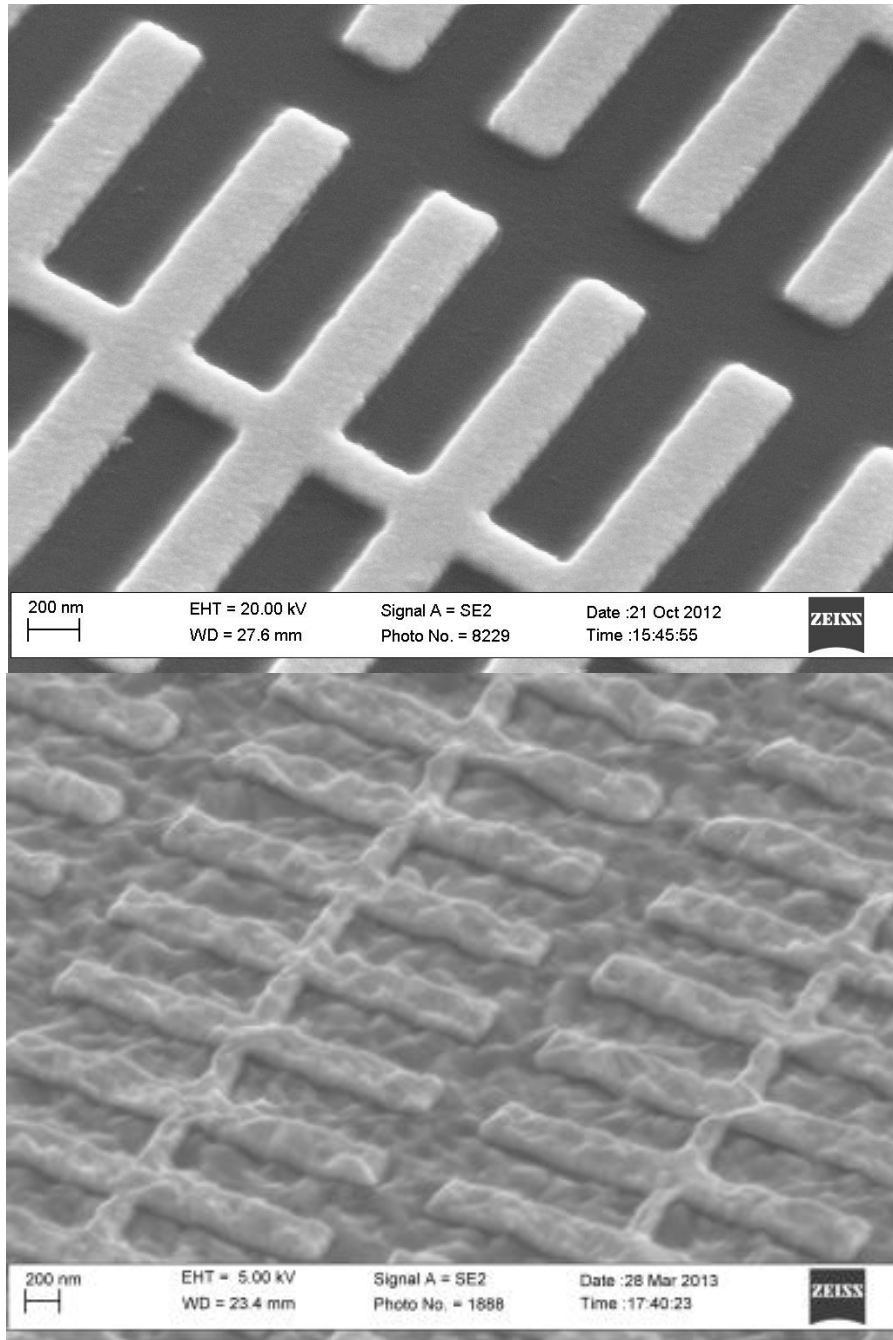


Figure 5.6.2.5: SEM images of material surface, both images contain identically processed metamaterial structures. *Top:* a MM patterned on a commercially available bulk GaAs wafer. *Bottom:* a MM patterned on 400 nm of GaAs on sapphire grown using molecular beam epitaxy.

Figure 5.6.2.5 provided a starting point into improving the GaAs on sapphire growth. These images showed a high loss in material quality. As such,

an exhaustive literature search was undertaken to obtain alternative epitaxial growth methods. The original sample growth was based on the procedure listed in the top of Figure 5.6.2.6. In order to improve on this method of growth, two alternative growth procedures are also proposed in Figure 5.6.7 to create a higher quality GaAs film. ^[227]

Current Growth Process

Step	Process
Initial Growth – 50nm	Low Temp – 350 C
Anneal	625 C
Final Growth - 350nm	580 C

Improved Quality Process

Step	Process
Initial Growth – 25nm	400 C – slow growth – 0.1um/hr
Ramping	580 C – continued growth – 0.1um/hr
Final Growth - 350nm	580 C – 1.0um/hr

High Quality Process

Step	Process
Initial Growth – 25nm	400 C – slow growth – 0.1um/hr
Buffer layer – 200nm	Graded In _{0.2} Ga _{0.8} As/GaAs SLS 560 C – 1.0um/hr
Final Growth GaAs - 200nm	580 C – 1.0um/hr

Note: All growths should be performed on R-plane (0112) sapphire

Figure 5.6.2.6: Alternate GaAs on sapphire growth process. *Top:* process currently used. *Middle:* Design proposed to improve crystal quality. *Bottom:* High quality process utilizing an SLS buffer layer to reduce crystal defects. ^[227]

While this work in itself does not create a voltage dependent metamaterial device, experimental evidence gives strong evidence that the proposed device will

act in a dynamic fashion with the application of an applied external voltage. For example, Figure 5.6.2.7 demonstrates the shift in resonance with increasing carrier concentration (doping). Also, Figure 5.6.2.3 has shown a decrease in transmission due to applied bias.

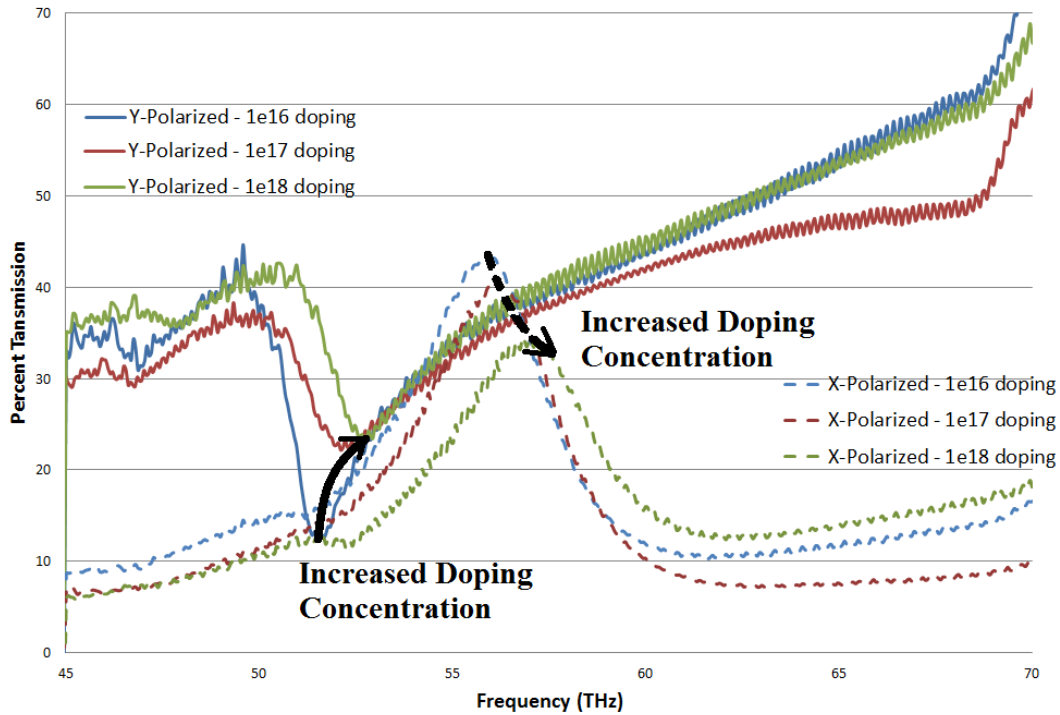
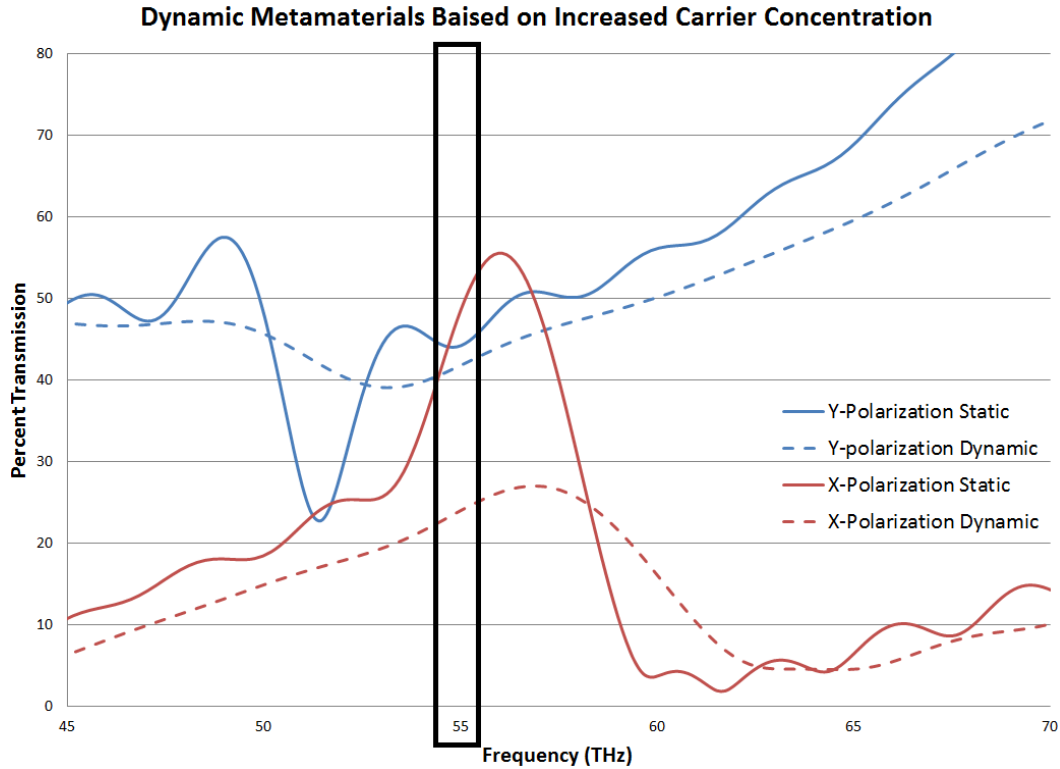


Figure 6.4.2.7: Metamaterial resonance shifts due to increases in doping. The substrate was determined to have low electrical conductivity during contact testing, and as such the increased doping concentration can also be modeled as an increase in carrier concentration independent of corresponding conductivity increases.

The experimental blue-shifts observed in Figure 6.4.2.7 are supported in literature studies. In general, these studies predict a small change in index of refraction with increased charge carriers.^{[228][229]} This includes increasing both doping concentration as well as through carrier injection. For example, at an optical frequency of 200 THz and doping of $1 \times 10^{18} \text{ cm}^{-3}$, Bennett *et al* predicts a decrease in index of refraction of $4 \times 10^{-3} \text{ cm}^{-3}$.^[228] As experimental corroboration,

Figure 6.4.2.7 shows that increasing the doping level from $1 \times 10^{16} \text{ cm}^{-3}$ to $1 \times 10^{18} \text{ cm}^{-3}$, can shift the resonance frequency by a significant amount (more than 3 THz).

With this information, we can calculate the resonance shift due to an increase in carrier concentration, shown in Appendix 6.4.2. In effect, it can be determined, with an applied voltage of 5 V and injection current of 410mA, an increase in carrier density of $1.5 \times 10^{18} \text{ cm}^{-3}$ will be experienced. The expected change in refractive index, and, therefore, optical response, should be similar to the doping change of $1 \times 10^{16} \text{ cm}^{-3}$ to $1 \times 10^{18} \text{ cm}^{-3}$ shown in Figure 6.4.2.7. Interestingly, the poor electrical conductivity of the doped GaAs on sapphire in Figure 6.4.2.7 allows the estimated index change, to be compared directly to carrier injection with results independent of conductivity. This allows for more accurate simulated dynamic results which can take into consideration resonance shifts due to conductivity as well as shifts due to index change. Based on both experimental dynamic evidence, and simulation data, Figure 6.4.2.8 depicts a realistic dynamic response characterized by carrier induced changes in refractive index as well as increases in substrate conductivity.



Bias	Actual Horizontal Pol. (Ideal)	Actual % Vertical Pol. (Ideal)
No / on	22 (0)	43 (100)
Yes / off	45 (100)	45 (100)

Ratio	Actual Horizontal Pol. (Ideal)	Actual Vertical Pol. (ideal)
On/Off	1:2 (0:100)	1:1 (1:1)

Ratio	Actual On (Ideal)	Actual Off (Ideal)
Polarization - H:V	1:2 (0:100)	1:1 (1:1)

Figure 6.4.2.8: *Top:* Simulated dynamic metamaterial response considering both a conductivity change of 3,000 S/m and an injection current of 410 mA. This simulation takes into consideration carrier induced refractive index changes as well as induced conductivity changes. *Bottom:* The corresponding filter characteristics of the simulated results. These filter characteristics can be even further improved with conductivity increases greater than 3,000 S/m or increased applied voltages and injection currents. As such, these figures should be considered realistic simulated data and not optimum data.

To provide experimental verification of this model, the growth procedures of Figure 5.6.2.6 are proposed in order to create a dynamic polarization grid.

Based on previous experimental evidence, this structure will provide high transmission for all polarizations when no bias is applied. When biased with at least 410 mA of current, the polarization grid will turn “on” reducing the transmission of a single optical polarization. The structure is designed to operate at approximately 60 THz (5 μm); however, as doping concentration increases, the operational frequency will be blue-shifted due to an altered material permittivity. The resulting structure designed to dynamically alter transmission characteristics, reducing the need for multi-pixel devices to sense all optical polarizations.

This section aimed to use dynamic metamaterials to create optical filters for photodetector applications. These filters were designed to provide dynamic on/off ratios to replace large filter wheels and increase available pixel counts in current polarization sensitive photodetector technology. To this end, a static MM device was constructed which aimed at providing a MM response which could be dynamically altered with an applied voltage. The MM was tested with a variety of doping concentrations and applied voltages, and it was shown that altering the conductivity and carrier injection of the static MM would alter the resonance of the MM. When an altered conductivity and carrier injection is due to an applied bias, the result is expected to be a dramatic decrease in MM resonance as well as a blue-shift in resonance frequency (Figure 6.4.2.8).

Beyond this thesis, the MM polarization grid must undergo an optimization procedure. The goal must be to increase the transmission characteristics nearer to the ideal characteristics of Figure 6.4.2.8. This will be done by adding more complicated MM features or reducing the GaAs layer

thickness. Also, two polarization grids will be incorporated monolithically in order to allow dynamic characteristics of multiple polarizations. A multilayer structure can be fabricated by adding a Si_3N_4 capping layer to an existing dynamic polarizer, growing a thin GaAs layer through metalorganic CVD, and orthogonally repeating the MM structure. The result will be a monolithic dynamic metamaterial with filter characteristics capable of competing with present polarization technologies.

6.5 Summary of Discussion

Photonic materials have an unlimited variety of potential applications. However, this dissertation focused on the use of photonic materials for two specific applications. First was the implementation of high temperature metamaterial emitters, metallic photonic crystal filters, and interfacial misfit arrays for TPV applications. The goal was to provide new devices for TPV applications as well as improving efficiencies for current technologies. The second application was the design and fabrication of dynamic MM polarizers for photodetection applications. This polarizer was constructed with specific aims to enable large area polarization grids which could be integrated with existing focal-plane-arrays. The end device can dynamically alter the MM transmission characteristics. This will result in increased pixel count as individual pixels will not need to be sensitive to individual polarizations. The following section summarizes the goals, results, and future work of each topic covered in this dissertation.

The fabrication and testing of a MM emitter constructed from Pt and Al_2O_3 was designed operate at temperatures greater than 1100 °C. The fabricated design was determined achieve an absorption peak of approximately 70%, a resonance wavelength of 1.0 μm , a full-width-half-max (FWHM) of less than 500 nm, and was also designed to withstand temperatures exceeding 1700 °C. This metamaterial will be optimized for Pt in order to increase emissivity to between 90 and 100 percent. This will allow specific band gap matching while providing a

simplified emitter model expected to operate up to 1700 °C. Also, a material study will occur for device operation at even higher temperatures. Specifically, the issue of coefficient of expansion must be examined. For this reason, a tungsten MM pattern is proposed on Al₂O₃. We expect this new structure to maintain structural integrity up to 2000 °C due to the high melting points of the individual components and provide optimal emission tailored to any semiconductor bandgap.

The purpose of a TPV filter is to reflect light with energy below, or above the bandgap of the diode stage, in order to provide the most efficiently converted spectrum possible for the TPV diode. To accomplish TPV filtering a metallic PhC pattern was integrated into a TPV diode. The metallic PhC was shown to act as a front-side spectral TPV filter as well as a front-side contact. It was also demonstrated that this structure provided a threefold benefit; operating as a front-side filter, an antireflective coating, and a top contact material. To this end, it is proposed that metallic PhCs can replace existing TPV front contact grids. This can be done for various photodiode geometries ranging from traditional geometries to monolithically interconnected modules. By integrating a MIMs structure utilizing only PhCs with a SiN_x layer, a much higher efficiency can be generated than by using only traditional contacts and ARCs.

An interfacial misfit array (IMF) layer was introduced to allow lattice mismatched GaSb and GaAs to be grown monolithically. With a successful IMF layer, many new options in TPV diode design can be opened. Previous work with IMF layers has examined optical and structural characteristics, or photon emitter

applications. However, no work has been examined using an IMF layer as a PV absorber. For this reason, this study of IMF layers demonstrating photovoltaic power generation is a significant step forward in IMF research. As such, IMF absorber optimization would provide research possibilities for previously uninvestigated technologies. These possibilities include lattice mismatched TPV diode stages, as well as, IMF integrated two junction monolithic interconnected modules (MIMs). In order to improve IMF absorbers, work must be done to understand exciton recombination and carrier transport issues; which may cause a decreased IMF performance in relation to traditional GaSb photodiode growth. Some design issues have been addressed, such as decreasing back contact doping concentration as well as decreased total device thickness. These improvements should allow for diode efficiencies approaching that of a traditional lattice matched growths. Successful integration of an IMF photodiode will allow many other IMF material combinations such as SLS structures, creating an entirely new field of custom bandgap multijunction TPV diodes.

Finally, dynamic metamaterial polarization grids were used to create optical filters for photodetector applications. These filters were designed to provide dynamic on/off ratios in order to replace large filter wheels and increase available pixel counts in current polarization sensitive photodetector technology. For this reason, a MM device was constructed which aimed at providing a MM response which could be dynamically altered with an applied voltage.

The MM structure itself is a combination of these three MM devices. The unique structure utilizes the parallel metallic bands of a split wire pair MM, the

ring resonator design of SRR, and the repeating “+” of a fishnet pattern. The result was combined resonances due to the SRR, SWP, and fishnet patterns. These properties allow for a high transmission of both polarizations in the “off” position. Also, with the addition of an injection current, the MM resonance decreases and shifts, effectively turning “on” the polarizer and only allow transmission of one polarization. In literature, all voltage controlled MMs utilize a reverse biased Schottky diode to create this effect. The dynamic MM in this work, however, operates similar to optically pumped MMs, using an increased carrier density to alter the MM response. Therefore, this device operates in a unique mode not shown in literature. The MM was tested with a variety of doping concentrations, applied voltages, and while changing both the conductivity and carrier injection. All four effects were shown to alter the MM transmission characteristics.

This dissertation focused on the use of photonic materials for two specific applications, energy generation and photodetection. To this end, photonic structures were implemented in energy generating devices, and a dynamic filter was created for photodetection. Specifically, high temperature metamaterial emitters were shown to have band pass emissivity when heated above 600 °C. Metallic photonic crystal patterns were shown to increase TPV diode efficiencies. Interfacial misfit arrays were shown capable of generating power as a photovoltaic diode. Finally, a unique metamaterial polarization sensitive device was designed and fabricated. It was shown that the resonance frequency of this metamaterial can be altered through increased conductivity as well as carrier

injection. The goal for each of these devices was to provide an improvement over existing technologies. Each device was successful at this task; either by demonstrating out-right improvement, or providing a leap forward in existing device applications. It is for this reason that the previously mentioned projects will continue to be optimized in order to provide lasting benefit to the field of optoelectronics, energy harvesting, and photodetection.

Bibliography

- [1] Margaritondo, Giorgio; “100 YEARS OF PHOTOEMISSION”. Physics Today, April, 1988 (66-72).
- [2] Hecht, Eugene. *Optics*. Twelfth Edition, Addison Wesley, Publishing, Reading, MA (2001) pg 16.
- [3] Rosa, Aldo V. da; *Fundamentals of Renewable Energy Processes*. Elsevier Academic Press, Burlington, MA, (2005) pg 4.
- [4] [Astronomy Department](#), 2006, [Cornell University](#), 30 May 2009 <<http://eetd.lbl.gov/coolroof/SPECTRUM.gif>>.
- [5] Lawrence Livermore National Laboratory, “US Energy Flowcharts,” 2012 <https://flowcharts.llnl.gov/index.html>, [Accessed: 04-Apr-2012].
- [6] US Environmental Protection Agency, “Green Power Equivalency Calculator Methodologies,” 2012. <http://www.epa.gov/greenpower/pubs/calcmeth.html> [Accessed: 04-Apr-2012].
- [7] United States Census Bureau, American Housing Survey (AHS), <http://www.census.gov/housing/ahs/> [Accessed: 12-28-2012].
- [8] Kaplan, S.M. (2008) Power Plants: Characteristics and Costs. Congressional Research Service CRS Report 7-5700 www.crs.gov RL34746
- [9] V.G. Veselago, “Electrodynamics of Substances with Negative ϵ and μ ,” Usp. Fiz. Nauk 92, 517-527, July 1964.
- [10] Neamen, Donald; *An Introduction to Semiconductor Devices.*, McGraw-Hill, New York, NY (2006) pg 41-45.
- [11] Sze, S.M.; *Physics of Semiconductor Devices Second Ed.*, John Wiley & Sons, Inc. Hoboken, NJ (1981) pg 13.
- [12] Neamen, Donald; *An Introduction to Semiconductor Devices.*, McGraw-Hill, New York, NY (2006) pg 46-48.
- [13] Neamen, Donald; *An Introduction to Semiconductor Devices.*, McGraw-Hill, New York, NY (2006) pg 49.
- [14] Sze, S.M.; *Physics of Semiconductor Devices Second Ed.*, John Wiley & Sons, Inc. Hoboken, NJ (1981) pg 39.
- [15] Sze, S.M.; *Physics of Semiconductor Devices Second Ed.*, John Wiley & Sons, Inc. Hoboken, NJ (1981) pg 41.
- [16] Neamen, Donald; *An Introduction to Semiconductor Devices.*, McGraw-Hill, New York, NY (2006) pg 52.
- [17] Neamen, Donald; *An Introduction to Semiconductor Devices.*, McGraw-Hill, New York, NY (2006) pg 53.
- [18] Neamen, Donald; *An Introduction to Semiconductor Devices.*, McGraw-Hill, New York, NY (2006) pg 54.
- [19] Kasap, S.O.; *Optoelectronics and Photonics: Principles and Practices*; Prentice Hall, Upper Saddle River NJ, (2001) pg 268.
- [20] Kittel, Charles; *Introduction to Solid State Physics Eighth Ed.* John Wiley & Sons, Inc. Hoboken, NJ (2005) pg 96.

- [21] Kittel, Charles; *Introduction to Solid State Physics Eighth Ed.* John Wiley & Sons, Inc. Hoboken, NJ (2005) pg 97.
- [22] Kittel, Charles; *Introduction to Solid State Physics Eighth Ed.* John Wiley & Sons, Inc. Hoboken, NJ (2005) pg 99.
- [23] Kittel, Charles; *Introduction to Solid State Physics Eighth Ed.* John Wiley & Sons, Inc. Hoboken, NJ (2005) pg 135.
- [24] Sze, S.M.; *Physics of Semiconductor Devices Second Ed.*, John Wiley & Sons, Inc. Hoboken, NJ (1981) pg 22.
- [25] Kittel, Charles; *Introduction to Solid State Physics Eighth Ed.* John Wiley & Sons, Inc. Hoboken, NJ (2005) pg 136.
- [26] Kittel, Charles; *Introduction to Solid State Physics Eighth Ed.* John Wiley & Sons, Inc. Hoboken, NJ (2005) pg 207.
- [27] Anderson, Betty Lise and Richard L. Anderson; *Fundamentals of Semiconductor Devices*, McGraw Hill Higher Education, New York, NY, (2005) pg 75.
- [28] Anderson, Betty Lise and Richard L. Anderson; *Fundamentals of Semiconductor Devices*, McGraw Hill Higher Education, New York, NY, (2005) pg 77.
- [29] Anderson, Betty Lise and Richard L. Anderson; *Fundamentals of Semiconductor Devices*, McGraw Hill Higher Education, New York, NY, (2005) pg 71.
- [30] Anderson, Betty Lise and Richard L. Anderson; *Fundamentals of Semiconductor Devices*, McGraw Hill Higher Education, New York, NY, (2005) pg 79.
- [31] Anderson, Betty Lise and Richard L. Anderson; *Fundamentals of Semiconductor Devices*, McGraw Hill Higher Education, New York, NY, (2005) pg 80.
- [32] Neamen, Donald; *An Introduction to Semiconductor Devices.*, McGraw-Hill, New York, NY (2006) pg 83.
- [33] Neamen, Donald; *An Introduction to Semiconductor Devices.*, McGraw-Hill, New York, NY (2006) pg 84-85.
- [34] Anderson, Betty Lise and Richard L. Anderson; *Fundamentals of Semiconductor Devices*, McGraw Hill Higher Education, New York, NY, (2005) pg 91.
- [35] Anderson, Betty Lise and Richard L. Anderson; *Fundamentals of Semiconductor Devices*, McGraw Hill Higher Education, New York, NY, (2005) pg 135.
- [36] Anderson, Betty Lise and Richard L. Anderson; *Fundamentals of Semiconductor Devices*, McGraw Hill Higher Education, New York, NY, (2005) pg 115.
- [37] Anderson, Betty Lise and Richard L. Anderson; *Fundamentals of Semiconductor Devices*, McGraw Hill Higher Education, New York, NY, (2005) pg 130.
- [38] Sze, S.M.; *Physics of Semiconductor Devices Second Ed.*, John Wiley & Sons, Inc. Hoboken, NJ (1981) pg 64.

- [39] Neamen, Donald; *An Introduction to Semiconductor Devices.*, McGraw-Hill, New York, NY (2006) pg 175.
- [40] Anderson, Betty Lise and Richard L. Anderson; *Fundamentals of Semiconductor Devices*, McGraw Hill Higher Education, New York, NY, (2005) pg 242.
- [41] Neamen, Donald; *An Introduction to Semiconductor Devices.*, McGraw-Hill, New York, NY (2006) pg 176.
- [42] Anderson, Betty Lise and Richard L. Anderson; *Fundamentals of Semiconductor Devices*, McGraw Hill Higher Education, New York, NY, (2005) pg 244.
- [43] Anderson, Betty Lise and Richard L. Anderson; *Fundamentals of Semiconductor Devices*, McGraw Hill Higher Education, New York, NY, (2005) pg 255.
- [44] Anderson, Betty Lise and Richard L. Anderson; *Fundamentals of Semiconductor Devices*, McGraw Hill Higher Education, New York, NY, (2005) pg 249.
- [45] Neamen, Donald A.; *Microelectronics Circuit Analysis and Design Third Ed.*, McGraw-Hill, New York, NY, (2007) pg 20-21.
- [46] Anderson, Betty Lise and Richard L. Anderson; *Fundamentals of Semiconductor Devices*, McGraw Hill Higher Education, New York, NY, (2005) pg 261.
- [47] Neamen, Donald A.; *Microelectronics Circuit Analysis and Design Third Ed.*, McGraw-Hill, New York, NY, (2007) pg 22.
- [48] Kasap, S.O.; *Optoelectronics and Photonics: Principles and Practices*; Prentice Hall, Upper Saddle River NJ, (2001) pg 132.
- [49] Neamen, Donald A.; *Microelectronics Circuit Analysis and Design Third Ed.*, McGraw-Hill, New York, NY, (2007) pg 24.
- [50] Anderson, Betty Lise and Richard L. Anderson; *Fundamentals of Semiconductor Devices*, McGraw Hill Higher Education, New York, NY, (2005) pg 269.
- [51] Kasap, S.O.; *Optoelectronics and Photonics: Principles and Practices*; Prentice Hall, Upper Saddle River NJ, (2001) pg 129.
- [52] Sze, S.M.; *Physics of Semiconductor Devices Second Ed.*, John Wiley & Sons, Inc. Hoboken, NJ (1981) pg 93.
- [53] Streetman, Ben G. and Sanjay Kumar Banerjee; *Solid State Electronic Devices Sixth Ed.*, Person Prentice Hall, Upper Saddle River, NJ (2006) pg 124-126.
- [54] Streetman, Ben G. and Sanjay Kumar Banerjee; *Solid State Electronic Devices Sixth Ed.*, Person Prentice Hall, Upper Saddle River, NJ (2006) pg 128.
- [55] Anderson, Betty Lise and Richard L. Anderson; *Fundamentals of Semiconductor Devices*, McGraw Hill Higher Education, New York, NY, (2005) pg 385.
- [56] Anderson, Betty Lise and Richard L. Anderson; *Fundamentals of Semiconductor Devices*, McGraw Hill Higher Education, New York, NY, (2005) pg 685.

- [57] Streetman, Ben G. and Sanjay Kumar Banerjee; *Solid State Electronic Devices Sixth Ed.*, Person Prentice Hall, Upper Saddle River, NJ (2006) pg 406-407.
- [58] Pedrotti, Frank L.; Leno S. Pedrotti; Leno Matthew Pedrotti “Introduction to Optics,” Pearson Prentice Hall, Upper Saddle River, NJ, 2007 pg 506-507;541.
- [59]Maier, Stefan Alexander; *Plasmonics Fundamentals and Applications.*, Springer Science, New York, NY, (2007) pg 25.
- [60] Griffiths, David J. “Introduction to Electrodynamics: Third Edition” Prentice-Hall, Inc. Upper Saddle River, NJ, 1999, pg 380.
- [61] J. B. Pendry, A. J. Holden, D. J. Robbins, W. J. Stewart, “Low frequency plasmons in thin-wire structures,” J. Phy. Condens. Matter 10 (1998) 4785-4809.
- [62] J. B. Pendry, A. J. Holden, D. J. Robbins, W. J. Stewart, “Magnetism from Conductors and Enhanced Nonlinear Phenomena,” IEEE Transactions on Microwave Theory and Techniques, Vol. 47, No. 11, Nov. 1999.
- [63] Smith, D. R.; Willie J. Padilla; D. C. Vier; S. C. Nemat-Nasser; and S. Schultz, “Composite Medium with Simultaneously Negative Permeability and Permittivity,” Physical Review Letters, Vol 84, Num. 18, May 1, 2000.
- [64] H. Chen, J. F. O’Hara, A. K. Azad, A. J. Taylor, R. D. Averitt, D. B. Shrekenhamer, W. J. Padilla, “Experimental demonstration of frequency-agile terahertz metamaterials,” Nature Photonics, Vol. 2, May (2008).
- [65] Joannapolous, John D.; Steven G. Johnson; Joshua N. Winn; Robert D. Meade. *Photonic Crystal Modeling the Flow of Light Second Ed.*, Princeton University Press, Princeton, NJ, (2008) pg 4.
- [66] Joannapolous, John D.; Steven G. Johnson; Joshua N. Winn; Robert D. Meade. *Photonic Crystal Modeling the Flow of Light Second Ed.*, Princeton University Press, Princeton, NJ, (2008) pg 74-75.
- [67]Joannapolous, John D.; Steven G. Johnson; Joshua N. Winn; Robert D. Meade. *Photonic Crystal Modeling the Flow of Light Second Ed.*, Princeton University Press, Princeton, NJ, (2008) pg 67.
- [68]Joannapolous, John D.; Steven G. Johnson; Joshua N. Winn; Robert D. Meade. *Photonic Crystal Modeling the Flow of Light Second Ed.*, Princeton University Press, Princeton, NJ, (2008) pg 76.
- [69]Joannapolous, John D.; Steven G. Johnson; Joshua N. Winn; Robert D. Meade. *Photonic Crystal Modeling the Flow of Light Second Ed.*, Princeton University Press, Princeton, NJ, (2008) pg 83.
- [70]Shenoi, R. V.; D. A. Ramirez; Y. Sharma; R. S. Attaluri; J. Rosenberg; O. J. Painter; S. Krishna; “Plasmon Assisted Photonic Crystal Quantum Dot Sensors,” Proc. of SPIE Vol. 6713 67130P-1, (2007).
- [71] Shawn Lin, J.G. Fleming, J. Moreno, “Photonic Crystals for Enhancing Thermophotovoltaic Energy Conversion,” SAND REPORT, Sandia National Laboratories, SAND2003-0845, March (2003).
- [72] J.G. Fleming, S. Y. Lin, I. El-Kady, R. Biswas, K. M. Ho,” All-metallic three-dimensional photonic crystals with a large infrared bandgap,” Letters to nature, VOL. 417, May 2, (2002).

- [73] J. M. Gee, J. B. Moreno, S. Y. Lin, J. G. Fleming, "Selective Emitters using Photonic Crystals for Thermophotovoltaic Energy Conversion," IEEE, 0-7803-7471-1/02, (2002).
- [74] H. Sai and H. Yugami, "Thermophotovoltaic generation with selective radiators based on tungsten surface gratings," Appl. Phys. Lett. 85, 3399 (2004).
- [75] S. Y. Lin, J.G. Fleming, J. B. Moreno, "Three-dimensional photonic-crystal emitter for thermal photovoltaic power generation," Appl. Phys. Lett. 83, No. 2, July 14, (2003).
- [76] G. B. Farfana, M. F. Sua, M. M. Reda Tahaab, I. El-Kady, "High-Efficiency Photonic Crystal Narrowband Thermal Emitters," Proc. of SPIE Vol. 7609, (2010).
- [77] M. U. Pralle, N. Moelders, M. P. McNeal, I. Puscasu, A. C. Greenwald, J. T. Daly, E. A. Johnson, T. George, D. S. Choi, I. El-Kady, R. Biswas, "Photonic crystal enhanced narrow-band infrared emitters," Appl. Phys. Lett. 81, No. 25, Dec. 16, (2002).
- [78] Ivan Celanovic, Francis O'Sullivan, Natalija Jovanovic, Minghao Qi, John Kassakian, "1D and 2D Photonic Crystals for Thermophotovoltaic Applications," *Proc. SPIE 5450*, 416 (2004).
- [79] Shawn-Yu Lin, J. G. Fleming, E. Chow, Jim Bur, K. K. Choi, A. Goldberg, "Enhancement and suppression of thermal emission by a three-dimensional photonic crystal," Physical Review B, **62**, No. 4 July 15, (2000).
- [80] Han-Kuei Fu, Yu-Wei Jiang, Ming-Wei Tsai, Si-Chen Lee, Yang-Fang Chen, "A thermal emitter with selective wavelength: Based on the coupling between photonic crystals and surface plasmon polaritons," J. Appl. Phys. 105, 033505 (2009).
- [81] Natalija Jovanovic, Ivan Celanovic, John Kassakian, "Two-dimensional Tungsten Photonic Crystals as Thermophotovoltaic Selective Emitters," *AIP Conf. Proc. 890*, 47 (2007).
- [82] Ivan Celanovic, Natalija Jovanovic, John Kassakian, "Two-dimensional tungsten photonic crystals as selective thermal emitters," Appl. Phys. Lett. Vol.92, 193101 (2008).
- [83] David L. C. Chan, Marin Soljačić, J. D. Joannopoulos, "Thermal emission and design in 2D-periodic metallic photonic crystal slabs," Optics Express, Vol. 14, No. 19. Sept. 18, (2006).
- [84] Veronika Rinnerbauer, Sidy Ndao, Yi Xiang Yeng, Walker R. Chan, Jay J. Senkevich, John D. Joannopoulos, Marin Soljacic, Ivan Celanovic, "Recent developments in high-temperature photonic crystals for energy conversion," Energy Environ. Sci., 2012, 5, 8815.
- [85] Kevin A. Arpin, Mark D. Losego, Paul V. Braun, "Electrodeposited 3D Tungsten Photonic Crystals with Enhanced Thermal Stability," Chem. Mater. 2011, 23, 4783–4788.
- [86] Veronika Rinnerbauer, Sidy Ndao, Yi Xiang Yeng, Jay J. Senkevich, Klavs F. Jensen, John D. Joannopoulos, Marin Soljacic, Ivan Celanovic, Robert D. Geil, "Large-area fabrication of high aspect ratio tantalum photonic crystals

- for high-temperature selective emitters,” J. Vac. Sci. Technol. B 31, 011802 (2013).
- [87] Irina Puscasu, William L. Schaich,” Narrow-band, tunable infrared emission from arrays of microstrip patches,” Appl. Phys. Lett. 92, 233102 (2008).
 - [88] N. I. Landy, S. Sajuyigbe, J. J. Mock, D. R. Smith, W. J. Padilla¹, “Perfect Metamaterial Absorber,” Phys. Rev. Lett. 100, 207402 (2008). May 23, (2008).
 - [89] Hu Tao¹, Nathan I. Landy, Christopher M. Bingham, Xin Zhang, Richard D. Averitt, and Willie J. Padilla, “A metamaterial absorber for the terahertz regime: Design, fabrication and characterization,” Optics Express, Vol. 16, No. 10, May 12, (2008).
 - [90] Hu Tao, C. M. Bingham, A. C. Strikwerda, D. Pilon, D. Shrekenhamer, N. I. Landy,² K. Fan,¹ X. Zhang,¹ W. J. Padilla, and R. D. Averitt, “Highly flexible wide angle of incidence terahertz metamaterial absorber: Design, fabrication, and characterization,” Phys. Rev. B. 78, 241103(R) (2008).
 - [91] N. I. Landy, C. M. Bingham, T. Tyler, N. Jokerst, D. R. Smith, W. J. Padilla, “Design, theory, and measurement of a polarization-insensitive absorber for terahertz imaging,” Phys. Rev. B. 79, 125104 (2009).
 - [92] Kamil Boratay Alici, Filiberto Bilotti, Lucio Vegni, Ekmel Ozbay, “Experimental verification of metamaterial based subwavelength microwave absorbers,” J. Appl. Phys. 108, 083113 (2010).
 - [93] Hu Tao, C M Bingham, D Pilon, Kebin Fan, A C Strikwerda, D Shrekenhamer, W J Padilla, Xin Zhang, R D Averitt, “A dual band terahertz metamaterial absorber,” J. Phys. D: Appl. Phys. 43 (2010) 225102.
 - [94] David Shrekenhamer, Wangren Xu, Suresh Venkatesh, David Schurig, Sameer Sonkusale, Willie J. Padilla, “Experimental Realization of a Metamaterial Detector Focal Plane Array” Phys. Rev. Lett. 109, 177401 (2012).
 - [95] David Shrekenhamer, Wen-Chen Chen, Willie J. Padilla, “Liquid Crystal Tunable Metamaterial Perfect Absorber,” Physics Optics, arXiv:1206.4214v1, Jun. 19, 2012.
 - [96] Xingzhan Wei, Hao-fei Shi, Xiaochun Dong, Yueguang Lu, Chunlei Du, “A high refractive index metamaterial at visible frequencies formed by stacked cut-wire plasmonic structures,” Appl. Phys. Lett. 97, 011904 (2010).
 - [97] Xianliang Liu, Tatiana Starr, Anthony Starr, and Willie J. Padilla, “An Infrared Spatial and Frequency Selective Metamaterial Perfect Absorber,” Phys. Rev. Lett. 104, 207403 (2010).
 - [98] Na Liu, Martin Mesch, Thomas Weiss, Mario Hentschel, Harald Giessen, “Infrared Perfect Absorber and Its Application As Plasmonic Sensor,” Nano Lett. 10, 2342–2348, (2010).
 - [99] M. Yan, “Metal–insulator–metal light absorber: a continuous structure,” J. Opt., **15** 025006 (2013) .
 - [100] Jiaming Hao, Jing Wang, Xianliang Liu, Willie J. Padilla, Lei Zhou, Min Qiu, “High performance optical absorber based on a plasmonic metamaterial,” Appl. Phys. Lett. 96, 251104 (2010).

- [101] Wen-Chen Chen, Machhindra Koirala, Xianliang Liu, Talmage Tyler, Kevin G. West, Christopher M. Bingham, Tatiana Starr, Anthony F. Starr, Nan M. Jokerst, Willie J. Padilla, "Characterization of Surface Electromagnetic Waves and Scattering on Infrared Metamaterial Absorbers," arXiv:1212.2868v1 [physics.optics] 12 Dec (2012).
- [102] Xianliang Liu, Tatiana Starr, Anthony F. Starr, Willie J. Padilla, "Infrared Spatial and Frequency Selective Metamaterial with Near-Unity Absorbance," *Phys. Rev. Lett.* 104, 207403 (2010).
- [103] Willie J. Padilla, "Taming the Blackbody with Metamaterials for Energy Harvesting Applications," *FiO/LS Technical Digest*, OSA (2012).
- [104] Xianliang Liu, Talmage Tyler, Tatiana Starr, Anthony F. Starr, Nan Marie Jokerst, Willie J. Padilla, "Taming the Blackbody with Infrared Metamaterials as Selective Thermal Emitters," *Phys. Rev. Lett.* 107, 045901 (2011).
- [105] Thomas Maier, Hubert Brueckl, "Multispectral microbolometers for the midinfrared," *Optics Letters* Vol. 35, No. 22, Nov. 15, (2010).
- [106] Jiaming Hao, Lei Zhou, and Min Qiu, "Nearly total absorption of light and heat generation by plasmonic metamaterials," *Phys. Rev. B* 83, 165107 (2011).
- [107] C. Shemelya, T. E. Vandervelde, "Comparison of Photonic-Crystal-Enhanced Thermophotovoltaic Devices With and Without a Resonant Cavity," *Journal of Electronic Materials*, Vol. 41, No. 5, 2012.
- [108] Ivan Celanovic, Francis O'Sullivan, Milos Ilak, John Kassakian, David Perreault, "Design and optimization of one-dimensional photonic crystals for thermophotovoltaic applications," *Optics Letters*, Vol. 29, No. 8, April 15, (2004).
- [109] Francis O'Sullivan, Ivan Celanovic, Natalija Jovanovic, John Kassakian, Shoji Akiyama, Kazumi Wada, "Optical characteristics of one-dimensional Si/SiO₂ photonic crystals for thermophotovoltaic applications," *Journal of Appl. Phys.* 97, 033529 (2005).
- [110] Samia I. Mostafa, Nadia H. Rafat, Sahar A. El-Naggar, "One-dimensional metallic-dielectric (Ag/SiO₂) photonic crystals filter for thermophotovoltaic applications," *Renewable Energy* 45 (2012), pg 245-250.
- [111] O. El Daif, E. Drouard, G. Gomard, X. Meng, A. Kaminski, A. Fave, M. Lemiti, E. Garcia Caurel, P. Roca i Cabarrocas, S. Ahn, H. Jeon, C. Seassal, "Absorbing photonic crystals for thin film photovoltaics," *Proc. of SPIE* Vol. 7713 771308-1, (2010).
- [112] G. Gomard, O. El Daifa, E. Drouard, X. Meng, A. Kaminski, A. Fave, M. Lemiti, E. Garcia-Caurel, P. Roca i Cabarrocas, C. Seassal, "Design and fabrication of photonic crystal thin film photovoltaic cells," *Proc. of SPIE* Vol. 7725 77250M-1 (2010).
- [113] S. Domínguez, I. Cornago, O. Garcí'a, M. Ezquer, M.J. Rodríguez, A.R. Lagunas, J. Pérez-Conde, J. Bravo, "Design, optimization and fabrication of 2D photonic crystals for solar cells," *Photon Nanostruct: Fundam Appl* (2012), <http://dx.doi.org/10.1016/j.photonics.2012.07.002>

- [114] B. Park, Mina Kim, Young In Lee , “Improved photovoltaic effect of polymer solar cells on planarized 2D photonic crystals ,” Sol. Energy Mater. Sol. Cells (2010), doi:10.1016/j.solmat.2010.12.038
- [115] M. Malekmohammad, M. Soltanolkotabi, R. Asadi, M.H. Naderi, A. Erfanian, M. Zahedinejad, S. Bagheri, M. Khaje, “Hybrid structure for efficiency enhancement of photodetectors,” Applied Surface Science 264 (2013) 1– 6
- [116] Shrestha Basu Mallick, Mukul Agrawal, Peter Peumans, “Optimal light trapping in ultra-thin photonic crystal crystalline silicon solar cells,” OPTICS EXPRESS Vol. 18, No. 6, March 15, (2010).
- [117] Hsin-Cheng Lee, Shich-Chuan Wu, Tien-Chung Yang, Ta-Jen Yen, “Efficiently Harvesting Sun Light for Silicon Solar Cells through Advanced Optical Couplers and A Radial p-n Junction Structure,” *Energies*, 3, (2010) 784-802; doi:10.3390/en3040784
- [118] Hari P. Paudel, Khadijeh Bayat, Mahdi Farrokh Baroughi, Stanley May, and David W. Galipeau, “Enhancement of Electromagnetic Field Intensity by Metallic Photonic Crystal for Efficient Upconversion,” IEEE 978-1-4244-5892-9, (2010).
- [119] Y. Tang, A. M. Mintairov, J. L. Merz, V. Tokranov, S. Oktyabrsky, “Characterization of 2D-Photonic Crystal Nanocavities by Polarization-Dependent Photoluminescence,” Proceedings of 2005 5th IEEE Conference on Nanotechnology, July (2005).
- [120] S. Schartner, S. Golka, C. Pflügl, W. Schrenk, A. M. Andrews, T. Roch, G. Strasser, “Band structure mapping of photonic crystal intersubband detectors,” Appl. Phys. Lett. **89**, 151107 (2006).
- [121] S. Schartner, M. Nobile, W. Schrenk, A. Maxwell Andrews, P. Klang, G. Strasser, “Photocurrent response from photonic crystal defect modes,” Optics Express, Vol. 16, No. 7, March 31, (2006).
- [122] J. Yang, M. Seo, I. Hwang, S. Kim, Y. Lee, “Polarization-selective resonant photonic crystal photodetector,” Appl. Phys. Lett. 93, 211103 (2008).
- [123] K. T. Posani, V. Tripathi, S. Annamalai, N. R. Weisse-Bernstein, S. Krishna, R. Perahia, O. Crisafulli, O. J. Painter, “Nanoscale quantum dot infrared sensors with photonic crystal cavity,” Appl. Phys. Lett. 88, 151104 (2006).
- [124] S. Schartner, S. Kalchmair, A. M. Andrews, P. Klang, W. Schrenk, G. Strasser, “Post-fabrication fine-tuning of photonic crystal quantum well infrared photodetectors,” Appl. Phys. Lett. 94, 231117 (2009).
- [125] J. Rosenberg, R. V. Shenoi, T. E. Vandervelde, S. Krishna, O. Painter, “A multispectral and polarization-selective surface-plasmon resonant midinfrared detector,” Appl. Phys. Lett. 95, 161101 (2009).
- [126] Chun-Chieh Chang, Yagya D. Sharma, Yong-Sung Kim, Jim A. Bur, Rajeev V. Shenoi, Sanjay Krishna, Danhong Huang, Shawn-Yu Lin, “A Surface Plasmon Enhanced Infrared Photodetector Based on InAs Quantum Dots,” *Nano Lett.* 10, (2010) 1704–1709

- [127] Eli Lansey and David T. Crous, "Design of photonic metamaterial multi-junction solar cells using rigorous coupled wave analysis," Proc. of SPIE Vol. 7772, 777205 (2010).
- [128] Jessie Rosenberg, Rajeev V. Shenoi, Sanjay Krishna, and Oskar Painter, "Design of plasmonic photonic crystal resonant cavities for polarization sensitive infrared photodetectors," Optics Express Vol. 18, No. 4, Feb. 15, (2010).
- [129] S. C. Lee, Y. Sharma, S. Krishna, S. R. J. Brueck, "Leaky-mode effects in InAs quantum-dot infrared photodetectors coupled to metal photonic crystals," CLEO Technical Digest OSA (2012).
- [130] S. Kalchmair, H. Detz, G. D. Cole, A. M. Andrews, P. Klang, M. Nobile, R. Gansch, C. Ostermaier, W. Schrenk, and G. Strasser, "Photonic crystal slab quantum well infrared photodetector," Appl. Phys. Lett. 98, 011105 (2011).
- [131] S. C. Lee, S. Krishna, S. R. J. Brueck, "Quantum dot infrared photodetector enhanced by surface plasma wave excitation," Optics Express, Vol. 17, No. 25, Dec. 17, (2009).
- [132] O. Glushko, R. Brunner, R. Meisels, S. Kalchmair, G. Strasser, "Extraordinary transmission in metal hole array-photonic crystal hybrid structures," Optics Express, Vol. 20, No. 15, July 16, (2012).
- [133] J. W. Matthews, A. E. Blakeslee, "Effects in Epitaxial Multilayers," *Journal of Crystal Growth* 27 (1974) I 18-125
- [134] S. H. Huang, G. Balakrishnan, A. Khoshakhlagh, A. Jallipalli, L. R. Dawson, and D. L. Huffaker, "Strain relief by periodic misfit arrays for low defect density GaSb on GaAs," Appl. Phys. Lett. 88, 131911 (2006).
- [135] Jun Tatebayashi, Baolai Liang, David A. Bussian, Han Htoon, Shenghong Huang, Ganesh Balakrishnan, Victor Klimov, L. Ralph Dawson, Diana L. Huffaker, "Formation and Optical Characteristics of Type-II Strain-Relieved GaSb/GaAs Quantum Dots by Using an Interfacial Misfit Growth Mode," IEEE Transactions on nanotechnology, Vol. 8, No. 2, March (2009).
- [136] G. Balakrishnan, T.J. Rottera, A. Jallipalli, L.R. Dawson, D.L. Huffaker, "Interfacial misfit dislocation array based growth of III-Sb active regions on GaAs/AlGaAs DBRs for high-power 2 μ m VECSELs," Solid State Lasers XVII: Technology and Devices, Proc. of SPIE Vol. 6871 687111-1
- [137] M. Mehta, G. Balakrishnan, S. Huang, A. Khoshakhlagh, A. Jallipalli, P. Patel, M. N. Kutty, L. R. Dawson, and D. L. Huffaker, "GaSb quantum-well-based "buffer-free" vertical light emitting diode monolithically embedded within a GaAs cavity incorporating interfacial misfit arrays," Appl. Phys. Letts. 89, 211110 (2006).
- [138] A. Jallipalli, M.N. Kutty, G. Balakrishnan, J. Tatebayashi, N. Nuntawong, S.H. Huang, L.R. Dawson, D.L. Huffaker, Z. Mi and P. Bhattacharya, "1.54 μ m GaSb=AlGaSb multi-quantum-well monolithic laser at 77 K grown on miscut Si substrate using interfacial misfit arrays," Electronics Letters, Vol. 43, No. 22, Oct. 25, (2007).
- [139] J. Tatebayashi, A. Jallipalli, M. N. Kutty, S. H. Huang, G. Balakrishnan, L. R. Dawson, D. L. Huffaker, "Room-temperature lasing at 1.82 μ m of

- GaInSb/AlGaSb quantum wells grown on GaAs substrates using an interfacial misfit array,” *Appl. Phys. Lett.* 91, 141102 (2007).
- [140] J. Tatebayashi, A. Jallipalli, M. N. Kutty, S. H. Huang, T. J. Rotter, G. Balakrishnan, L. R. Dawson, D. L. Huffaker, “Device Characteristics of GaInSb/AlGaSb Quantum Well Lasers Monolithically Grown on GaAs Substrates by Using an Interfacial Misfit Array,” *Journal of Elect. Mat.*, Vol. 37, No. 12, (2006).
- [141] Kalyan Chakravarthy Nunna, Siew Li Tan, Charles J. Reyner, Andrew Robert Julian Marshall, Baolai Liang, Anitha Jallipalli, John P. R. David, Diana L. Huffaker, “Short-Wave Infrared GaInAsSb Photodiodes Grown on GaAs Substrate by Interfacial Misfit Array Technique,” *IEEE Photonics Technology Letters*, Vol. 24, No. 3, Feb. 1, (2012).
- [142] D.L. Huffaker, M. Mehta, G. Balakrishnan, S. Huang, A. Khoshakhlagh, P. Patel, M.N. Kutty, L. R. Dawson, “GaSb QW-based ‘buffer-free’ vertical LED monolithically embedded within a GaAs cavity using interfacial misfit arrays,” *IEEE*, 0-7803-9556-5 (2006).
- [143] D.L.Huffaker, G.Balakrishnan, A.Jallipalli, M.N.Kutty, S.H.Huang, L.R.Dawson, “Monolithically integrated III-Sb diode lasers on Si using interfacial misfit arrays,” *Proc. of SPIE* Vol. 6775 67750L-1 (2007).
- [144] M. Mehta, G. Balakrishnan, M.N. Kutty, P. Patel, L.R. Dawson, D.L. Huffaker, “1.55 μm GaSb/AlGaSb MQW diode lasers grown on GaAs substrates using interfacial misfit (IMF) arrays,” *OSA*, 1-55752-834-9 (2007).
- [145] D. L. Huffaker, L. R. Dawson, G. Balakrishnan. Misfit Dislocation Forming Interfacial Self-Assembly for Growth of Highly-Mismatched III-SB Alloys. U.S. Patent No.: US 2007/0160100 A1. Issued Jul. 12, 2007.
- [146] A. Jallipalli, G. Balakrishnan, S.H. Huang, A. Khoshakhlagh, L.R. Dawson, D.L. Huffaker, “Atomistic modeling of strain distribution in self-assembled interfacial misfit dislocation (IMF) arrays in highly mismatched III–V semiconductor materials,” *Journal of Crystal Growth* 303 (2007) 449–455.
- [147] S. H. Huang, G. Balakrishnan, M. Mehta, A. Khoshakhlagh, L. R. Dawson, D. L. Huffaker, “Epitaxial growth and formation of interfacial misfit array for tensile GaAs on GaSb,” *Appl. Phys. Lett.* 90, 161902 (2007).
- [148] Y.D. Sharma, G.Bishop, H.S. Kim, J.B. Rodriguez, E. Plis, G. Balakrishnan, L.R. Dawson, D.L. Huffaker, S. Krishna, “ Type II Strain Layer Superlattices (SLS’s) grown on GaAs Substrates,” *IEEE*, 1-4244-0925-X (2007).
- [149] S. H. Huang, G. Balakrishnan, A. Khoshakhlagh, L. R. Dawson, and D. L. Huffaker, “Simultaneous interfacial misfit array formation and antiphase domain suppression on miscut silicon substrate,” *Appl. Phys. Lett.* 93, 071102 (2008).
- [150] Shenghong Huang, Ganesh Balakrishnan, Diana L. Huffaker, “Interfacial misfit array formation for GaSb growth on GaAs,” *Journal of Applied Physics* 105, 103104 (2009).
- [151] Charles J. Reyner, Jin Wang, Kalyan Nunna, Andrew Lin, Baolai Liang, Mark S. Goorsky, D. L. Huffaker, “Characterization of GaSb/GaAs interfacial misfit arrays using x-ray diffraction,” *Appl. Phys. Lett.* 99, 231906 (2011).

- [152] Wei Zhou, Xiang Li, Sujing Xia, Jie Yang, Wu Tang, K.M. Lau, "High Hole Mobility of GaSb Relaxed Epilayer Grown on GaAs Substrate by MOCVD through Interfacial Misfit Dislocations Array," J. Mater. Sci. Technol., 2012, 28(2), 132-136.
- [153] Jie Wu¹, Shaobin Liu, Wei Zhou, Wu Tang, Kei. May. Lau, "Effect of antimony ambience on the interfacial misfit dislocations array in a GaSb epilayer grown on a GaAs substrate by MOCV," International Conference on Optoelectronics and Microelectronics (ICOM), (2012).
- [154] Kurt G. Eyink, David H. Tomich, William C. Mitchel, Lawrence Grazulis, John A. Carlin, Krishnamurthy Mahalingam, Anitha Jallipalli, Ganesh Balakrishnan, Diana Huffaker, Said Elhamri, "Electrical and structural characterization of a single GaSb/InAs/GaSb quantum well grown on GaAs using interface misfit dislocations," Journal of Applied Physics 104, 074901 (2008).
- [155] Shenghong Huang, Ganesh Balakrishnan, Diana L. Huffaker, "Characterization of Interfacial Misfit Array Formation for GaSb Growth on GaAs by Transmission Electron Microscopy," Microsc Microanal 15(Suppl2), (2009).
- [156] A. Jallipalli, G. Balakrishnan, S. H. Huang, T. J. Rotter, K. Nunna, B. L. Liang, L. R. Dawson, D. L. Huffaker, "Structural Analysis of Highly Relaxed GaSb Grown on GaAs Substrates with Periodic Interfacial Array of 90 Degree Misfit Dislocations," Nanoscale Res Lett (2009) 4:1458–1462.
- [157] A. Jallipalli, G. Balakrishnan, S.H. Huang, A. Khoshakhlagh, L.R. Dawson, D.L. Huffaker, "Modeling Misfit Dislocation Arrays for the Growth of Low-Defect Density AlSb on Si," Mater. Res. Soc. Symp. Proc. Vol. 934 (2006).
- [158] V M Andreev, V P Khvostikov, V R Larionov, V D Rumyantsev, S V Sorokina, M Z Shvarts, V I Vasil'ev, A S Vlasov, "Tandem GaSb/InGaAsSb thermophotovoltaic cells" Conf. Record of the 26th IEEE PVSC (Anaheim) (1997) pp 935–8
- [159] V M Andreev, V P Khvostikov, V R Larionov, V D Rumyantsev, S V Sorokina, M Z Shvarts, V I Vasil'ev, A S Vlasov, "Single and dual junction GaSb/InGaAsSb TPV cells," 2nd World Conference and Exhibition on Photovoltaic Solar Energy Conversion (Vienna)(1998) pp 330–3
- [160] A. Datas, C. Algora, "Global optimization of solar thermophotovoltaic systems," Prog. Photovolt: Res. Appl. (2012).
- [161] S. Maimona, G. W. Wicks, "*nBn* detector, an infrared detector with reduced dark current and higher operating temperature," Appl. Phys. Letts. 89, 151109 (2006).
- [162] A. Khoshakhlagh, J. B. Rodriguez, E. Plis, G. D. Bishop, Y. D. Sharma, H. S. Kim, L. R. Dawson, S. Krishna, "Bias dependent dual band response from InAs/Ga_{1-x}In_xSb type II strain layer superlattice detectors," Appl. Phys. Letts. 91, 263504 (2007).
- [163] J. B. Rodriguez, E. Plis, G. Bishop, Y. D. Sharma, H. Kim, L. R. Dawson, S. Krishna, "*nBn* structure based on InAs/GaSb type-II strained layer superlattices," Appl. Phys. Lett. 91, 043514 (2007).

- [164] H. S. Kim, E. Plis, J. B. Rodriguez, G. D. Bishop, Y. D. Sharma, L. R. Dawson, S. Krishna, J. Bundas, R. Cook, D. Burrows, R. Dennis, K. Patnaude, A. Reisinger, M. Sundaram, "Mid-IR focal plane array based on type-II InAs/GaSb strain layer superlattice detector with nBn design," Appl. Phys. Lett. 92, 183502 (2008).
- [165] Cory J. Hill, Alexander Soibel, Sam A. Keo, Jason M. Mumolo, David Z. Ting, Sarath D. Gunapala, "Demonstration of large format mid-wavelength infrared focal plane arrays based on superlattice and BIRD detector structures," Infrared Physics & Technology 52 (2009) 348–352.
- [166] Elena Plis, Stephen Myers, Arezou Khoshakhlagh, Ha Sul Kim, Yagya Sharma, Nutan Gautam, Ralph Dawson, Sanjay Krishna, "InAs/GaSb strained layer superlattice detectors with nBn design," Infrared Physics & Technology 52 (2009) 335–339.
- [167] G. W. Wicks, G. R. Savich, J. R. Pedrazzini, S. Maimon, "Infrared detector epitaxial designs for suppression of surface leakage current," Proc. of SPIE Vol. 7608, 760822 (2010).
- [168] A. Khoshakhlagh, H. S. Kim, S. Myers, N. Gautam, S. J. Lee, E. Plis, S. K. Noh, L. R. Dawson, S. Krishna, "Long Wave InAs/GaSb Superlattice Detectors Based on nBn and pin Design," Proc. of SPIE Vol. 7298, 72981P (2009).
- [169] Martin Husnik, Stefan Linden, Richard Diehl, Jens Niegemann, Kurt Busch, Martin Wegener, "Quantitative Experimental Determination of Scattering and Absorption Cross-Section Spectra of Individual Optical Metallic Nanoantennas," Physical Review Letters 109, 233902 Dec. 7 (2012).
- [170] S. Linden, F. B. P. Niesler, J. Forstner, Y. Grynko, T. Meier, M. Wegener, "Collective Effects in Second-Harmonic Generation from Split-Ring-Resonator Arrays," 109, 015502 July 6, (2012)
- [171] Felix von Cube, Stephan Irsen, Richard Diehl, Jens Niegemann, Kurt Busch, Stefan Linden, "From Isolated Metaatoms to Photonic Metamaterials: Evolution of the Plasmonic Near-Field," Nano Lett. [dx.doi.org/10.1021/nl3043757](https://doi.org/10.1021/nl3043757) Jan. 17, (2013).
- [172] Boubacar Kanté, Shah Nawaz Burokur, Frédérique Gadot, André de Lustrac, "Fully characterization of planar infrared metamaterials from far field diffraction pattern," Proc. of SPIE Vol. 6987 69870F-1 (2008).
- [173] Nigel P. Johnsona, Basudev Lahiria, Ali Z. Khokhara, Richard M. De La Ruea, Scott McMeekin, "Optical Properties of Split Ring Resonator Metamaterial Structures on Semiconductor Substrates," Proc. of SPIE Vol. 6987 69871F-1 (2008).
- [174] T. J. Yen, W. J. Padilla, N. Fang, D. C. Vier, D. R. Smith, J. B. Pendry, D. N. Basov, X. Zhang, "Terahertz Magnetic Response from Artificial Materials," *Science* 303, 1494 (2004)
- [175] J. Zhou, Th. Koschny, M. Kafesaki, E. N. Economou, J. B. Pendry, C. M. Soukoulis, "Saturation of the Magnetic Response of Split-Ring Resonators at Optical Frequencies," Physical Review Letters 95, 223902 (2005).

- [176] Hou-Tong Chena, John F. O'Haraa, Abul K. Azada, Willie J. Padillab, Richard D. Averittc, Antoinette J. Taylor, "Terahertz metamaterials" Proc. of SPIE Vol. 7214 721417-1 (2009).
- [177] Zheng-Gao Dong, Hui Liu, Tao Li, Zhi-Hong Zhu, Shu-Ming Wang, Jing-Xiao Cao, Shi-Ning Zhu, X. Zhang, "Modeling the directed transmission and reflection enhancements of the lasing surface plasmon amplification by stimulated emission of radiation in active metamaterials," Physical Review B 80, 235116 (2009).
- [178] Evgenia Kima, Y. Ron Shen, "Modulation of negative index metamaterials in the near-IR range," Applied Physics Letters 91, 173105 (2007).
- [179] Neilanjan Dutta, Iftekhar O. Mirza, Shouyuan Shi, Dennis W. Prather, "Fabrication of Large Area Fishnet Optical Metamaterial Structures Operational at Near-IR Wavelengths," *Materials*, 3, 5283-5292 (2010).
- [180] Joachim M. Hamm, Sebastian Wuestner, Kosmas L. Tsakmakidis, Ortwin Hess, "Theory of Light Amplification in Active Fishnet Metamaterials," Physical Review Letters, Oct. 14, (2011).
- [181] Jason Valentine, Shuang Zhang, Thomas Zentgraf, Erick Ulin-Avila, Dentcho A. Genov, Guy Bartal, Xiang Zhang, "Three-dimensional optical metamaterial with a negative refractive index," Nature Letters, vol. 455, Sept. 18, (2008).
- [182] Maxim R. Shcherbakov, Polina P. Vabishchevich, Tatyana V. Dolgova, Alexander A. Zaitsev, Alexander S. Sigov, Andrey A. Fedyanin, "Plasmon-Induced Wavelength-Dependent Polarization Switching in Optical Metamaterials," Proc. of SPIE Vol. 7353 (2009).
- [183] G. Dolling, C. Enkrich, M. Wegener, J. F. Zhou, C. M. Soukoulis, S. Linden, "Cut-wire pairs and plate pairs as magnetic atoms for optical metamaterials," Optics Letters, Vol. 30, No. 23, Dec. 1, (2005).
- [184] Xingzhan Wei, Haofei Shi, Xiaochun Dong, Yueguang Lu, Chunlei Du, "A high refractive index metamaterial at visible frequencies formed by stacked cut-wire plasmonic structures," Applied Physics Letters 97, 011904 (2010).
- [185] Kaan Guven, M. Deniz Caliskan, Ekmel Ozbay, "Experimental observation of left-handed transmission in a bilayer metamaterial under normal-to-plane propagation," Optics Express, Vol. 14, No. 19, Sept. 18 (2006).
- [186] Shuang Zhang, Dentcho A. Genov, Yuan Wang, Ming Liu, Xiang Zhang, "Plasmon-Induced Transparency in Metamaterials," Physical Review Letters, July 25, (2008).
- [187] Na Liu, Lutz Langguth, Thomas Weiss, Jürgen Kästel, Michael Fleischhauer, Tilman Pfau, Harald Giessen, "Plasmonic analogue of electromagnetically induced transparency at the Drude damping limit," NATURE MATERIALS, VOL 8, SEPTEMBER (2009).
- [188] Andreas Rottler, Malte Harland, Markus Brohl, Stephan Schwaiger, Daniel Stickler, Andrea Stemmann, Christian Heyn, Detlef Heitmann, Stefan Mendach, Appl. Phys. Lett. 100, 151104 (2012)
- [189] Xinhua Hu, Ming Li, Zhuo Ye, Wai Y. Leung, Kai-Ming Ho, Shawn-Yu Lin, "Design of midinfrared photodetectors enhanced by resonant cavities

- with subwavelength metallic gratings,” *Applied Physics Letters* 93, 241108 (2008).
- [190] D.J. Shelton, J.W. Cleary, J.C. Ginn, S.L. Wadsworth, R.E. Peale, D.K. Kotter and G.D. Boreman, “Gangbuster frequency selective surface metamaterials in terahertz band,” *Electronics Letters*, Vol. 44, No. 22, Oct. 23 (2003).
- [191] M. Guillaumée, L. A. Dunbar, Ch. Santschi, E. Grenet, R. Eckert, O. J. F. Martin, R. P. Stanley, “Polarization sensitive silicon photodiodes using nanostructured metallic grids,” *Applied Physics Letters* 94, 193503 (2009).
- [192] O. Hess, J. B. Pendry, S. A. Maier, R. F. Oulton, J. M. Hamm, K. L. Tsakmakidis, “Active nanoplasmonic metamaterials,” *Nature Materials*, Vol. 11, July (2012).
- [193] Jianqiang Gu, Ranjan Singh, Abul K. Azad, Jiaguang Han, Antoinette J. Taylor, John F. O’Hara, Weili Zhang, “An active hybrid plasmonic metamaterial,” *Optical Materials Express*, Vol. 2, No. 1, January (2012).
- [194] Nian-Hai Shen, Maria Kafesaki, Thomas Koschny, Lei Zhang, Eleftherios N. Economou, Costas M. Soukoulis, “Broadband blueshift tunable metamaterials and dual-band switches,” *Physical Review B*, 79, 161102(R) (2009).
- [195] J.-M. Manceau, N.-H. Shen, M. Kafesaki, C. M. Soukoulis, S. Tzortzakis, “Dynamic response of metamaterials in the terahertz regime: Blueshift tunability and broadband phase modulation,” *Appl. Phys. Lett.* 96, 021111 (2010).
- [196] W. J. Padilla, A. J. Taylor, C. Highstrete, Mark Lee, R. D. Averitt, “Dynamical Electric and Magnetic Metamaterial Response at Terahertz Frequencies,” *Physical Review Letters*, 96, 107401 (2006).
- [197] R. D. Averitt, H. -T. Chen, A. J. Taylor, C. Highstrete, Mark Lee, W. J. Padilla, “Dynamical Metamaterials at Terahertz Frequencies,” *IEEE*, 0-7803-9556-5, (2006).
- [198] H. T. Chen, J. F. O’Hara, A. K. Azad, A. J. Taylor, R. D. Averitt, D. B. Shrekenhamer, W. J. Padilla, “Experimental demonstration of frequency-agile terahertz metamaterials,” *Nature Photonics*, Vol. 2, May (2008).
- [199] Yuanmu Yang, Ran Huang, Longqing Cong, Zhihua Zhu, Jianqiang Gu, Zhen Tian, Ranjan Singh, Shuang Zhang, Jiaguang Han, Weili Zhang, “Modulating the fundamental inductive-capacitive resonance in asymmetric double-split ring terahertz metamaterials,” *Appl. Phys. Lett.* 98, 121114 (2011).
- [200] Evgenia Kim, Y. Ron Shen, Wei Wu, Ekaterina Ponizovskaya, Zhaoning Yu, Alexander M. Bratkovsky, Shih-Yuang Wang, R. Stanley Williams, “Modulation of negative index metamaterials in the near-IR range,” *Appl. Phys. Lett.* 91, 173105 (2007).
- [201] Hou-Tong Chen, Willie J. Padilla, Michael J. Cich, Abul K. Azad, Richard D. Averitt, Antoinette J. Taylor, “A metamaterial solid-state terahertz phase modulator,” *Nature Photonics*, Vol. 3, March (2009).

- [202] Hou-Tong Chen, Willie J. Padilla, Joshua M. O. Zide, Arthur C. Gossard, Antoinette J. Taylor, Richard D. Averitt, "Active terahertz metamaterial devices," *Nature*, Vol 444, Nov. 30, (2006).
- [203] Young Chul Jun, Edward Gonzales, John L. Reno, Eric A. Shaner, Alon Gabbay, Igal Brener, "Active tuning of mid-infrared metamaterials by electrical control of carrier densities," *Optics Express*, Vol. 20, No. 2, (2012).
- [204] Yaroslav Urzhumov, Jae Seung Lee, Talmage Tyler, Sulochana Dhar, Vinh Nguyen, Nan M. Jokerst, Paul Schmalenberg, David R. Smith, "Electronically reconfigurable metal-on-silicon metamaterial," *Physical Review B* 86, 075112 (2012).
- [205] Nathan I. Landy, Hou-Tong Chen, John F. OHara, Joshua M. O. Zide, Arthur C. Gossard, Clark Highstrete, Mark Lees, Antoinette J. Taylor, Richard D. Averitt, Willie J. Padilla, "Metamaterials for Novel Terahertz and Millimeter Wave Devices," *IEEE 1-4244-1449-0*, (2007).
- [206] T. Driscoll, S. Palit, M. M. Qazilbash, M. Brehm, F. Keilmann, Byung-Gyu Chae, Sun-Jin Yun, Hyun-Tak Kim, S. Y. Cho, N. Marie Jokerst, D. R. Smith, D. N. Basov, "Dynamic tuning of an infrared hybrid-metamaterial resonance using vanadium dioxide," *Appl. Phys. Letts.* 93, 024101 (2008).
- [207] Jianguang Han, Akhlesh Lakhtakia, "Semiconductor split-ring resonators for thermally tunable terahertz metamaterials," *Journal of Modern Optics*, 56:4, 554-557 (2009).
- [208] Wan-xia Huang, Xiao-gang Yin, Cheng-ping Huang, Qian-jin Wang, Teng-fei Miao, Yong-yuan Zhu, "Optical switching of a metamaterial by temperature controlling," *Appl. Phys. Letts.* 96, 261908 (2010).
- [209] W. M. Zhu, J. H. Teng, X. H. Zhang, J. M. Tsai, Q. Y. Wu, H. Tanoto, H. C. Guo, T. Bourouina, G. Q. Lo, D. L. Kwong, A. Q. Li, "Polarization Selective Tunable Filter Via Tuning of Fano Resonances in MEMS Switchable Metamaterials," *IEEE 978-1-4673-0325-5, MEMS (2012)*, Paris, France.
- [210] Lumerical Inc., < <http://www.lumerical.com/tcad-products/fdtd/>> Copyright 2003-2013 Lumerical Solutions, Inc. Accessed March 30, 2013.
- [211] CST – Computer Simulation Technology, <<http://www.cst.com/Content/Products/MWS/Overview.aspx>> Copyright 2013 CST Computer Simulation Technology AG. Accessed March 30, 2013.
- [212] Kasap, S.O.; *Optoelectronics and Photonics: Principles and Practices*; Prentice Hall, Upper Saddle River NJ, (2001) pg 5-13.
- [213] Xudong Chen, Tomasz M. Grzegorzcyk, Bae-Ian Wu, Joe Pacheco, Jr., and Jin Au Kong, "Robust method to retrieve the constitutive effective parameters of metamaterials," *Physical Review E* **70**, 016608 (2004).
- [214] D. R. Smith, S. Schultz, P. Markos, and C. M. Soukoulis, "Determination of effective permittivity and permeability of metamaterials from reflection and transmission coefficients," *Physical Review B*, Vol. 65, 195104 (2002).
- [215] Tufts Micro & Nano Fabrication, 2010, Tufts University, March 23, 2010, <http://engineering.tufts.edu/microfab/index_files/Page1009.htm>
- [216] Center for Nanoscale Systems, 2012, Harvard University, Dec. 2012, <<http://www.cns.fas.harvard.edu/facilities/tool.php?MID=171>>

- [217] Center for Nanoscale Systems, 2012, Harvard University, Dec. 2012,
<<http://www.cns.fas.harvard.edu/facilities/tool.php?MID=27>>
- [218] Center for Nanoscale Systems, 2012, Harvard University, Dec. 2012,
<<http://www.cns.fas.harvard.edu/facilities/tool.php?MID=189>>
- [219] F. Krumeich, Swiss Federal Institute of Technology Zurich, "SEM: Imaging with Secondary Electrons," <<http://www.microscopy.ethz.ch/se.htm>>
Modified: 14 May, 2012, Accessed: Dec. 2012.
- [220] F. Krumeich, Swiss Federal Institute of Technology Zurich, "Scanning Electron Microscopy (SEM)," <<http://www.microscopy.ethz.ch/sem.htm>>
Modified: 14 May, 2012, Accessed: Dec. 2012.
- [221] Jasco Analytical Instruments, "FT/IR-4000 SERIES," <
<http://www.jascoinc.com/products/spectroscopy/ft-ir-spectrometers/ft-ir-4000-series>> Copyright 2012. Accessed: Dec 2012.
- [222] Thermo Fisher Scientific Inc, "Nicolet 6700 FT-IR Spectrometer," <
<http://qa.thermoscientific.com/ecom/servlet/productsdetail?storeId=11152&langId=-1&productId=11961710&categoryId=82243>> Accessed: Dec. 2012.
- [223] Center for Nanoscale Systems, 2010, Harvard University, March 23, 2010,
http://www.cns.fas.harvard.edu/facilities/tool_detail.php?MID=54
- [224] M. A. Ordal, R. J. Bell, R. W. Alexander, Jr, L. L. Long, M. R. Querry,
"Optical properties of fourteen metals in the infrared and far infrared: Al, Co, Cu, Au, Fe, Pb, Mo, Ni, Pd, Pt, Ag, Ti, V, and W," Applied Optics, Vol. 24, No. 24, Dec. 15, 1985.
- [225] H. Okamoto, T. B. Massalski, "The Au-Si (Gold-Silicon) System," Bulletin of Alloy Phase Diagrams, Vol. 4, No. 2, 1983, pg 190-191.
- [226] Djurišić, A.B.; E.H. Li; D. Raklć; M.L. Majewski;" Modeling the optical properties of AlSb, GaSb, and InSb," Applied physics. A, Materials science & processing, 2000, vol. 70, pp. 29-32.
- [227] A. chin, P. Bhattacharya, K. H. Chang, D. Biswas, " Optical and structural properties of molecular-beam epitaxial GaAs on sapphire," J. Vac. Sci. Techno, B 7 (2), Mar/Apr 1989.
- [228] B. R. Bennett, J. A. Del Alamo, R. A. Soref, "Carrier-Induced Change in Refractive Index of InP, GaAs, and InGaAsP," IEEE Journl. Of Quan. Elec., Vol. 26, No. 1, Jan. (1990).
- [229] J. G. MendozaAlvarez, F. D. Nunes, N. B. Patel, "Refractive index dependence on free carriers for GaAs," J. Appl. Phys. 51, 4365 (1980).

Appendix

Appendix 1.1

Boundary Conditions for TE polarized light

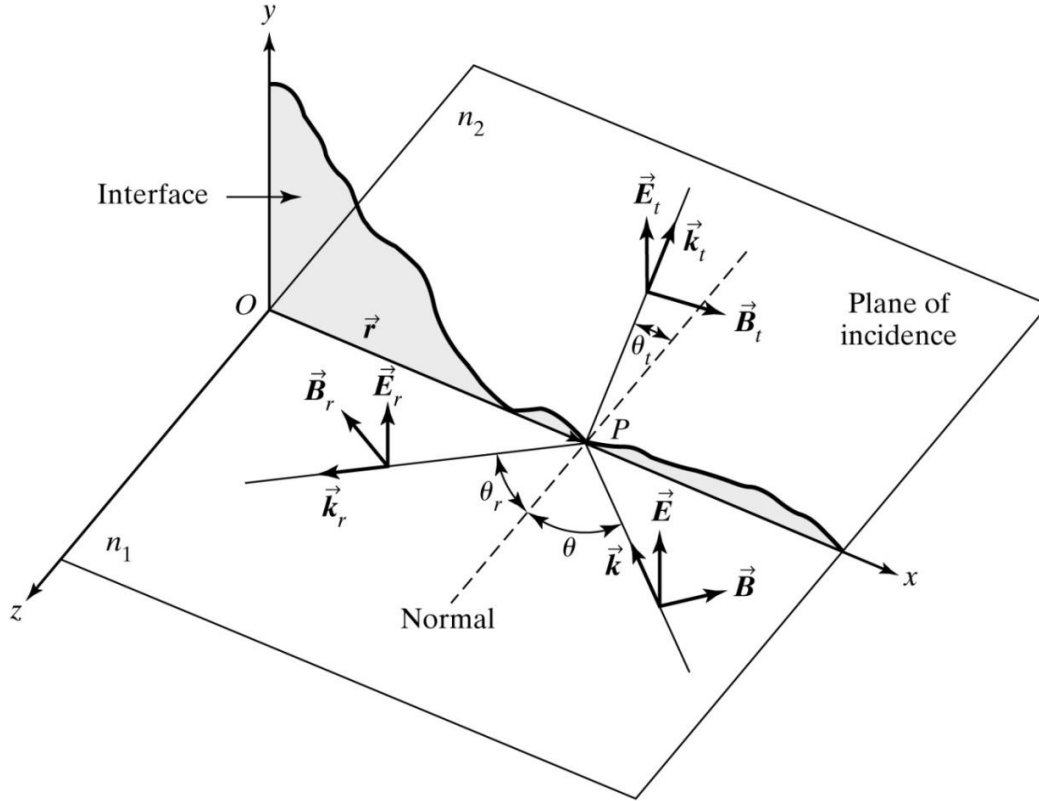


Figure A.1.1: TE polarized light at an interface.

$$\mathbf{E}_o = E \hat{\mathbf{y}}$$

$$\mathbf{E}_{or} = E_r \hat{\mathbf{y}}$$

$$\mathbf{E}_{ot} = E_t \hat{\mathbf{y}}$$

These equations state that the entire electric field is in the y-plane for incident, reflected, and transmitted beams. Also, continuity requires that:

$$E_i + E_r = E_t \quad \dots \text{A.1.1}$$

For the magnetic field similar equations apply:

$$\mathbf{B}_i = (B \cos \theta_i \hat{\mathbf{x}} - B \sin \theta_i \hat{\mathbf{z}}) e^{i(k_i r - \omega t)}$$

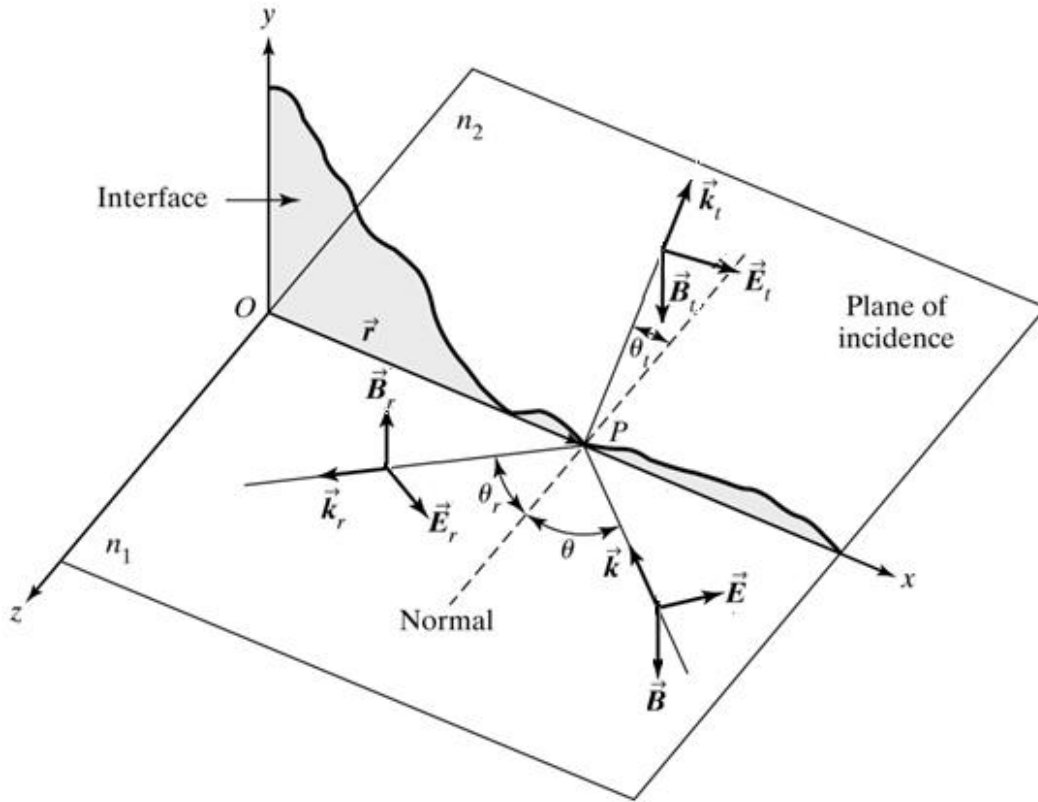
$$\mathbf{B}_r = (-B_r \cos \theta_r \hat{\mathbf{x}} - B_r \sin \theta_r \hat{\mathbf{z}}) e^{i(k_r r - \omega t)}$$

$$\mathbf{B}_t = (B_t \cos \theta_t \hat{\mathbf{x}} - B_t \sin \theta_t \hat{\mathbf{z}}) e^{i(k_t r - \omega t)}$$

Likewise, continuity requires:

$$B_i \cos \theta - B_r \cos \theta = B_t \cos \theta_t \quad \dots \text{A.1.2}$$

Boundary Conditions for TM polarized light



The electric field is no longer completely in the plane of the interface; as such the electric field is now described as:

$$\mathbf{E} = (E \cos \theta \hat{\mathbf{x}} - E \sin \theta \hat{\mathbf{z}}) e^{i(kr - \omega t)}$$

$$\mathbf{E}_r = (E_r \cos \theta_r \hat{\mathbf{x}} + E_r \sin \theta_r \hat{\mathbf{z}}) e^{i(k_r r - \omega t)}$$

$$\mathbf{E}_t = (E_t \cos \theta_t \hat{\mathbf{x}} - E_t \sin \theta_t \hat{\mathbf{z}}) e^{i(k_t r - \omega t)}$$

Therefore, due to continuity, the E-field is described by:

$$E_i \cos \theta + E_r \cos \theta = E_t \cos \theta_t \quad \dots \text{A.1.3}$$

The magnetic field in the TM case is described by:

$$\begin{aligned} \mathbf{B}_o &= -B \hat{\mathbf{y}} \\ \mathbf{B}_{or} &= B_r \hat{\mathbf{y}} \\ \mathbf{B}_{ot} &= -B_t \hat{\mathbf{y}} \end{aligned}$$

Therefore, due to continuity, the B-field over the interface can be written as:

$$B_i + B_r = B_t \quad \dots \text{A.1.4}$$

If equations A.1.2 and A.1.4 are solved in terms of E-field and combined with equations A.1.1 and A.1.3, the reflection and transmission coefficients can be found by eliminating E_t and E_r respectively.

Reflection and Transmission Coefficients

r_{TE} and r_{TM} are the reflection coefficients (r) where reflectance is equal to r^2

$$\begin{aligned} r_{TE} &= \frac{E_r}{E_i} = \frac{\cos \theta - \sqrt{\left(\frac{n_2}{n_1}\right)^2 - \sin^2 \theta}}{\cos \theta + \sqrt{\left(\frac{n_2}{n_1}\right)^2 - \sin^2 \theta}} \\ r_{TM} &= \frac{-\left(\frac{n_2}{n_1}\right)^2 \cos \theta + \sqrt{\left(\frac{n_2}{n_1}\right)^2 - \sin^2 \theta}}{\left(\frac{n_2}{n_1}\right)^2 \cos \theta + \sqrt{\left(\frac{n_2}{n_1}\right)^2 - \sin^2 \theta}} \end{aligned}$$

t_{TE} and t_{TM} are the transmission coefficients (t) where transmittance equals t^2

$$t_{TE} = \frac{E_t}{E_i} = \frac{2 \cos \theta}{\cos \theta + \sqrt{\left(\frac{n_2}{n_1}\right)^2 - \sin^2 \theta}}$$

$$t_{TM} = \frac{2 \left(\frac{n_2}{n_1}\right) \cos \theta}{\left(\frac{n_2}{n_1}\right)^2 \cos \theta + \sqrt{\left(\frac{n_2}{n_1}\right)^2 - \sin^2 \theta}}$$

Appendix 1.2.1 – Greenland Energy Example

Greenland Energy Center a \$600 million Plant

- Max Capacity of 553 megawatts^[8]
- \$1.09/kWh^[8]

60 million in TPV cells (10% extra start-up)

At 260 C a blackbody curve is centered at 5.4μm

Produces a total energy of 4586 W/m²

15% efficiency leaves a total power of 688 W/m²

688W/m² * 178m² ~122kW

In 1 hour roughly **0.688kWh for a 1m² panel** is generated

Cost per watt is projected to be:

\$1.87 per kWh of TPV energy

-No fuel cost for TPV

Another Example (High Volume purchasing of TPV material ~\$75 for 3in X 3in):

-\$600/9in² TPV cells \$103,334/m²

-for \$60M you get 580.6m²

-260°C heat source gives 4586W/m²

-30% system efficiency gives 1376W/m²

-1376W/m² * 580.6m² ~800kW

-800kW * 30years = 18.75GWh

-\$60M / 18.75GWh = \$0.25/kWh of TPV energy

(15% @ 1000C = \$0.0176/kWh)

Gas Plant 30yr operation

\$0.0795/kWh – total production costs 2008 (7.39c fuel; 4.86c/kWh 2010
 4.36c/kWh fuel)
 $(553\text{MW}) \times (30\text{years}) \times (\$0.0795/\text{kWh}) = \$11.55\text{B} + \$0.6\text{B construction} = \12.15B
 $\$12.15\text{B} / (553\text{MW} \times 30\text{years} \times 8766\text{hr/yr}) = \mathbf{\$0.0836/\text{kWh} (\$0.0527/\text{kWh in 2010)}$

Appendix 4.1

MATLAB Calculation of effective permeability and permittivity

```

% need four files to run, the real and imaginary parts of the
% reflection
% and transmission in .txt format. these can be copied and pasted
% straight
% out of cst. First click on the curve in CST, "then copy". Then
% paste into
% an Excel spreadsheet and delete the top information header.
% Finally save
% as .txt file and tab delimited. This program was created using
% an
% article published by Xudong Chen in Physical review e 70,
% 016608 (2004)

```

```

%define mode for effective index
clear
m = 1;

%define thickness of metamaterial in nanometers
d = 1000;

%Desired Plot
Plot1 = 1;
Plot2 = 4;

%Axis area
xmax = 40;
xmin = 10;
ymax = 20;
ymin = -10;

% Insert these variables above for the desired plot
% turn off plot = 0
% magnitude of epsilon = 1
% Imaginary component of epsilon = 2
% Real part of epsilon = 3
% magnitude of mui = 4
% real part of mui = 5

```

```

% imaginary part of mui = 6
% magnitude of refractive index = 7
% real part of refractive index = 8
% imaginary part of refractive index = 9
% magnitude of impedance = 10

>Loading the file names, if yours arn't named this you are
wrong!!!!
%%%%%%%%%%%%%%%%%%%%%%%%%%%%%%%%%%%%%%%%%%%%%%%%%%%%%%%%%%%%%%%%%%%%%%%%
%%%%%%%%
load reflectionRe.txt;
load reflectionIm.txt;
load transmissionRe.txt;
load transmissionIm.txt;

%actual code, you shouldn't need to change anything below here
%%%%%%%%%%%%%%%%%%%%%%%%%%%%%%%%%%%%%%%%%%%%%%%%%%%%%%%%%%%%%%%%%%%%%%%%
%%%%%%%%
F = reflectionRe (:,1);
Rre = reflectionRe (:,2);
Rim = 1i.*reflectionIm (:,2);
Tre = transmissionRe (:,2);
Tim = 1i.*transmissionIm (:,2);
datapoints = length(F);
%good idea to make one file with both real and imaginary parts
rT = Rre+Rim;
tT = Tre+Tim;

%Finding the impedance

%need thickness, speed of light, and wavevector
c = 3*10^8;
d = d*10^-9;
k = 2.*pi().*(F*10^12)/c;
kd = k*d;
%first magnitude of reflection and transmission
r = (Rre.^2 + (1i.*Rim).^2).^(.5);
t = (Tre.^2 + (1i.*Tim).^2).^(.5);

%also need to know normalized transmission coefficient (tn)
%tn is both real and imaginary

tn = tT.*exp(1i.*k.*d);

%impedence calculation
%%%%%%%%%%%%%%%%%%%%%%%%%%%%%%%%%%%%%%%%%%%%%%%%%%%%%%%%%%%%%%%%%%%%%%%%
%%%%%%%%
ZTop = (1+rT).^2-tn.^2;

```

```

ZBottom = (1-rT).^2-tn.^2;
z = (ZTop./ZBottom).^(.5);

zre = real(z);
zRe = zre;

%the real part of the impedance must be positive
for p = (1:datapoints);
    if zRe(p,1) < 0
        zRe(p,1) = zRe(p,1)*-1;
    else zRe(p,1) = zRe(p,1);
    end
end

%the sign of the real impedance before the above correction
determines the
%sign of the imaginary part
for p = 2;
    if zre(2,1) < 0
        zsign = -1;
    else zsign = 1;
    end
end

zim = imag(z);
zIm = zsign.*zim;

%magnitude of the impedance
zmag = (zRe.^2 + zIm.^2).^(.5);

%effective index of refraction
%%%%%%%%%%%%%%%%%%%%%%%%%%%%%%%%%%%%%%%%%%%%%%%%%%%%%%%%%%%%%%%%%%%%%%%%%%%%%%
%%%%%%%%%%%%%%%%%%%%%%%%%%%%%%%%%%%%%%%%%%%%%%%%%%%%%%%%%%%%%%%%%%%%%%%%%%%%%%

%finding reflection squared
r2 = (real(rT).^2-imag(rT).^2)+2.*1i.*(imag(rT).*real(rT));
tn2 = (real(tn).^2-imag(tn).^2)+2.*1i.*(imag(tn).*real(tn));

%Inside the arc cos
%complicated because we are multiplying complex numbers
ICLeft = (real(tn)./(real(tn).^2+imag(tn).^2));
ICRight = (-imag(tn)./(real(tn).^2+imag(tn).^2));
left = ICLeft+1i.*ICRight;
Inside = left.*(1-r2-tn2);

%the arccos
nTop = acos(Inside);
nBottom = kd;

```

```

%Real n calculations
%first need imaginary for the sign of the real
nIm = imag(nTop./nBottom);

%using continuity of the index to calculate the real index
for p = 2;
    if nIm(2,1) < 0
        nsign = -1;
    else nsign = 1;
    end
end

%calculation of the real
nRe = nsign.*real(nTop./nBottom)+(2.*pi().*m./(kd));

%calculation of the imaginary
nImr = nIm;
for p = (1:datapoints);
    if nIm(p,1) < 0
        nImr(p,1)= nIm(p,1)*-1;
    else nImr(p,1) = nIm(p,1);
    end
end

%calculation of the total index and it's magnitude
n = nRe+1i.*nImr;
nmag = (nImr.^2 + nRe.^2).^(.5);

%Finally permittivity and permeability n./z;
%%%%%%%%%%%%%%%%%%%%%%%%%%%%%%%%%%%%%%%%%%%%%%%%%%%%%%%%%%%%%%%%%%%%%%%%
%%%%%%%%%%%%%%%%%%%%%%%%%%%%%%%%%%%%%%%%%%%%%%%%%%%%%%%%%%%%%%%%%%%%%%%%

%multiplying complex numbers of the real part of epsilon
RepsiTop = (real(n).*real(z))+(imag(n).*imag(z));
RepsiBottom = (real(z).^2)+(imag(z).^2);
%Real part of epsilon
Repsi=(RepsiTop./RepsiBottom);

%multiplying complex numbers of the imaginary part of epsilon
IepsiTop = (imag(n).*real(z))-(real(n).*imag(z));
IepsiBottom = (real(z).^2)+(imag(z).^2);
%imaginary part of epsilon
Iepsi = (IepsiTop./IepsiBottom);

%magnitude and complex epsilon
epsi = 1i.*Iepsi+Repsi;
epsimag = (Iepsi.^2 + Repsi.^2).^(.5);

%calculation of mui
mui = n.*z;
Rmui = real(mui);
Imui = imag(mui);
muimag = (real(mui).^2 + imag(mui).^2).^(.5);

```



```

%Plotting
%%%%%%%%%%%%%%%%%%%%%%%%%%%%%%%%%%%%%%%%%%%%%%%%%%%%%%%%%%%%%%%%%%%%%%%%
%%%%%%%%%%%%%%%%%%%%%%%%%%%%%%%%%%%%%%%%%%%%%%%%%%%%%%%%%%%%%%%%%%%%%%%%

%Takes input at the begining and assigns the correct data array
for p = (0:10);
    if p == Plot1
        A = p;
    end
    if p == Plot2
        B = p;
    end
end
Graph1 = 1;
Graph2 = 1;

if A == 0
    Graph1 = 0;
end
if B == 0
    Graph2 = Graph1;
end
if A == 1
    Graph1 = epsimag;
end
if B == 1
    Graph2 = epsimag;
end
if A == 2
    Graph1 = Repsi;
end
if B == 2
    Graph2 = Repsi;
end
if A == 3
    Graph1 = Iepsi;
end
if B == 3
    Graph2 = Iepsi;
end
if A == 4
    Graph1 = muimag;
end
if B == 4
    Graph2 = muimag;
end
if A == 5
    Graph1 = Rmui;
end
if B == 5
    Graph2 = Rmui;
end
if A == 6
    Graph1 = Imui;

```

```

end
if B == 6
    Graph2 = Imui;
end
if A == 7
    Graph1 = nmag;
end
if B == 7
    Graph2 = nmag;
end
if A == 8
    Graph1 = nRe;
end
if B == 8
    Graph2 = nRe;
end
if A == 9
    Graph1 = nImr;
end
if B == 9
    Graph2 = nImr;
end
if A == 10
    Graph1 = zmag;
end
if B == 10
    Graph2 = zmag;
end

%%%%%%%%%%%%%%%%%%%%%%%%%%%%%%%%%%%%%%%%%%%%%%%%%%%%%%%%%%%%%%%%%%%%%%%%%%%%%%
%%%%%%%%%%%%%%%%%%%%%%%%%%%%%%%%%%%%%%%%%%%%%%%%%%%%%%%%%%%%%%%%%%%%%%%%%%%%%%
plot(F,Graph1,F,Graph2,F,0)
axis([xmin xmax ymin ymax])

```

Appendix 5.1

Metamaterial emitter fabrication procedure

1) Grounding Plane Deposition

Dicing - Opportunity to dice into smaller sizes

- Use specialty sapphire blade
-Si or glass blades cannot withstand a sapphire substrate

Pre-lithography clean - sapphire

- HF:H₂O (1:9) – 30 sec soak
- DI water rinse
- HCl:H₂O (1:1) – 90 sec soak
- DI water rinse
- N₂ Air gun dry

Grounding Plane Deposition

(Denton E-Beam-want base pressure of at least 2e-6)

*****DO NOT PERFORM AT TUFTS*****

- Any metal can be used - must match metal of MM pattern
- Typically Pt on sapphire - 100nm

Atomic Layer Deposition (ALD)

*****Perform directly after metal deposition*****

- Standard Al_2O_3 recipe

1st precursor - $\text{Al}(\text{CH}_3)_3$

2nd precursor - H_2O

Pressure- 1 Torr pulses

Temperature- 250 C

Apprx. Rate - 5.5 Å/min

*** Check pulses to make sure precursors are flowing***

Dicing - Opportunity to dice into smaller sizes

- Use specialty sapphire blade
- Si or glass blades cannot withstand a sapphire substrate

2) E-Beam Lithography and Deposition

E-Beam lithography

- Dynamic clean – IPA, Acetone, spin dry
- Spin PMMA C2 – 4000 RPM – 45 sec – 5min bake at 180C
- Exposure dose – 480 mW/cm²
- Paint corner of chip with conductive paste, and perform align write field to the shapes on the paste
- Development – MIBK (3:1) Developer – 60 sec
–IPA – 30 sec
–N₂ Air gun dry

Contact Deposition

(Denton -want base pressure of at least 2e-6)

- Pt ~35nm
- Immediate lift-off recommended in Acetone
- Sonication will be needed

3) Confirm Structure in SEM

Appendix 5.2.1

Photonic Crystal Fabrication Procedure

The first step in fabricating an operational PhC for a TPV application is diode fabrication described in Appendix 5.3

This procedure covers the fabrication of a metallic PhC on either a TPV diode or bulk semiconductor substrate.

4) Diode Preparation

***** If using a fabricated photodiode*****

Pre-lithography clean

- Acetone sonication – 2 min
- IPA rinse
- DI water bath – 5 min
- N₂ Air gun dry
- Hot plate bake 150 C – 5 min

Photolithography – For etching of ARC layer

- Dynamic clean – Acetone, IPA spray, Spin Dry
- Spin SPR 1813 – 4000 RPM –45 sec
- Mask – SiNx etch Mask 3 (Mask 2 if non-MIMs design) “MIMS and Fingers” Mask
- Exposure dose – 4 sec – 20 mW power – I line
- 6 sec – Harvard MJB4 (any lamp intensity)
- Development – MFCD 26 – 25 sec

SiNx etching

Dry Etch – South Bay RIE (preferred)

SF6 – 6 sccm

O2 – 12 sccm

Power – 150W

Pressure ~100mTorr

Time: 90 sec.

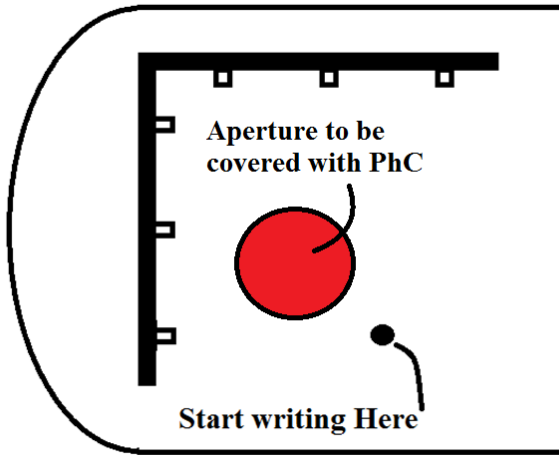
Remove resist in acetone

5) E-Beam Lithography and Deposition

E-Beam lithography

- Dynamic clean – Acetone, IPA, spin dry

- Spin PMMA C6 – 3000 RPM – 45 sec – 5min bake at 180C
- Exposure dose – With contact pad 440 mW/cm²
- PhC recipe should be ~100-200um larger then aperture to be covered



- Paint corner of chip with conductive paste, and perform align write field to the shapes on the paste
- Development – MIBK (3:1) Developer – 60 sec
–IPA – 30 sec
–N₂ Air gun dry

Contact Deposition

(Denton or Sharon E-Beam-want base pressure of at least 2e-6)

- Paint S1813 resist on chip prior to deposition – do not cover pattern!
- Ti/Au – 4nm/96nm
- Immediate lift-off recommended in Acetone
- **Sonication will be needed – BE CAREFUL!!!!**

6) SiN_x Deposition and Etch in CVD

SiN_x Deposition

- Clean sample
(solvent or HCL:H₂O [1:1] – NO HF!! If using GaSb)
- Deposit Si₃N₄
(STS PECVD HFSiN recipe for ~10 mins should yield ~110nm)

Measured thickness with ocean optics reflectometer is ~110

SiN_x Etching - Lithography

- Before spinning always run a dynamic clean
- During a 40s spin cycle: Acetone spray, IPA spray, spin dry

- Immediately follow:

Resist: S1822 for 45s @3k RPM

Pre-exposure bake: 75s @115°C

Yields ~2.65-2.8um

Alternatively:

Resist:S1813 for 45s @4k RPM

Pre-exposure bake for 75s @115°C

Yields ~1.38um

- Expose resist with **Mask 5**
(**Mask 4 if no isolation trench in process flow**)
S1822: dosage 19.8 mW i-line, 40mW h-line for 8 sec
S1813: dosage 19.8 mW i-line, 40mW h-line for 6 sec
- Develop :
S1822: MFCD26 for 50-55sec
S1813: MFCD26 for 25 sec

Etch SiNx – RIE

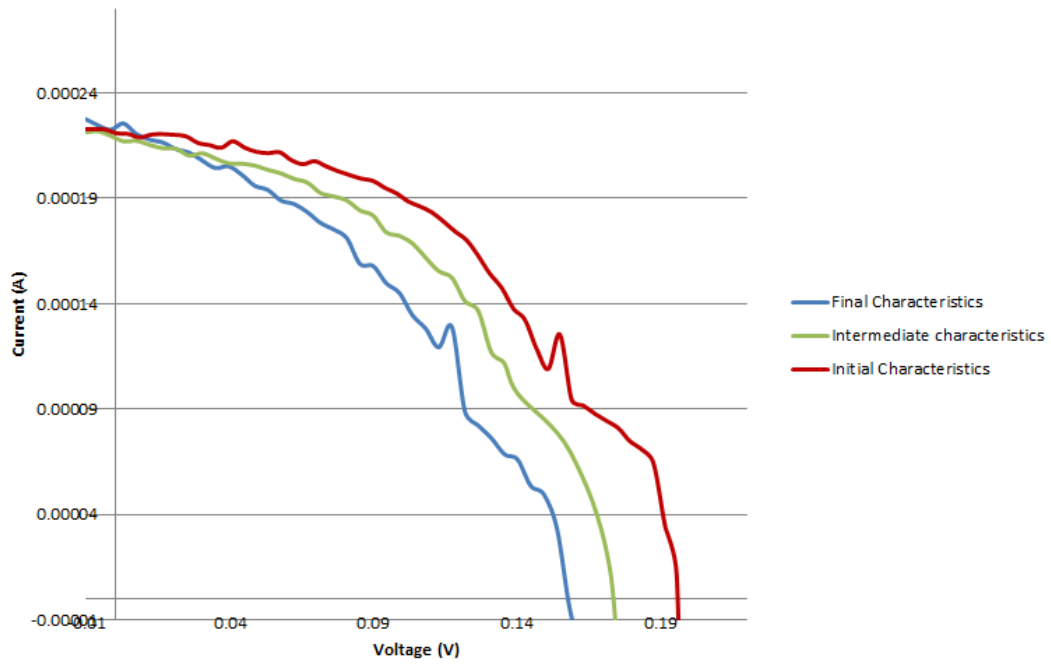
- SOUTHBAY RIE: Recipe: SF6 (12 sccm), O2 (6 sccm), 1 min for ~110nm
Sonicate for two minutes in acetone
Acetone rinse, IPA rinse, DI rinse
Blow dry

7) Confirm Structure in SEM

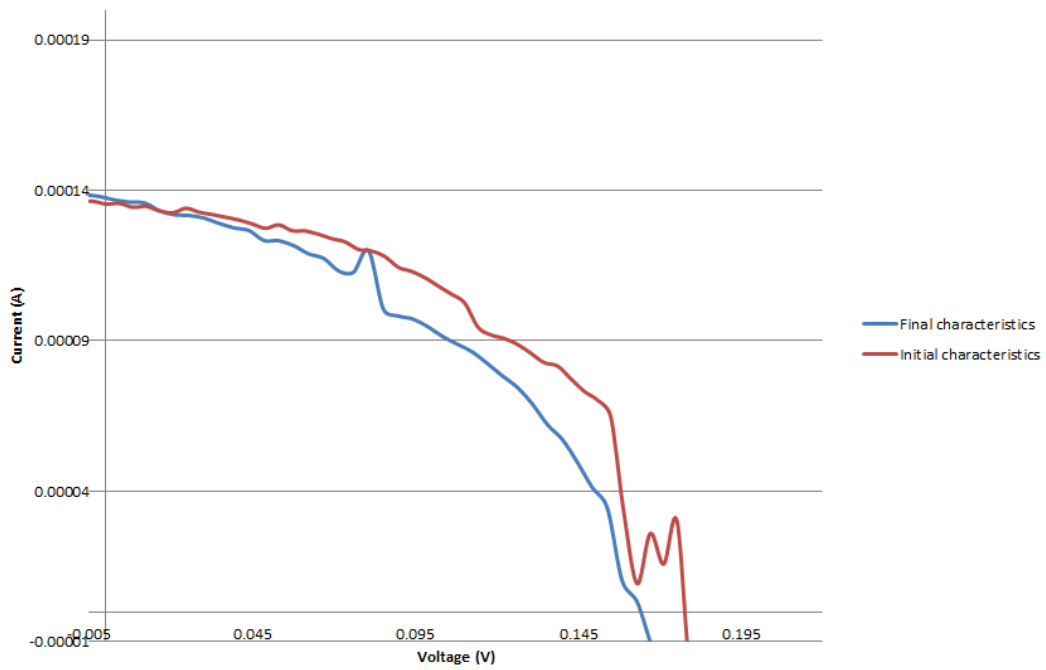
Appendix 5.2.2

Photodiodes *without PhC enhancements* after side by side processing with samples from chapter 4.1. Initial IV curves before photonic crystal processing (Red), and final IV curves after processing (Blue) are shown.

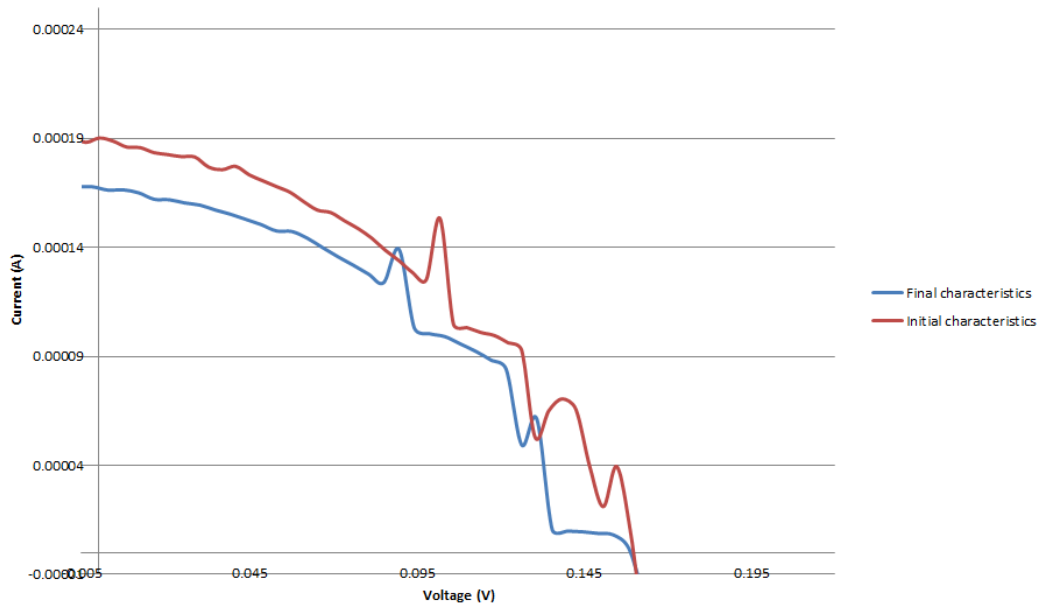
Apperture over course of processing



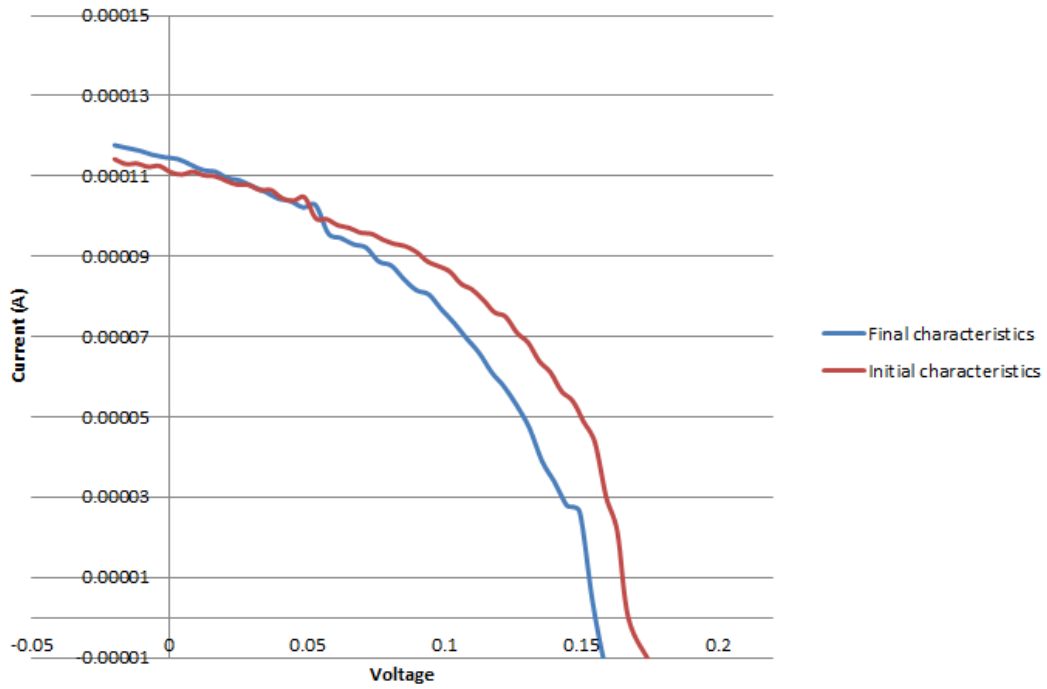
Apperture over course of processing



Apperture over course of processing



Apperture over course of processing

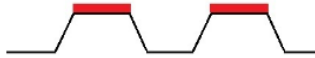


Appendix 5.3

Diode and MIMs processing procedure – used for IMF diodes and apertures

Prep: Dice or Cleave wafer (recommend cutting into quarters for a 1cm chip to leave plenty of extra room on the edges because you'll get a few mm of unusable area on the edges due to resist edge bead.)

1. Mesa etch



- a. Clean sample:
 - Sonicate in acetone, IPA rinse, DI rinse(dynamic clean absolute minimum)
- b. Before spinning always run a dynamic clean
 - During a 40s spin cycle: Acetone spray, IPA spray, spin dry
- c. **Immediately follow:** spin on resist (S1822 preferred or Az9245):
 - i. S1822: 40s @3k RPM, bake for ~75s @115°C
 - ii. AZ9245: 40s @3.5k RPM and pre-exposure bake for 140sec @115°C yields ~4.9-5um
- d. Expose resist with **Mask 1** (soft contact)
 - i. S1822: dosage 19.8 mW i-line, 40mW h-line for 8 sec
 - ii. AZ9245: dosage requirement: 900mJ i-line
Have used: 28s @31.5mW i-line, 58.7 mW h-line Develop

– make sure there are no “cloudy” or “rainbow” areas

 - iii. S1822: 50-55 sec in MFCD26
 - iv. AZ9245: ~5min in MFCD26
- e. Etch to bottom contact layer (UNAXIS RIE)
 - i. Apply **small** amount thermal paste and **carefully** push edges of chip down to flatten
 - ii. **ALWAYS RUN A TEST ETCH FIRST TO GET ETCH RATE**
 - this is because etch rate will fluctuate daily
 - iii. UNAXIS RIE:
 1. etch rate for GaSb ~17.3-18.1 nm/s - resist etch rate ~0.337um/min
 2. etch rate for SLS(L12-24_ is ~4.77-5nm/s
(Measured with dektak profilometer)
 - iv. Recipe is GaAs_Vandervelde: RF power=500W, bias power = 100W, 15sccm BCl₃, 5sccm Cl₂, 7.5sccm Ar, 3.8sccm N₂
- f. Remove resist and thermal paste residue
 - i. Acetone rinse to remove most of the thermal paste residue

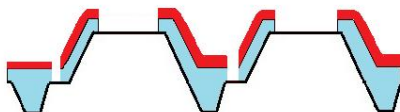
- ii. Sonicate for two minutes in acetone, followed by acetone rinse, IPA rinse, DI rinse
- iii. Blow dry
- g. Measure in dektak and repeat Step 1 if not at correct etch depth.

2. Trench Etch (Optional for Fingers-Required for MIMs)



- a. Before spinning always run a dynamic clean
 - During a 40s spin cycle: Acetone spray, IPA spray, spin dry
- b. **Immediately follow:** spin on resist (S1822 preferred or Az9245):
 - i. S1822: 40s @3k RPM, bake for ~75sec @115°C
 - ii. AZ9245: 40s @3.5k RPM and pre-exposure bake for 140sec @115°C yields ~4.9-5um
- c. Expose resist with **Mask 2** (soft contact)
 - i. S1822: dosage 19.8 mW i-line, 40mW h-line for 8 sec
 - ii. AZ9245: dosage requirement: 900mJ i-line
Have used: 28s @31.5mW i-line, 58.7 mW h-line
- d. Develop – make sure there are no “cloudy” or “rainbow” areas left-check with microscope
 - i. S1822: 50-55 sec in MFCD26
 - ii. AZ9245: ~5min in MFCD26
- e. Etch to bottom contact layer (UNAXIS RIE)
 - i. Apply **small** amount thermal paste and **carefully** push edges of chip down to flatten
 - ii. Perform a 2 micron etch depth using rates from Step 1.
 - iii. UNAXIS RIE:
 - 1. etch rate for GaSb ~17.3-18.1 nm/s - resist etch rate ~0.337um/min
 - 2. etch rate for SLS(L12-24_ is ~4.77-5nm/s)
(Measured with dektak profilometer)
 - iv. Recipe is GaAs_Vandervelde: RF power=500W, bias power = 100W, 15sccm BCl₃, 5sccm Cl₂, 7.5sccm Ar, 3.8sccm N₂
- f. Remove resist and thermal paste residue
 - i. Acetone rinse to remove most of the thermal paste residue
 - ii. Sonicate for two minutes in acetone, followed by acetone rinse, IPA rinse, DI rinse
 - iii. Blow dry

- g. A specific Etch Depth is not completely require, we tend to use a time to give us a two micron depth utilizing etch rates from Step 1. However, It is still required to measure the depth with a Profilometer.



3. Si_3N_4 isolation layer

- Clean sample
- Deposit Si_3N_4 (STS PECVD HFSiN recipe for ~10 mins should yield ~110nm)
 - Measured thickness with ocean optics reflectometer is ~110
- Before spinning always run a dynamic clean
 - During a 40s spin cycle: Acetone spray, IPA spray, spin dry
- Immediately follow:** Spin on resist
 - (S1822 for 45s @3k RPM and pre-exposure bake for 75s @115°C yields ~2.65-2.8um)
 - (S1813 for 45s @4k RPM and pre-exposure bake for 75s @115°C yields ~1.38um)
- Expose resist with **Mask 3 (Mask 2 if no isolation trench in process flow)**
 - S1822: dosage 19.8 mW i-line, 40mW h-line for 8 sec
 - S1813: dosage 19.8 mW i-line, 40mW h-line for 6 sec
- Develop (
 - S1822: MFCD26 for 50-55sec
 - S1813: MFCD26 for 25 sec
- Etch Si_3N_4
 - SOUTHBAY RIE: Recipe: SF_6 (12 sccm), O_2 (6 sccm), 1 min for ~110nm
- Remove resist and thermal paste residue
 - Acetone rinse to remove most of the thermal paste residue
 - Sonicate for two minutes in acetone, followed by acetone rinse, IPA rinse, DI rinse
 - Blow dry



4. Contact Deposition/window etch

- Before spinning always run a dynamic clean
 - During a 40s spin cycle: Acetone spray, IPA spray, spin dry
- Immediately follow:** spin on resist
 - AZ9245: 40s @3.5k RPM and pre-exposure bake for 140sec @115°C yields ~4.9-5um

- c. Expose resist with **Mask 4 (Mask 3 if no isolation trench in process flow)**
 - i. AZ9245: dosage requirement: 900mJ i-line
Have used: 28s @31.5mW i-line, 58.7 mW h-line Develop – make sure there are no “cloudy” or “rainbow” areas left-check with microscope
- d. O₂ plasma descum (75W, 20s, 40sccm O₂)
- e. Chemical Clean:
 - HCl:H₂O (1:1) clean for 1 min
 - HF:H₂O (1:9) clean for 15 sec (**GaAs chips only**)
- f. Deposit ohmic contact recipe (EE-3 e-beam @harvard)
 - i. GaSb recipe (N and P type) = Ti/Pt/Au (50/50/300nm)
 - ii. GaAs recipe (N type) = Ge/Au/Ni/Au (26/54/15/300nm) – RTP – 30sec. 380C
 - iii. GaAs recipe (P type) = Ti/Pt/Au (50/50/300nm)
 - iv. Si recipe (N and P type) = Cr/Au (12/300nm)
 - v. Have used base pressure of 2e-6 or better
- g. Liftoff resist
 - i. Soak in Acetone watch carefully for liftoff
 - ii. If lift-off is not occurring lightly brush with a swab
 - iii. To speed up liftoff, sonicate in acetone for 1 or 2 sec at a time (last resort)
 - iv. Remove the substrate Acetone, and rinse with isopropanol/ DI water, then blow dry with nitrogen

5. ARC deposition and etch

- a. Clean sample
- b. Deposit Si₃N₄ (STS PECVD HFSiN recipe for ~10 mins should yield ~110nm)
 - i. Measured thickness with ocean optics reflectometer is ~110
- c. Before spinning always run a dynamic clean
 - During a 40s spin cycle: Acetone spray, IPA spray, spin dry
- d. **Immediately follow:** Spin on resist
 - (S1822 for 45s @3k RPM and pre-exposure bake for 75s @115°C yields ~2.65-2.8um)
 - (S1813 for 45s @4k RPM and pre-exposure bake for 75s @115°C yields ~1.38um)
- e. Expose resist with **Mask 5 (Mask 4 if no isolation trench in process flow)**
 - ii. S1822: dosage 19.8 mW i-line, 40mW h-line for 8 sec
 - iii. S1813: dosage 19.8 mW i-line, 40mW h-line for 6 sec
- f. Develop
 - iv. S1822: MFCD26 for 50-55sec
 - v. S1813: MFCD26 for 25 sec
- g. Etch Si₃N₄

- vi. SOUTHBAY RIE: Recipe: SF₆ (12 sccm), O₂ (6 sccm), 1 min for ~110nm
 - h. Remove resist and thermal paste residue
 - vii. Acetone rinse to remove most of the thermal paste residue
 - viii. Sonicate for two minutes in acetone, followed by acetone rinse, IPA rinse, DI rinse
 - ix. Blow dry
6. **Post Processing:** dice to get chips, mount and wirebond to LCC; SEM to see quality of deposition and liftoff, etc.

Appendix 5.4

Metamaterial polarizer fabrication procedure:

1) Ohmic Contact Deposition

Note: Should also create an Ohmic contact TLM pattern with this step

Pre-lithography clean

- Acetone sonication – 2 min
- IPA rinse
- DI water bath – 5 min
- N₂ Air gun dry
- Hot plate bake 150 C – 5 min

Photolithography

- Dynamic clean – Acetone, IPA spray, Spin Dry
- Spin SPR 1813 – 4000 RPM – 45 sec
- Mask – “U” shaped contact pad – 100um larger than MM to be created
Largest “U” shape is 1mm² and decreases by 100um per pattern
- Exposure dose – 4 sec – 20 mW power – i line
- 6 sec – Harvard MJB4 (any lamp intensity)
- Development – MFCD 26 – 25 sec

Oxygen Plasma Descum

- Tufts: Oxygen flow 100 sccm – 200 Watts – 35 sec
- Harvard: Oxygen flow 10 sccm – 100 Watts – 60 sec

Pre-Deposition Clean

***** Must occur IMMEDIATELY before deposition – Pre-vent chamber and IMMEDIATELY begin pump down*****

- HCl:H₂O (1:1) – 1 min soak
- DI water rinse
- HF:H₂O (1:9) – 30 sec soak (4:1 mix of bottled 50% HF solution)
- DI water rinse
- N₂ Air gun dry

Ohmic Contact Deposition – n-type GaAs

(Sharon E-Beam-want base pressure of at least 2e-6)

*****DO NOT PERFORM AT TUFTS*****

- Ge/Au/Ni/Au – 26nm/54nm/14nm/100nm – Rate(A/s) 2/2/1/2
– Approx. current – (0.08/0.12/0.08/0.12)
- Immediate lift-off recommended in Acetone
- **No Sonication!**

Thermal Processing

- RTP – 30 sec – 380 C – Ar gas (recipe in the RTP – Vanderv_GaAs)
Use RTP-2 at CNS

SiN_x Deposition

- Done Immediately after RTP
- Perform a chemical clean prior to SiN_x deposition
HCl:H₂O (1:1) – 1 min soak
DI water rinse
HF:H₂O (1:9) – 30 sec soak
DI water rinse
N₂ Air gun dry
- Place immediately in STS PECVD – 15min - HT:SiN recipe
– Approx. Thickness 150nm

2) E-Beam Lithography Deposition

Photolithography

- Dynamic clean – Acetone, IPA spray, Spin Dry
- Spin SPR 1813 – 4000 RPM – 45 sec – bake 75s @ 115°C
- Mask – Use large square pattern; “U” shaped ohmic contact should be exposed to light
- Exposure dose – 4 sec – 20 mW power – i line
– 6 sec – Harvard MJB4 (any lamp intensity)
- Development – MFCD 26 – 25 sec

SiN etching

Dry Etch – South Bay RIE (preferred)

SF6 – 6 sccm
O2 – 12 sccm
Power – 150W
Pressure ~100mTorr
Time: 90 sec.

Wet Etch

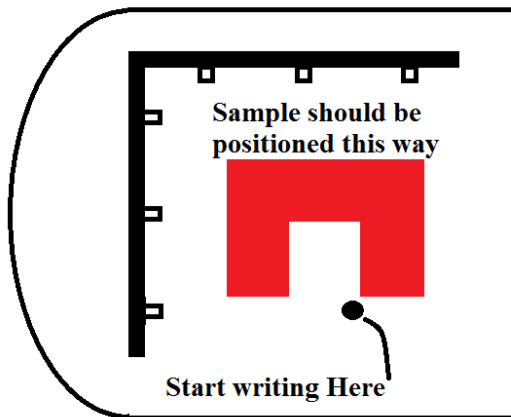
HF:H₂O (1:9) – 25 sec soak
HCl:H₂O (1:1) – 1 min soak
DI water rinse
HF:H₂O (1:9) – 15 sec soak
DI water rinse

E-Beam lithography

- Dynamic clean – Acetone, IPA, spin dry
- Spin PMMA C6 – 3000 RPM – 45 sec – 5min bake at 180C
- Exposure dose – With contact pad 440 mW/cm²
– Without contact pad 400 mW/cm²

Note: Contact pad creates a slightly thicker resist. The second dosage is in case one wants to test their patten without contacts. A contact pad should be present at this point in the procedure.

- “U” shape should be placed in sample holder as shown below



- Paint corner of chip with conductive paste, and perform align write field to the shapes on the paste
- Development – MIBK (3:1) Developer – 60 sec
–IPA – 30 sec
–N₂ Air gun dry

Contact Deposition

(Denton or Sharon E-Beam-want base pressure of at least 2e-6)

- Paint S1813 resist on chip prior to deposition – do not cover pattern!
- Ti/Au – 4nm/96nm
- Immediate lift-off recommended in Acetone
- Sonication will be needed

3) Schottky Contact Deposition

Photolithography

- Dynamic clean – Acetone, IPA, spin dry
- Spin SPR 1813 – 4000 RPM – 45 sec - bake 75s @ 115°C
- Mask- rectangle shape which matches “U” shaped ohmic contact
Align just next to hole in U
- Exposure dose – 4 sec – 20 mW power – i line
- 6 sec – Harvard MJB4 (any lamp intensity)
- Development – MFCD 26 – 25 sec

*****DO NOT CLEAN WITH HF, No chemical clean needed*****

(It will remove the SiNx)

Contact Deposition

(Denton or Sharon E-Beam-want base pressure of at least 2e-6)

- Ti/Au – 12nm/150nm
- Immediate lift-off recommended in Acetone
- **No Sonication!**

4) Confirm Structure in SEM

Appendix 6.4.2

Calculation of increased carrier generation for an 800 μm X 800 μm metamaterial

Applied Current: 410 mA

Applied Voltage: 5 V

GaAs carrier mobility: 8,500 cm²/V_s

Contact area: 0.64 cm^2

Semiconductor volume: $2.56 \times 10^{-5} \text{ cm}^3$

Charge of electron: $1.602 \times 10^{-19} \text{ C}$

Finding #electrons per sec.:

$$\text{mobility} \left(\frac{\text{Applied voltage}}{\text{Contact area}} \right) = 66,385 \frac{\text{electrons}}{\text{sec}}$$

Finding carrier concentration [$1/\text{cm}^3$]:

$$\frac{\text{Applied Current}}{(\text{charge of electron})(\text{Semiconductor Volume})} = 9.992 \times 10^{22} \left[\frac{\text{electrons}}{(\text{cm}^3 \text{s})} \right]$$
$$\frac{9.992 \times 10^{22} \left[\frac{\text{electrons}}{(\text{cm}^3 \text{s})} \right]}{66,385 \left[\frac{\text{electrons}}{\text{sec}} \right]} = 1.51 \times 10^{18} \left[\frac{1}{\text{cm}^3} \right]$$